INTERNATIONAL DOCTORAL
SCHOOL OF THE USC

Verónica
Villa Ortega

PhD Thesis

Analysis and follow-up of gravitational wave signals from mergers of compact binaries

Santiago de Compostela, 2024

Doctoral Programme in Nuclear and Particles Physics

ESCOLA DE DOUTORAMENTO
INTERNACIONAL DA USC

DOCTORAL THESIS

ANALYSIS AND FOLLOW-UP OF GRAVITATIONAL WAVE SIGNALS FROM MERGERS OF COMPACT BINARIES

Author

Verónica Villa Ortega

Supervisors: Thomas Dent and Juan Calderón Bustillo

Tutor: Jaime Álvarez Muñiz

DOCTORAL PROGRAMME IN NUCLEAR AND PARTICLE PHYSICS

SANTIAGO DE COMPOSTELA

A mis abuelos, y al sofá de la cocina.

Verónica Villa Ortega acknowledges support from the Ministry of Science, Innovation and Universities (MICIU) of Spain (FPI grant ref. PRE2018-085436), from a fellowship from "la Caixa" Foundation (ID100010434) and from the European Union's Horizon2020 research and innovation programme under the Marie Sklodowska-Curie grant agreement No 847648. This work has received financial support from the Xunta de Galicia (CIGUS Network of Research Centres), by European Union ERDF, and by the "María de Maeztu" Units of Excellence program MDM-2016-0692 and the Spanish Research State Agency and the Spanish Agencia Estatal de Investigaci´on through the grant PID2020- 118635GB-I00 funded by MCIN/AEI/10.13039/501100011033. This material is supported by computational resources provided by the LIGO Laboratory and supported by National Science Foundation Grants PHY-0757058 and PHY-0823459. This research has also made use of data or software obtained from the Gravitational Wave Open Science Center (gw-openscience.org), a service of LIGO Laboratory, the LIGO Scientific Collaboration, the Virgo Collaboration, and KAGRA. LIGO Laboratory and Advanced LIGO are funded by the United States National Science Foundation (NSF) as well as the Science and Technology Facilities Council (STFC) of the United Kingdom, the Max-Planck-Society (MPS), and the State of Niedersachsen/Germany for support of the construction of Advanced LIGO and construction and operation of the GEO600 detector. Additional support for Advanced LIGO was provided by the Australian Research Council. Virgo is funded, through the European Gravitational Observatory (EGO), by the French Centre National de Recherche Scientifique (CNRS), the Italian Istituto Nazionale di Fisica Nucleare (INFN) and the Dutch Nikhef, with contributions by institutions from Belgium, Germany, Greece, Hungary, Ireland, Japan, Monaco, Poland, Portugal, Spain. The construction and operation of KAGRA are funded by Ministry of Education, Culture, Sports, Science and Technology (MEXT), and Japan Society for the Promotion of Science (JSPS), National Research Foundation (NRF) and Ministry of Science and ICT (MSIT) in Korea, Academia Sinica (AS) and the Ministry of Science and Technology (MoST) in Taiwan.

Summary

Since the first detection of a gravitational wave from the coalescence of a binary black hole in September 2015, 90 gravitational-wave signals from compact binary coalescence systems have been observed by the LIGO-Virgo-KAGRA Collaboration. Among these signals, the detection of the merger of two neutron stars followed by an electromagnetic signal in August 2017 opened the doors to multi-messenger astronomy with gravitational waves, enabling the study of extreme astrophysical processes. Since then, efforts in gravitational wave searches have increased to rapidly identify events involving neutron stars in order to send quick alerts to electromagnetic and neutrino observatories. In this context, being able to estimate the parameters of the gravitational wave sources becomes crucial for guiding these follow-up observation decisions. Unfortunately, parameters such as component masses and spins are measured with high uncertainty by real-time searches and must be estimated after the candidate event detection.

This thesis focuses on the development and implementation of two algorithms to aid guiding follow-up decisions in PyCBC Live, one of the existing low-latency searches for signals from compact binary coalescences. The first algorithm is a classification method that assigns probabilities of containing neutron star or black hole components to the candidate events, taking less than 1 minute to compute. The second method utilizes the trigger event detected by the search as a starting point and estimates the uncertainties in the parameters across the different directions of the parameter space using a Fisher matrix approximation, with a computing time around 1 minute.

Overall, this research contributes to the ongoing efforts to refine GW analysis methods, ultimately aiming to provide the astrophysical community with timely and precise information for follow-up investigations.

Objectives

The main goal of this thesis is to improve the existing methods used for detecting and analyzing gravitational-wave signals generated in the mergers of binary compact objects. The detection of these signals in the data from the ground-based detector network of the LIGO-Virgo-KAGRA Collaboration and their subsequent characterization are carried out by search pipelines operating on two different timescales or latencies. Low-latency (or *online*) searches allow to identify potential events in near real-time, sending rapid alerts to follow-up observatories to seek for their possible multi-messenger counterparts. In *offline* searches, more effort is directed to optimizing the sensitivity and accuracy of the results based on a more intensive study of the data properties over extended periods of time. Once signals are identified, parameter estimation algorithms are applied to infer the astrophysical properties of their sources. This process results in the publication of gravitational-wave catalogs.

At the time of writing, these searches have successfully identified and cataloged 90 gravitational-wave observations from mergers of binary compact systems. Nevertheless, there is still potential for improvement in various areas. The work presented in this thesis has been conducted within the `PyCBC` search, and focuses on refining both offline and online (`PyCBC Live`) analysis methods. The specific objectives of this work include:

O.1 Characterize the rate of high-SNR triggers around times of loud non-Gaussian auto-gated transients in the *offline* search, and develop a new veto in order to remove them. Subsequently, implement this veto in the new PyCBC-based search for signals from intermediate-mass black hole binaries and study the changes in search sensitivity.

O.2 Improve the existing *online* classification method that estimates the probabilities of a gravitational-wave candidate to be a binary neutron star, a binary black hole or a neutron star-black hole binary. To do so, develop a new classification method based on the chirp mass of the candidate event and implement it in `PyCBC Live`.

O.3 Develop a new *low-latency* rapid parameter estimation method to forecast the uncertainties of the binary masses and spins within the first minutes after detection to improve the information recovered by online searches.

Index

Acronyms and symbols

ASD	amplitude spectral density
BBH	binary black hole
BH	black hole
BNS	binary neutron star
CBC	compact binary coalescence
CE	Cosmic Explorer
EM	electromagnetic
EOB	effective-one-body
EOS	equation of state
ET	Einstein Telescope
FAR	false alarm rate
FF	fitting factor
FFT	Fast Fourier Transform
GCN	Gamma-ray Coordinates Network
GR	General Relativity
GraceDb	Gravitational-Wave Candidate Event Database
GRB	gamma-ray burst
GW	gravitational wave
HOM	higher-order multipoles
IFAR	inverse false alarm rate
IMBH	intermediate-mass black hole
IMR	inspiral-merger-ringdown
ISCO	innermost stable circular orbit
KDE	kernel density estimate
LIGO	Laser Interferometer Gravitational-wave Observatory
LISA	Laser Interferometer Space Antenna
LL	low-latency
LSC	LIGO Scientific Collaboration
LVK	LIGO-Virgo-KAGRA Collaboration
MG	mass gap
ML	maximum likelihood
NR	Numerical Relativity
NS	neutron star
NSBH	neutron star-black hole
PDF	probability density function
PE	parameter estimation
PN	post-Newtonian

PSD	power spectral density
SMBH	super-massive black hole
SNR	signal-to-noise ratio

Frequently used symbols

h_+, $h_\times$	plus and cross polarization of the gravitational wave
h	gravitational-wave strain, $h = h_+ - ih_\times$
F_+, $F_\times$	antenna pattern functions
m_1, m_2	component masses of a binary system
M	total mass of the binary, $M = m_1 + m_2$
q	mass ratio of the binary, $q = m_2/m_1$
η	symmetric mass ratio of the binary, $\eta = m_1 m_2/M^2$
$\mathcal{M}$	chirp mass of the binary, $\mathcal{M} = \eta^{3/5} M$
$\mathrm{M}_\odot$	solar mass unity
$\vec{S}_1$, $\vec{S}_2$	component spin angular momentums
$\vec{L}$	total angular momentum of the binary
$\vec{\chi}_1$, $\vec{\chi}_2$	dimensionless spin vectors
χ_{eff}	effective inspiral spin
D_{L}	luminosity distance
D_{eff}	effective distance
z	redshift
v	orbital velocity of a CBC
ω	orbital angular frequency of a CBC
R	orbital separation of a CBC
ω_{gw}	angular frequency of a GW
f_{gw}	frequency of a GW
ρ	signal-to-noise ratio
$\langle h_1 \vert h_2 \rangle$	inner product between two waveforms
$\Vert h \Vert$	norm of a waveform
Λ	likelihood ratio
$\mathcal{O}(h_1, h_2)$	overlap between two waveforms
$M(h_1, h_2)$	match between two waveforms
$\bar{M}(h_1, h_2)$	mismatch between two waveforms, $\bar{M} = 1 - M$
$S_n(f)$	power spectral density
Γ_{ij}	Fisher matrix
$\digamma$	fudge-factor

1

INTRODUCTION TO GRAVITATIONAL WAVES

Gravitational waves (GWs) are tiny fluctuations in the curvature of spacetime caused by the accelerated motion of massive bodies. These waves propagate the Universe at the speed of light, carrying information of the properties of the source with them. While predicted by Albert Einstein in 1916 as solutions to his theory of General Relativity (GR) [1], direct observation of GWs was not accomplished until September 14, 2015, when the first signal from a binary black hole (BBH) merger was detected [2]. At the time of writing, during the fourth observing run, nearly 100 sources have been confirmed and cataloged as GW events. These discoveries have provided new insights into the complexities of the Universe and offered new tests of fundamental physics.

This chapter provides a brief overview of the basic concepts of GW theory, accompanied by a description of the various types of GW sources and the instruments developed for their detection.

1.1 Gravitational Waves

The first section of this chapter provides an introduction of gravitational waves (GWs) within the framework of GR [3–5]. Beginning with an exposition of the foundational principles of GR, we study how GWs arise as wave-like solutions of the linearized Einstein equations. Subsequently, we study the propagation of GWs and its interaction with matter. After, we demonstrate how the motion of matter generates gravitational radiation. Finally, we provide an overview of potential sources of GWs.

1.1.1 Introduction to General Relativity

In the framework of General Relativity (GR), the *spacetime* is a four-dimensional curved manifold, whose curvature is completely determined by a *metric* $g_{\mu\nu}$ of signature (−,+,+,+). This metric has the following properties:

i) It is symmetric: has only 10 independent components.

ii) Permits raising and lowering indices as $V_\mu = g_{\mu\nu}V^\nu$.

iii) Has to be *self-inverse*

$$g^{\mu\nu}g_{\mu\lambda} = \delta^\mu_\lambda \,. \tag{1.1}$$

The curvature can be described in terms of the *Riemann tensor*

$$R^\rho_{\sigma\mu\nu} = \partial_\mu\Gamma^\rho_{\nu\sigma} - \partial_\nu\Gamma^\rho_{\mu\sigma} + \Gamma^\rho_{\mu\lambda}\Gamma^\lambda_{\nu\sigma} - \Gamma^\rho_{\nu\lambda}\Gamma^\lambda_{\mu\sigma} \,, \tag{1.2}$$

where the $\Gamma^\rho_{\mu\nu}$ are named *Christoffel symbols*, and can be expressed in terms of the partial derivatives of the components of $g_{\mu\nu}$ as

$$\Gamma^\rho_{\mu\nu} = \frac{1}{2}g^{\rho\lambda}\left(\partial_\mu g_{\lambda\nu} + \partial_\nu g_{\lambda\mu} - \partial_\lambda g_{\mu\nu}\right) \,. \tag{1.3}$$

Two particular contractions of the Riemman tensor known as the *Ricci tensor* $R_{\mu\nu} = R^\lambda_{\mu\lambda\nu}$ and the *Ricci scalar* $R = R^\mu_\mu$ can be combined into a single quantity that represents the nature of the geometry of spacetime: the *Einstein tensor*

$$G_{\mu\nu} = R_{\mu\nu} - \frac{1}{2}g_{\mu\nu}R \,. \tag{1.4}$$

While the curvature is encoded in the Einstein tensor, the source of gravity lies in the distribution of mass and energy, which is mathematically described by the *energy-momentum* tensor $T_{\mu\nu}$. The *Einstein equations* relate the geometry of spacetime with matter and energy as

$$R_{\mu\nu} - \frac{1}{2}g_{\mu\nu}R = \frac{8\pi G}{c^4}T_{\mu\nu} \,, \tag{1.5}$$

where c is the speed of light in vacuum and G is the gravitational constant.

Gravitational waves are typically studied under the *weak-field approximation*, which assumes that the background spacetime through which the waves propagate is flat, described by the Minkowski metric. This approximation holds because, when measuring GWs from Earth, we are typically at a considerable distance from the source and experience a weak local gravitational field.

Therefore, considering the background spacetime as flat is a reasonable approximation. We consider a flat Minkowski metric $\eta_{\mu\nu}$ with a small perturbation $h_{\mu\nu}$:

$$g_{\mu\nu} = \eta_{\mu\nu} + h_{\mu\nu}, \qquad |h_{\mu\nu}| \ll 1\,. \tag{1.6}$$

To study how Einstein equations transform in a metric of this form, we expand them to linear order in the perturbation h. This process involves recalculating the Christoffel symbols using the perturbed metric, followed by the determination of the Riemann tensor, and subsequently, the Ricci tensor and Ricci scalar. These calculations require the use of the inverse metric in the contravariant form

$$g^{\mu\nu} = \eta^{\mu\nu} - h^{\mu\nu} + \mathcal{O}(h^2)\,, \tag{1.7}$$

that satisfies (1.1).

Now, with the new perturbed metric we can recompute the Christoffel symbols of (1.3) up to linear order in $h_{\mu\nu}$

$$\Gamma^{\rho}_{\mu\nu}{}^{(1)} = \frac{1}{2}\eta^{\rho\lambda}\left(\partial_\mu h_{\lambda\nu} + \partial_\nu h_{\lambda\mu} - \partial_\lambda h_{\mu\nu}\right)\,, \tag{1.8}$$

and apply them in (1.2) to get the linearized Riemman tensor

$$R^{(1)}_{\rho\sigma\mu\nu} = \frac{1}{2}\left(\partial_\mu\partial_\sigma h_{\rho\nu} + \partial_\nu\partial_\rho h_{\mu\sigma} - \partial_\mu\partial_\rho h_{\nu\sigma} - \partial_\nu\partial_\sigma h_{\rho\mu}\right)\,. \tag{1.9}$$

Computing the Ricci tensor as the trace part of the Riemann tensor

$$R^{(1)}_{\mu\nu} = \eta^{\alpha\lambda}R^{(1)}_{\mu\alpha\nu\lambda} = \frac{1}{2}\left(\partial^\lambda\partial_\mu h_{\nu\lambda} + \partial^\lambda\partial_\nu h_{\mu\lambda} - \partial_\mu\partial_\nu h - \partial^\lambda\partial_\lambda h_{\mu\nu}\right)\,, \tag{1.10}$$

and the Ricci scalar as the contraction of the Ricci tensor

$$R^{(1)} = \eta^{\mu\nu}R^{(1)}_{\mu\nu} = \partial^\mu\partial^\nu h_{\mu\nu} - \partial^\mu\partial_\mu h \tag{1.11}$$

where $h = \eta^{\mu\nu}h_{\mu\nu}$ and, in the context of linearized theory, $\Box$ is the flat-space d'Alembertian operator $\Box = \eta_{\mu\nu}\partial^\mu\partial^\nu = \partial^\mu\partial_\mu$.

Inserting (1.9), (1.10) and (1.11) in (1.5) we obtain the linearized Einstein equations. These can be simplified by using the *trace-reverse* metric

$$\bar{h}_{\mu\nu} = h_{\mu\nu} - \frac{1}{2}\eta_{\mu\nu}h\,, \tag{1.12}$$

resulting in

$$\Box\bar{h}_{\mu\nu} + \eta_{\mu\nu}\partial^\rho\partial^\sigma\bar{h}_{\rho\sigma} - \partial^\rho\partial_\nu\bar{h}_{\mu\rho} - \partial^\rho\partial_\mu\bar{h}_{\nu\rho} = -\frac{16\pi G}{c^4}T_{\mu\nu}\,. \tag{1.13}$$

The next step in is to fix the *gauge freedom*. Since GR is a covariant theory, it is invariant under any coordinate transformation $x^\mu \to x'^\mu(x)$. In linearized theory, imposing (1.6) is equivalent to choose a specific reference frame and, therefore, breaking the invariance of GR under coordinate transformations. However, the freedom to make an infinitesimal variation of order $h_{\mu\nu}$ maintains a residual gauge symmetry given by small *gauge transformations*

$$x'^\mu = x^\mu + \xi^\mu(x)\,, \tag{1.14}$$

where $|\partial_\mu\xi_\nu| \leq |h_{\mu\nu}|$. Under this change of coordinates, the perturbation metric transforms as

$$h'_{\mu\nu}(x') = h_{\mu\nu}(x) - (\partial_\mu\xi_\nu + \partial_\nu\xi_\mu)\,. \tag{1.15}$$

The gauge choice that simplifies linearized gravity to the most is the *Lorenz gauge*, given by the condition

$$\partial^\nu\bar{h}_{\mu\nu} = 0\,. \tag{1.16}$$

By imposing this gauge, some terms of (1.13) vanish, remaining

$$\Box\bar{h}_{\mu\nu} = -\frac{16\pi G}{c^4}T_{\mu\nu}\,, \tag{1.17}$$

which has the form of a wave equation travelling at the speed of light and sourced by a matter field given by $T_{\mu\nu}$, i.e., of a *gravitational wave*.

1.1.2 Propagation and interaction with matter

To study how gravitational waves propagate and interact with matter far outside the source, they need to be described in the *vacuum*, where $T_{\mu\nu} = 0$ and the wave equation simplifies to

$$\Box\bar{h}_{\mu\nu} = 0\,. \tag{1.18}$$

This equation has a general complex solution in the form of superposition of *plane waves* as

$$\bar{h}_{\mu\nu} = A_{\mu\nu}e^{ik_\alpha x^\alpha}\,. \tag{1.19}$$

To satisfy the condition given by the Lorenz gauge (1.16), the amplitude tensor $A_{\mu\nu}$ must obey

$$A_{\mu\nu}k^{\mu} = 0\,. \tag{1.20}$$

This restriction implies that the amplitudes of the oscillations are *transverse* to the direction of propagation, defined by the wave vector k^{μ}. The amplitude can be further restricted by the remaining residual symmetry of (1.14). The Lorenz condition $\partial^{\nu}\bar{h}_{\mu\nu} = 0$ does not fix the gauge completely, since the transformation

$$(\partial^{\nu}\bar{h}_{\mu\nu})' = \partial^{\nu}\bar{h}_{\mu\nu} - \Box\xi_{\mu}\,, \tag{1.21}$$

maintains its validity when $\Box\xi_{\mu} = 0$. We can use this symmetry to choose $\bar{h}_{\mu\nu}$ to be *traceless*

$$\bar{h} = 0\,, \tag{1.22}$$

so $\bar{h}_{\mu\nu} = h_{\mu\nu}$. These restrictions on the metric are known as the *transverse-traceless gauge*, ot TT gauge, and can be summarized as

$$h_{0i} = 0\,, \quad h^{i}_{i} = 0\,, \quad \partial^{j}h_{ij} = 0\,. \tag{1.23}$$

Given its symmetric nature, $h_{\mu\nu}$ is formed by 10 independent components, that get reduced to 6 when the Lorenz gauge of (1.16) is applied. After imposing the TT gauge, these 6 degrees of freedom are reduced to just two: h_{+} and $h_{\times}$, known as the *plus* and *cross polarizations* of the wave. Finally, choosing the z-axis as the direction of propagation, the metric perturbation in the TT gauge takes the form

$$h^{\mathrm{TT}}_{\mu\nu} = \begin{pmatrix} 0 & 0 & 0 & 0 \\ 0 & h_{+} & h_{\times} & 0 \\ 0 & h_{\times} & -h_{+} & 0 \\ 0 & 0 & 0 & 0 \end{pmatrix}\,. \tag{1.24}$$

The interaction of GWs with matter can be modeled by their effect over a ring of freely falling test particles perpendicular to the direction of propagation. Considering a GW travelling along the z-axis, the displacements of the particles with respect to their unperturbed positions $(x_0,\, y_0,\, z_0)$ are

$$\delta x(t) = \frac{1}{2}\left[h_{+}x_0 + h_{\times}y_0\right]\,, \quad \delta y(t) = \frac{1}{2}\left[h_{\times}x_0 - h_{+}y_0\right]\,, \quad \delta z(t) = 0\,, \tag{1.25}$$

with all coordinates measured with respect to the center point of the ring. To easily understand this motion, one can study the effect of both polarizations separately. Considering the *plus* mode as the only one present in the wave,

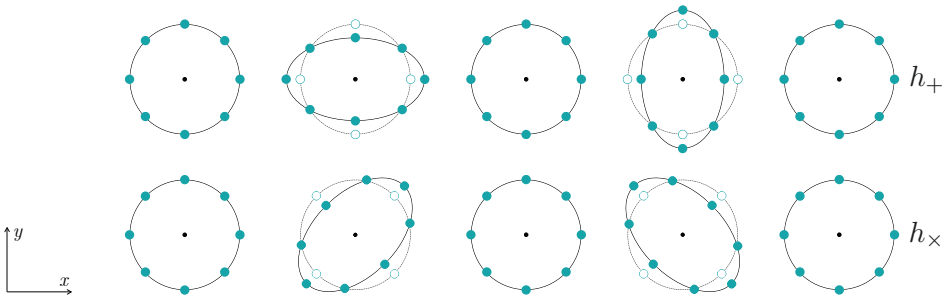

Figure 1.1: Effect of both polarizations of a GW propagating in the z-axis over a ring of test masses at the x-y plane. Dotted lines represent the original ring shape, with no presence of the GW, and solid lines show the distortion produced by the GW during its different phases.

an increment of h_+ implies a expansion on the x-axis and a contraction on the y-axis, and when h_+ decreases the opposite behaviour is observed. This ellipse-shaped deformation can be seen in the upper part of Fig. 1.1. When only the $h_\times$ polarization is present, the deformation takes also the shape of an ellipse, rotated by 45° with respect to the h_+ polarization. This effect is shown in the lower part of Fig. 1.1. Therefore, a typical gravitational wave can be perceived as the combination of two oscillating tidal fields traveling at the speed of light. For a GW traveling along the z-axis, this can be represented as a linear combination of both polarization states as

$$\mathbf{h} = h_+ \mathbf{e}_+ + h_\times \mathbf{e}_\times \,, \tag{1.26}$$

where $\mathbf{e}_+$ and $\mathbf{e}_\times$ are the *polarization tensors*

$$\mathbf{e}_+ = \begin{pmatrix} 0 & 0 & 0 & 0 \\ 0 & 1 & 0 & 0 \\ 0 & 0 & -1 & 0 \\ 0 & 0 & 0 & 0 \end{pmatrix} \quad \text{and} \quad \mathbf{e}_\times = \begin{pmatrix} 0 & 0 & 0 & 0 \\ 0 & 0 & 1 & 0 \\ 0 & 1 & 0 & 0 \\ 0 & 0 & 0 & 0 \end{pmatrix} . \tag{1.27}$$

From the displacements of (1.25) several implications regarding gravitational wave detectors can be deduced. First, the displacement of the particles on the x-y plane is proportional to its original position with respect to an origin. This implies that gravitational waves create a bigger distance difference when the original separation is bigger. This is the motivation to build gravitational wave detectors on very large scales, where fractional changes in

distances are measured over many kilometers for ground-based detectors and millions of kilometers for detectors in space. Also, since the displacements are proportional to the metric perturbation $h^{\mathrm{TT}}_{\mu\nu}$, they are quite small. The amplitude of these components is typically of order 10^{-21} or smaller, meaning gravitational wave detectors need to be sensitive to fractional changes in distance of, at least, one part in 10^{21}.

1.1.3 Generation of gravitational waves

After observing how propagating gravitational waves can impact the movement of matter, we can demonstrate the reciprocal relationship: that the motion of matter generates gravitational radiation. To study how GW are generated, we solve the linearized equation (1.13) for a wave produced by a distant, slow-moving source of energy-momentum tensor $T_{\mu\nu}$. We set the geometry of Fig. 1.2, where the vectors $\mathbf{x}$ and $\mathbf{y}$ indicate respectively the position of the observer and a point inside the source measured from its center of mass. We consider the source to have a typical size R and to be located at a distance $r \gg R$ from the observer.

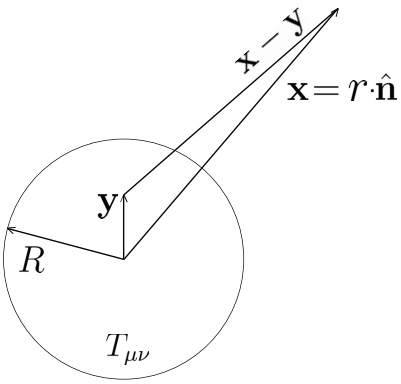

Figure 1.2: Geometry of the source of gravitational waves described in this section. The source has a typical size of R but it is not necessarily spherical. Adapted from [4].

Since the equation (1.13) is linear in $h_{\mu\nu}$, it can be solved by Green's functions methods. In particular, the solution for this radiation problem is

$$\bar{h}_{ij}(t,\mathbf{x}) = \frac{4G}{c^4}\int \frac{T_{ij}(t_{\mathrm{ret}},\mathbf{y})}{||\mathbf{x}-\mathbf{y}||}d^3y\,, \tag{1.28}$$

expressed in terms of the *retarded time* [5]

$$t_{\text{ret}} = t - \frac{||\mathbf{x}-\mathbf{y}||}{c}\,. \tag{1.29}$$

With the assumption of a distant, slowly-varying source, it is valid to approximate $||\mathbf{x}-\mathbf{y}|| \approx ||\mathbf{x}|| = r$, and the solution simplifies to

$$\bar{h}_{ij}(t,\mathbf{x}) = \frac{4G}{c^4}\frac{1}{r}\int T_{ij}(t-\frac{r}{c},\mathbf{y})\,d^3y\,. \tag{1.30}$$

Using the conservation law $\partial^\mu T_{\mu\nu} = 0$ and assuming an isolated, non-relativistic source, this equation can be expressed as a multipolar expansion of the moments of the mass density $\rho = T^{00}/c^2$. Since the emissions of monopolar and dipolar gravitational radiation are forbidden by the conservation laws of mass and linear momentum [4], the leading term of this expansion is the so-called *quadrupolar approximation*

$$\bar{h}_{ij}(t,\mathbf{x}) = \frac{2G}{c^4}\frac{1}{r}\ddot{M}_{ij}(t-r/c)\,, \tag{1.31}$$

where $\ddot{M}_{ij}$ is the second derivative over time of the *quadrupole moment* tensor of the mass distribution

$$M_{ij}(t,\mathbf{x}) = \int \rho\, x^i x^j\, d^3x\,. \tag{1.32}$$

The simplest form of this solution is the one projected in the TT gauge

$$h^{TT}_{ij}(t,\mathbf{x}) = \frac{2G}{c^4}\frac{1}{r}\ddot{Q}^{TT}_{ij}(t-r/c)\,, \tag{1.33}$$

where Q_{ij}, known as the *reduced quadrupole moment tensor*, is the trace-free part of M_{ij} defined as

$$Q_{ij} = M_{ij} - \frac{1}{3}\delta_{ij}M^k_k\,. \tag{1.34}$$

In the TT gauge, the two polarization amplitudes for a GW travelling in the z-axis are [4]

$$\begin{aligned} h_+ &= \frac{G}{c^4}\frac{1}{r}\left(\ddot{M}_{xx} - \ddot{M}_{yy}\right)\,, \\ h_\times &= \frac{2G}{c^4}\frac{1}{r}\ddot{M}_{xy}\,, \end{aligned} \tag{1.35}$$

where the elements of $\ddot{M}_{ij}$ are evaluated at t_{ret}.

The *power radiation* distribution per unit solid angle Ω is given in the quadrupolar approximation by

$$\frac{dP}{d\Omega} = \frac{r^2 c^3}{32\pi G} \langle \dot{h}_{ij}^{\mathrm{TT}} \dot{h}_{ij}^{\mathrm{TT}} \rangle \,, \tag{1.36}$$

where the average $\langle \cdot \rangle$ is performed over several periods of GW cycles. These quantities, as well as expressions derived from them, can be simplified by assuming a binary system, whose detection and followup are the main goals of this thesis. This the aim of Sec. 1.3.

1.1.4 Sources of gravitational waves

In the last section we saw that, to first order, the emission of GWs is triggered by any non-vanishing quadrupole moment, i.e., any massive source experimenting a non-spherical acceleration. This condition is very broad, allowing for a wide range of sources to exist. However, the typical amplitude of these perturbations of spacetime is extremely small, making them non-detectable for the majority of sources. This weak nature of GWs restricts the sources able to produce detectable radiation to sytems undergoing relativistic velocities, or existing within strong gravitational fields. These will typically be highly dynamic astrophysical systems, such as CBCs, core-collapse supernova explosions or non-axisymmetric rotating neutron stars (NSs).

Gravitational wave signals are typically categorized based on their duration and the extent to which they can be theoretically modeled. Following this classification, the main types of signals explored in gravitational wave astronomy are: CBC transients (short, modeled), continuous waves (long, modeled), burst signals (short, unmodeled) and stochastic background (long, unmodeled). Examples of GW signals belonging to these four types can be seen in Fig. 1.3. A brief description of each signal category is presented below.

Compact binary coalescences (CBCs)

Gravitational waves from compact binary coalescences are produced when two compact objects, such as neutron stars (NSs) or black holes (BHs), orbit each other in close proximity. This orbital movement induces a change in the quadrupole moment, causing the system to emit GW radiation. The emission carries away some orbital energy, causing their orbit to gradually reduce in an *inspiral* process that eventually leads to a merger into a single, more massive object. For BBH and neutron star-black hole (NSBH) coalescences, the

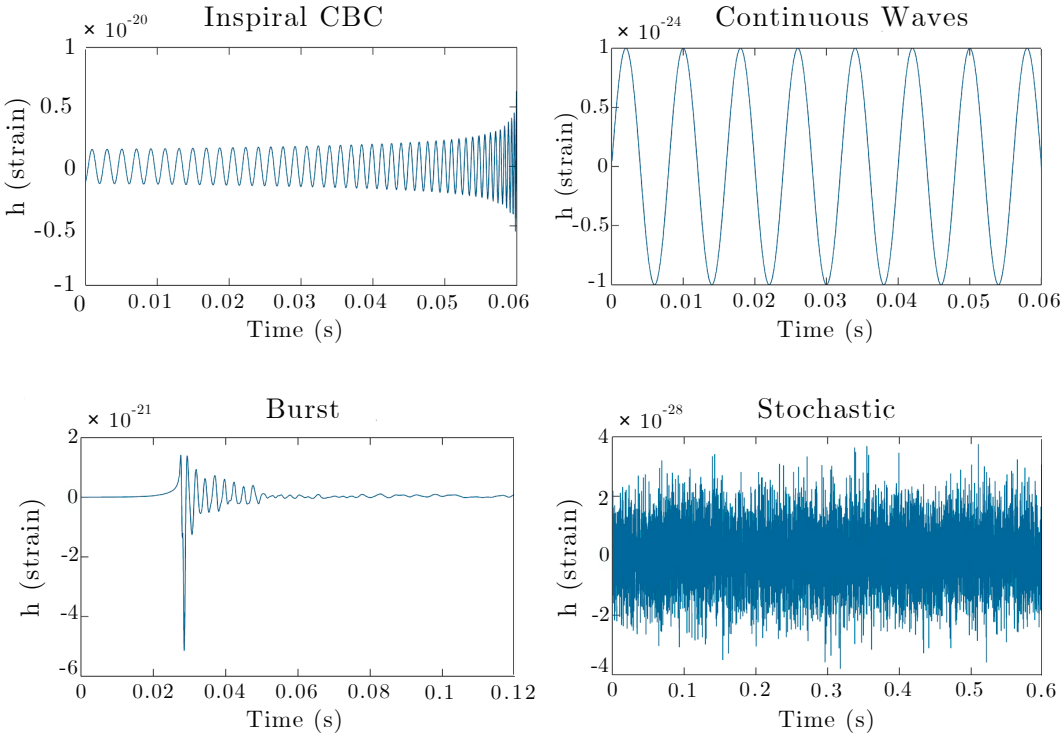

Figure 1.3: Examples of GW signals belonging to the four types described in this section. Adapted from A. Stuver/LIGO.

remnant object will be a black hole, while binary neutron star (BNS) mergers can also lead to the formation of a more massive neutron star.

At the moment of writing, CBCs are the only GW sources that have been directly detected by the existing network of ground-detectors. During the three first periods of observation, O1, O2 [6] and O3 [7, 8], the LIGO-Virgo-KAGRA (LVK) Collaboration confirmed the detection of 90 GW signals consistent with a CBC origin.

Mergers of other compact objects such as white-dwarf stars, intermediate-mass black holes (IMBHs) or super-massive black holes (SMBHs) are expected to be detected by future generation space-based detectors as LISA.

Continuous waves

Continuous gravitational waves expected sources are rapidly-spinning asymmetric objects, such as NSs with non-axisymmetric deformities or pulsars with

irregularities in their rotation. These asymmetries break the constancy of their quadrupole moment, causing the emission of GW radiation. Continuous waves are characterized by their nearly constant frequency and amplitude over short times, consequence of their small amplitude and low orbital energy loss. While these sources are comparably weaker, their signals can be integrated over long periods of time in order to accumulate detectable signals.

Bursts

Gravitational wave bursts are short-duration transients, in a timescale of milliseconds to tens of seconds, produced by astrophysical unmodeled sources. Potential scenarios are asymmetric core-collapse supernovae, short gamma-ray bursts, highly eccentric BBH mergers or cosmic strings. Despite extensive efforts are put in targeted searches for these scenarios, along with generic searches sensitive to a wider range of source morphologies, no GW bursts have been detected at the moment.

Stochastic background

The stochastic background of GW signals is the result of an unresolvable overlap of independent sources, too faint or numerous to be individually detected. Some of these signals have a galactic origin, as a superposition of a vast amount of transients, whose radiation reaches us with random frequencies and from random directions. More interestingly, this signals can also have a cosmological origin, coming from inflation inhomogeneities or anisotropies in the very early universe.

1.2 Detection of gravitational waves

The era of detection of gravitational waves began in 1974 with the observation of the orbital period of the binary pulsar system PSR B1913+16 [9]. J. Taylor and J. Weisberg [10] measured a gradual decrease of this period, and matched it with the orbital decay predicted by GR in case of GW emission. This indirect evidence of the existence of GWs encouraged scientists to explore methods able to achieve direct detections.

One of these approaches, pioneered by J. Weber in the 1960s, involved the use of *resonant bars*, cylindrical metal antennas designed to resonate in response to passing GWs [11]. Although by design these detectors could detect strong signals in our galactic area, the fact that their sensitivity was limited

to explore extra-galactic distances and the lack of detections motivated the search for more advanced methods.

Because gravitational waves have a quadrupolar nature, the idea of measuring their induced change on the proper distance between objects using *interferometers* soon arose. Initially pushed by R. Weiss, R. Drever and others in the 1970s, their design, building and development required an enormous amount of human effort to reach the achievement of the first direct detection of a GW signal in September 2015 [2].

In this section we will discuss the basic design of a gravitational wave interferometric detector, their response to GWs, their sensitivity to different sources of noise and a brief review of the state of the art of existing and future detectors.

1.2.1 Michelson-Morley interferometer

Current GW detectors are advanced Michelson-Morley interferometers with two orthogonal kilometer-scale arms, designed to measure the change on the length of the arms when reached by a GW. At a fundamental level, their functioning is as follows: A pre-stabilized coherent *laser beam* enters the interferometer, where is split into two equal-power beams by a *beam-splitter* mirror. Each resulting beam travels along one of the arms, encounters a high-reflective mirror at the end, and is then reflected back to the beam-splitter, where it interferes with the beam from the other arm. If the distance traveled by both beams differs, they reach the beam-splitter with a phase difference, and an optical signal proportional to this difference is transmitted to the output *photodetector*. If both laser beams travel the same distance, they interfere destructively, and there is no light at the output of the detector. A simplified layout of an interferometric detector is shown in Fig. 1.4.

Assuming that the arm length of the detector L is small compared to the wavelength of the GW, from (1.25) it can be seen that the length change ΔL produced by a GW of strain amplitude h can be expressed at first order as

$$\Delta L \sim \frac{h}{2} L \,. \tag{1.37}$$

Considering that the arms of the interferometer are aligned with the x and y axis of the GW plane, one of them will be stretched as $L_x = L + \Delta L$, and the other will decrease in the same amount $L_y = L - \Delta L$, so the length difference between them is

$$\frac{\Delta L_{\text{arms}}}{L} \sim h \,. \tag{1.38}$$

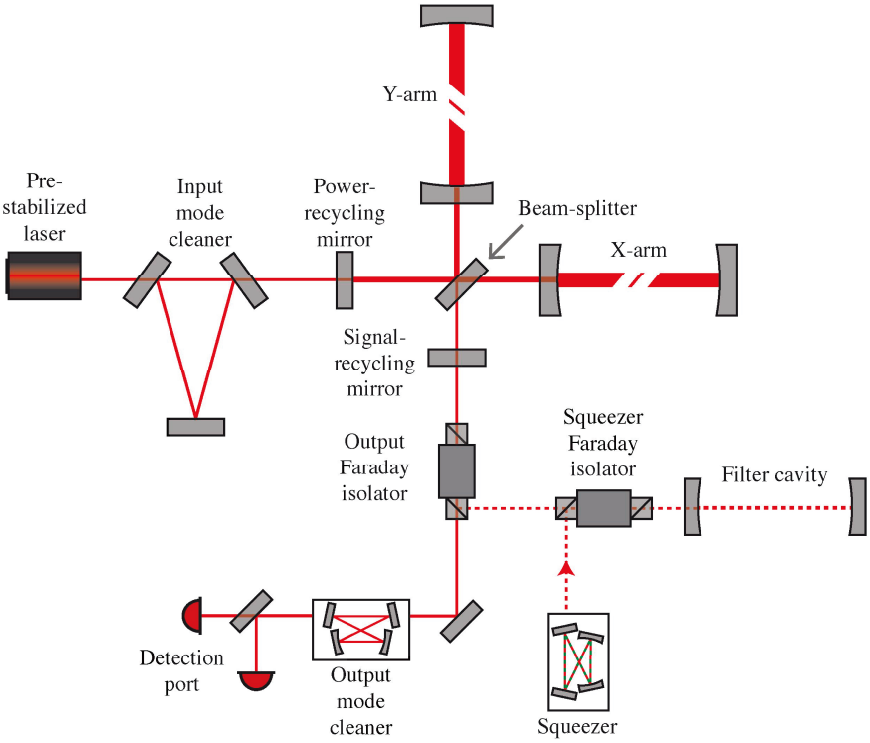

Figure 1.4: Simplified layout of the optical components of the LIGO detectors for the fourth observing run (O4). The pre-stabilized laser (solid red) first goes through the input mode cleaner to further stabilize the beam before entering the interferometer. Then, it transmits through the power-recycling mirror, the beam-splitter, the Fabry-Pérot arm cavities, the signal-recycling mirror, an output Faraday isolator and output mode cleaner until reaching the output detection port. Dashed red line is the squeezed light path from the squeezer cavity. Figure reproduced from [12].

Given that the amplitude of the strain of a typical CBC event is on the order of 10^{-21}, an interferometer with kilometer-scale arms would need to measure length differences of

$$\Delta L_{\text{arms}} \sim 10^{-18} \left(\frac{h}{10^{-21}}\right) \left(\frac{L}{\text{km}}\right) \text{m}\,, \tag{1.39}$$

which is a thousand times smaller than the size of a proton.

To achieve enough sensitivity to measure these minute differences, several enhancements were implemented on the basic Michelson detectors. First, each arm contains an extra *test mass* mirror placed near the beam-splitter forming a resonant optical cavity with the mirror at the end of the arm. In this setup, called a *Fabry-Pérot* cavity, the laser beam bounces back and forth before interference, effectively increasing the light path by several hundred times, thereby enhancing the power response on the detector. Current detectors also include a dual-recycling system, with a *power-recycling* mirror, that reflects light back into the main interferometer, increasing the beam power [13], and a *signal-recycling* mirror, used to enlarge the bandwidth of the detector [14]. Other system is the *squeezer* cavity, a source of squeezed vacuum that reduces the intrinsic uncertainty associated with measurements of photon arrival times [15].

1.2.2 Detector response to GWs

Due to the quadrupolar directionality of GWs, the detector's response to the passage of a GW will depend on the relative orientation of the incoming wave plane with respect to the detector. The incoming GW is defined in the *radiation frame*, a plane orthogonal to the direction of travel. The *detector frame* is situated in the x-y plane, with the beam-splitter in the origin of the coordinate system, and the x and y axes along the arms of the interferometer. Both reference frames are related by three Euler angles: a polar angle θ and an azimuthal angle ϕ, which determine the sky location of the source, and a *polarization* angle ψ, indicating the relative rotation of the detector arms with respect to the h_+ and $h_\times$ components of the GW. See Fig 1.5 for a schematic illustration of both reference frames and the associated Euler angles.

The amplitude of the time-dependent strain $h(t)$ projected into the interferometer axes is described by

$$h(t) = h_+(t)F_+(\theta, \phi, \psi) + h_\times(t)F_\times(\theta, \phi, \psi)\,, \tag{1.40}$$

where the directional variations in sensitivity are encoded in the detector *an-*

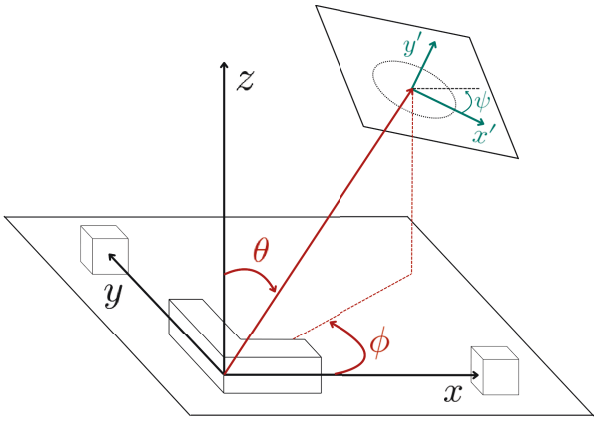

Figure 1.5: Schematic diagram illustrating the relationship between the detector frame $\{x,\ y,\ z\}$ and the radiation frame $\{x',\ y',\ z'\}$, along with the corresponding Euler angles $(\theta,\ \phi,\ \psi)$ that describe their relative orientation and polarization.

tenna pattern functions [16]

$$\begin{aligned} F_+(\theta,\phi,\psi) &= \frac{1}{2}\left(1+\cos^2\theta\right)\cos 2\phi\cos 2\psi - \cos\theta\sin 2\phi\sin 2\psi\,, \\ F_\times(\theta,\phi,\psi) &= -\frac{1}{2}\left(1+\cos^2\theta\right)\cos 2\phi\sin 2\psi - \cos\theta\sin 2\phi\cos 2\psi\,, \end{aligned} \tag{1.41}$$

whose maximum value is 1. For a single interferometer, the polarizations can be chosen to be aligned with the detector's reference frame; thus $\psi = 0$. The squared antenna amplitude pattern or *antenna power pattern* [17] is given by

$$\begin{aligned} F_{\rm rms}(\theta,\phi)^2 &= F_+(\theta,\phi,\psi)^2 + F_\times(\theta,\phi,\psi)^2 = \\ &= \frac{1}{4}(1+\cos^2\theta)^2\cos^\phi + \cos^2\theta\sin^2\phi\,, \end{aligned} \tag{1.42}$$

which is independent of the polarization angle ψ. The amplitude pattern $F_{\rm rms}(\theta,\phi)$ represents the maximum detection reach of the detector in different directions. Visualizations of the antenna patterns for F_+, $F_\times$ and $F_{\rm rms}$ can be seen at Fig. 1.6. From the antenna patterns it can be seen that a single interferometer is more sensitive to GWs coming from both directions orthogonal to the detector's plane, and that has blind spots for GWs coming from the bisectors of the arms. To overcome these blind spots and improve the overall sensitivity and directional coverage, a network of GW detectors is distributed at

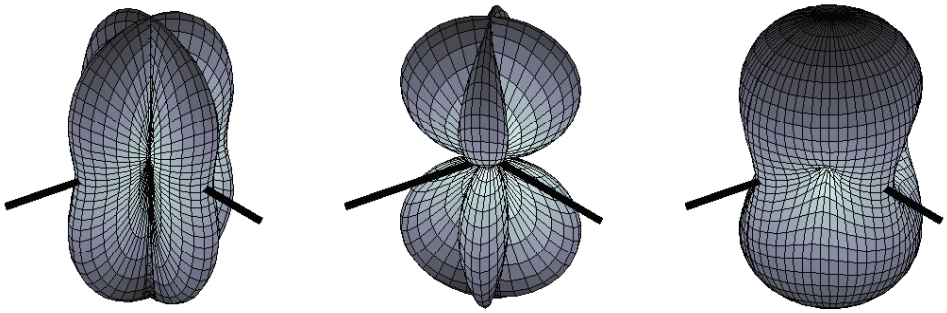

Figure 1.6: Antenna sensitivity patterns for the detector's response to the + polarization (left) and the × polarization (center) with $\psi = 0$, and the amplitude pattern (right). Black lines point at the orientation of the arms of the detector. The sensitivity is shown as the distance from the center of the arms to the surface. Figure reproduced from [19].

different locations on Earth. By combining data from multiple detectors with complementary antenna patterns, the network can effectively cover a larger portion of the sky and allows for a more precise localization of the source by triangulation techniques [18]. This is specially relevant for effectively observing events with multimessenger counterparts, since precise localization allows electromagnetic (EM) and neutrino observatories to focus on specific regions in the sky.

1.2.3 Detector noise sources

Given the ability of laser interferometers to measure minute differences in length, power fluctuations will constantly appear at the detection port. When these fluctuations are not caused by GWs, they are referred to as *noise*, and they can arise from a wide range of sources, typically classified as *fundamental* or *technical* [12, 20]. Known noise sources are measured and can be characterized as an amplitude spectral density (ASD) curve named *noise budget*. Fig 1.7 collects different curves from the main known sources of noise for LIGO Hanford interferometer in the third observing run (O3).

a) Fundamental noise

Fundamental noises are inherent to the design of the detector. Since they arise from physical principles, their limitations cannot be entirely eliminated,

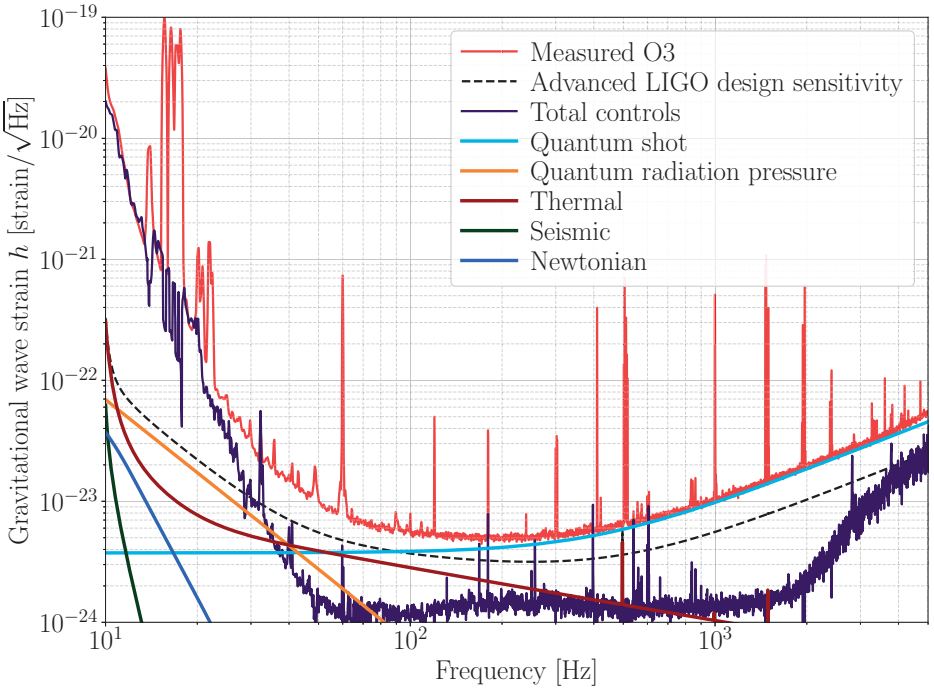

Figure 1.7: Noise budget curves for LIGO Hanford in O3. Red curve shows the measured ASD during O3, representing the detector sensitivity to GWs. Dashed black curve represents the Advanced LIGO design sensitivity. All other curves are estimations or measurements of the different contributions to the total measured noise. Figure reproduced from [12].

and they are considered the interferometer noise floor. This category includes seismic noise, Newtonian noise, thermal noise, and quantum noise.

Seismic noise At low frequencies, around 10 Hz, sensitivity is limited by *seismic noise*, ground vibrations caused by natural phenomena and human activity that couple to the motion of the mirrors. To mitigate this effect, a combination of passive and active isolation techniques is employed. Passive methods involve isolating the core optics from ground motion by suspending mirrors from quadruple-stage pendulums and using vibration-damping materials. Active isolators monitor ground motion and make real-time adjustments to the position of the detector to maintain stability.

Newtonian noise Newtonian noise, also known as *gravity-gradient noise*, arises from changes in ground density due to seismic activity, changes in the atmosphere density, or even from flying objects near the detector [21]. This causes fluctuations in the local gravitational field around the optics, affecting the measurements. It can be mitigated by going underground, or by active monitoring and subsequent subtraction.

Thermal noise Thermal noise is caused by the random thermal motion of the atoms in the mechanical components such as suspensions and mirrors. The dominant noise in the mirrors is the *brownian noise* that arises from mechanical dissipation in the coatings and is present at high frequencies. The *suspension thermal noise* is mainly caused by the energy loss in the fused silica fibres used in the suspension pendulums, and limits the sensitivity for low frequencies. KAGRA utilizes cryogenization techniques to mitigate thermal effects.

Quantum noise Quantum noise is a sum of the *radiation pressure noise* (RPN), which dominates the low-frequency region of the spectrum, and the *shot noise* (SN), which predominates at high frequencies. RPN arises from the pressure exerted by the laser beam on the mirrors. SN is caused by the uncertainty in the number of photons reaching the mirrors at a certain time. This uncertainty causes fluctuations in the pressure exerted by the photons on the mirrors and, consequently, fluctuations in the mirror positions. Since O3, the shot noise effect has been reduced by injecting squeezed vacuum states into the interferometer [22].

b) Technical noise

Technical noises arise from technical imperfections or limitations rather than from physical principles. Examples of these include electromagnetic noise, laser frequency and intensity noise, control noise, scattered light, and residual gas noise. A thorough description can be found in [23].

1.2.4 Current GW detectors

At the time of writing, just at the beginning of the second half of O4, five interferometer GW detectors are in operation, all of them ground-based.

LIGO The LIGO Scientific Collaboration (LSC) operates two 4km-arm long GW detectors, located in the sites of Hanford (Washington, USA) and Liv-

ingston (Louisiana, USA). After undergoing a major upgrade to their current Advanced configuration in 2015 [20], both sites made the first GW detection on September 14th, 2015. Since then, they have undergone multiple upgrades to achieve their design sensitivity, and reported 90 CBC candidates during the first three observing runs [8]. It has been observing in O4 since May 2023, and the collected data is being now analyzed.

Virgo The Advanced Virgo interferometer is situated in Cascina, Italy, and its arms are 3 km long [24]. Although its sensitivity is typically lower than LIGO's, its integration into the GW network in 2017 was key to improve the source sky localization. The first three-interferometer detection occurred on August 14th, 2017. Since then, it has been in operation, with occasional downtime periods for construction and commissioning. Virgo joined O4 for its second half, starting on April 2024.

KAGRA KAGRA is an underground interferometer built in the Kamioka mine in Gifu, Japan [25]. It has 3 km long arms and is the first GW interferometer to implement cryogenic mirrors. Although its sensitivity currently falls below the design target, plans are underway for it to join LIGO and Virgo at the end of O4.

GEO 600 GEO 600 is a 600-meter long tube interferometer located near Hannover, Germany [26]. Unlike its counterparts, GEO 600 does not incorporate Fabry-Pérot cavities, but its 1200 m long arms are folded inside the tubes. Due to its size, it is unlikely that it will reach a sensitivity able to detect GWs, but it currently serves as a testing ground for researching and demonstrating new systems and technologies, some of which could potentially be implemented in other detectors.

1.2.5 Future planned detectors

In order to broad our current understanding of the nature of GWs, several detectors are expected to expand the existing network. ASD sensitivity curves for some of them are presented in Fig. 1.8.

LIGO-India In the short term future, a third LIGO interferometer is planned to be constructed near Aundha, in India [27]. Given its location on Earth, the addition of LIGO-India is expected to increase the precision of source sky localization by at least an order of magnitude. It is expected to become operational by the end of the decade.

3G GW detectors Looking further ahead, plans are underway to construct a new generation of ground-based detectors expected to start operations in the mid-2030s. The so-called third-generation (3G) is expected to cover a similar frequency range as current detectors, while improving the sensitivity up to 10 times the design sensitivity of Advanced LIGO. At the moment, two projects are in advanced stages of preparation, the Einstein Telescope (ET) in Europe and the Cosmic Explorer (CE) in the United States. ET is designed as an underground triangular-shaped interferometer with an arm length of 10 km [28]. The design concept for CE ifeatures two facilities, one measuring 40 km per side and the other 20 km per side, each accommodating a single L-shaped detector.

Space-based missions In order to detect GWs from more massive sources such as SMBH, detectors need to go much lower in the frequency range, into the sub-Hertz regime. This is impossible for ground-base detectors, whose sensitivity is limited by the residual seismic noise. The Laser Interferometer Space Antenna (LISA) project is designed to deploy three spacecrafts in triangular formation, separated by 2.5 million km, moving in an Earth-like orbit around the Sun [29]. Each spacecraft will contain a pair of free-falling test masses shielded from external forces, and it will use time delay interferometry to avoid the fluctuations in the length of its laser arms. After the mission LISA Pathfinder successfully provided an in-flight test of several key technologies [30], LISA is scheduled to be launched in 2035.

1.3 GWs from compact binary coalescences

While gravitational waves can originate from a wide spectrum of sources, this thesis focuses on the detection and follow-up of signals produced in the mergers of binary compact objects such as black holes and neutron stars. In this section we define the space of parameters that characterizes a compact binary coalescence (CBC) and establish reference frames. Additionally, we explore the three distinct stages of a CBC waveform: inspiral, merger, and ringdown, and analyze the evolution of the binary system during the inspiral phase. Finally, we consider the impact of cosmological distances.

1.3.1 Parameter space

Within the framework of GR, a full description of a CBC waveform requires knowledge of at least 15 independent parameters, usually divided in *intrinsic*

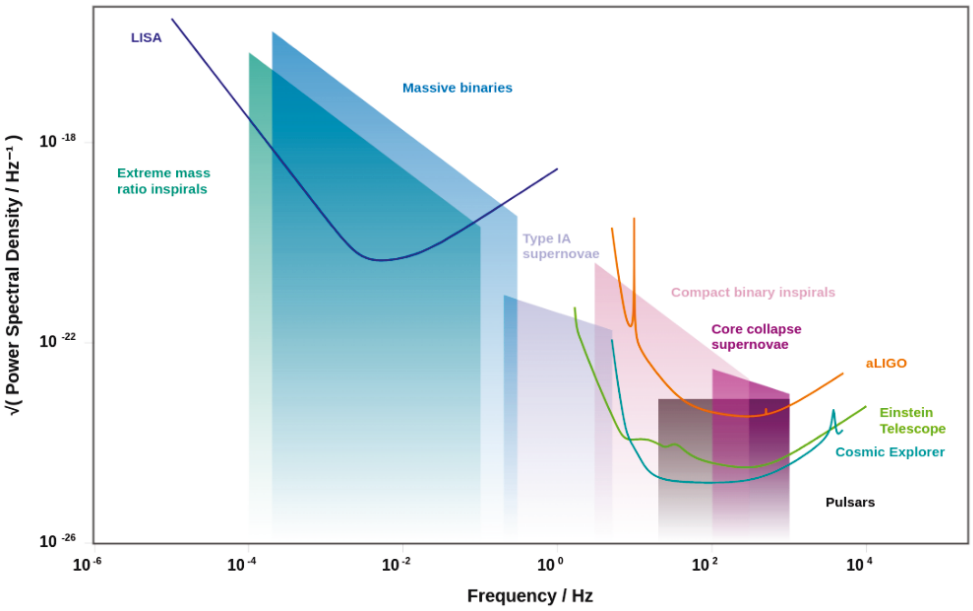

Figure 1.8: Noise budget sensitivity curves for several future GW detectors compared with AdvancedLIGO design sensitivity curve. Colored areas represent the ASD for various GW sources. Figure generated with Gravitational Wave Sensitivity Curve Plotter (see [31]).

and *extrinsic*, depending on if they describe the nature of the compact objects or their position in relation to Earth. A visual representation of these parameters can be seen in Fig. 1.9.

Intrinsic parameters

Intrinsic parameters affect the dynamics of the binary system and influence the amplitude and phase evolution of the signal. The basic intrinsic parameters that characterize a binary of compact objects are their two component masses m_1, m_2 (called the *primary* and *secondary* masses, since $m_1 \geq m_2$) and the six cartesian components of their dimensionless spin vectors $\vec{\chi}_1$, $\vec{\chi}_2$. These are related to their spin angular momentum $\vec{S}_i$ by

$$\vec{\chi}_i = \frac{c}{G}\frac{\vec{S}_i}{m_i^2}\,, \tag{1.43}$$

and their magnitude can theoretically vary from 0 (non-spinning) to 1 (Kerr limit for BHs). Some combinations of these parameters are extremely useful to model CBC waveforms. Important combinations of masses are the *total mass* of the system $M = m_1 + m_2$, the *mass ratio* $q = m_2/m_1$, the *symmetric mass ratio* $\eta = m_1 m_2/M^2$ and the *chirp mass*

$$\mathcal{M} = \frac{(m_1 m_2)^{3/5}}{(m_1 + m_2)^{1/5}} = \eta^{3/5} M\,. \tag{1.44}$$

The two spin vectors can be combined with the masses to form the *effective inspiral spin*

$$\chi_{\rm eff} = \frac{(m_1\vec{\chi}_1 + m_2\vec{\chi}_2)\cdot\hat{L}}{M}\,, \tag{1.45}$$

where $\hat{L}$ is the unit vector in the direction of the total orbital angular momentum $\vec{L}$. The *spin tilt* angle for each component object

$$\theta_i = \arccos\left(\vec{\chi}_i \cdot \hat{L}/|\vec{\chi}_i|\right)\,, \tag{1.46}$$

quantifies the angle between its spin vector and the orbital angular momentum vector.

When at least one of the objects is a neutron star, the matter effects present influence the binary inspiral, and an extra parameter that quantifies this effect needs to be added to the set for each NS present: the dimensionless quadrupole *tidal deformability* Λ_i.

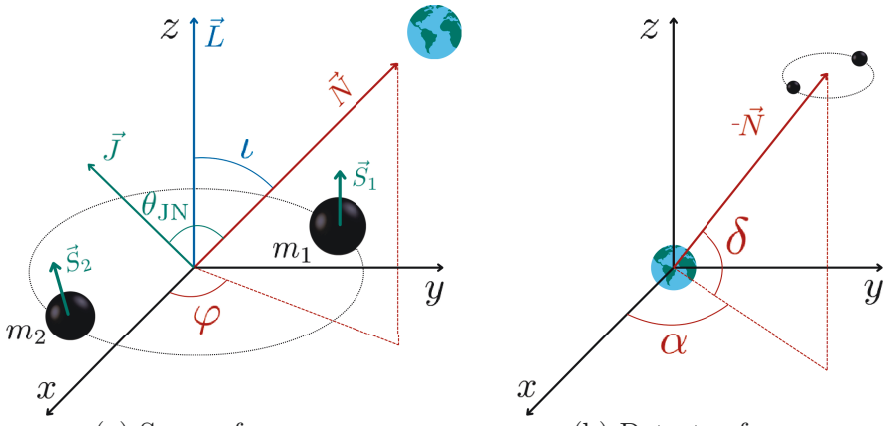

(a) Source frame (b) Detector frame

Figure 1.9: Representation of the geometry of the extrinsic parameters of a binary with respect to the Earth.

Lastly, in the case of non-circular orbits, additional parameters to account for the *eccentricity* of the system need to be added to the set. However, since the long inspiral phase is known to circularize binaries shortly after their formation, sources are expected to be have quasi-circular orbits when they reach the detector sensitivity band [32]. Special cases with dynamically formed binaries may show residual eccentricity, but these will not be studied in this thesis.

Extrinsic parameters

Seven extrinsic parameters fully localize the source with respect to each detector on Earth. The distance between the source and the Earth is given by the *luminosity distance* $D_{\rm L}$. The orientation of the binary seen from the detector are given by the sky-location angles (*right ascension* α and *declination* δ). The direction of the detector from the source is given by the *inclination* angle ι between the orbital momentum $\vec{L}$ and the line-of-sight $\vec{N}$. Finally, the *polarization* angle ψ of Fig. 1.5, the *coalescence time* $t_{\rm c}$, and the *coalescence phase* $\Phi_{\rm c}$ complete the set of extrinsic parameters. Another parameter that is typically used is $\theta_{\rm JN}$, between the line-of-sight and the total angular momentum $\vec{J} = \vec{L} + \vec{S}_1 + \vec{S}_2$. Lastly, the angle φ is the polar angle that defines the direction of the line-of-sight measured over the orbital plane, complementing the previously defined angle ι in the source reference frame.

1.3.2 Waveform strain anatomy

The signals emitted in these scenarios are classified as *modeled* because their theoretical waveforms can be predicted within the GR framework. A compact binary coalescence is typically divided into three distinct stages: the inspiral, the merger, and the ringdown (IMR), and each of them is modeled using different mathematical and computational techniques. These stages are summed up below and represented in Fig 1.10.

Inspiral In the *inspiral* phase, both bodies orbit each other, emitting GWs in the process and gradually shrinking the orbit due to the loss of energy carried away by the waves. During this stage, that can last for hundred of millions of years, the amplitude and frequency of the GWs steadily increase, creating a characteristic chirping signal.

Merger The *merger* occurs when the two bodies come into close proximity and eventually collide in a high energetic event where GWs are emitted in a burst of radiation. This stage typically has a duration of a fraction of a second and is characterized in the waveform of the signal by a sharp peak in the amplitude.

Ringdown For two binary black holes, the *remnant* object after the merger is a perturbed Kerr BH. This newly formed object undergoes a period of oscillation and relaxation, known as the *ringdown*, where it settles into its final state, emitting gravitational waves with a rapidly decreasing frequency and amplitude. The ringdown signal provides valuable information about the properties of the remnant, such as its mass, spin, and internal structure. For NSBH and BNS systems, the final state can also be a massive NS, presenting a more complicated behaviour.

1.3.3 Inspiral of compact binaries

In this section, we study the inspiral stage by modeling the binary as two Newtonian point particles in a quasi-circular orbit. To do so, we mostly follow the approach in [4]. We assume that the distance between the objects is large enough that their velocity v is much lower than the speed of light c, and that the gravitational effect of one object over the other is low enough to allow for a Newtonian description.

Initially, we consider a binary system of point-like masses m_1, m_2 situated at $\mathbf{x}_1$ and $\mathbf{x}_2$, separated by a distance R in a circular orbit with *orbital frequency*

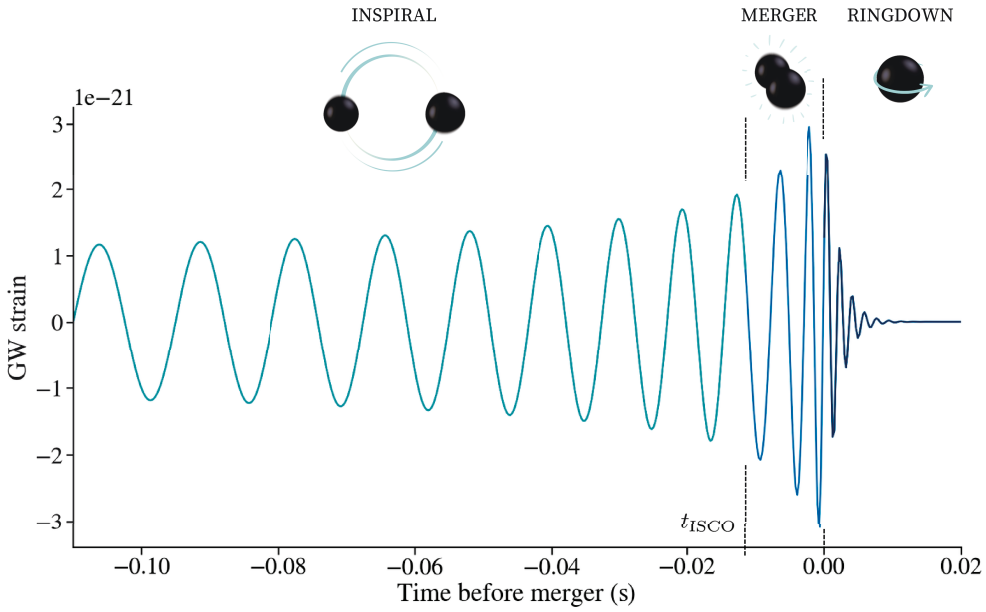

Figure 1.10: Representation of the plus polarization of a GW generated during the coalescence of two non-spinning black holes with masses of $20\,M_\odot$ and $10\,M_\odot$ at a distance of 100 Mpc. The three stages of the coalescence are represented in the figure, delineated by black dotted lines positioned at the moment when the orbit reaches the innermost stable circular orbit (ISCO) limit and the time of merger. The waveform approximant used is `SEOBNRv4` [33].

ω. In the Newtonian approximation, these parameters are related by Kepler's law

$$\omega = \sqrt{\frac{GM}{R^3}}\,, \tag{1.47}$$

where $M = m_1 + m_2$ is the total mass of the system. In a coordinate system centered at the center of mass $\mathbf{x}_{\rm CM} = 0$, the dynamics of the binary can be described as those of a particle of *reduced mass* $\mu = m_1 m_2/M$ situated at the *relative coordinate* $\mathbf{x}_0 = \mathbf{x}_1 - \mathbf{x}_2$. In the CM frame, the mass density of a system with these characteristics is

$$\rho(t, \mathbf{x}) = \mu\, \delta^3(\mathbf{x} - \mathbf{x}_0(t))\,, \tag{1.48}$$

and the second mass moment of (1.32) becomes

$$M_{ij}(t) = \mu\, x_0^i(t) x_0^j(t)\,. \tag{1.49}$$

Considering a $\mathbf{x} = \{x, y, z\}$ reference frame where the binary orbit is in the x-y plane, the trajectory of the effective mass μ is given by

$$x_0(t) = R\,\cos(\omega t + \frac{\pi}{2})\,, \quad y_0(t) = R\,\sin(\omega t + \frac{\pi}{2})\,, \quad z_0(t) = 0\,. \tag{1.50}$$

In these coordinates, the only non-vanishing components of the second derivative of the M_{ij} on (1.49) are

$$\begin{aligned} \ddot{M}_{xx} &= -\ddot{M}_{yy} = 2\mu R^2\omega^2\cos(2\omega t)\,, \\ \ddot{M}_{xy} &= \quad \ddot{M}_{yx} = 2\mu R^2\omega^2\sin(2\omega t)\,. \end{aligned} \tag{1.51}$$

Inserting these expressions in a more generic version of (1.35), for a GW in a direction $\vec{N}$ defined by the polar angles $(\iota,\ \varphi)$ with respect to the orbital momentum $\vec{L}$ (see Fig. 1.9) we get

$$\begin{aligned} h_+(t) &= \frac{4G\mu R^2\omega^2}{c^4 r}\left(\frac{1+\cos^2\iota}{2}\right)\cos(2\omega t_{\rm ret} + 2\varphi)\,, \\ h_\times(t) &= \frac{4G\mu R^2\omega^2}{c^4 r}\cos\iota\,\sin(2\omega t_{\rm ret} + 2\varphi)\,, \end{aligned} \tag{1.52}$$

where r is the distance from the observer to the binary system, assumed constant, and $t_{\rm ret}$ is the retarded time from (1.29). From these equations it can be seen that the frequency of the emitted GW radiation at quadrupole order is twice the orbital frequency of the binary $\omega_{\rm gw} = 2\omega$. The origin of time can be shifted to get rid of the dependence on φ and change $t_{\rm ret} \to t$.

In the quadrupolar approximation, the angular GW radiated power distribution can be obtained using (1.36) as

$$\frac{dP}{d\Omega} = \frac{2G\mu^2R^4\omega^6}{\pi c^5}\left[\left(\frac{1+\cos^2\iota}{2}\right)^2 + \cos^2\iota\right]\,, \tag{1.53}$$

where the angular dependence on ι gives it the classical "peanut" shape of Fig. 1.11, with a maximum when the orbit is seen *face-on* ($\iota = 0$) and a minimum when the observation is *edge-on* ($\iota = \pi/2$). The total radiated power is

$$P = \frac{G\mu^2R^4\omega^6}{10c^5}\,. \tag{1.54}$$

The emission of GWs carries away orbital energy, leading to a decrease in the orbital separation $R(t)$, and an increase in the orbital frequency $\omega(t)$

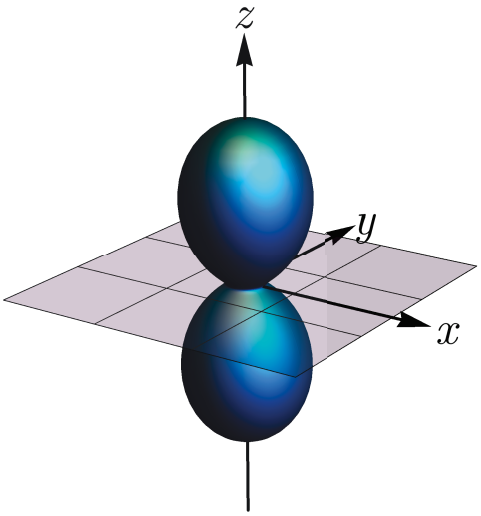

Figure 1.11: Angular distribution of the power radiated by a binary in the quadrupole approximation. The binary orbit is assumed circular and over the x-y plane.

until coalescence occurs. During the inspiral stage, it can be assumed that R decreases at a slow rate, such that the radial velocity $\dot{R}$ is much smaller than the orbital velocity $v = \omega R$. Therefore, the binary can be considered to be in a *quasi-circular* adiabatic orbit. In this regime, the energy of the orbit is given by

$$E_{\rm orbit} = -\left(\frac{G^2}{32}\right)^{1/3} \mathcal{M}^{5/3}\, \omega_{\rm gw}^{2/3}(t)\,, \tag{1.55}$$

where $\mathcal{M}$ is the chirp mass of Eq. (1.44). Assuming that all the orbital energy loss corresponds to GW radiation, the radiated power P of (1.54) corresponds to $-dE_{\rm orbit}/dt$, giving a frequency evolution of

$$\dot{f}_{\rm gw} = \frac{96\pi^{8/3}}{5}\left(\frac{G\mathcal{M}}{c^3}\right)^{5/3} f_{\rm gw}^{11/3}\,, \tag{1.56}$$

with $f_{\rm gw} = \omega_{\rm gw}/(2\pi)$. In terms of the *time to coalescence* $\tau = t_{\rm c} - t$ between a particular moment t and the coalescence time $t_{\rm c}$, the frequency can be integrated to

$$f_{\rm gw}(\tau) = \frac{1}{\pi}\left(\frac{5}{256\,\tau}\right)^{3/8}\left(\frac{G\mathcal{M}}{c^3}\right)^{-5/8}\,. \tag{1.57}$$

To find the waveform evolution during the inspiral, it is useful to define the *orbital phase* $\Phi(t)$ as

$$\Phi(t) = \int \omega_{\rm gw}(t) dt \,. \tag{1.58}$$

Through (1.57), the orbital phase in terms of $\tau = t_c - t$ is given by

$$\Phi(\tau) = \Phi_{\rm c} - 2\left(\frac{5\,G\mathcal{M}}{c^3}\right)^{-5/8} \tau^{5/8} \,, \tag{1.59}$$

where $\Phi_{\rm c}$ is the coalescence phase. Then, the two polarizations of the GW can be expressed as

$$\begin{aligned} h_+(t) &= \frac{G\mathcal{M}}{c^2 r}\left(\frac{\tau}{5\,G\mathcal{M}/c^3}\right)^{-1/4}\left(\frac{1+\cos^2\iota}{2}\right)\cos[\Phi(\tau)] \,, \\ h_\times(t) &= \frac{G\mathcal{M}}{c^2 r}\left(\frac{\tau}{5\,G\mathcal{M}/c^3}\right)^{-1/4}\cos\iota\,\sin[\Phi(\tau)] \,. \end{aligned} \tag{1.60}$$

This is called the *chirp waveform*, since both the frequency and the amplitude present a monotonic increase as the coalescence approaches. This behaviour can be seen in the strain evolution of Fig. 1.10. It is worth noting that, at Newtonian order, the amplitude and the phase of the emitted GWs depend on the component masses only through the chirp mass $\mathcal{M}$. Systematic corrections to this Newtonian approximation are known as post-Newtonian (PN) expansions, and we will discuss them in the next chapter.

The assumption of adiabatic quasi-circular orbits loses its validity when the orbit reaches a radial distance known as the innermost stable circular orbit (ISCO), after which the dynamics are dominated by strong-field effects. In the Schwarzschild geometry, this corresponds to a radial separation $r_{\rm ISCO} = 6G/c^2M$. Then, all previous expressions are only valid up to a maximum GW frequency

$$(f_{\rm gw})_{\rm ISCO} = \frac{c^3}{6\pi\sqrt{6}GM} \,. \tag{1.61}$$

1.3.4 Effect of cosmological distances

When the binary systems are found at cosmological distances, the expansion of the Universe during the propagation from the source to the detector will produce a non-negligible effect on the binary inspiral. We consider an homogeneous and isotropic Universe, characterized by a Friedmann-Lemaitre-Robertson-Walker (FLRW) metric. In a expanding Universe, the time at the

detector presents a dilatation with respect to the time of the source, given by the *redshift* parameter z as $dt^{\rm det} = (1+z)dt^{\rm src}$. The frequency measured at the detector carries the same dependency as

$$f^{\rm det} = (1+z)^{-1} f^{\rm src}\,. \tag{1.62}$$

Therefore, it can be seen [4] that the GW amplitude from a binary at a cosmological distance will take the same form as in (1.60), but taking into account that the chirp mass is the one measured at the detector, with

$$\mathcal{M}^{\rm det} = (1+z)\mathcal{M}\,, \tag{1.63}$$

and that the distance is represented by the luminosity distance $D_{\rm L}(z)$. While the same relation as in (1.63) holds for any mass measured at the detector, obtaining an analytical relation between the luminosity distance and the redshift is more complicated. In this thesis we assume a standard flat ΛCDM cosmology, where the luminosity distance is given by [34]

$$D_{\rm L}(z) = \frac{c(1+z)}{H_0}\int_0^z \frac{dz'}{\sqrt{\Omega_m(1+z')^3 + (1-\Omega_m)}}, \tag{1.64}$$

with Hubble parameter $H_0 = 67.90\,{\rm km\,s^{-1}\,Mpc^{-1}}$ and matter density parameter $\Omega_m = 0.3065$ [35].

2

CBC WAVEFORMS AND DATA ANALYSIS METHODS

In this chapter, we outline the current methods used to analyze data recorded by GW detectors, ranging from the detection of the signal to the estimation of the parameters that characterize the source. For modeled sources, such as compact binary coalescences (CBCs), the optimal technique to extract the GW signal from the data is matched filtering. Since this technique relies on accurate predictions of the potential detectable GW waveforms, an introduction to waveform modeling is also included.

2.1 Waveform modeling

In Section 1.3.3, we derived an analytical solution for the linearized Einstein equations governing compact binary systems, under the assumptions of a quadrupolar approximation and a Newtonian quasi-circular orbit. However, for the purpose of detecting GW signals from CBCs in the data collected by detectors, a much more accurate description of the solutions is required. This entails considering additional factors such as including higher-order terms in the multipolar expansion, strong gravitational effects, non-linear effects, radiation reaction, and the coupling of spins with the total angular momentum (spin-orbit) or between each other (spin-spin).

Given the inherent complexity of the two-body problem in GR, analytical solutions for the full Einstein equations are challenging, if not impossible, to obtain. Consequently, significant effort has been directed towards developing waveform models capable of accurately reproducing the behavior of GW radiation throughout all stages of the coalescence process, known as inspiral-merger-ringdown (IMR), as described in Section 1.3.2. In the next section, we

will introduce some of the various approaches to wavefom modeling, known as waveform families or *approximants*.

2.1.1 Waveform approximants

The varied waveform approximants can take the form of analytical models, numerical simulations, or a combination of both, each with a different balance between accuracy and computational cost. Different approximants describe distinct physical effects and therefore typically apply within a limited parameter range or specific frequency band [36].

During the inspiral, the separation between the compact objects is sufficiently large to consider that the gravitational interaction between them is weak. In this phase, characterized by low orbital velocities ($v \ll c$) and adiabatically decreasing quasi-circular orbits, the GW signal can be accurately modeled by an analytical *post-Newtonian* (PN) expansion (see Sec. 2.1.2). A few orbits before the merger, the gravitational strong-field interactions start to dominate, breaking down the adiabatic approximation. During this phase, that lasts until the merger, the dynamics of the system are highly non-linear, requiring the full Einstein equations to be solved. This is achieved through computationally expensive *numerical relativity* (NR) techniques. After the merger, the dynamics depend on the nature of the resulting perturbed object. A perturbed Kerr BH will settle down to a stationary state, radiating away energy through a superposition of quasi-normal modes (QNMs), and can be described by *perturbation theory* within the gravitational self-force (GSF) formalism. Conversely, for a resulting super-massive NS, the dynamics will be highly dependent on a large number of factors, such as the masses of the original binary, the equation of state (EOS) or the presence of thermal effects [37, 38]. A review on NS post-merger modeling can be seen in [39].

The analytical perturbative calculations and Numerical Relativity (NR) simulations can be combined to construct waveform models valid during the entire coalescence, known as inspiral-merger-ringdown (IMR) waveforms. The IMR approximant families can be classified into three main groups depending on their approach: effective-one-body (EOB) simulations [40, 41], phenomenological models (Phenom) [42], and interpolations of NR simulations (Surrogate) [43].

A schematic representation of some of these approximants along with their ranges of validity can be seen in Fig. 2.1.

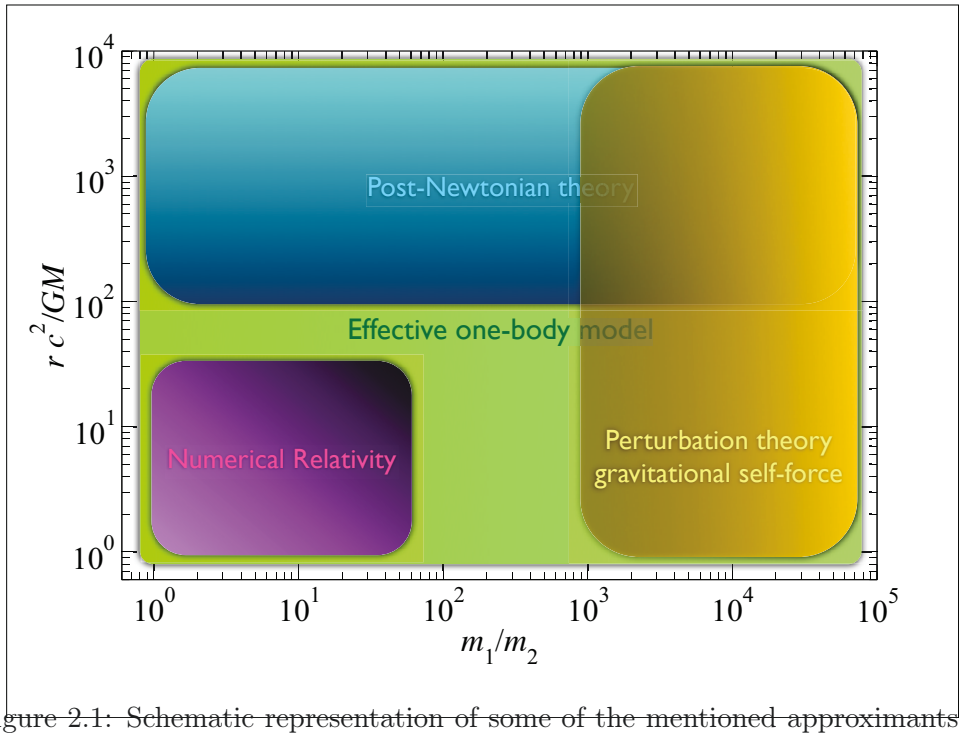

Figure 2.1: Schematic representation of some of the mentioned approximants and their ranges of validity in the space of $x^{-1} = Rc^2/GM$ vs. the inverse mass ratio m_1/m_2. Figure reproduced from [36].

2.1.2 Post-Newtonian expansion

In this section, we discuss the post-Newtonian (PN) expansion approximant. An extensive and up-to-date review of the state of the development of this approach can be consulted at [44].

The basis of the PN approximation lies in expanding the full Einstein equations around the Newtonian prediction in powers of a small parameter $x^n \sim (v/c)^{2n}$. For a compact binary system, v represents the orbital velocity, and $2n$ is the maximum power of v/c retained in a n-PN order expansion. Since CBCs are systems held together by gravitational forces, the virial theorem implies a relation between the velocity of the system and the strength of the gravitational field near the source

$$x \sim \left(\frac{v}{c}\right)^2 \sim \frac{GM}{c^2 R}\,, \tag{2.1}$$

where R is the orbital separation and M is the total mass of the system. This

relation gives the validity regime of the PN expansion: slowly moving, weakly stressed ($v \ll c$) and weakly self-gravitating sources ($GM/c^2R \ll 1$).

For quasi-circular orbits, the time evolution of the frequency and phase during the inspiral is entirely driven by the *energy balance* equation

$$\frac{dE}{dt} = -\mathcal{F}\,, \tag{2.2}$$

which relates the change in the orbital energy E with the total energy flux $\mathcal{F}$ emitted by GWs. For gravitational waves propagating radially outward from the source, the total radiated flux is given by [4]

$$\mathcal{F} = -\frac{dE}{dt} = \frac{c^3 r^2}{32\pi G}\int \langle \dot{h}_{ij}^{TT}\dot{h}_{ij}^{TT}\rangle\, d\Omega = \frac{c^3 r^2}{16\pi G}\int \langle \dot{h}_{+}^{2} + \dot{h}_{\times}^{2}\rangle\, d\Omega\,, \tag{2.3}$$

where h_{ij}^{TT} is the complete gravitational waveform and the integral is performed over a surface at a large distance from the source $r \gg R$.

The restricted PN waveform

In the PN approximation, the polarizations of a GW emitted by a quasi-circular binary system present the following general structure in terms of x up to n-PN order [45, 46]

$$h_{+,\times} = \frac{2G\mu x}{c^2 R}\sum_{N=0}^{2n} x^{N/2} H_{+,\times}^{N/2}\,, \tag{2.4}$$

The leading order ($n = 0$) is

$$\begin{aligned} H_{+}^{0}(t) &= -(1+\cos^2\iota)\cos[2\psi(t)]\,,\\ H_{\times}^{0}(t) &= -2\cos\iota\sin[2\psi(t)]\,, \end{aligned} \tag{2.5}$$

where ψ is the GW half phase, related to the orbital phase ϕ by

$$\psi(t) = \phi(t) - \frac{2\pi G M f}{c^3}\ln\left(\frac{f}{f_0}\right)\,. \tag{2.6}$$

Here, f_0 is a constant arbitrary frequency that can be chosen as the minimum frequency in the detector sensitivity band.

Most PN approximants are described within the framework of the so-called *restricted PN approximation*. In this approach, the expansion of the amplitudes $H_{+,\times}^{n}$ is retained at leading order, while the orbital phase $\phi(t)$ is expanded up to the maximum available order in the PN expansion. This choice is moti-

vated by the necessity of correcting the phase up to at least 3.5PN order for accurately extracting signals from detector data, while the amplitude terms beyond leading order become negligible for small x [4]. Since the restricted PN approximation maintains the quadrupole approximation, the frequency of the GW is twice the orbital frequency $\omega_{\rm gw} = 2\omega$. This approximation holds well for non-precessing binaries, where the quadrupolar mode carries the majority of the emitted power. However, a brief introduction to the effects of accounting for higher modes in the multipolar expansion is provided in Section 2.1.3.

Phasing evolution

To derive the PN time evolution of the frequency f and orbital phase ϕ of the binary from (2.2), the energy E and the flux $\mathcal{F}$ are expanded up to certain order in the PN parameter

$$x = \left(\frac{GM\pi f}{c^3}\right)^{2/3} . \tag{2.7}$$

The complete expressions for $E(x)$ and $\mathcal{F}(x)$ up to 4.5PN order for non-spinning binaries can be found in equations Eq. (3) and Eq. (4) of [47], respectively. Subsequently, knowing the expanded expressions for $E(x)$ and $\mathcal{F}(x)$, applying the chain rule to the energy balance equation

$$\frac{df}{dt} = \frac{dE/dt}{dE/df} = \frac{-\mathcal{F}}{dE/df} , \tag{2.8}$$

and solving the resulting differential equation in x, the time evolution of the GW frequency can be obtained. The orbital phase $\phi(t)$ is then obtained by integrating

$$\phi(t) = \pi \int f dt . \tag{2.9}$$

Since $E(x)$ and $F(x)$ are defined perturbatively, there are multiple methods to solve equations (2.8) and (2.9). Consequently, there is no unique solution for $\phi(t)$, but rather different PN approximants that describe slightly different waveforms [48, 49]. A brief description of the most commonly used PN approximant, the TaylorF2, is given below.

TaylorF2

The TaylorF2 approximant is expressed in the frequency domain, and it can be computed using an approximation for the integral of the Fourier transform

known as the *stationary phase approximation* (SPA) [50]. This approximation assumes that the amplitude of the signal is slowly-varying with respect to the phase. The waveform for this approximant is given by [49]

$$\tilde{h}(f) = \mathcal{A} f^{-7/6} e^{i\Psi_{\rm PN}(f)}\,, \tag{2.10}$$

where $\mathcal{A}$ is an amplitude proportional to $\mathcal{M}^{5/6}$, and $\Psi_{\rm PN}(f)$ is the frequency-domain GW half-phase

$$\Psi_{\rm PN}(f) = 2\pi f t_c - 2\phi_c - \frac{\pi}{4} + \phi_{\rm PN}(f)\,, \tag{2.11}$$

which is an expansion in frequency, with $v = (\pi G M f)^{1/3}$. The half-phase $\Psi(f)$ terms for non-spinning binaries can be calculated up to 4.5PN order (see Eq. (9) of [47]). Terms that include spin effects are known up to less order in the PN expansion (see Eq. (A.21) of [51]). A more detailed description of the phasing terms of the TaylorF2 approximant will be given in Chapter 5.

2.1.3 Multipole expansion

Up to this point, all calculations have been conducted under the quadrupolar approximation, retaining only the leading term of the multipolar expansion of the stress-energy tensor. In this approximation, a binary inspiraling in a circular orbit radiates GWs with a frequency twice its orbital frequency (see Eq. (1.52)). However, GW radiation is a composition of different harmonics of the orbital frequency that arise form higher-order multipoles, such as the mass-octupole or the current-quadrupole. To understand the behaviour of the gravitational waveform beyond the quadrupolar approximation, it is useful to express the complex GW strain h with respect to a basis of *spherical harmonics* Y^{lm}_s of spin-weight $s = -2$ [52, 53] as

$$h(t) = h_+(t) - i h_\times(t) = \sum_{l=2}^{\infty} \sum_{m=-l}^{l} Y^{lm}_{-2}(\iota, \varphi) h_{lm}(t)\,, \tag{2.12}$$

where h_{lm} are the different *modes* of the GW radiation. The contribution of each mode to the observed signal depends on their respective Y^{lm}_{-2}, which is a function of the spherical angles (ι, φ) defining the direction of propagation of the GW (see Fig. 1.9). The *dominant mode* $(l,m) = (2,\pm2)$ corresponds to the quadrupole mass moment and it is the largest contribution to the signal. Modes beyond $(2,\pm2)$ are known as higher-harmonics or *higher-order multipoles* (HOM) and become relevant for different situations, such as sources close to

the edge-on configuration, very unequal-mass binaries such as GW190814 [54] and GW190412 [55], or massive BBH systems. For non-precessing systems, the most dominant higher-order multipoles (HOM) are the (2,1), (3,2), (3,3) and (4,4) modes [56].

To apply the PN expansion, it is useful to factorize the h_{lm} modes as a complex amplitude A_{lm} and a phase Φ_{lm} as

$$h_{lm} = A_{lm} e^{-i\Phi_{lm}} \,. \tag{2.13}$$

For inspiral binaries, this phase is approximately $\Phi_{lm} \simeq m\Phi_{\rm orbit}$ [57] and therefore the frequency of a mode (l, m) is related to the orbital frequency as $\omega_{lm} \simeq m\omega_{\rm orbit}$. Therefore, each mode can be expanded to n-PN order as

$$h_{lm} = \sum_{n;m} A^n_{lm} e^{-im\Phi_{\rm orbit}} \,. \tag{2.14}$$

In this formalism, the *restricted waveform* described in the previous section is the Newtonian amplitude of the (2,±2) mode and its phase, corrected up to a certain PN order.

2.2 Bayesian approach to signal detection

As discussed in Sec. 1.2, interferometric gravitational wave detectors measure the phase shifts of the recombined light after it has traveled through the arms and record it as a time series $d(t)$, representing the *output* data of the detector. Typically, this output consists of a superposition of background noise $n(t)$ and a potential real GW signal $h(t)$ described by a set of parameters θ, in the form

$$d(t) = h(t;\theta) + n(t) \,. \tag{2.15}$$

The detection problem then lies in distinguishing the signal from the noise, a task especially complex given that the amplitude of the majority of GW signals is comparable to the background noise.

Since noise has statistical properties due to be a random process, in order to claim a detection we need to construct a statistic that quantifies the probability that the data contains a GW signal, known as an *optimal detection statistic*. Therefore, the detection process can be seen as a model selection problem between the hypothesis of the data containing a GW signal or only Gaussian noise. The consideration of model selection ultimately leads to the use of *matched filtering*, the optimal technique to search for known GW signals in

the detector data.

2.2.1 Fundamentals of Bayesian inference

Detecting a signal and estimating the parameters of the source are probabilistic processes and they must be described in a statistical framework. We use the Bayesian approach [58], where the knowledge about an hypothesis A is described by a probability $P(A) \in [0, 1]$, and about an unknown parameter as a probability density function (PDF) $p(\theta|A)$, with

$$\int p(\theta|A)d\theta = 1\,. \tag{2.16}$$

In this framework, the conditional probability of an hypothesis or model A given the data d is defined by the Bayes theorem as

$$P(A|d) = \frac{\mathcal{L}(d|A)\pi(A)}{\mathcal{Z}}\,, \tag{2.17}$$

where the denominator is a normalization factor named the *evidence*. In this framework, the probability of the hypothesis given the data $P(A|d)$ is called the *posterior* probability. Since the evidence is just a number, the posterior is only proportional to two factors. The first is the probability of the data given the hypothesis, known as the *likelihood* $\mathcal{L}(d|A)$. The likelihood function is the chosen probability distribution from which the data d is drawn. We will discuss the likelihood function choice in the next subsection. The other factor is the *prior* probability $\pi(A)$, a representation of our preexisting belief on the probability of the hypothesis.

In the case the model A is a continuous variable, for example, a set of parameters θ, the evidence is

$$\mathcal{Z} = \int \mathcal{L}(d|\theta)\pi(\theta)d\theta\,, \tag{2.18}$$

which can be converted to a sum in the case of A being discrete.

Marginalization

If the model A is determined by a set of parameters θ, the posterior probability for a subset of parameters θ_i can be obtained by integrating over all the other $\theta_{k\neq i}$, called *nuisance* parameters. This process is known as *marginalization*,

and allows to obtain a marginalized posterior

$$p(\theta_i|d) = \int \left(\prod_{k \neq i} d\theta_k \right) p(\theta|d) \,, \tag{2.19}$$

and a marginalized likelihood

$$\mathcal{L}(d|\theta_i) = \int \left(\prod_{k \neq i} d\theta_k \right) \pi(\theta_k) \mathcal{L}(d|\theta) \,. \tag{2.20}$$

If the last integral is performed over all θ parameters, we recover the expression for the evidence of Eq. (2.18). Therefore, we can refer to the evidence as the *completely marginalized likelihood* function.

Model selection

If we are considering more than one possible model to fit the data, we can compare their evidences to determine which one is statistically preferred by the data. The metric to compare two different models A and B is the *odds ratio*, which is the ratio of posterior probabilities

$$\mathcal{O}^A_B = \frac{P(A|d)}{P(B|d)} = \frac{\mathcal{Z}_A}{\mathcal{Z}_B} \frac{\pi A}{\pi B} \,. \tag{2.21}$$

In many practical cases, the prior odds ratio $\pi(A)/\pi(B)$ is set to unity, and we can employ the ratio of evidences or *Bayes factor*

$$\mathcal{B}^A_B = \frac{\mathcal{Z}_A}{\mathcal{Z}_B} \,, \tag{2.22}$$

often expressed in its logarithmic form as

$$\log \mathcal{B}^A_B = \log(\mathcal{Z}_A) - \log(\mathcal{Z}_B) \,. \tag{2.23}$$

The sign of $\mathcal{B}$ and its absolute value informs respectively about which model is preferred over the other, and how large is that preference. The $|\log \mathcal{B}|$ threshold to claim a strong evidence of one model over another is not a definite value, but some commonly used thresholds are $|\log_{10} \mathcal{B}| > 1$ and $|\ln \mathcal{B}| > 5$ [59].

Since the evidence is formally a completely marginalized likelihood function, for two models with no unknown parameters the Bayes factor is equivalent

to the likelihood ratio

$$\Lambda^A_B = \frac{\mathcal{L}(d|A)}{\mathcal{L}(d|B)}\,. \tag{2.24}$$

Once we established the statistical framework, we discuss the probability of distinguish a signal from the noise in the detector data in the following sections.

2.2.2 Noise in the detector data

The background noise present in the detector is a combination of two different classes of noise. The main component is stationary and Gaussian, caused by the fundamental processes described in Sec. 1.2.3. The non-Gaussian component for the noise are instead transients of technical origin, which might arise from instrumental artifacts or environmental issues. In the context of GW detection, the emphasis is placed on modeling the stationary Gaussian component, as matched filtering techniques are particularly effective for well-understood processes. Search algorithms employ a number of data analysis techniques to deal with real non-Gaussian noise that we will discuss in Chapter 3.

Gaussian noise likelihood

In the previous section, we defined the likelihood as the probability function where the observed data is drawn from. In GW analysis, the data time series from the output of the detector $d(t)$ is a linear combination of a signal $h(t)$ and the sum of all noise sources present in the detector $n(t)$. Since the signal is completely determined by a set of parameters θ, the likelihood that a signal $h(t;\theta)$ is embedded in the detector data is given by the probability of the *residual* $r(t) = d(t) - h(t;\theta)$ to be drawn from the noise distribution p_N [60]. In the case of Gaussian noise, the likelihood is given by a Gaussian function with an schematic form

$$\mathcal{L}(d|h) = p_N(r) = \frac{1}{\sqrt{2\pi\sigma^2}} \exp\left[-\frac{1}{2}\frac{|d(t) - h(t;\theta)|^2}{\sigma^2}\right], \tag{2.25}$$

where σ is the detector noise. A more accurate expression for the likelihood will be given in Sec. 2.2.3.

Properties of the noise

To study the noise in the detector we start with a situation where there is no signal present, and the data in the detector is pure Gaussian noise $d(t) = n(t)$.

The noise in the detector is *stochastic*, so $n(t)$ can be pictured as a random time-series taken from a larger noise ensemble. Then, to measure the expected properties of a quantity in the presence of noise, we can measure $n(t)$ over a certain time T, which is known as a *realization* of the noise, and average that quantity over multiple independent realizations. This technique is called the *ensemble average*, and is denoted as $\langle\cdot\rangle$ [4].

The noise is assumed to be *stationary*, meaning its mean value $\mu = \langle n(t)\rangle$ is constant with time and it can be set to zero $\langle n(t)\rangle = 0$ without loss of generality. The stationary condition also assures that the auto-covariance function $\langle n(t)n(t')\rangle$ depends only on the time difference $t-t'$. To translate this condition to the frequency domain, we use the Fourier transform

$$\tilde{n}(f) = \int_{-\infty}^{\infty} n(t)e^{-2\pi i f t}dt\,. \tag{2.26}$$

Then, in the Fourier domain the different realizations are uncorrelated

$$\langle \tilde{n}^*(f)\tilde{n}(f')\rangle = \delta(f-f')\frac{1}{2}S_n(f)\,, \tag{2.27}$$

where $S_n(f)$ is the noise *one-sided* power spectral density (PSD), defined by the Wiener-Khinchin theorem as the Fourier transform of the auto-covariance function of the noise. This function gives a description of the noise present in the detector, and can be either estimated from the data or from the physics of the detector. Assuming $n(t)$ is dimensionless, the PSD has units of Hz^{-1}. Alternatively, the Gaussian noise at the detector can be characterized by the ASD curve, denoted as $\sqrt{S_n(f)}$, with dimensions $\mathrm{Hz}^{-1/2}$. This function is sometimes preferred, as it increases linearly with the noise $n(t)$.

The probability of a given noise realization $n(t)$ is given by a multivariate Gaussian distribution [4]

$$p_N(n(t)) = \mathcal{N}\exp\left[-\int_0^{\infty}\frac{\tilde{n}(f)^*\tilde{n}(f)}{\frac{1}{2}S_n(f)}df\right]\,, \tag{2.28}$$

where $\mathcal{N}$ is a normalization constant. Defining the *inner product* [61] of two functions $h(t)$ and $g(t)$ as

$$\big\langle h(t)\big|g(t)\big\rangle = 4\,\mathrm{Re}\int_0^{\infty}\frac{\tilde{h}(f)\tilde{g}^*(f)}{S_n(f)}df\,, \tag{2.29}$$

the probability of a noise realization $n(t)$ can we written as

$$p_N(n(t)) \propto \exp\left[-\frac{1}{2}\langle n(t)|n(t)\rangle\right] . \tag{2.30}$$

2.2.3 Detecting signals with unknown parameters

In the last subsection, we discussed the stochastic nature of the noise where the potential signal is buried. Now, we face the problem of distinguishing the signal from the noise. The fundamental idea in signal detection is the alteration on the statistical properties of the data due to the presence of a signal. In particular, the data follows a probability density function (PDF) $\mathcal{L}(d|N)$ in the absence of a signal, whereas in its presence the PDF becomes $\mathcal{L}(d|S)$ [61].

Therefore, the step of detecting a GW signal $h(t)$ in the output of the detector $d(t)$ can be considered a model selection problem between two hypotheses [62]

$$\begin{aligned} &S : \text{There is a signal in the data} && d_S(t) = h(t) + n(t)\,, \\ &N : \text{The output of the detector is only noise} && d_N(t) = n(t)\,. \end{aligned} \tag{2.31}$$

The ratio of posterior probabilities is given by

$$\frac{P(S|d)}{P(N|d)} = \frac{\mathcal{L}(d|S)}{\mathcal{L}(d|N)}\frac{\pi(S)}{\pi(N)} = \Lambda^S_N(d)\frac{\pi(S)}{\pi(N)}\,, \tag{2.32}$$

where $\Lambda^S_N(d)$ is the likelihood ratio between both hypotheses.

In the Bayesian framework for signal detection, there exists an optimal method to search through the data provided that the statistical characteristics of the detector noise and the prior probability distribution for signals are understood. This involves computing the probability $P(S|d)$ of a certain signal h being present in the measured data d. The criterion for signal detection is that the probability $P(S|d)$ surpasses a predefined threshold value [63, 64].

The statistical criterion described above is susceptible to two categories of errors [65], each associated with its own probability of occurrence:

i) Type I or *false alarm error*: rejecting the *null* hypothesis (no signal present) when it is actually true.

ii) Type II or *false dismissal error*: accepting the *null* hypothesis when it is actually false.

The Neyman-Pearson optimal criterion for signal detection is to maximize the

detection probability for a fixed value of the false alarm probability. Since the probability $P(S|d)$ (2.32) increases monotonically with the likelihood ratio, setting a threshold on the probability of a signal being present in the data is effectively the same as setting a threshold on $\Lambda^S_N(d)$ to detect signals. We will address this in the next subsections.

Signal with known parameters

Before studying the case of a signal with unknown parameters, we consider the case of an exactly known signal h. In Gaussian noise, as demonstrated in the previous subsection, the likelihood for each model is proportional to

$$\begin{aligned} \mathcal{L}(d|N) &= p_N(n = d) \propto \exp\left[-\frac{1}{2}\langle d|d\rangle\right] , \\ \mathcal{L}(d|S) &= p_N(n = d - h) \propto \exp\left[-\frac{1}{2}\langle d - h|d - h\rangle\right] . \end{aligned} \tag{2.33}$$

Expanding the inner product of $d - h$ as

$$\langle d - h|d - h\rangle = \langle d|d\rangle - 2\langle d|h\rangle + \langle h|h\rangle , \tag{2.34}$$

the likelihood ratio gives

$$\Lambda^S_N(d) = \exp\left[\langle d|h\rangle - \frac{1}{2}\langle h|h\rangle\right] . \tag{2.35}$$

Since $\langle h|h\rangle$ is constant for a known h and $S_n(f)$, the likelihood ratio is only monotonically increasing with $\langle d|h\rangle$. This quantity is called the *matched filter* [66], and it is the optimal statistic to detect a known signal h in the detector data d.

With the definition of the inner product (2.29), the matched filter is the correlation of the whitened detector data, filtered by the whitened known signal. The *whitening* process weights each waveform by a factor of $1/\sqrt{S_n(f)}$, so the frequencies where the detector data is specially noisy are downweighted.

We define the signal-to-noise ratio (SNR)

$$\rho = \frac{\langle d|h\rangle}{\sqrt{\langle h|h\rangle}} . \tag{2.36}$$

as the statistic value that is compared to a threshold to decide if a signal is present in the data. The denominator $\sqrt{\langle h|h\rangle} = ||h||$ is the *norm* of $h(t)$.

The known signal h is called a *template*. In a case when the output of the detector is only the signal $d(t) = h(t)$, the matched filter is the squared *optimal* SNR

$$\rho^2_{\rm opt}(h) = \langle h|h\rangle \,. \tag{2.37}$$

If the output of the detector h is filtered with another template g, then the SNR of the signal is given by

$$\rho(h) = \frac{\langle h|g\rangle}{\sqrt{\langle g|g\rangle}} = \frac{\langle h|h\rangle}{\sqrt{\langle h|h\rangle}} \frac{\langle h|g\rangle}{\sqrt{\langle h|h\rangle\langle g|g\rangle}} \,, \tag{2.38}$$

where the first factor is $\rho_{\rm opt}(h)$. The second factor is defined as the *overlap* between the two waveforms

$$\mathcal{O}(h,g) = \frac{\langle h|g\rangle}{\sqrt{\langle h|h\rangle\langle g|g\rangle}}, \tag{2.39}$$

which is a positive number with a maximum value $\mathcal{O}(h,h) = 1$. Therefore, when the data is filtered with a template that is not exactly the same as the signal, the SNR will decrease from its optimal value with the overlap.

Signal with unknown parameters

In this case, the GW signal is a function of a set of unknown parameters θ, which forms a vector in the parameter space. The signal can be parametrized as an unknown amplitude $\mathcal{A}$ that describes the strength of the signal, and a normalized waveform $\hat{h}(\theta)$ that describes its shape. Then,

$$h(\theta) = \mathcal{A}\hat{h}(\theta), \text{ with } \langle \hat{h}|\hat{h}\rangle = 1, \text{ and } \langle h|h\rangle = \mathcal{A}^2 \,. \tag{2.40}$$

In this case, the likelihood ratio is

$$\Lambda^S_N(d;\mathcal{A},\theta) = \frac{\mathcal{L}(d|S;\mathcal{A},\theta)}{\mathcal{L}(d|N)} = \exp\left[\mathcal{A}\langle d|\hat{h}(\theta)\rangle - \frac{\mathcal{A}^2}{2}\right] \,, \tag{2.41}$$

which is again monotonic in $\langle d|h\rangle$. Now, finding the amplitude $\mathcal{A}$ that gives the maximum likelihood (ML) ratio is an optimization problem

$$\frac{\partial}{\partial\mathcal{A}}\Lambda^S_N = 0 \,, \tag{2.42}$$

that results in $\mathcal{A}_{\rm ML} = \langle d|\hat{h}\rangle$. With this result, the maximum Λ_N^S is

$$\max_{\mathcal{A}} \Lambda_N^S = \exp\left[\frac{1}{2}\langle d|\hat{h}\rangle^2\right] . \tag{2.43}$$

With the previous definition of the SNR (2.36), we can write

$$\langle d|\hat{h}\rangle = \frac{\langle d|h\rangle}{\sqrt{\langle h|h\rangle}} = \rho(\theta) , \tag{2.44}$$

and the likelihood ratio for a signal defined by the parameters θ is

$$\Lambda_N^S(d;\theta) = \exp\left[\frac{1}{2}\rho^2(\theta)\right] . \tag{2.45}$$

Note that looking for a signal in the data filtering with a normalized template $\hat{h}$ and with the same template multiplied by an amplitude factor $h_0 = \mathcal{A}\hat{h}$ would yield the same SNR $\rho = \langle d|\hat{h}\rangle$. Therefore, amplitude factors are unimportant for matched filtering, and we can set them as global factors that normalize the templates.

In general, the parameters θ of the sought-after signal are not known a priori, so it is necessary to construct a *bank* of waveform templates over all the parameter space. This bank needs to be sufficiently populated that any combination of parameters will produce a waveform close enough to any template. The output data from the detector $d(t)$ will be then matched filtered against all the templates of the bank, looking for a peak in SNR.

2.3 Detecting GW signals from CBCs

In this section we apply the matched filter technique to the detection of GW signals from compact binary inspirals in the detector data. During section 2.1, we have seen that waveform signals from CBCs can be difficult to model due to their complicated structure. Nevertheless, as discussed in 2.1.2, the inspiral can be modeled in a good approximation by the restricted waveform approximation. This waveform is a function of the intrinsic λ and extrinsic parameters Ξ of the binary, described in Sec. 1.3.1. As a first approach, we assume quasi-circular orbits and neglect NS matter effects, so the total number of parameters is 15.

2.3.1 Waveform in the detector

As we discussed in Sec. 1.2.2, a GW strain $h(t)$ projected into the detector is a linear combination of the amplitude polarizations weighted by the antenna factors (1.40). With the above considerations about the waveform, the strain into a particular detector can be expressed as [67]

$$h(t) = -\left(\frac{G\mathcal{M}}{c^2 D_{\text{eff}}}\right)\left(\frac{t_0 - t}{5\,G\mathcal{M}/c^3}\right)^{-1/4} \cos[2\Phi_0 + 2\Phi(t - t_0)]\,, \tag{2.46}$$

where t_0 is the *termination time*, the time at the detector when the arriving waveform reaches coalescence. It is related to the coalescence time parameter by $t_0 = t_c + \tau$, where τ is the propagation time from the source to the detector. Analogously, Φ_0 is the *termination phase*, related to the coalescence phase by

$$\Phi_0 = \Phi_c - \frac{1}{2}\arctan\left(\frac{F_\times}{F_+}\frac{2\cos\iota}{1+\cos^2\iota}\right)\,. \tag{2.47}$$

Lastly, D_{eff} is the *effective distance* to the source, given by

$$D_{\text{eff}} = D\left[F_+^2\left(\frac{1+\cos^2\iota}{2}\right)^2 + F_\times^2\cos^2\iota\right]^{-1/2}\,, \tag{2.48}$$

related to the actual distance D by the extrinsic parameters that describe the location and orientation of the source. Since these parameters are not known during the detection, it is convenient to combine them into a single observable. For an *optimally oriented* source, the effective distance is the true distance D, whereas for sub-optimally oriented systems, $D_{\text{eff}} > D$.

In the frequency domain, the strain $h(t)$ of eq. (2.46) can be obtained with the SPA approximation [50] as

$$\tilde{h}(f) = \frac{\mathcal{A}}{D_{\text{eff}}} f^{-7/6} e^{-i\Psi_{\text{PN}}(f)}\,, \tag{2.49}$$

where the amplitude $\mathcal{A}$ is proportional to $\mathcal{M}^{5/6}$, and the phase $\Psi_{\text{PN}}(f)$ is the TaylorF2 phase (2.11) expanded up to a certain order in the PN approximation. Templates for IMR waveforms do not follow exactly this form, but they can still be written in terms of a function of frequency for the amplitude and another function for the phase.

2.3.2 Matched filtering the data

In order to detect a signal, the data from the detector has to be filtered against the templates of the bank to find the one that maximizes the SNR [67].

For a template waveform as the one described in (2.49), all the dependence on the extrinsic parameters $\Xi = \{D, \alpha, \delta, \iota, \psi, t_c, \Phi_c\}$ is embedded in the $D_{\rm eff}$ factor, with the exception of the coalescence time t_c and the coalescence phase Φ_c. For a template waveform, $\mathcal{A}/D_{\rm eff}$ is just an amplitude factor, unimportant for the matched filter, and therefore can be normalized. The maximization over t_0 is typically performed by using the inverse Fourier transform. The SNR of a signal filtered by a normalized template with termination time t_0 is

$$\left\langle d\middle|h(f;t_0)\right\rangle = 4\,\mathrm{Re}\int_0^\infty \frac{\tilde{d}(f)^*\tilde{h}(f;t_0=0)}{S_n(f)}e^{2\pi i f t_0}df\,. \tag{2.50}$$

The use of a Fast Fourier Transform allows to search over all possible termination times.

For non-precessing binaries, with spins oriented along the direction of the orbital momentum, the dependence with the coalescence phase can be removed by maximizing the norm of the complex SNR z, which arises from removing the real projection of the inner product (2.29) [67]. Therefore, the inner product maximized over amplitude and time and phase shifts is

$$z(t_0) = 4\left|\int_0^\infty \frac{\tilde{d}(f)^*\hat{\tilde{h}}_0(f)}{S_n(f)}e^{2\pi i f t_0}df\right|\,, \tag{2.51}$$

where $\hat{\tilde{h}}_0(f)$ is a normalized template with $t_0 = 0$ and $\Phi_0 = 0$. Therefore, the matched-filter search maximizes over the parameters that affect the overall amplitude and phase of the observed signal. However, these parameters can be recovered through a subsequent analysis of parameter estimation.

With all these assumptions, the waveform templates are only constructed in the 4-dimensional space of the intrinsic parameters $\lambda = \{\, m_1, m_2, \chi_{1_z}, \chi_{2_z}\}$. The generated templates are collected in *template banks*, which are the topic of discussion of the next section. To sum up, the matched filtering technique follows the next steps: It begins by filtering the detector data against a bank of templates constructed in the space of intrinsic parameters of masses and aligned spins. The optimal filter is the inner product between the whitened data and a whitened template. Then, the output of the filter is maximized with respect to the time of arrival t_0 and the phase offset ϕ_0 to align the templates with the observed data. The output is a SNR time series that will peak in case

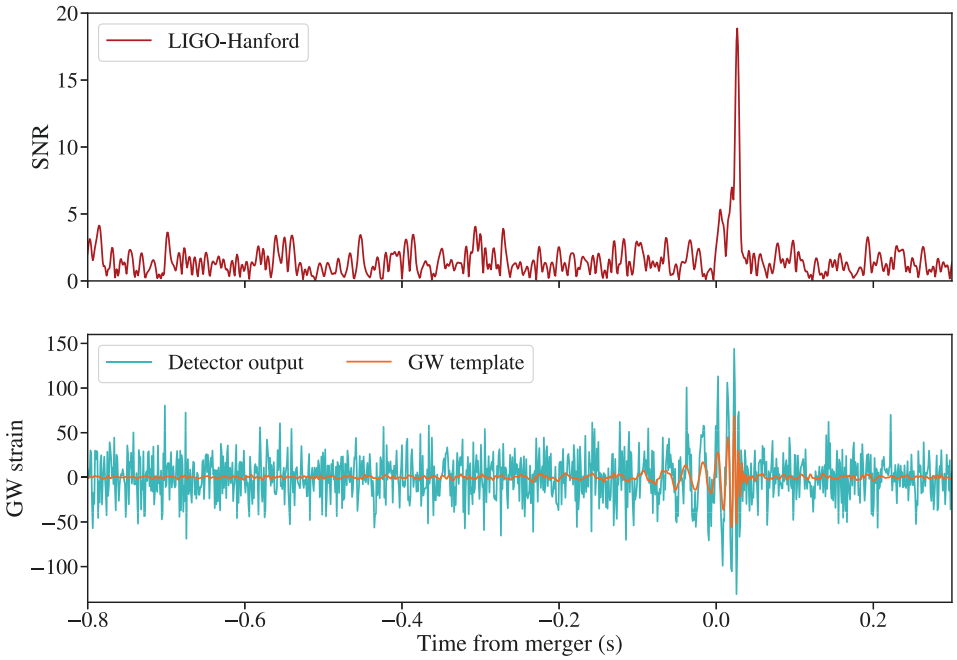

Figure 2.2: Matched filtering ilustration for BBH event GW150914. The data from the detector is whitened and correlated with a template of masses $m_1 = m_2 = 37\,\mathrm{M}_\odot$ generated with the approximant `IMRPhenomD` using `PyCBC` modules. A peak of SNR can be observed around the time of coalescence.

of a high match between a template and the data. A visual example of the matched filter applied to GW150914 is presented in Fig. 2.2.

2.4 Template banks

Template banks are collections of points in the parameter space used to construct waveform templates for performing matched filtering detection of GW signals. In this section we discuss the geometrical structure of the parameter space, as well as some basics on the construction of template banks.

2.4.1 Geometry of parameter space

In this subsection, we address the geometric structure of the parameter space [68]. As we have seen, a gravitational waveform from a CBC system can be com-

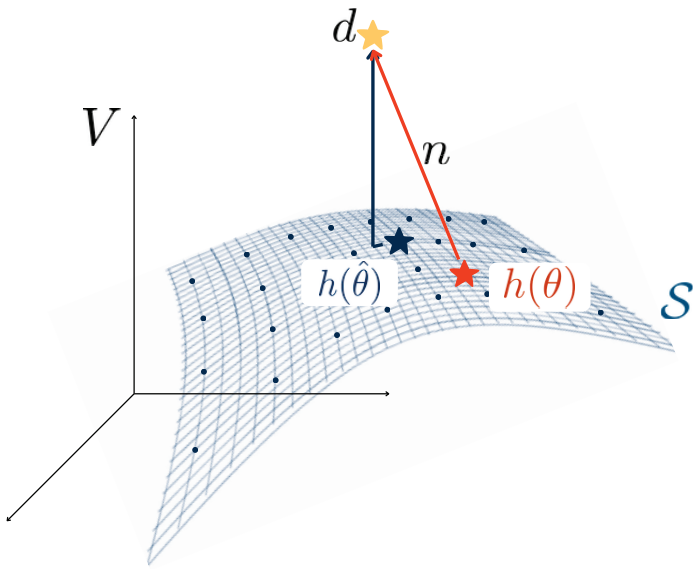

Figure 2.3: Geometrical description of the parameter space as a manifold, where the templates characterized by the parameters θ form a surface $\mathcal{S}$ in the space of all possible signals $\mathcal{V}$. The yellow star $d = n + h(\theta)$ represents a signal in the detector, displaced from its true waveform $h(\theta)$ (orange star) due the presence of noise. The template $h(\hat{\theta})$ (blue star) represents the *best fit* of the matched filter.

pletely characterized by a finite number of parameters $\theta = (\theta_1, ..., \theta_k)$. The set of waveforms $h(t;\theta)$ can be seen as a k-dimensional surface $\mathcal{S}$ embedded in the vector space $\mathcal{V}$ of all possible signals d. The parameters θ_i behave as the *coordinates* of the surface, each θ forming a vector in this space. A visual representation of this geometry can be seen in Fig. 2.3.

Typically, signals in the detector data $d = h(\theta) + n$ fall out of the surface $\mathcal{S}$ due to the presence of the noise n. The detection procedure, as we described in Sec. 1.2, filters this signal against all the templates in the surface, finding a best match with the template $h(\hat{\theta})$ that maximizes the SNR. However, the *best-fit* parameters $\hat{\theta}$ may not be the ones of the true waveform θ. Also, due to the discretization of the templates, the point of the surface that maximizes the SNR may lay between the templates.

These problems suggest the necessity of defining *distances* in the parameter space. To do so, we start defining the *match* between two templates h_1 and h_2

as their overlap (2.39) maximized over time and phase shifts

$$M(h_1, h_2) = \max_{\Delta t, \Delta\phi} \frac{\langle h_1 | h_2 \rangle}{||h_1|| ||h_2||} \,. \tag{2.52}$$

For two normalized templates $h(\theta)$ and $h(\theta + \Delta\theta)$, the match between them, notated $M(\theta, \theta + \Delta\theta)$, gives the fraction of the optimal SNR obtained by filtering a signal $h(\theta)$ with an identical template with intrinsic parameters $\theta + \Delta\theta$. Since the match have a peak at $\Delta\theta = 0$, it can be expanded around $\Delta\theta$ as a measure of the *closeness* of the templates.

$$M(\theta, \theta + \Delta\theta) \approx 1 + \frac{1}{2} \frac{\partial^2 M}{\partial \Delta\theta_i \Delta\theta_j} \Delta\theta_i \Delta\theta_j + \mathcal{O}(\Delta\theta_i^3) \,. \tag{2.53}$$

This leads to the definition of a *metric*

$$g_{ij}(\theta) = -\frac{1}{2} \frac{\partial^2 M}{\partial \Delta\theta_i \Delta\theta_j} \,, \tag{2.54}$$

so that the *mismatch* $\bar{M} = 1 - M$ between two templates *close* in the parameter space is equivalent to the distance between them dl squared

$$\bar{M} = dl^2 = g_{ij} \Delta\theta_i \Delta\theta_j \,. \tag{2.55}$$

This metric gives a geometrical structure to the parameter space of a Riemann manifold.

2.4.2 Template bank construction

The fundamental idea behind constructing a template bank of gravitational waveform templates is to be able to cover the entire parameter space so the matched filter finds at least one template with parameters sufficiently close to surpass a threshold in the loss of optimal SNR.

The *effectualness* of a template bank towards a signal s is measured as the maximum match of the signal over the entire family of templates h_k. This is quantified with the *fitting factor* (FF) [69] as

$$\mathrm{FF} = \max_k M(s, h_k) \,. \tag{2.56}$$

The fitting factor quantifies the fraction of optimal SNR that we get when the data is filtered with the approximate templates of the bank. The ideal case is a fitting factor of 1, meaning the signal s has been detected in the data without

loss in SNR. For values of the fitting factor below than 1, the signals need their optimal SNR to be greater than the threshold for detection by a factor of 1/FF to be detected. Therefore, the loss $1 - \mathrm{FF}$ is a measure of the amount of signals missed compared to the ideal perfectly matching template bank.

Missing signals is equivalent to a loss in the search sensitive volume. Due to the dependence of the amplitude of the signals with $1/D$, and assuming that GW sources are uniformly distributed, the ratio of detected signals against all that are ideally detectable scales approximately by FF^3. A frequently employed criterion involves accepting a maximum loss of approximately 10% of the signals, requiring the fitting factor to be no less than $\mathrm{FF} \sim 0.97$.

To achieve this level of efficiency, the templates in the bank are overlapped, giving the bank a characteristic *thickness* [70]. If the overlap is too low, more signals are missed due to their SNRloss, whereas a very high overlap makes detection too computationally expensive. Therefore, the goal is to design a method that maximizes the number of templates while keeping a minimum FF. There exist various methods to solve the problem of template placing, typically classified into three categories: geometrical [71, 72], stochastic [73, 74] and hybrid [75].

2.5 Overview of parameter estimation

Once a GW signal has been detected, we focus on how to extract the parameters of the source that match the observed signal most accurately [58]. The complete information about these parameters is encoded in the posterior PDF $p(\theta|d)$ of the set of unknown parameters θ given the detector data stream d. Therefore, the aim of parameter estimation (PE) is to construct the posterior distribution using Bayesian inference techniques, and use that information to compute *credible intervals* in the parameter space.

As explained in Sec. 2.2.1, the posterior is calculated with use of the Bayes theorem, proportional to the likelihood of the data given the parameters $\mathcal{L}(d|\theta)$, and to the prior of the parameters $\pi(\theta)$. Furthermore, the normalization factor $\mathcal{Z}$ provides the Bayesian evidence for the signal model employed.

Since the dimension of the posterior distribution equals the dimension of the parameter space, which for CBCs is at least 15, evaluating the complete posterior simultaneously becomes impractical. Instead, parameter estimation methods marginalize the posteriors over the parameters of interest θ_i, integrating over the nuisance parameters θ_k as in the equation (2.19). Calculating these marginalized probability densities involves the evaluation of multidimensional integrals, for which *sampling* PE algorithms are employed [76]. We give

an overview of them in the next subsection, and finish the section with a note about confidence intervals.

Stochastic samplers

The high dimensionality of compact binaries parameter space makes computationally impossible to construct posterior probabilities by direct evaluation of the likelihood. Stochastic samplers, instead, generate posterior samples from the posterior distribution itself, in a way that the density of the samples is proportional to the posterior. Using this sampling, the integrals proportional to the posterior PDF are immediately evaluated using Monte Carlo methods. The main sampling algorithms are MCMC [77, 78] and Nested Sampling [79–81].

Credible intervals

Credible intervals for source parameters θ are constructed from their (marginalized) posterior PDFs. Credible intervals are regions of the parameter space where some fraction of the posterior probability is accumulated [58]. They have to be constructed defining both the percentage of the posterior inside the interval and their relative position with respect to the limits of the posterior. A frequently used method is to construct *symmetric credible intervals*, that are built by means of the cumulative distribution function

$$P(x) = \int_{-\infty}^{x} p(x')dx' \,. \tag{2.57}$$

Then, a credible region of $X\%$ would just be $P(x)$ between the limits

$$\frac{1}{2}\left(1 - \frac{X}{100}\right) < P(x) < \frac{1}{2}\left[1 + \frac{X}{100}\right] \,. \tag{2.58}$$

Credible intervals and the cumulative distribution function are powerful tools for testing parameter inference methods. We will be back at them at Sec. 5.

3

THE PyCBC SEARCH FOR COMPACT BINARY COALESCENCES

In Chapter 2, we outlined the basic methods for detecting candidate gravitational-wave events in the data stream and assessing their significance against the background of detector noise. These complex processes are carried out by *search algorithms* in two timescales: near real-time (*online*) and after data calibration (*offline*).

In this chapter, we provide a general description of the GW search algorithms employed by the LVK collaboration in Section 3.1. Specifically, we outline the general characteristics of PyCBC, one of the modeled searches for GW signals from CBC sources. PyCBC is a python-based software, composed of a highly modular set of libraries that enable configurations for various types of analyses. We describe the methods employed by the PyCBC offline pipeline in Section 3.2, and by its online version, PyCBC Live, in Section 3.3. In Section 3.4, we describe our contribution to the development of a PyCBC focused search for intermediate-mass black hole (IMBH) binaries.

Publications derived from this chapter

[1] Optimized PyCBC search for gravitational waves from intermediate-mass black hole mergers (2021)

Koustav Chandra[1], **Verónica Villa-Ortega**[2], Thomas Dent[2], Connor McIsaac[3], Archana Pai[1], Ian W. Harry[3], Gareth S. Cabourn Davies[3] and Kanchan Soni[4]

[1] *Department of Physics, Indian Institute of Technology Bombay, Powai, Mumbai 400 076, India*

[2] *IGFAE, Campus Sur, Universidade de Santiago de Compostela, 15782 Santiago de Compostela, Spain*

[3] *University of Portsmouth, Portsmouth PO1 3FX, United Kingdom*
[4] *Inter-University Centre for Astronomy and Astrophysics, Pune 411007, India*

Published in: *Physical Review D* **104**, 042004 – August 2021. DOI: 10.1103/PhysRevD.104.042004
Published by: American Physical Society.

[2] Salient features of the optimised PyCBC IMBH search (2023)

Koustav Chandra[1], Archana Pai[1], **Verónica Villa-Ortega**[2], Thomas Dent[2], Connor McIsaac[3], Ian W. Harry[3], Gareth S. Cabourn Davies[3] and Kanchan Soni[4]

[1] *Department of Physics, Indian Institute of Technology Bombay, Powai, Mumbai 400 076, India*
[2] *IGFAE, Campus Sur, Universidade de Santiago de Compostela, 15782, Spain*
[3] *University of Portsmouth, Portsmouth PO1 3FX, United Kingdom*
[4] *Inter-University Centre for Astronomy and Astrophysics, Pune 411007, India*

Published in: *The Sixteenth Marcel Grossmann Meeting: On Recent Developments in Theoretical and Experimental General Relativity, Astrophysics, and Relativistic Field Theories.* eISBN: 978-981-12-6977-6, pp. 3277-3285 – March 2023. DOI: 10.1142/9789811269776_0269
Published by: World Scientific.

3.1 Searches

The process of detecting gravitational wave events within the LVK collaboration begins with the data output from the detectors and progresses through a series of data analysis procedures aimed at identifying candidate signals and inferring the properties of their sources. This process culminates in the publication of GW transient catalogs. A simplified diagram outlining the primary stages in LVK data processing is presented in Fig. 3.1.

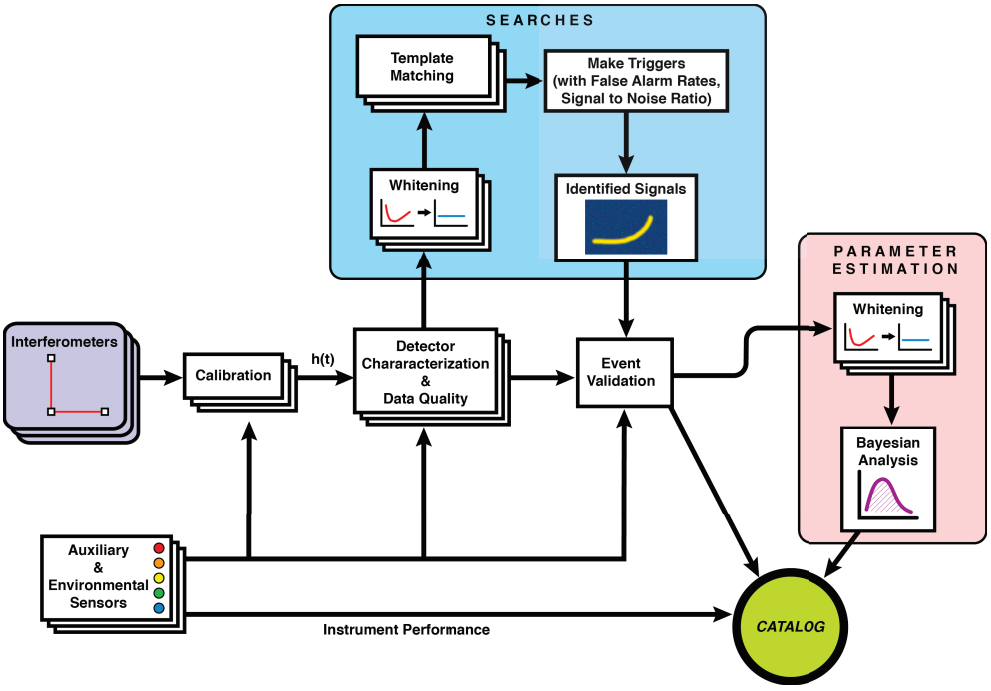

Figure 3.1: A simplified schematic illustrating the key stages in LVK data processing, from the initial data output to the findings presented in a catalog of transient events. Figure reproduced from [60].

In this process, the steps of identifying potential gravitational-wave events within the data stream and evaluating their significance against detector noise are carried out by search pipelines.

Candidate identification is performed at two different ranges of time, or *latencies*. Low-latency searches, also referred to as *online* searches, seek signals in near real-time as data is being read from the detector output, whereas *offline* searches are conducted once the data has been calibrated and cleaned. One ob-

jective of low-latency pipelines is to release alerts of potential candidate events as soon as possible to facilitate decisions regarding the search for multimessenger counterparts. Consequently, they operate under limited computational time constraints, and their results may exhibit significant uncertainties. In contrast, offline searches are performed with better statistics of background noise, utilize calibrated and conditioned data, and employ more computationally expensive calculations. With these considerations, offline searches are expected to be more sensitive than online analysis, being capable to identify GW signals in the data that were not initially detected in low-latency, and to reevaluate the significance of the ones already reported. The candidate events that are found offline with enough significance to claim a detection are then published by the LVK collaboration in GW transient *catalogs* such as GWTC-1 (O1, O2) [6], GWTC-2.1 (O3a) [7] and GWTC-3 (O3b) [8].

Current search analyses are classified in *modeled*, using templates of CBC waveforms to match-filter the data, and *weakly-modeled*, coherently analyzing the data in the network of detectors for any transient signal without expecting a known waveform template.

During O3, the LVK collaboration used four offline analysis: three modeled searches, PyCBC [82–85], GstLAL [86–88] and MBTA [89] and one weakly-modeled, cWB [90, 91]. These four pipelines are currently being used in O4 in their low-latency configurations [92–95], along with SPIIR [96, 97].

Current modeled searches limit their waveform templates with the assumptions explained in Sec. 2.3.2, i.e., the signal model is restricted to the dominant mode of emission of quasi-circular, non-precessing systems, and templates are marginalized over extrinsic parameters. Nevertheless, continuous efforts are being made to incorporate precession templates [98, 99] and higher modes [100] to enhance the sensitivity of the searches to these sources.

3.2 PyCBC offline search

In this section, we outline the various methods employed by the PyCBC pipeline to identify signals in detector data at higher latencies during O3. A flowchart illustrating the different steps of the search pipeline is provided in Fig. 3.2.

Previously to the start of the analysis of the detector data, a template bank is computed with CBC waveform models. The input data is calibrated and investigated for low-quality periods of time before entering the pipeline. A further gating veto is applied to mitigate the effect of remaining loud noise transients. Then, the pipeline computes the matched-filter SNR for each tem-

plate of the bank, identifying times of high SNR in the detector data, yielding a list of matches or *triggers* that are then clustered. Then, the SNR of the triggers is re-weighted using a χ^2 test to remove the large tails caused by non-Gaussian noise. A signal consistency check between different detectors is performed to identify candidate events. Finally, the significance of the signal is estimated against the background noise.

For the O3 catalog [8], two different analysis were conducted using the PyCBC algorithm. A general analysis, called `PyCBC-broad`, aims for the detection of all combinations of compact binaries across a wide parameter space. Additionally, an alternative pipeline configuration, `PyCBC-BBH`, is optimized to present a higher sensitivity to BBH signals within the range of total masses $10\,\mathrm{M}_\odot \leq M \leq 500\,\mathrm{M}_\odot$ and mass ratios $1/3 \leq q \leq 1$. Since the BBH-dedicated search is outside the scope of this thesis, the focus of this section is on the broad search. Furthermore, a dedicated PyCBC search specifically targeting signals from IMBH sources was carried out during O3, and will be discussed in Section 3.4.

In the following sections, we follow the data flow through the pipeline, discussing the different stages of the search.

3.2.1 Template bank

Since the signal parameters are not known *a priori*, the detector data is filtered against a template bank of pre-computed waveform signals (see Sec. 2.4 for a general description of template banks). As discussed previously, the space of parameters of the template bank is restricted to the four-dimensional space of component masses and component aligned spins. Before constructing the bank, a noise PSD is calculated as the harmonic mean of the distinct PSDs from all detectors of the network.

During O3, `PyCBC-broad` employed a bank [101] composed of 430,000 templates spanning over a range of redshifted total masses $2\,\mathrm{M}_\odot \leq M \leq 500\,\mathrm{M}_\odot$. The limit for minimum component masses was $1\,\mathrm{M}_\odot$, and the higher mass for a NS was placed at $2\,\mathrm{M}_\odot$. Aligned component spins were limited to 0.05 for NSs, and to 0.998 for BHs. A projection of this parameter space is depicted in Fig. 3.3.

The waveform approximants used for computing the template bank during O3 were `TaylorF2` [49] up to 3.5PN order for templates with total mass below $4\,\mathrm{M}_\odot$, and `SEOBNRv4_ROM` [102] for higher-mass systems.

The template placement technique employed to create this bank was a hybrid geometric-random method described in [75, 103] with some variations described in [101]. Due to the hybrid nature of the bank, with different regions

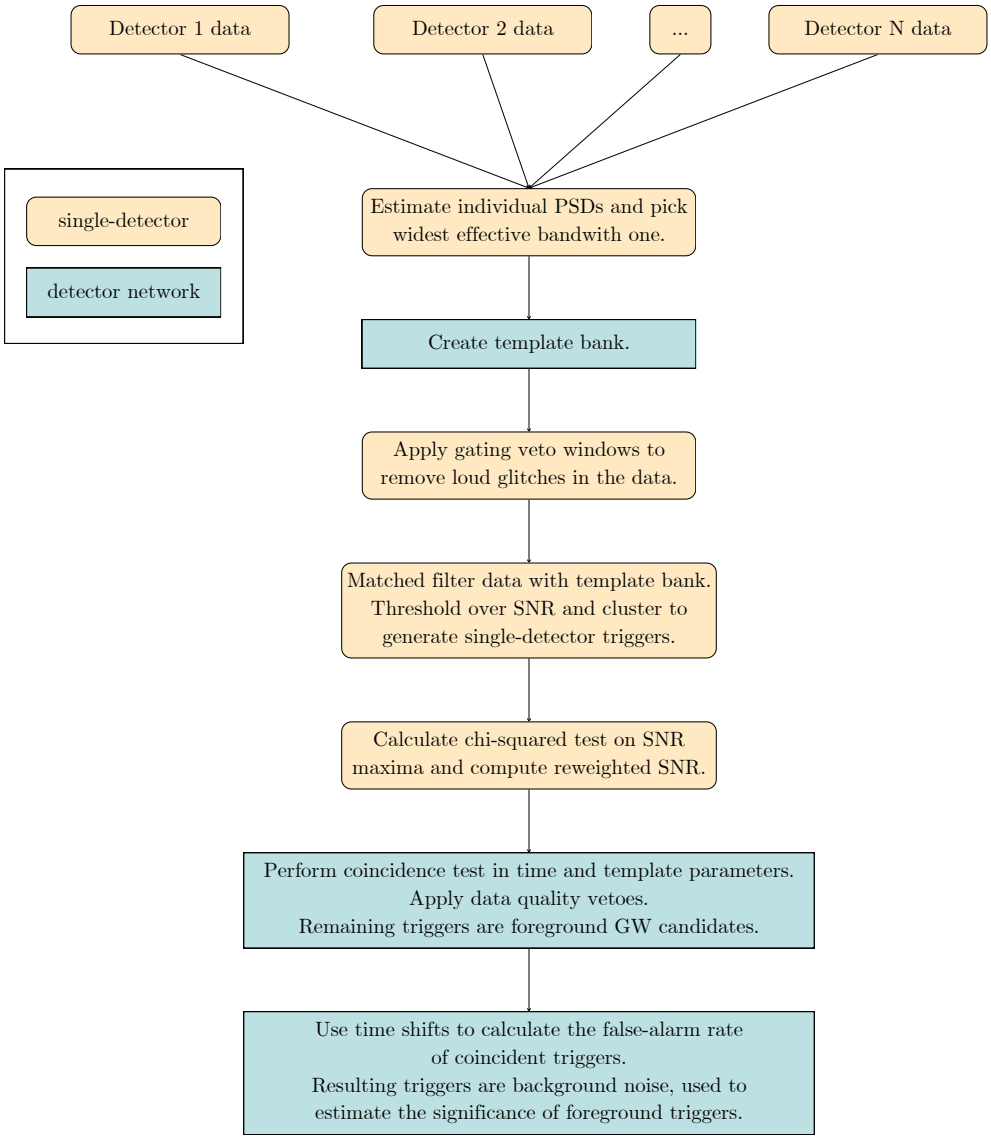

Figure 3.2: Flowchart of the different steps conducted by PyCBC to identify candidate events in the detector data. Steps performed individually in each detector's data are highlighted in yellow, while processes performed coherently across all detectors in the network are depicted in blue. Figure adapted from [82].

covered employing different template placement techniques, points in the bank show abrupt changes in density between regions.

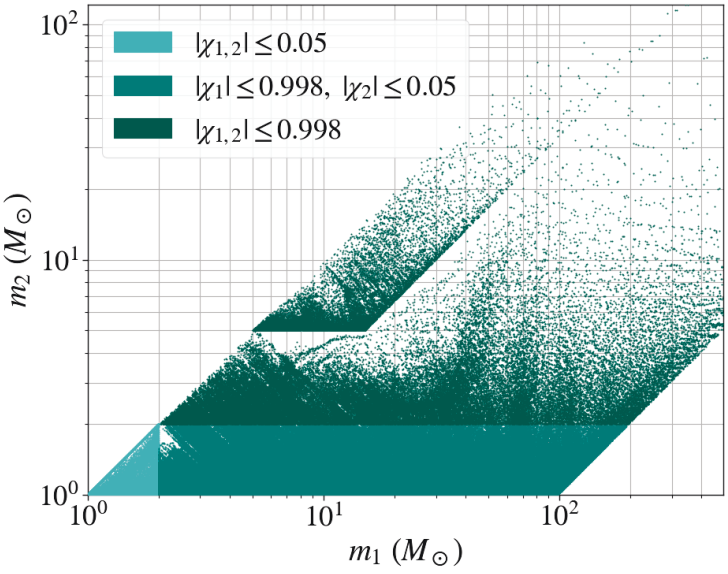

Figure 3.3: Distribution of templates in the mass plane, with the different aligned spin ranges, of the template bank employed during O3. Figure adapted from [101].

3.2.2 Data quality and gating

During the section 2.3, we described the matched filtering technique as the optimal to extract known waveform signals from Gaussian stationary noise. However, noise in GW detectors is not stationary, and can contain non-Gaussian transients, known as *glitches*, that can mimic GW signals in the matched-filtering process [104]. A number of techniques to deal with non-Gaussian noise are employed through the pipeline. In this section we discuss two noise-mitigating processes applied to the data before starting the matched filter.

Data quality vetoes

As discussed in Section. 1.2.3, a wide number of noise sources affecting the detector data are from known origin. These noise sources are controlled by

hundreds of thousands of sensors, that record continuously the internal state of the detectors and their environments. This monitored data allows to identify short lapses of time where excess power coming from technical and environmental noise sources is present in the detector data [60, 105]. These periods of poor data quality are flagged at various levels, called *category vetoes*, depending on the severity of the problem. The vetoes can either flag the data as unsuitable for analysis, removing it from the search, or indicate the possible presence of non-Gaussian artifacts, decreasing the significance of candidate events during the affected time. This technique has shown to improve the sensitivity of CBC searches [106].

Gating vetoes

Despite the efforts made to correlate artifact transients with monitored known noise sources, these are not optimized to find short-duration loud glitches of unknown origin, and are usually missed by data quality vetoes. These loud transients can produce high SNR matches with the templates, affecting negatively to the sensitivity of the search [107]. Moreover, in the presence of a loud glitch, the persistent impulse response of the filters used in the SNR computation from a specific template can lead to the generation of multiple high SNR triggers over a timescale significantly longer than the glitch itself. These erroneous high SNR matches can overshadow potential GW signals and add more noise background to the search.

A *gating* algorithm is implemented in PyCBC to deal with these short loud transients [82]. It identifies them and removes them from the data prior to matched-filtering. The identification is made through a search for loud excursions on the whitened strain data [108]. The removal is done by windowing the short affected period of data by an inverted Tukey window function centered at the time of the glitch [109]. This window smoothly zeroes the data, with a cosine tapered region at each end. The reason to use a tapered region before the zero window is to reduce the risk of introduce discontinuities in the data. An example of the effect of the gating technique on a loud transient can be seen in Fig. 3.4.

3.2.3 Matched filtering

As a modeled search, PyCBC look for signals in the data using the matched-filtering technique previously described in Sec. 2.3.2. However, even though the technique is typically described in terms of continuous quantities, the input strain data is discretely sampled, with a fixed sampling interval. The data and

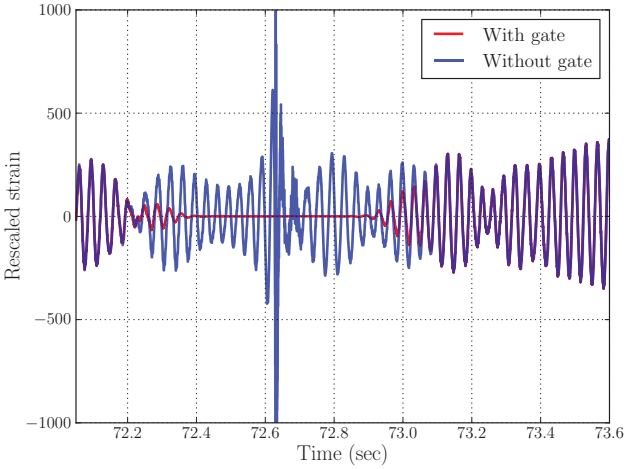

Figure 3.4: Example of a gate applied on a loud noise transient. The blue line represent the detector strain prior to gating, and the red line shows the data after. Figure reproduced from [82].

the templates are transformed to the frequency domain using a Fast Fourier Transform (FFT) algorithm in blocks of length $T_B = 512\,\mathrm{s}$. The PSD in the denominator of the matched filter is estimated by dividing each block of data in smaller blocks of 16 s and estimating the PSD for each block. These sub-blocks are then linearly interpolated to coincide with the frequency resolution of the data.

Then the input strain is filtered against the templates in the bank, generating a a matched-filter SNR time series. The times on which the SNR exceeds a fixed threshold ($\rho > 4$ for PyCBC), are called *triggers*. The pipeline applies then a *clustering* algorithm, dividing the SNR time series in windows of 1 s and identifying the loudest trigger in each window for further analysis.

3.2.4 Signal consistency tests

Since the data in the detector is deeply affected by the presence of non-stationary and non-Gaussian noise, the PyCBC search implemented two different chi-squared (χ^2) consistency tests to discriminate between triggers caused by loud noise artifacts and GW signals.

Time-frequency χ^2 test

For the time-frequency χ^2 test [110], the found template is divided into p separate frequency bins, where each bin contributes equally to the expected SNR of the template. The distribution of SNR over different bins is employed to fit how the signal should behave over the different frequencies. This allows to distinguish glitches, since their SNRs are typically concentrated in narrow frequency bands or time periods instead of the expected template bandwidth or duration. For each bin, we calculate the fraction of the matched-filter SNR ρ_i in the data. If the data contains an astrophysical signal, we expect ρ_i to be around $1/p$ of the total SNR of the template. A χ^2 statistic is then computed to estimate the residual power in each frequency bin. In Gaussian noise, χ^2 has an expected value that depends on the number of bins p as $\langle\chi^2\rangle = (2p-2)$ [110]. In order to be able to compare the results for different number of bins, we compute a reduced chi-squared statistic as

$$\chi^2_r = \frac{\chi^2}{(2p-2)}\,. \tag{3.1}$$

In this statistic, a value of χ^2_r close to unity means that the trigger is more likely to be a real signal. In PyCBC, this quantity is combined with the SNR of the trigger to produce a *ranking statistic* as a re-weighting of the SNR, given by

$$\hat{\rho} = \begin{cases} \rho & \text{if} \quad \chi^2_r <= 1 \\ \rho \left[\frac{1}{2}\left(1 + (\chi^2_r)^3\right)\right]^{-1/6} & \text{if} \quad \chi^2_r > 1 \end{cases}\,. \tag{3.2}$$

This re-weighted SNR is specially effective for suppressing noise triggers for low-mass binaries ($M < 25\,\mathrm{M}_\odot$), since they spend more cycles in the sensitive frequency band of the detector. Conversely, signals of higher mass systems are only observable for fractions of seconds, causing their morphologies to be more difficult to distinguish from glitches.

High-frequency sine-Gaussian χ^2 veto

Short-duration glitches can mimic the time-frequency behaviour of a short waveform template in the low-frequency range, causing them to pass the time-frequency χ^2 test. However, some short glitches present excess signal power at higher frequencies than any template they matched with would have. With the frequency of the ringdown of the dominant harmonic as a maximum frequency limit for CBC signals, a number of sine-Gaussian tiles are placed at frequencies over this limit at the time of the trigger [83]. We generate the reduced sine-

Gaussian veto $\chi^2_{r,sg}$ by summing the ρ_i^2 of each sine-Gausian tile i as

$$\chi^2_{r,sg} = \frac{1}{2N} \sum_{i}^{N} \rho_i^2 \,. \tag{3.3}$$

This discriminator is most effective at rejecting glitches matched with high-mass templates, which have ringdown frequencies $\gtrsim 100\,\mathrm{Hz}$, thus increasing the sensitivity of the search to high-mass BBHs. It can be combined with the re-weighted SNR to generate the detector statistic $\chi^2_{r,sg}$.

3.2.5 Multi-detector coincidence test

Up to this point, we only have addressed the problem of a signal being detected in a single detector. However, the detection pipeline requires that a trigger is detected with consistent parameters in at least two detectors in the network [111]. This *coincidence test* is performed on the search triggers after the mitigation of glitches, requiring that the triggers are consistent in arrival time and template parameters between detectors. Recent studies have enabled single-detector candidate identification [85], but we do not describe these methods here.

Arrival time consistency

For a two-detector network, the triggers are required to be observed in both detectors within a time difference close to the light-travel time between them. The search records the shifts in arrival times and phase of the signal for different pairs of detectors in the network. Since we expect the noise to be uncorrelated among detectors, the distribution of noise triggers over these time and phase shifts is expected to be stochastic and uniform.

Template parameters consistency

Since the same waveform signal is expected to be observed in all detectors, the search requires an *exact-match* coincidence, and the signal has to match the same template in each detector. This requirement has shown to be particularly useful for complicated gravitational waveforms, such as those from high-mass BBHs or spinning compact objects, leading to an improvement in search sensitivity.

3.2.6 Ranking statistic

Coincident triggers that pass the time and parameter coincident test are now *candidate events*. Since the search will produce various candidate events close to the time of merger, each of them has to be assigned a *ranking statistic*, where a higher ranking statistic corresponds to a higher probability for the candidate event to be of astrophysical origin, and lower statistic values correspond to a higher probability of being noise. The search employs a ranking statistic that estimates the degree of belief for a candidate to be of astrophysical origin [111]. The final ranking statistic is a complicated recipe given by

$$\mathcal{R} = -\log A_{N\{d\}} - \sum_{d} \log r_{d,i}(\hat{\rho}_d) + \log p(\vec{\Omega}|S) - \log p(\vec{\Omega}|N) + R_{\sigma,i}\,, \quad (3.4)$$

where $\{d\}$ is the set of detectors in the coincidence, $A_{N\{d\}}$ is the size of the window of allowed coincidences, $r_{d,i}(\hat{\rho}_d)$ is the expected rate of triggers in a template i at a re-weighted SNR $\hat{\rho}_d$, $p(\vec{\Omega}|S)$ is the probability of a signal to have the extrinsic parameters $\vec{\Omega}$, and $R_{\sigma,i}$ represents the network sensitive volume for a given coincidence of detectors and a given template. A thorough description of these parameters can be found in [111].

3.2.7 Significance of candidate events

The statistical significance of a candidate event is quantified by the False Alarm Rate (FAR) of the search. This is the expected number of candidate events of noise origin (or false alarms) that would be detected by the search with a ranking statistic as high as the actual candidate in a certain amount of time. The lower the FAR value is, the higher is the probability of the candidate event to be astrophysical.

Because the noise distribution is not ideal, it cannot be predicted directly from theory, and it has to be estimated empirically [112]. The PyCBC pipeline fabricates a collection of background noise coincidences by *time-shifting* triggers from the different detectors. The data from one of the detectors is shifted in time with respect to the others by an interval larger than the light-travel time between the farthest sites. The detected noise coincidences ranked higher than the candidate event generate the background distribution [111]. With this technique, time-shifting only a few days of data allows for generating over ten thousand years of noise backgrounds. The FAR of a candidate event is then estimated by comparing its ranking statistic against the one of the artificial background coincidences. A visual representation of the time-shift technique is presented in Fig. 3.5.

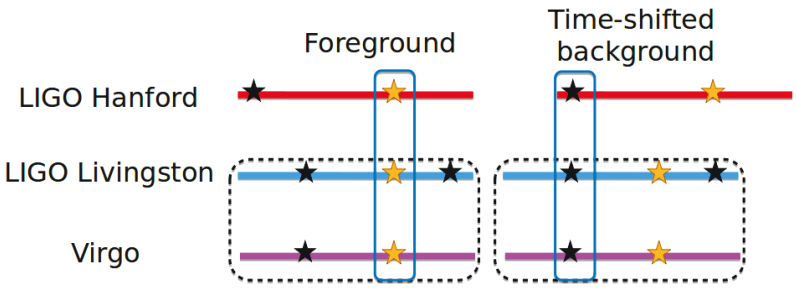

Figure 3.5: Visual representation of the time-shifting method. Here, the shifted detector is Hanford, while the others remain fixed to one another. The gold star triggers correspond to candidate coincidences, while blue stars show non- coincident triggers. The original candidate coincidence (left) belongs to the signal foreground, while the artificial candidate coincidence (right) formed by time-shifting the data, is part of the noise background. Figure reproduced from [111].

To mitigate the accidental overlaps between the noise and signal triggers, PyCBC strategically removes loud triggers to reduce the impact of the overlap. Then, in periods when more than one detector is active, coincident triggers are clustered in 10 s windows, and the candidate with highest ranking statistic is kept, regardless of the combination of detectors that produced it. When more than one detector combination is active, the total FAR is calculated by adding the estimated FARs from all different combinations to the ranking statistic threshold of the candidate event. This technique down-ranks candidate events that are not detected by the highest sensitive combination if active. The minimum FAR of a multiple detector search is given by the minimum measurable FAR of each combination of detectors. For a three-detector search (HLV), the minimum FAR is given by

$$\mathrm{FAR}_{\mathrm{min}} = \frac{1}{t_{\mathrm{bg,HLV}}} + \frac{1}{t_{\mathrm{bg,HL}}} + \frac{1}{t_{\mathrm{bg,HV}}} + \frac{1}{t_{\mathrm{bg,LV}}}\,, \tag{3.5}$$

with $t_{\mathrm{bg,X}}$ the total background time analyzed for a given combination X.

3.2.8 Sensitivity of the search

A measure of the search sensitivity is given by the *sensitive time-volume* averaged over a population of astrophysical signals as

$$\langle \mathrm{VT} \rangle = \int \frac{dV_c}{dz} \frac{1}{1+z} p_{\mathrm{pop}}(\theta) f(z,\theta) T_{\mathrm{obs}}\, dz\, d\theta\,. \tag{3.6}$$

Here, dV_c/dz is the co-moving volume, $p_{\rm pop}(\theta)$ is the distribution of the parameters of the binary θ estimated by the astrophysical population, $f(z,\theta)$ is the probability to detect a signal with θ parameters at a redshift z, and $T_{\rm obs}$ is the observation time of the search. The sensitivity is evaluated using a set of simulated signals with randomized parameters to validate the performance of the search. These simulations can be introduced into the pipeline by adding waveform signals to the input strain data.

The sensitivity can be improved by either increasing the measured SNR of a signal, or reducing the FAR of the search at a given SNR. The SNR value can be increased by reducing the instrumental noise in the detectors [113] or enhancing the fit between the template waveforms and the GW signals.

3.3 PyCBC Live

PyCBC Live is the low-latency version of the PyCBC pipeline that searches for CBC signatures in the detectors network strain data in near-real time. One of its main goals is to generate rapid alerts of candidate events in order to enable follow-up observation campaigns in collaboration with electromagnetic (EM) and neutrino observatories [114–116]. The identified candidate events are uploaded to the Gravitational-Wave Candidate Event Database (GraceDB)[1] and the corresponding alerts are then distributed by the Gamma-ray Coordinates Network (GCN)[2]. The specific content of these alerts will be discussed in Sec. 4.1.1.

PyCBC Live was developed for LIGO detectors in the second observing run (O2) [92]. During the course of the third observing run (O3), with the addition of Virgo to the network, a number of new methods were added to the search [93]. We summarize these methods below.

3.3.1 Methods from PyCBC offline

A number of methods to identify and rank potential candidate events already discussed for the offline search were implemented in PyCBC Live for O3. The template bank covers the same parameter space and template duration than the offline bank described in Sec. 3.2.1. The mentioned template placement method based on an optimized hybrid geometric-random approach was introduced to PyCBC Live for O3. Another recent implementation was the gating procedure discussed in Sec. 3.2.2, given the high amount of loud transients present during

[1] https://gracedb.ligo.org
[2] https://gcn.nasa.gov

the first weeks of O3. Each Tukey gating window is configured as 0.5 s of zeros around the central time of the glitch, and 0.25 s of smooth rolling taper in each side. This gating duration is justified by the short duration of high-SNR transients, typically less than 1 s [105]. Another improvement from the offline search was the inclusion of the sine-Gaussian χ^2 veto of Sec. 3.2.4.

3.3.2 Multiple- and single- detector search

Since Advanced Virgo joined the detectors network for O3, the PyCBC Live pipeline was upgraded to include additional detectors for coincident searches. A double-coincidence analysis is performed independently for each detector pair combination, and a FAR statistic is computed with the last 5 hours of data to check for possible changes in the performance of the detectors. If multiple coincidences occur, the pipeline selects the one with the lowest FAR, or the highest ranking statistic in case of a tie. The detectors excluded from the selected coincidence remain as follow-up detectors. For single-detector candidates, the FAR is extrapolated beyond one per live time to generate low-latency rapid alerts [85].

3.3.3 Source classification

In the later period of O3, the source classification method to estimate the probability of the candidate event to belong to the different astrophysical categories was updated from a "hard-cuts" decision given the template component masses to an estimation using the well-measured chirp mass of the template. The development of this method is one of the main topics of this thesis, and it is exhaustively discussed in Chapter 4.

3.3.4 SNR optimization

The *SNR-optimization* method starts once a candidate event is uploaded to GraceDB by the search. Through a differential evolution process [117], a short block of the time strain around the candidate is analyzed to find the template parameters that maximizes the network SNR, given by

$$\rho^2_{\text{net}} = \sum_i^N \rho_i^2 \,, \tag{3.7}$$

where N is the number of detectors in the network. This maximization is performed over the continuous masses and spins parameter space, without

the restriction of template placement. Then, the new SNR-optimized candidate is uploaded to GraceDB, allowing for generating new sky-localization and source classification estimates. The candidate event resulting of this SNR maximization will be the starting point of the fast parameter estimation method discussed in Chapter 5.

3.4 Enhancing the sensitivity of a PyCBC search for IMBH mergers

In this final section, we outline the work conducted during this thesis to contribute to the development of a new PyCBC-based search optimized for detecting GW signals from intermediate-mass black hole (IMBH) binaries [118]. Specifically, we developed a new veto that enhances the sensitivity of the search by removing loud triggers around times in the data where a loud non-Gaussian transient was auto-gated. The autogating procedure of PyCBC was described previously in Sec. 3.2.2.

3.4.1 Optimized PyCBC search for GWs from IMBHs

Typically, black holes (BHs) can be classified into three categories according to their masses. The lightest category, with masses up to $\sim 100\,\mathrm{M}_\odot$, are stellar-mass BHs. The heaviest, with masses above $\sim 10^5\,\mathrm{M}_\odot$, are the supermassive black holes (SMBHs) located at the centers of galaxies [119]. Lying between them, with masses in the approximate range $100 - 10^5\,\mathrm{M}_\odot$, are the *intermediate-mass black holes* (IMBHs) [120]. Observations of IMBH binaries would not only provide a deeper understanding on the formation and evolution of massive BHs, but they will also enable us to perform more detailed tests of general relativity in the strong-field regime [121]. Signals from binary systems that include IMBHs are extremely short-lived, spending $\lesssim 1\,\mathrm{s}$ within the detector bandwidth. This, among other factors, makes them difficult to detect, especially for searches based on matched-filtering.

Motivation for a PyCBC-IMBH focused search

The analysis of the data published in the first transient catalog GWTC-1 [6], corresponding to O1 and O2, was performed by a `PyCBC-broad` search covering a total mass range of $\mathrm{M_T}(1+z) \in [2, 500]\,\mathrm{M}_\odot$ with mass ratios $q \in [1/98, 1]$. For the second catalog, GWTC-2 [122], corresponding to the data of the first half of O3, the `PyCBC-broad` search template bank covered the same parameter space as in GWTC-1. As can be seen in Fig. 3.3, templates in this bank are

much more scarce for components in the IMBH range of masses, limiting the sensitivity of the search to these systems. Besides, due to the effect of redshift, the template masses required to detect high-mass BBHs are even larger.

The GWTC-2 data was also analyzed with the already mentioned `PyCBC-BBH` focused search, with $M_T(1+z) \in [10, 500]\,M_\odot$ and $q \in [1/3, 1]$. However, this search is too tight-tuned to signals closely matching stellar-mass BBH templates. Furthermore, the template banks of both searches are designed to include waveforms with durations greater than 0.15 s, further limiting their sensitivity to shorter-duration signals. Therefore, neither analysis is specifically designed to identify IMBH binary mergers, resulting in significantly reduced sensitivity to such signals.

Up to the third period of observation, there is a lack of observed systems with $m_1 \gtrsim 45\,M_\odot$. However, GWTC-2 lists several events with systems in this range, indicating additional structure in the BBH population distribution [123]. One of these events is GW190521, whose remnant, with mass $\sim 142\,M_\odot$, is the first conclusively observed IMBH [124, 125]. We expect the number of massive BBH events to increase with the sensitivity of the current detectors and with the deployment of the future detectors described in Sec. 1.2.5. Future ground detectors such as Cosmic Explorer and Einstein Telescope are expected to detect more BBH mergers at larger redshifts, possibly up to $z \sim 20$ and higher. The space detector LISA will potentially allow us to observe even further and for more massive BBHs. As mentioned above, GW signals from high redshift binaries will have higher detector frame masses, up to an order of magnitude or larger than the source masses. For these reasons, it is necessary to extend the target space of current PyCBC searches and tune them to prevent missing these potential signals.

With this objective, we developed and ran a new PyCBC-based search specifically designed to detect short-duration signals from potential IMBH binaries. Due to its design, the search is also sensitive to highly redshifted stellar-mass BBH mergers.

Outline of the search

We constructed a template bank of quasi-circular, non-precessing (aligned spins) binaries in the restricted approximation (dominant mode). The waveforms of the bank have detector frame total masses $M_T(1+z) \in [100, 600]\,M_\odot$ and mass ratios $q \in [0.1, 1]$, while requiring the mass of the secondary component to be $m_2 > 40\,M_\odot$. The components have aligned dimensionless spins χ_1 and χ_2 with values ranging $\chi_i \in [-0.998, 0.998]$. A justification of these choices is given in the search publication [118]. Because signals from high-mass sys-

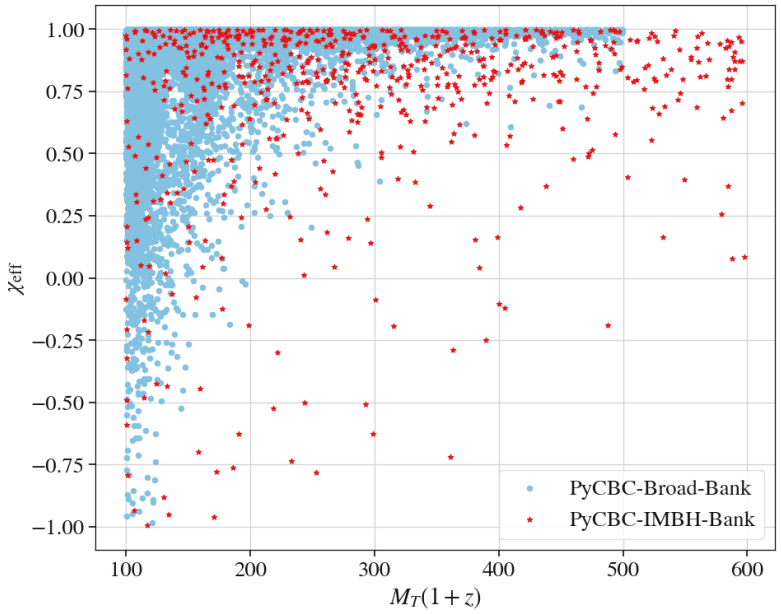

Figure 3.6: Template bank comparison between `PyCBC-broad` (light blue dots) and `PyCBC-IMBH` (red dots) in terms of the templates redshifted total masses $\mathrm{M_T}(1+z)$ and their effective spins $\chi_{\rm eff}$. For `PyCBC-broad`, only templates with redshifted total mass greater than $100\,\mathrm{M}_\odot$ are included. Figure reproduced from [118].

tems are more prone to be affected by false alarms from short-duration noise transients [126], waveform templates are required to have durations greater than 0.07 s measured from a starting frequency of 15 Hz. A comparison of the designed `PyCBC-IMBH` template bank with respect to the one employed by the `PyCBC-broad` search (see Sec. 2.4) is presented in Fig. 3.6. In this figure, it can be seen that the `PyCBC-broad` template bank is denser in the comparatively lower total mass region. This is due to a lower mass ratio limit and lower minimum component mass requirements. Despite that, the `PyCBC-broad` bank has a coarser coverage over shorter-duration templates because of the template duration-cut of 0.15 ms (measured from a starting frequency of 20 Hz). Additionally, the `PyCBC-broad` bank has no templates beyond $\mathrm{M_T}(1+z) = 500\,\mathrm{M}_\odot$, as opposed to the `PyCBC-IMBH` template bank.

Because of the target space chosen of high-mass systems, the search is susceptible to a larger number of noise triggers, requiring the implementation of stricter noise vetoes and discriminators. Among these, described in [118], we developed a new "gating veto" to remove loud triggers present around the

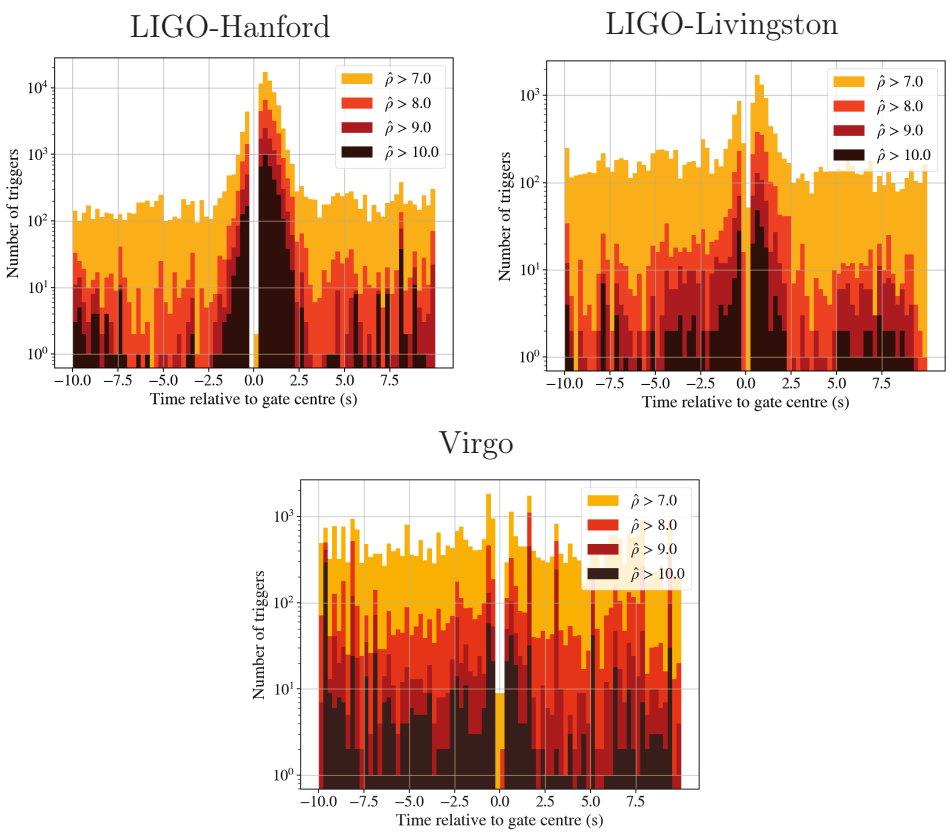

Figure 3.7: Histograms of triggers close to auto-gated times in O3a data within the `PyCBC-broad` pipeline.

auto-gated times of the data. This new veto and its effects on the sensitivity of the search are presented in the following subsections.

3.4.2 Motivation of gating veto

The motivation for the development of the *gating veto* arose during the offline analysis of some blocks of data corresponding to the first half of the third observing run (O3a) within the `PyCBC-broad` pipeline. In this analysis, we noticed several instances where the loud glitch prompting an auto-gate was correlated with nearby, lower frequency glitches. Although these nearby glitches had relatively high SNRs, they were not loud enough to be auto-gated by the search, and were outside the autogating time window. The effect of this correlation can be seen in the histograms of Fig. 3.7, which show an elevated relative rate

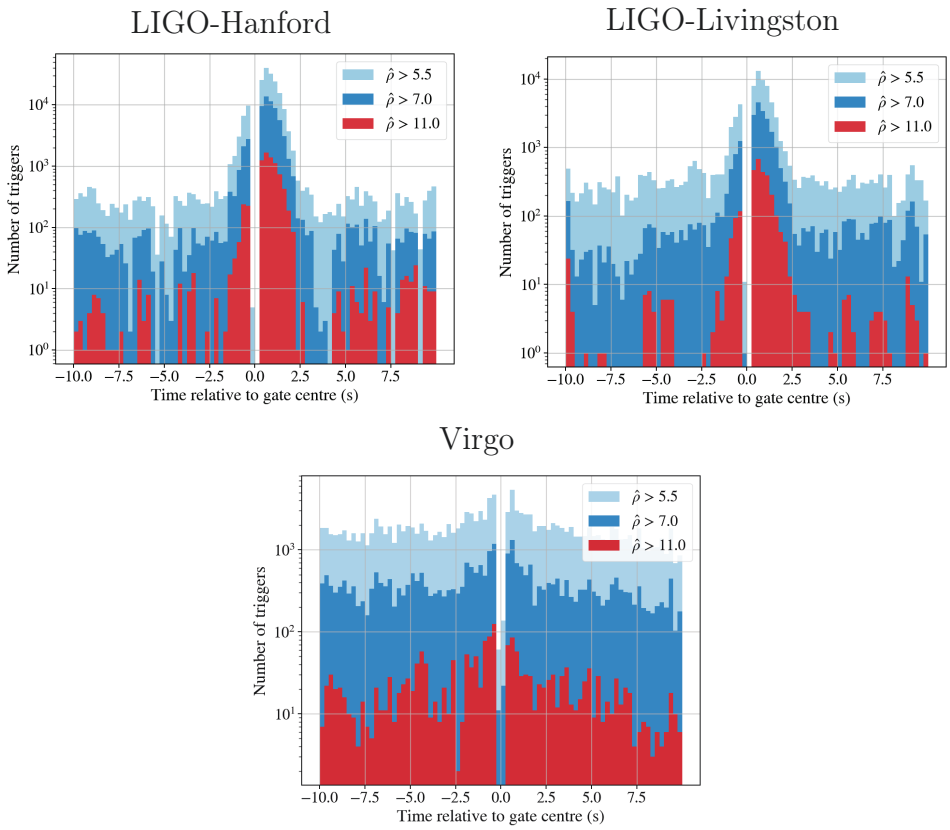

Figure 3.8: Histograms of triggers close to auto-gated times in O3a data within the `PyCBC-IMBH` pipeline.

of triggers with high re-weighted SNR $\hat{\rho}$ (see Eq. 3.2) within a few seconds of auto-gated glitches.

This effect is mainly visible in both LIGO detectors' data, increasing up to two orders of magnitude, being much subtler or absent for Virgo data. We repeated the same study during a preliminary analysis of O3a data with the new `PyCBC-IMBH` search, finding a similar behaviour of triggers close to auto-gated times. The histograms corresponding to this study can be seen in Fig. 3.8. As a first approach to this issue, we veto all triggers between 1 second before and 2.5 seconds after the central auto-gating times of Advanced LIGO data. The tuning limits were chosen empirically and are subject to future improvements. The inclusion of this veto yields additional suppression of high-statistic background events, leading to an increase in sensitive volume-time,

which implies that a GW signal belonging to the target space will be detected with an improved significance. We will see the effect of this improvement in the next section.

3.4.3 Improvement in the sensitivity of the search

To quantify the improvement in the search due to the addition of the gating veto, we compare the sensitivity of `PyCBC-IMBH` with and without it. We estimate the sensitivity using a set of simulated signals injected in the data as described in Sec. 3.2.8. For this study, we injected the simulated signals in ~ 30 days of O3a data. The metric we use to compare the search sensitivities is the sensitive volume-time (VT) that the search can survey [82]. With this metric, we can compute VT ratios between the sensitivity of the search before the gating veto and after. Boxplots showing these ratios for different values of redshifted total masses and inverse mass ratios can be seen in Figures 3.9 and 3.10 respectively. These plots show an overall improvement in the sensitivity of the `PyCBC-IMBH` search due to the implementation of the gating veto. This enhancement is specially significant at an IFAR of 100 years, with an improvement in sensitivity VT that ranges between a factor of 1.2 to 1.5 for the different total masses, and between 1.2 and 1.3 for the inverse mass ratios.

To sum up, we have developed an additional veto to remove the excess of loud triggers that tend to be close in time to very loud non-Gaussian transients but are not loud enough to be auto-gated by the search. This veto was applied to the new focused `PyCBC-IMBH` search, resulting in a contribution to the enhancement of the sensitivity of the search. However, the applied method of trigger removal can be significantly improved. A suggestion for future work is to replace it with a more detailed reduction of the SNR of the triggers close to gate times.

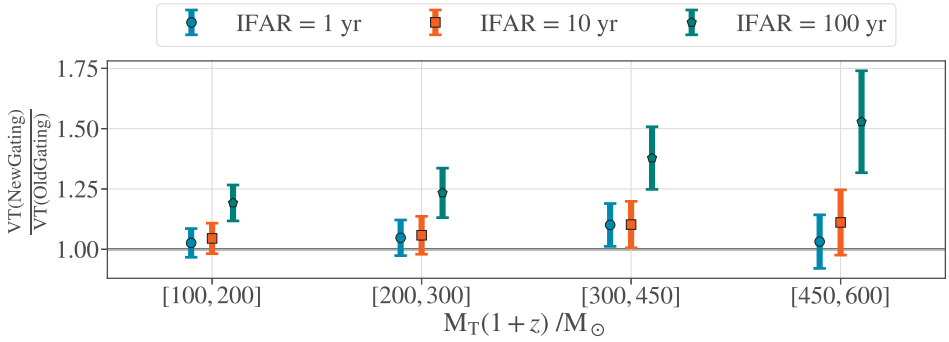

Figure 3.9: Boxplot showing the ratio of the sensitive volume-time (VT) of the search with the gating veto (New Gating) and without it (Old Gating) for different redshifted total mass intervals and three distinct IFAR values.

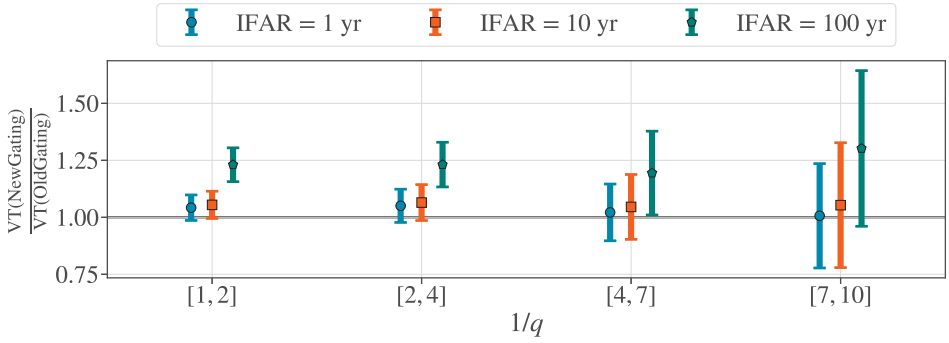

Figure 3.10: Boxplot showing the ratio of the sensitive volume-time (VT) of the search with the gating veto (New Gating) and without it (Old Gating) for different intervals of inverse mass ratio and three distinct IFAR values.

4

FOLLOW-UP OF GW CBCs I: RAPID SOURCE CLASSIFICATION AND DISTANCE ESTIMATION WITH PyCBC LIVE

Publications derived from this chapter

[1] Rapid source classification and distance estimation for compact binary mergers with PyCBC live (2022)

Verónica Villa-Ortega[1], Thomas Dent[1] and Andrés Curiel Barroso[1]

[1] *Instituto Galego de Física de Altas Enerxías, Universidade de Santiago de Compostela, Rúa de Xoaquín Díaz de Rábago s/n, E-15782, Spain*

Published in: *Monthly Notices of the Royal Astronomical Society*, Vol. 515, Iss 4, pp. 5718–5729 – October 2022. DOI: 10.1093/mnras/stac2120
Published by: Oxford University Press on behalf of Royal Astronomical Society.

[2] Real-time Search for Compact Binary Mergers in Advanced LIGO and Virgo's Third Observing Run Using PyCBC Live (2021)

Tito Dal Canton[1,2,3], Alexander H. Nitz[4,5], Bhooshan Gadre[2], Gareth S. Cabourn Davies[6,7], **Verónica Villa-Ortega**[6], Thomas Dent[6], Ian Harry[2,7] and Liting Xiao[8]

[1] *NASA Goddard Space Flight Center, 8800 Greenbelt Road, Greenbelt, MD 20771, USA*
[2] *Max Planck Institute for Gravitational Physics (Albert Einstein Institute), Am Mühlenberg 1, D-14476 Potsdam-Golm, Germany*
[3] *Université Paris-Saclay, CNRS/IN2P3, IJCLab, F-91405 Orsay, France*
[4] *Max Planck Institute for Gravitational Physics (Albert Einstein Institute), D-30167 Hannover, Germany*
[5] *Leibniz Universität Hannover, D-30167 Hannover, Germany*

[6] *Instituto Galego de Física de Altas Enerxías, Universidade de Santiago de Compostela, E-15782 Santiago de Compostela, Galicia, Spain*
[7] *Institute for Cosmology and Gravitation, University of Portsmouth, 1-8 Burnaby Road, Portsmouth, P01 3FZ, UK*
[8] *LIGO Laboratory, California Institute of Technology, MS 100-36, Pasadena, CA 91125, USA*

Published in: *The Astrophysical Journal* **923**, 254 – December 2021.
DOI: 10.3847/1538-4357/ac2f9a
Published by: American Astronomical Society.

[3] GWTC-3: Compact Binary Coalescences Observed by LIGO and Virgo during the Second Part of the Third Observing Run (2023)

LIGO Scientific Collaboration, Virgo Collaboration, and KAGRA Collaboration (incl. **Verónica Villa-Ortega**)
Published in: *Physical Review X* **13**, 041039 – December 2023.
DOI: 10.1103/PhysRevX.13.041039
Published by: American Physical Society.

[4] GWTC-2.1: Deep extended catalog of compact binary coalescences observed by LIGO and Virgo during the first half of the third observing run (2024)
The LIGO Scientific Collaboration and the Virgo Collaboration (incl. **Verónica Villa-Ortega**
Published in: *Physical Review D* **109**, 022001 – January 2024.
DOI: 10.1103/PhysRevD.109.022001
Published by: American Physical Society.

4.1 Introduction to follow-up of CBC signals

On August 17 2017, the Advanced LIGO and Advanced Virgo detectors made the first detection of a gravitational wave (GW) signal from a binary neutron star (BNS) coalescence, the event GW170817 [127]. Independently, a gamma-ray burst (GRB) was detected by the gamma-ray space telescope Fermi, barely 1.7 seconds after the time of the merger [128]. Given the coincidence in time, multiple electromagnetic (EM) observatories started to scan the sky, especially in the precise region that LIGO and Virgo reported with a well-constrained sky localization. Less than 11 hours later, the kilonova AT2017gfo was observed in the optical spectrum band [129, 130]. A timeline of the subsequent observations across the EM spectrum is shown in Fig. 4.1. The *multi-messenger* observation of the BNS merger in both GW and EM bands has enhanced the preexisting efforts to develop coordinate *follow-up* strategies for gravitational wave events. While no counterpart is expected after BBH coalescences in the majority of scenarios, counterparts are anticipated in BNSs mergers and possibly in NSBHs mergers if the NS is tidally disrupted by the BH before the merger, rather than being swallowed whole by it. Therefore, the main efforts are devoted to the follow-up of low-mass events, which are more likely to involve at least one NS.

With this purpose, when a candidate event is detected by online GW searches, *public alerts* are sent in low-latency to EM and neutrino observatories through the Gamma-ray Coordinates Network (GCN) [131]. These alerts contain estimates for properties of the GW source, that we will revise in detail in Sec. 4.1.1. However, despite efforts to increase coverage, the capacities of both terrestrial and space-based observatories to follow up frequent GW alerts are limited in speed of pointing, field of view and survey depth. Therefore, with the expected increasing sensitivity of the GW detector network [132] and corresponding increase in detection rate [133], being able to prioritize interesting GW events for follow-up is essential. As discussed in Chapter 3, binary merger GW signals are identified in the data streams from the global detector network almost exclusively by the use of matched filter methods, that yield the parameters of the best-fit template. Although we could then hope that these parameters would indicate the type of source and the probability of presence of NS components, they present large uncertainties due to technical, statistical and systematic biases. We will revise these sources of uncertainties in Sec. 4.1.2.

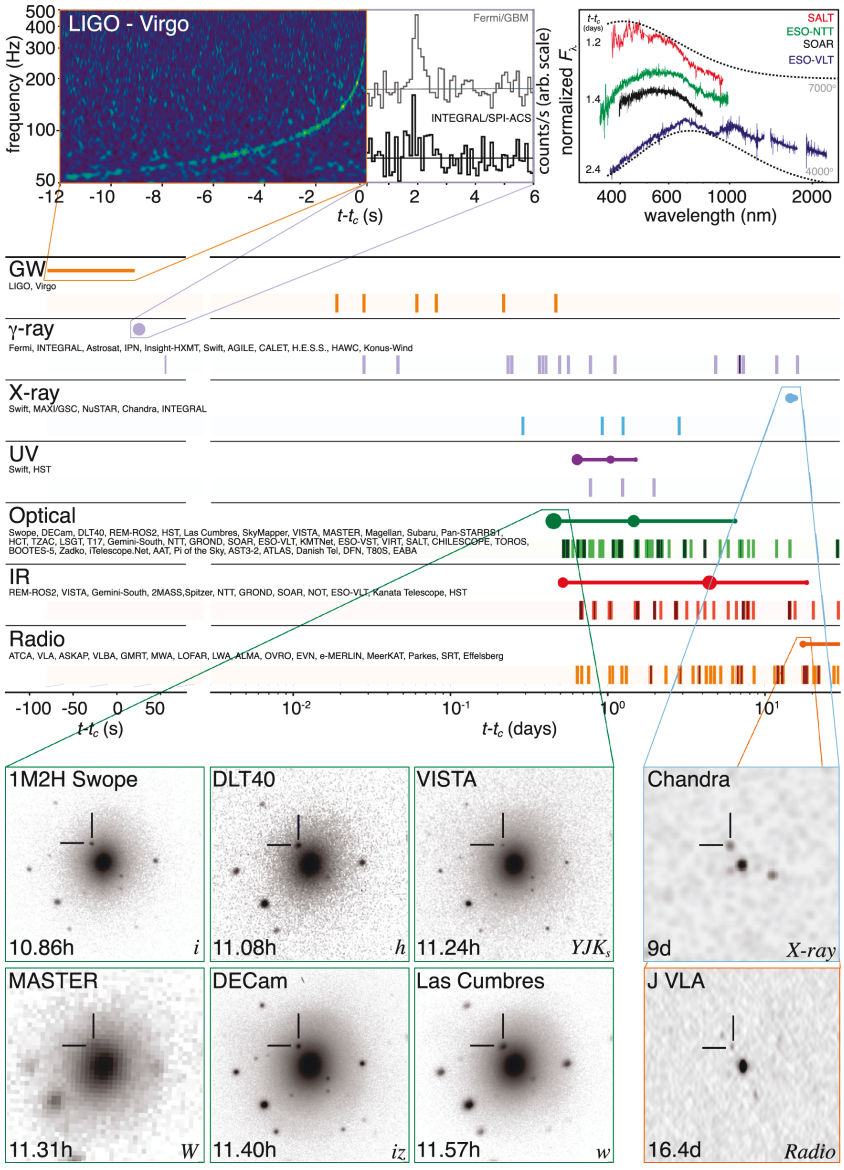

Figure 4.1: Timeline of the detection of the GW event GW170817, the GRB 170817A, the kilonova AT2017gfo, and the follow-up EM observations, with respect to the time of merger t_c. The time of the first observation in each band is represented with a solid circle, while solid lines show the times where the sources were detectable by telescopes. Magnifications for the first detections in the GW, gamma-ray, optical, X-ray and radio are also shown. More details of the different signals can be seen at [114]. Figure reproduced from [114].

4.1.1 Low-Latency rapid alert products

The rapid alerts generated by the LIGO-Virgo-KAGRA (LVK) collaboration after the detection of a GW candidate event to aid EM and neutrino observatories in their follow-up decisions, contain the first estimates about the candidate. For an up-to-date detail discussion of the content of these alerts see [116, 134]. A summary of the released information of the candidate event is the following.

- The significance of the event, given by the False Alarm Rate (FAR).
- A 3D sky-localization, that gives the posterior probability distribution of the position of the source in the sky, as well as the estimated luminosity distance. This estimation is done with the algorithms `BAYESTAR` [135] in very low-latency, and `BILBY` [136] within the subsequent parameter estimation.
- The probability of the event of being of terrestrial origin [137] $p_{\rm terr}$, and the probabilities that the source belongs to the different astrophysical CBC categories: $p_{\rm BNS}$, $p_{\rm NSBH}$ and $p_{\rm BBH}$. These four probabilities add up to 1.
- The probability that the binary contains at least one object with mass below $3\,M_\odot$, named `HasNS`.
- The probability of observing remnant matter from the merger during the post-merger [138], called `HasRemnant`.
- The probability of at least one component of the binary to be in the lower mass-gap region i.e. with a source-mass between 3-5 $M_\odot$, known as `HasMassGap`.

These low-latency products are distributed through the GCN as a series of notices and circulars, starting by a preliminary alert within 1-10 minutes after the detection, and updating the content after more detailed investigations are performed. A timeline of the different alerts sent after the detection of a GW event is shown in Fig. 4.2. At the moment, no information about the intrinsic parameters of the templates recovered by low-latency pipelines is included in the rapid alerts. We will discuss the motives and caveats of this decision in the next sections.

4.1.2 Uncertainties and biases in intrinsic parameters

The best-fit template parameters measured by CBC low-latency searches (named *point estimates*) suffer from a variety of sources of bias. These pipelines employ template banks of waveforms to matched-filter the data, yielding a point estimate corresponding with the parameters of the template of the most significant trigger (see Sec. 3.2.7). However, these point estimates of masses and

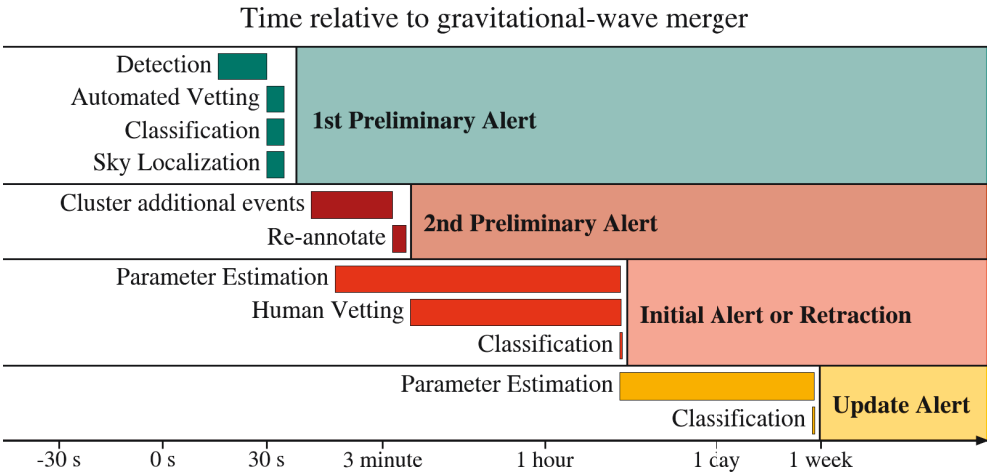

Figure 4.2: Timeline of rapid alerts distributed through the GCN after the detection of a GW candidate event. Figure adapted from [134].

aligned spins have been probed not to be accurate compared with the values obtained after a subsequent exhaustive parameter estimation calculation [139, 140]. We summarize some of the potential sources of bias below.

Template bank bias

A first source of bias arises from the discreteness of the template bank. Even though the bank is constructed with a minimum fitting factor (FF) (2.56) requirement, the templates do not cover every combination of parameters. Additionally, template waveforms neglect a number of physical effects such as precession, eccentric orbits, contributions from higher harmonic modes, and matter effects of NSs. GW signals presenting these physics can still be detected with the simplified bank, but the point estimates recovered by the search will not resemble the true physics missing in the bank. Moreover, the presence of non-Gaussian noise in the detector deviates the detected template from the true GW signal.

Redshift bias

Another source of bias is the fact that low-latency searches are only sensitive to masses measured in the detector-frame, which for cosmological sources are larger than source-frame masses by a factor of $(1 + z)$, where z is the redshift

of the source [141]. Therefore, the waveforms of GW signals from sources at larger redshifts can be matched during detection with templates corresponding to larger detector-frame total masses. This is known as the mass-redshift degeneracy [142].

Degeneracy of intrinsic parameters

GW signals emitted by low-mass binaries tend to spend a large amount of cycles orbiting within the sensitive frequency band of the detector, and then coalesce at frequencies close to the maximum (or even above) this band. Their waveforms are then dominated by the inspiral stage of the signal, and therefore the parameters that affect the evolution of the phase will be the best measured. Although this corresponds to the intrinsic parameters of masses and spins, the detector is more sensitive to certain combinations of these parameters rather than to the parameters themselves. In post-Newtonian (PN) theory, at leading order, the waveform depends solely on the chirp mass $\mathcal{M}$ (1.44), making it the best measured parameter for signals dominated by the inspiral [139]. Since the chirp mass is a combination of the masses of the binary, these will be correlated and constrained to a line of constant chirp mass in the mass plane. This degeneracy could be broken with an accurate measure of the symmetric mass ratio η, which enters at next-to-leading-order in the PN expansion. However, the mass ratio is as well degenerated with the effective spin χ_{eff} on the subsequent expansion order term [143, 144]. This spin term can mimic the effects on the waveform that would allow η to be measured accurately. Due to these degeneracies, while for low-mass systems the chirp mass is well constrained, the uncertainties in the mass ratio and the spins are large, and they tend to be poorly measured in low-latency [140].

4.1.3 Motivation for follow-up

Despite the described difficulties to provide accurate values of the intrinsic parameters in low-latency, discussions in [145] argue that a rapid release of the chirp mass estimate would allow EM observatories to better prioritize their follow-up resources. A more recent discussion in [146] states that the intrinsic parameters of the binary components can be used to estimate certain properties of kilonovas. This would allow to predict the feasibility of detection beforehand, helping the telescopes to better distribute their exposure time and coverage of the sky.

Therefore, providing an accurate estimation of the probability of the binary to contain at least one NS component, as well as a more accurate estimation of

the binary parameters, are of great importance to guide follow-up searches for EM and neutrino counterparts. Since some of the EM counterparts only last for short periods of time before decaying, as in the case of short gamma-ray bursts (SGRBs), the main challenge for online GW pipelines is to provide these accurate predictions in very-low latency.

The development of algorithms able to estimate the properties of the source in very low-latency is the common goal of the results presented in this chapter and the following. This chapter summarizes the work devoted to estimate the relative probabilities of a GW signal to belong to the different astrophysical categories while adding less than 50 ms of latency to the search. In Chapter 5, we will describe the ongoing efforts to develop a method able to estimate the uncertainties of the intrinsic parameters of the point estimate, keeping the running time around 1 minute.

4.2 Introduction to source classification

During the third observing run (O3) of the Advanced LIGO and Advanced Virgo detectors, dozens of candidate gravitational wave (GW) events were catalogued. A challenge of this observing run was the rapid identification and public dissemination of compact binary coalescence (CBC) signals, a task carried out by low-latency searches such as PyCBC Live. During the later part of O3, we developed a method of classifying CBC sources via their probabilities of containing neutron star or black hole components, within PyCBC Live, in order to facilitate immediate follow-up observations by electromagnetic and neutrino observatories. This fast classification uses the chirp mass recovered by the search as input, given the difficulty of measuring the mass ratio with high accuracy for lower-mass binaries. We also use a distance estimate derived from the search output to correct for the bias in chirp mass due to the cosmological redshift. We present results for simulated signals, and for confirmed candidate events identified in low latency over O3.

4.3 Objectives

The search for compact binary coalescence (CBC) signals in the detector data is performed in low latency by the following matched-filter based analysis pipelines: PyCBC Live, GstLAL [87, 147], MBTAOnline [95] and SPIIR [148]. When a candidate GW signal is detected, it is saved in GraceDB[1] as a *candidate*

[1] https://gracedb.ligo.org/

event. To unify all candidates from the different searches that are neighbours in time, the events collected within a given time window form a *superevent*. One of the candidates is chosen as the *preferred event* based on maximising search SNR, for the purposes of issuing public alert information such as sky localization [134].

The probability of a CBC candidate event of being of astrophysical origin, $p_{\rm astro}$, is obtained via a Poisson mixture formalism that models foreground and background event rates and distributions [149]; the probability of terrestrial noise origin is thus $p_{\rm terr} = 1 - p_{\rm astro}$. The latter is distributed in the LVK Public Alerts, along with the probabilities of the candidate event to belong to each of the CBC astrophysical categories considered in the observing run. This method only estimates the *relative* astrophysical probabilities of these categories, that have to sum to $p_{\rm astro}$. A detailed description of these categories is given in the next section.

During the period of the third observing run (O3), astrophysical source classification for PyCBC Live candidates was performed by the LIGO/Virgo rapid alert infrastructure using a "hard cuts" method, which assigns Boolean weights (either 1 or 0) to the different source types based on component mass cuts applied to the reported search template [150]. As we discussed in Sec. 4.1.2, the component masses taken from the point estimates of the search are measured with large uncertainties that are not taken into account in the classification. The uncertainty due to the fact that template component masses are redshifted with respect to the true masses of the source [151] was is also ignored by the previous method.

As stated previously, for GW signals dominated by the inspiral stage, the parameter measured by the pipelines with more accuracy is the chirp mass $\mathcal{M}$. To study the magnitude of the uncertainty of this parameter, we compare the fractional errors in PyCBC Live's estimation of the redshifted (detector-frame) chirp mass $\mathcal{M}^{\rm det} = (1+z)\mathcal{M}$ and in the mass ratio $q \equiv m_2/m_1$. This study was performed using a set of simulated astrophysical signals, described in detail in Section 4.5. The comparison is shown in Fig. 4.3, where errors in the search recovered $\mathcal{M}^{\rm det}$ and q are presented for several ranges of $\mathcal{M}^{\rm det}$. For low chirp mass binaries, considered more interesting for possible follow-up, the relative error in $\mathcal{M}$ is around two orders of magnitude smaller than the relative error in q. For high chirp mass binaries the difference between the uncertainties decreases to under one order of magnitude. These trends roughly match expectations from overlap calculations in [140].

These differences in accuracy, along with the mentioned bias caused by redshift, suggest an improvement in the source classification for PyCBC Live:

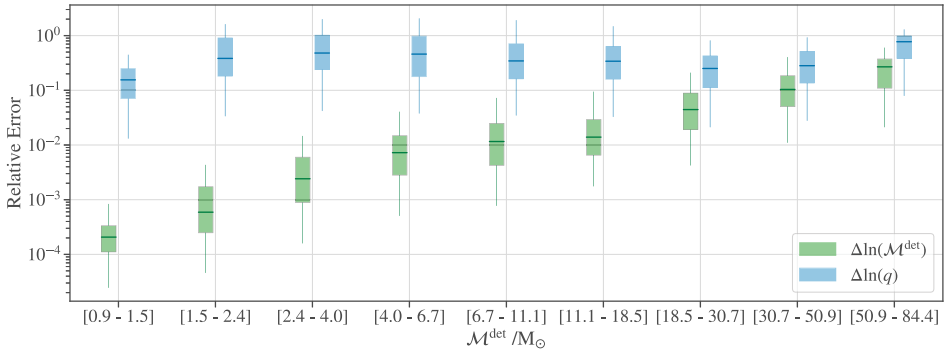

Figure 4.3: Boxplot comparison of redshifted chirp mass $\mathcal{M}^{\rm det}$ and mass ratio q relative errors for different detector frame chirp mass intervals. Median values and 50% and 90% credible intervals are presented in each case.

the proposed new method is described in the next section.

4.4 Methodology

In this section, we describe the method we developed to estimate the probability of a candidate event to belong to one of the different astrophysical categories based on the search pipeline outputs. The definition of what accounts as astrophysical category changed between O3 and O4. Therefore, we start by discussing the different sets of categories.

4.4.1 Astrophysical categories

During O3, source classification was performed over four astrophysical categories: BNS, NSBH, BBH and MassGap. For this classification, we considered every object with a mass below $3\,\mathrm{M}_\odot$ as a NS, every object with a mass above $5\,\mathrm{M}_\odot$ as a BH, and every candidate event with at least one component mass between these limits as a MassGap. The MassGap category was included at the beginning of O3 motivated by the possible existence of a limit on the minimum mass of a black hole around $5\,\mathrm{M}_\odot$. However, for O4, MassGap status was changed from a source class to a source property, along with the already existing `HasNS` and `HasRemnant` [134] already described in Sec. 4.1.1. Then, the current categories are BNS, NSBH and BBH, with $3\,\mathrm{M}_\odot$ as the limit between a NS and a BH.

Since the development of the method and the corresponding results were conducted during O3, the description and main discussion are presented according to this classification. Nevertheless, the method can be easily adapted, and we include results for its application in both cases. A summary of the two sets of astrophysical categories and their limits in the space of component masses can be seen in Fig. 4.4.

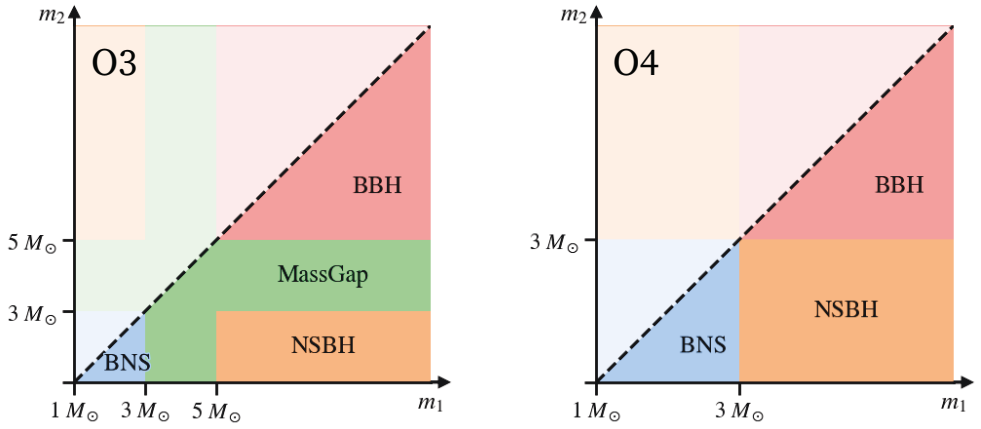

Figure 4.4: Mass limits for the four astrophysical categories considered in O3 (left figure), and for the three categories currently used in O4. Note that our convention in both cases is $m_1 \geq m_2$.

4.4.2 Outline of the method

This source classification method uses the chirp mass $\mathcal{M}$ recovered by the search pipeline as an input. Since this value is measured with high accuracy (up to a correction due to redshift, which we will discuss in Sec. 4.4.3), the component masses m_1 and m_2 are constrained to be close to a line of constant chirp mass over the mass plane. Assuming an uncertainty on the chirp mass, $\Delta\mathcal{M}$, this line becomes a contour of $\mathcal{M} \pm \Delta\mathcal{M}$ over the mass plane; we discuss our uncertainty estimate $\Delta\mathcal{M}$ in more detail in Sec. 4.4.4. In Fig. 4.5 we show some chirp mass contours corresponding to PyCBC Live triggers of events of O3a.

The main idea of this estimation method is that the probabilities of the different categories are taken to be proportional to the area of each region of the plane that is inside the contour of chirp mass. The method thus assumes an uniform prior of candidate signals over the plane of component masses m_1,

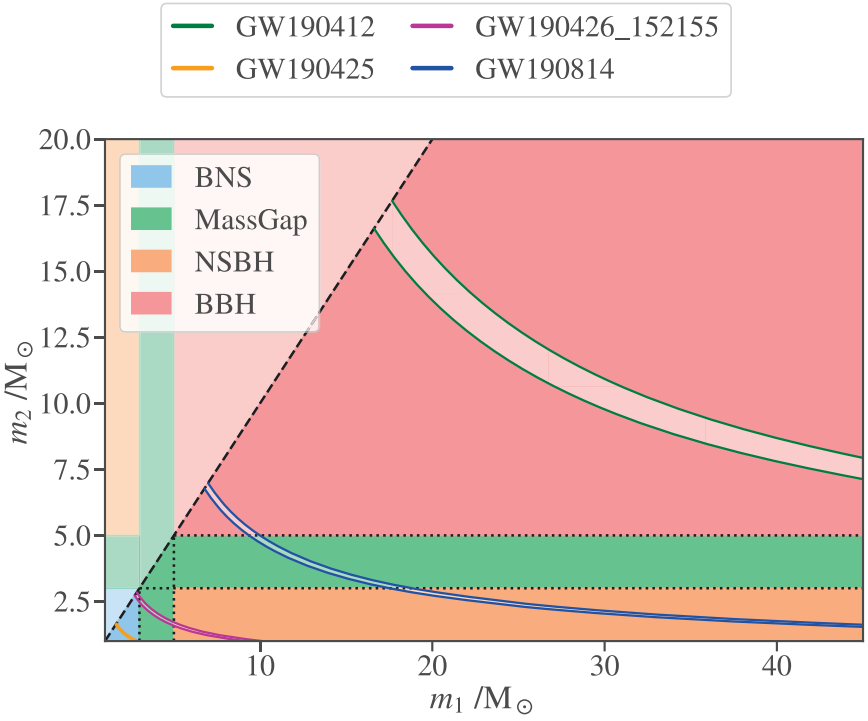

Figure 4.5: Chirp mass contours over the plane of component masses, m_1, m_2, for several O3 PyCBC Live triggers. Our (source frame) chirp mass estimates are: GW190412 ($14.91 \pm 0.46\,\mathrm{M}_\odot$), GW190425 ($1.43 \pm 0.02\,\mathrm{M}_\odot$), GW190426_151255 ($2.42 \pm 0.05\,\mathrm{M}_\odot$), GW190814 ($5.99 \pm 0.09\,\mathrm{M}_\odot$).

m_2. The output of this method for a candidate event is a list of probabilities $\{p_{\mathrm{BNS}}, p_{\mathrm{MG}}, p_{\mathrm{NSBH}}, p_{\mathrm{BBH}}\}$ summing to unity.

Component masses m_1, m_2, measured in the source frame, are constrained to the range $1 < m/\mathrm{M}_\odot < 45$, which results in a chirp mass range $0.87 < \mathcal{M}/\mathrm{M}_\odot < 39.17$. The lower bound on the component masses is the lower limit on the template bank mass space adopted by the pipeline during O3a [101], and the upper bound is chosen based on BBH population studies from the first and second observing runs (O1 and O2) [152] and O3a [123]. Given these limits, every object with a chirp mass lower than $0.87\,\mathrm{M}_\odot$ will be considered a BNS, and every object with a chirp mass greater than $39.17\,\mathrm{M}_\odot$ will be considered a BBH.

4.4.3 Estimation of the redshift

As discussed in the introduction, the chirp mass value recovered by the pipeline is that of the matched filter templates: since the templates are designed to match the signal as it appears in the data stream, the template mass corresponds to the redshifted chirp mass, $\mathcal{M}^{\rm det} = (1+z)\mathcal{M}$. To recover the true chirp mass of the event we estimate the redshift by assuming some set of cosmological parameters to relate it to the luminosity distance $D_{\rm L}$. One can deduce $D_{\rm L}$ from the amplitude of a CBC signal at a given detector, which is inversely proportional to $D_{\rm L}$ but also depends on the masses and spins of the source and on its position and orientation relative to the detector. For low-latency analysis, the luminosity distance is estimated by the rapid Bayesian algorithm `BAYESTAR` [153] as a part of the sky localization process. This follow-up process starts after the candidate event trigger has been uploaded to GraceDB and hence the search pipeline does not have access to `BAYESTAR` estimated luminosity distances. To overcome this problem we estimate the luminosity distances using the *effective distance* $D_{\rm eff}$ (2.48) [154], which is estimated by the search as follows.

The expected SNR of a signal in a detector i, assuming that the template waveform is perfectly matched to the signal, is given by

$$\bar{\rho}_i = \frac{\sigma_i}{D_{{\rm eff},i}}, \tag{4.1}$$

where σ_i is a (mass- and spin-dependent) measure of the detector sensitivity given by the expected SNR for a source at 1 Mpc distance, directly overhead the detector and with zero inclination (angle between the direction to the observer and the orbital angular momentum of the binary) [154]. Using Eq. (4.1), the effective distance is estimated by PyCBC Live for each of the instruments present for a given event as

$$\hat{D}_{{\rm eff},i} = \frac{\sigma_i}{\rho_i}\,{\rm Mpc}, \tag{4.2}$$

where ρ_i is the matched filter SNR.

To estimate the luminosity distance using these estimated effective distances, we study the relation between them. We collect the $\hat{D}_{{\rm eff},i}$ values in each detector and the luminosity distance computed using `BAYESTAR`, $D_{\rm B}$, for PyCBC Live triggers from all the public candidate events from O3a.[2] We do

[2] As this fit was initially performed during O3, the set of simulated signals later used in Sec. 4.5 was not available.

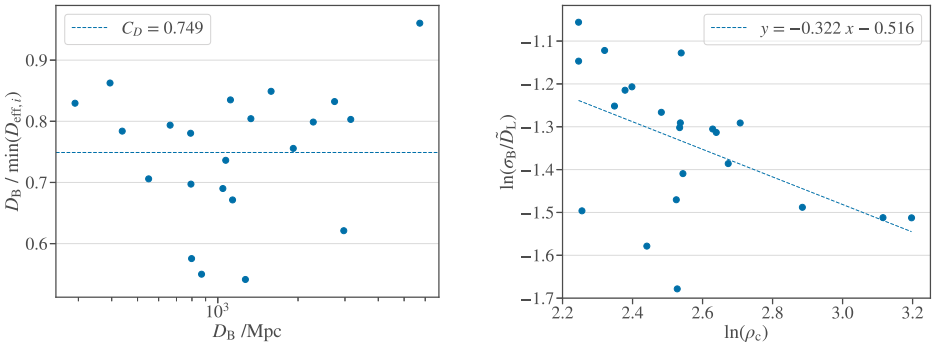

Figure 4.6: Fitting plots for the luminosity distance $\tilde{D}_{\mathrm{L}}$ (left) and its uncertainty $\tilde{\sigma}_{D_{\mathrm{L}}}$ (right).

not expect that the effective distance estimated by any one pre-determined detector will be a good predictor of D_{B}, so we choose for each candidate event the closest effective distance to D_{B}, which is also the smallest one: $\min(D_{\mathrm{eff},i})$. Note that $D_{\mathrm{eff},i} \geq D_{\mathrm{L}}$ for all detectors. We then estimate luminosity distances as

$$\tilde{D}_{\mathrm{L}} = C_D \cdot \min(\hat{D}_{\mathrm{eff},i}), \tag{4.3}$$

where C_D is a constant, for which we take the mean of the ratios $D_{\mathrm{B}}/\min(D_{\mathrm{eff},i})$ of all selected triggers to obtain $C_D = 0.749$. This can be seen in the left plot of Fig. 4.6. We also estimate the uncertainty on luminosity distance using the same selection of triggers from O3a, by performing a log-linear regression of the (1σ) luminosity distance uncertainties computed using `BAYESTAR`, σ_{B}, relative to the estimated luminosity distances of Eq. (4.3), against the network SNR of the trigger, ρ_{c}.[3] This fit, shown in the right plot of Fig. 4.6, gives a estimate of the uncertainty

$$\tilde{\sigma}_{D_{\mathrm{L}}} = \mathrm{e}^{-0.516} \cdot \tilde{D}_{\mathrm{L}} \cdot \rho_{\mathrm{c}}^{-0.322}. \tag{4.4}$$

From the estimated luminosity distance and relative uncertainty, we derive the redshift $\tilde{z}$ and redshift uncertainty $\tilde{\sigma}_z$ estimates assuming a standard flat ΛCDM cosmology, where the function $D_{\mathrm{L}}(z)$ is given by the expression on Eq. (1.64), with a Hubble parameter $H_0 = 67.90\,\mathrm{km\,s^{-1}\,Mpc^{-1}}$ and matter density parameter $\Omega_m = 0.3065$ [35].

[3] $\rho_c = \sqrt{\sum_i \rho_i^2}$, being i each detector present in the event detection.

4.4.4 Chirp mass uncertainty

To finally estimate the source frame $\mathcal{M}$ uncertainty $\Delta\mathcal{M}$, we combine the propagated redshift uncertainty $\tilde{\sigma}_z$ with a small nominal uncertainty of 1% in the detector-frame chirp mass recovered by the search pipeline. As shown in Fig. 4.3, this 1% nominal error is a representative value for signals around the centre of the total mass range we consider. Also, in most cases we expect the redshift uncertainty will be comparable to or larger than uncertainty in $\mathcal{M}^{\rm det}$. For higher-mass signals, a highly accurate estimate of $\Delta\mathcal{M}$ is not necessary as the classification will be dominated by BBH; for low-mass signals, the 1% nominal error is an overestimate, however we have verified that the effect on the resulting source probabilities is negligibly small.

4.5 Check with simulated signals

In order to check the accuracy of the classification method and test the luminosity distance fitting constants used in Eq. (4.3) and (4.4), we use a population of simulated astrophysical signals injected into the O3a data and recovered using PyCBC Live. The simulated population campaign was originally performed for testing the improvements made to PyCBC Live for O3, and therefore is described in detail in [93]. In summary, for the simulated binaries, neutron stars have masses distributed uniformly between $1\,\mathrm{M}_\odot$ and $3\,\mathrm{M}_\odot$, and black holes have masses distributed uniformly between $3\,\mathrm{M}_\odot$ and $97\,\mathrm{M}_\odot$. This masses are measured in the detector frame. All CBC simulated sources are distributed uniformly in *chirp distance* [154] between $5-300\,\mathrm{Mpc}$.

The PyCBC Live search has various internal thresholds for generating candidate events, for instance to generate a two-detector event a minimum SNR of 4.5 is required in both detectors As a result, not all simulated signals are recovered by the search; the recovered signals have network SNRs distributed from a minimum of 7.9 up to several hundred, and FARs ranging from $\sim$2 per hour down to 1 per thousands of years. For uploading to GraceDB, a further FAR threshold of 1 per 2 hours was applied in O3, whereas issuing a public alert required a much more stringent threshold of 1 per 10 months ($3.8\times10^{-8}\,\mathrm{Hz}$) [134] . While the accuracy of the mass parameters is slightly improved by imposing tighter FAR thresholds, the classification performance is essentially unchanged (as discussed later in Sec. 4.5.2), hence we give results without applying any FAR threshold.

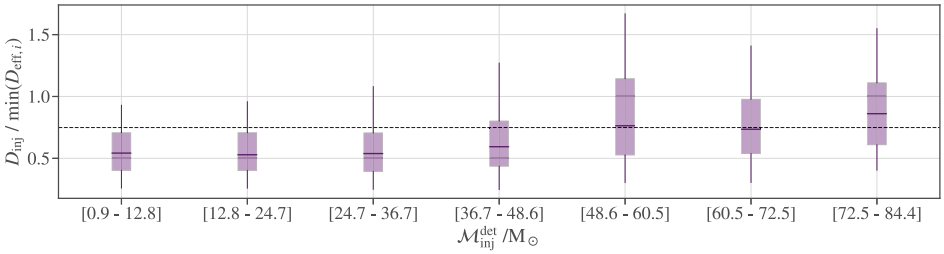

Figure 4.7: Boxplot showing the ratio between the simulated (true) distances and the minimum effective distances recovered by PyCBC Live for different detector-frame chirp mass intervals. Dotted line corresponds to a value of $D_{\rm inj}/\min(D_{{\rm eff},i}) = 0.749$, the fitting constant of Eq. (4.3).

4.5.1 Accuracy of distance estimation

First, we present a test on the reliability of the luminosity distance estimation of Eq. (4.3). In Fig. 4.7 we show a boxplot of the ratio of the simulated luminosity distances, $D_{\rm inj}$, and the minimum effective distances recovered by PyCBC Live, $\min(D_{{\rm eff},i})$ for simulated signals binned over detector-frame chirp mass. The dotted line in the plot represents the fit obtained in the previous section, $C_D = 0.749$. The plot shows a deviation from the fitting constant for low chirp mass and very high chirp mass binaries. Up to $\sim$50 M$_\odot$, this ratio is overestimated; conversely, for chirp mass values over $\sim$70 M$_\odot$, the fitting constant is underestimated. As expected, the fit is more accurate for chirp masses toward the center of the range, since it was estimated using O3a events which mostly fall into this region.

A possible reason for this bias may be that the search template sensitivity σ_i, used in Eq. (4.2) to estimate the source distance, is biased with respect to the sensitivity for a template corresponding to the true source parameters. Figure 4.8 shows a boxplot of the ratio between the injected (redshifted) chirp masses and the chirp masses recovered by PyCBC Live, binned over chirp mass: for low chirp mass signals the search shows an unbiased recovery, however for signals with $\mathcal{M}(1+z) \gtrsim 50\,{\rm M}_\odot$ there is a clear bias towards underestimating injection chirp masses, which may result from the limited extent of the template bank. Since the sensitivity σ_i is largely determined by the template chirp mass, this recovery bias will contribute to a bias in the estimation of source distances.

For low-chirp-mass systems, which are of most interest for potential EM follow-up, we may thus obtain a distance estimate that is not affected by

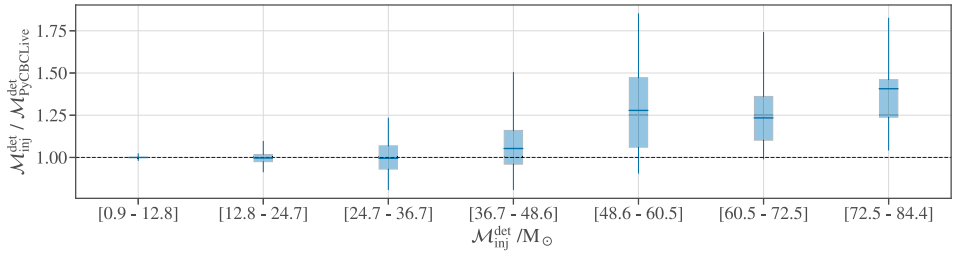

Figure 4.8: Boxplot showing the ratio between the simulated chirp masses and the chirp masses measured by PyCBC Live for different chirp mass intervals. All chirp masses are in the detector frame. Dotted line corresponds to a ratio equals to unity.

this bias, at the cost of a higher bias for high-mass BBH signals. For this, we repeat the linear fit of the previous section taking the mean of the ratio $D_{\rm inj}/\min(D_{{\rm eff},i})$ only for simulated signals with $\mathcal{M}^{\rm det}_{\rm inj} < 40\,{\rm M}_\odot$, giving a revised value of $C_D = 0.576$. However, the results presented in this chapter use the original value $C_D = 0.749$ of (4.3).

4.5.2 Accuracy of classification method

In order to check the accuracy of the chirp-mass based classification, we impose an additional constraint on the simulated signal parameters. Given the component mass limits described in Section 4.4, asymmetric high-mass NSBH systems outside these limits are not representative of the accuracy of the method. Therefore, we restrict the black hole components of simulated NSBH events to be below $50\,{\rm M}_\odot$. We present two different visualizations of the performance of the method: a confusion matrix and a kernel density estimate (KDE) of predicted probabilities.

The confusion matrix, shown in Fig. 4.9, compares the category of the simulated signals (*true category*), defined by their given source masses, against the category found with the highest probability by the classification method (*predicted category*). BBH and NSBH simulated events are assigned with highest probability to their correct categories in a large majority of cases: 95% and 88% respectively. BNS signals have a 61% probability of being classified correctly, but a notable 34% of cases are found more likely to be MassGap sources. Simulations of MassGap sources are mostly classified as NSBH, with a 63% probability, followed by BBH and MassGap. This bias between NSBH and MassGap categories can be justified considering the high uncertainty on rates

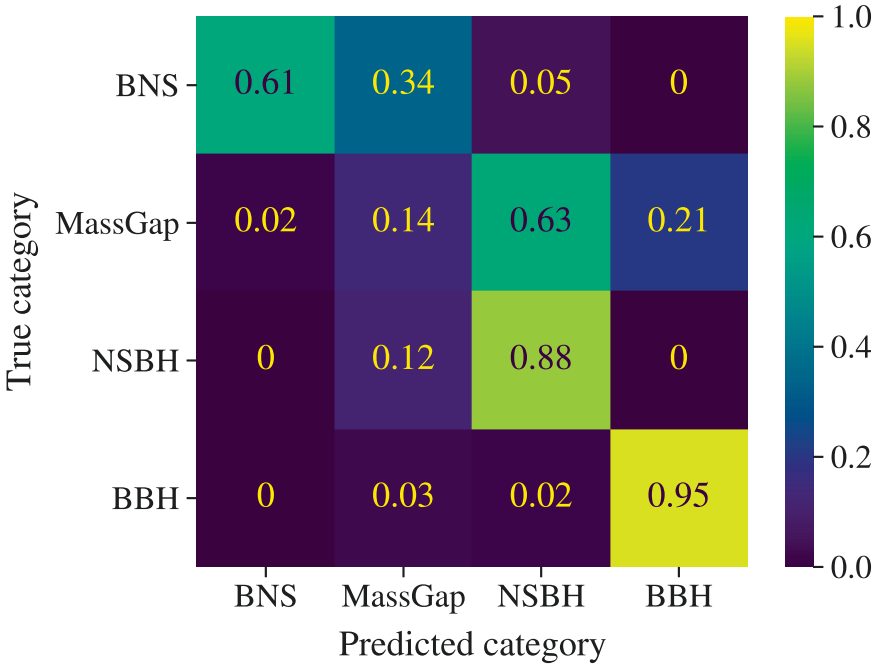

Figure 4.9: Confusion matrix comparing the true categories of the simulated signals versus the category found with highest probability in each event.

and masses of both CBC sources, and implies a conservative approach of the classification method: it will suggest a follow-up for possible EM counterparts of NSBH signals even if the source is a MassGap binary. When applying the FAR required for public alerts we obtain very similar probabilities, differing by at most 0.03.

The KDE plot, presented in Fig. 4.10, shows the distribution of the estimated probabilities that our method assigns to the correct CBC category of each simulated signal. The correct category is determined from the given source component masses of the signal, according to the mass boundaries described in Section 4.4. BNS and BBH simulated signals are assigned correctly with probabilities over 80% for a large or very large majority of cases. These high probabilities are expected, due to the location of both classes in the plane of component masses m_1, m_2: chirp mass contours over BNS or BBH areas do not necessarily overlap other target regions. This is not the case of NSBH or MassGap simulated events, whose chirp mass contours always overlap other

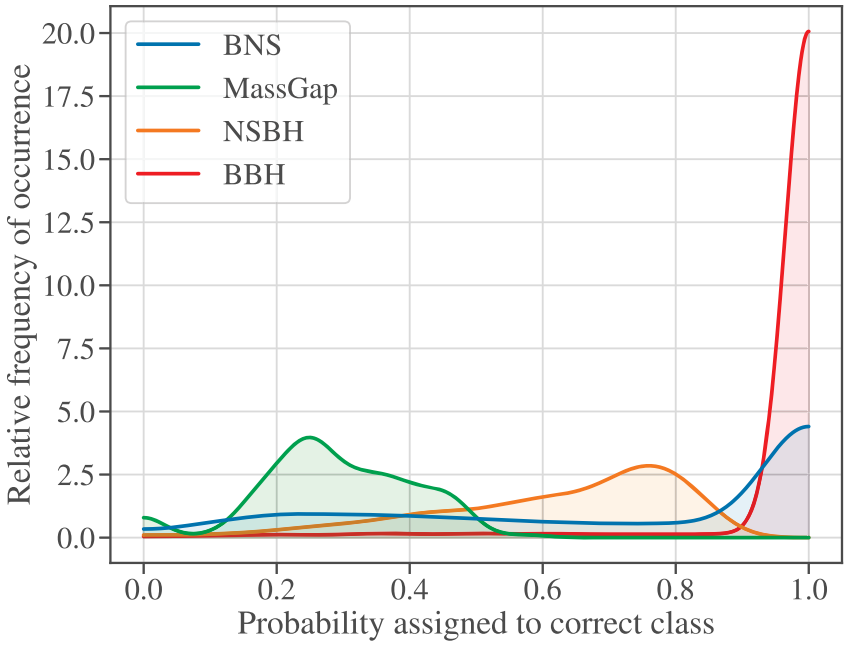

Figure 4.10: Density distribution of the probabilities estimated by our method for the correct CBC category of the simulated population. Correct categories are determined from the given source component masses.

source areas, and this lowers the probabilities assigned to the correct category. The majority of NSBH simulations are assigned to the correct class with probabilities p_{NSBH} over 50%, but the narrowness of the MassGap region causes the p_{MG} probabilities to fall under the 50% for the majority of cases.

4.5.3 Removal of MassGap category

As discussed in Sec. 4.4.1, the MassGap category was included in O3 motivated by the existence of a possible limit on the minimum mass of a black hole around $5\,\mathrm{M}_{\odot}$. For O4, the MassGap was changed to be a source property. In view of this change, we present the same visualization plots for the chirp-mass based classification of the mentioned population of simulated signals in the remaining BNS, NSBH and BBH categories: in this case, every component with mass greater than $3\,\mathrm{M}_{\odot}$ is considered a BH.

The confusion matrix of Fig. 4.11 shows a slight change in the probability of a BBH to be assigned correctly, from 95% to 93%, where the remaining

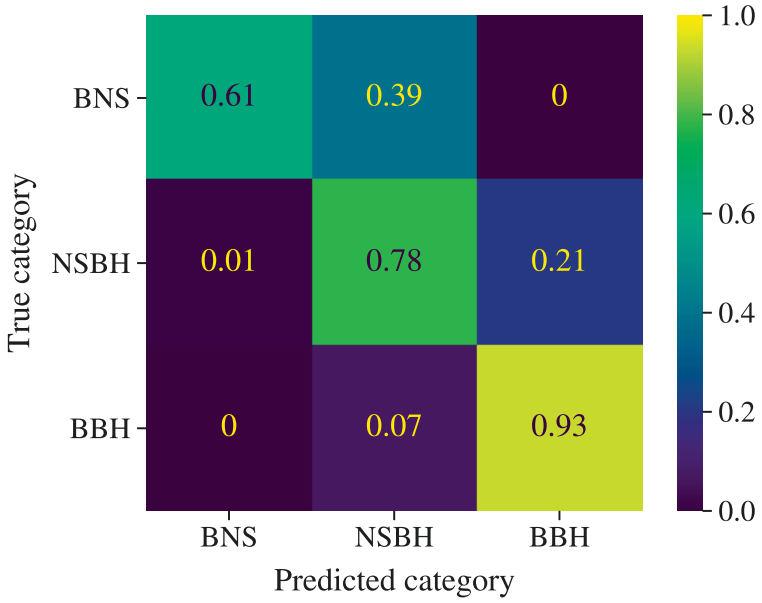

Figure 4.11: Confusion matrix comparing the true categories of the simulated signals versus the category found with highest probability by our method for BNS, NSBH and BBH categories.

7% will be classified as NSBH. In the case of NSBH simulated signals, the rate of correct assignations changes from 88% to 78%, and 21% of cases are now classified as most likely to be BBH. Lastly, there is no change in the 61% of BNS simulations correctly assigned, and the remaining cases are found as most likely to be NSBH, meaning that an EM follow-up would be always recommended for this range of masses. As in the case including the MassGap category, these probabilities are stable under applying a more stringent FAR threshold.

The KDE plot, presented in Fig. 4.12, shows a main change in the distribution of NSBH probabilities, where a notable amount of cases are now assigned very high correct class probabilities. This behaviour is consistent with the decrease of the overlap between the NSBH area with the other source class regions.

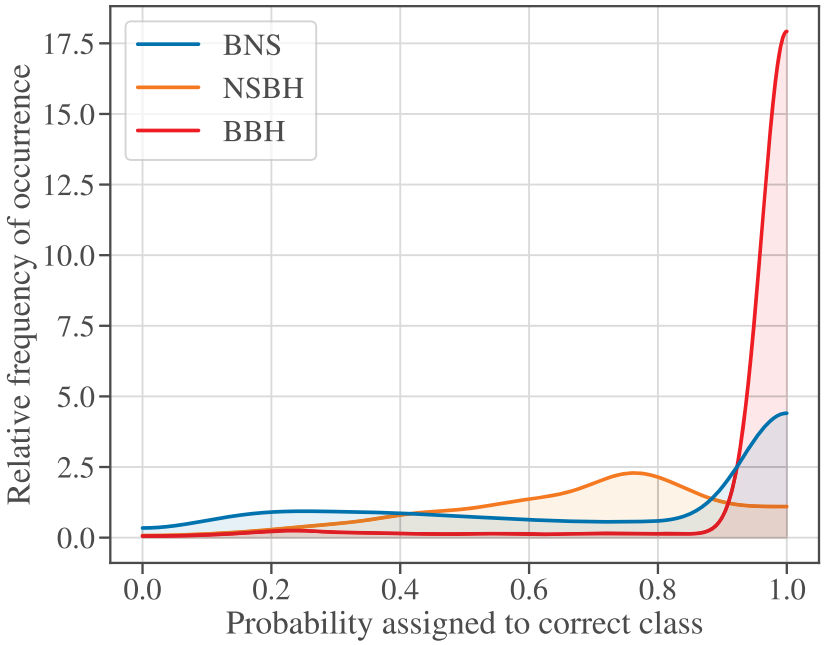

Figure 4.12: Density distribution of the probabilities estimated by our method for the correct CBC category of the simulated population, among BNS, NSBH and BBH. Correct categories are determined from the given source component masses.

4.6 Results for O3 confirmed events

In this section we present the probabilities obtained applying the chirp-mass based classification method to 26 events detected during O3a, and 19 during the second half of the third observing run (O3b). The selected events follow these criteria: they were candidate events disseminated in the public GCN notices and circulars during O3, and they pass the publication thresholds of GWTC-2 [122] and GWTC-3 [155], respectively.

We want to compare the accuracy of our method against the classification sent in the public low-latency GCN Circulars and the detailed offline PE results [76] obtained afterwards for GWTC-2 and GWTC-3. The results are presented in Table 4.1 for events corresponding to O3a, and in Table 4.2 for O3b events. The second column of each table gives the probabilities obtained by the method described in this chapter. These results are compared with the probabilities distributed in the GCN Circulars [156], in the third column,

and with the probabilities obtained by the PE techniques of GWTC-2 and GWTC-3, in the fourth column. The source chirp mass computed with PE is also shown as context for further discussion. The section is organized as follows: in the three first subsections we describe in more detail how the probability estimates were obtained for each of the methods we compare, and the last subsection is devoted to an extended discussion of this comparison.

4.6.1 Chirp-Mass based probabilities

We apply the chirp-mass based method to a total of 45 online triggers belonging to public candidate events that were submitted to GraceDB near the time of the event. The same candidate event may be reported to GraceDB by different analysis pipelines, so a trigger choice has to be made in order to perform the analysis. The trigger selection is motivated as follows: as we plan to implement this method in PyCBC Live, we use the data of the online trigger of this pipeline, if available; if no PyCBC Live trigger is available, we take the information of the *preferred trigger* of the event. The criteria for choosing the *preferred trigger* can be found in the LVK Alerts User Guide [134]. Trigger data is not publicly available, but it can be computed analyzing the Data Releases of GWTC-2 [157] and GWTC-3 [158] with the corresponding online pipeline codes.

O3a events For 21 of the 26 candidate events selected, a PyCBC Live trigger is available in the GraceDB database. To apply the chirp-mass based method, we extract from them their chirp mass, their effective distances and their SNR. The candidate event GW190425 is a special case, since it was detected by PyCBC Live as a LIGO Livingston single-detector trigger. During O3, the single-detector significance calculation method [93] was not yet implemented into the PyCBC Live pipeline, and thereby the trigger was not reported in GraceDB. However, since it was detected by PyCBC Live in low latency, we use its single-trigger parameters to compute the chirp-mass based probabilities.

The 4 remaining O3a candidate events with no PyCBC Live trigger available are GW190513_205428, GW190630_185205, GW190728_064510 and GW190915_235702. All of them have a *preferred trigger* from the GstLAL online search. Since this pipeline does not compute effective distances, we directly use the preliminary luminosity distances computed with `BAYESTAR` to apply the chirp-mass based method, besides the chirp mass and the SNR values.

O3b events In this case, 14 candidate events out of the 19 selected have a PyCBC Live trigger available in GraceDB. As in the O3a events, we use

Event Name	Chirp-Mass Based				Public Alerts				GWTC-2 PE				
	BNS	MG	NSBH	BBH	BNS	MG	NSBH	BBH	BNS	MG	NSBH	BBH	$\mathcal{M}(M_\odot)$
GW190408_181802	0	0	0	100	0	0	0	100	0	0	0	100	18.3
GW190412	0	0	0	100	0	0	0	100	0	0	0	100	13.3
GW190421_213856	0	0	0	100	0	0	0	100	0	0	0	100	31.2
GW190425	100	0	0	0	100	0	0	0	99.5	<0.1	0	0	1.4
GW190426_152155	6.0	40.3	53.7	0	57.4 15.0	27.6 25.0	15.0 60.0	0 0	1.1	29.4	64.2	0	2.4
GW190503_185404	0	0	0	100	0	3.2	0.5	96.3	0	0	0	100	30.2
GW190512_180714	0	0	0	100	0	0	0	100	0	0	0	100	14.6
GW190513_205428 †	0	0	0	100	0	5.2	0.5	94.3	0	0	0	100	21.6
GW190517_055101	0	0	0	100	0	1.7	<0.1	98.3	0	0	0	100	26.6
GW190519_153544	0	0	0	100	0	0	0	100	0	0	0	100	44.5
GW190521	0	0	0	100	0	0	0	100	0	0	0	100	69.2
GW190521_074359	0	0	0	100	0	0	0	100	0	0	0	100	32.1
GW190602_175927	0	0	0	100	0	0	0	100	0	0	0	100	49.1
GW190630_185205 †	0	0	0	100	0	5.2	0.5	94.3	0	0	0	100	24.9
GW190701_203306	0	0	0	100	0	0	0	100	0	0	0	100	40.3
GW190706_222641	0	0	0	100	0	0	0	100	0	0	0	100	42.7
GW190707_093326	0	46.2	7.2	46.6	0	0	0	100	0	<0.1	0	>99.9	8.5
GW190720_000836	0	46.8	4.0	49.2	0	0	0	100	0	0.9	0	99.1	8.9
GW190727_060333	0	0	0	100	0	3.0	0.2	96.8	0	0	0	100	28.6
GW190728_064510 †	0	47.2	2.4	50.4	0 0	51.6 4.6	14.4 0	34.0 95.4	0	1.8	0	98.2	8.6
GW190814	0	31.4	51.7	16.9	0 0	100 0.2	0 99.8	0 0	0	0	100	0	6.1
GW190828_063405	0	0	0	100	0	0	0	100	0	0	0	100	25.0
GW190828_065509	0	0	0	100	0	0	0	100	0	0	0	100	13.3
GW190915_235702 †	0	0	0	100	0	0	0	100	0	0	0	100	25.3
GW190924_021846	0	30.1	55.7	14.2	0	100	0	0	0	44.8	3.9	51.3	5.8
GW190930_133541	0	44.0	13.7	42.3	0	100	0	0	0	8.0	<0.1	92.0	8.5

Table 4.1: Source classification percentage probabilities for confirmed O3a events identified in low-latency alerts. Chirp-mass based probabilities, in the second column, are estimated using search template chirp masses and estimates of the distance to the source. PyCBC Live distance estimates are available for all events, except the ones with a dagger (†), where GstLAL triggers and `BAYESTAR` distance estimates are used. Probabilities issued as low-latency public alerts, in the third column, are derived from the preferred search trigger in GraceDB. Bold-faced events correspond to PyCBC Live preferred triggers, events in italics correspond to MBTAOnline preferred triggers, typewriter-font corresponds to a SPIIR preferred trigger, and the rest correspond to GstLAL preferred triggers. If two sets of GCN probabilities are shown, the second set is a later update based on posterior support from parameter estimation. To compute PE probabilities, in the fourth column, we use samples reweighted to a prior with uniform merger rate in the co-moving frame. The source chirp mass computed from PE is also shown.

Event Name	Chirp-Mass Based				Public Alerts				GWTC-3 PE				
	BNS	MG	NSBH	BBH	BNS	MG	NSBH	BBH	BNS	MG	NSBH	BBH	$\mathcal{M}(M_\odot)$
GW191105_143521	0	44.5	12.2	43.3	0	0	0	100	0	1.3	<0.1	98.7	7.8
GW191109_010717	0	0	0	100	0	0	0	100	0	0	0	100	47.5
GW191129_134029	0	39.3	28.1	32.6	0	0	0	100	0	4.6	0	95.4	7.3
GW191204_171526 †	0	47.2	4.2	48.6	0	0	0	100	0	< 0.1	0	> 99.9	8.6
GW191215_223052	0	0	0	100	0	0	0	100	0	0	0	100	18.4
GW191216_213338	0	47.5	0.6	51.9	0	100	0	0	0	2.0	0	98.0	8.3
					0	0.9	0	99.1					
GW191222_033537 †	0	0	0	100	0	0	0	100	0	0	0	100	33.8
GW200105_162426	0	15.0	85.0	0	0	0	100	0	0	0.7	99.3	0	3.4
GW200112_155838 †	0	0	0	100	0	0	0	100	0	0	0	100	27.4
GW200115_042309	7.0	40.8	52.2	0	0	100	0	0	0.7	28.0	70.8	0	2.4
GW200128_022011	0	0	0	100	0	0	0	100	0	0	0	100	32.0
GW200129_065458	0	0	0	100	0	0	0	100	0	0	0	100	27.2
GW200208_130117	0	0	0	100	0	0	0	100	0	0	0	100	27.7
GW200219_094415	0	0	0	100	0	0	0	100	0	0	0	100	27.6
GW200224_222234	0	0	0	100	0	0	0	100	0	0	0	100	31.1
GW200225_060421	0	0	0	100	0	0	0	100	0	0	0	100	14.2
GW200302_015811 †	0	0	0	100	0	0	0	100	0	0	0	100	23.4
GW200311_115853	0	0	0	100	0	0	0	100	0	0	0	100	26.6
GW200316_215756 †	0	46.4	2.6	51.0	0	100	0	0	0	5.4	< 0.1	94.5	8.8

Table 4.2: Source classification percentage probabilities for confirmed O3b events identified in low-latency alerts. Chirp-mass based probabilities, in the second column, are estimated using search template chirp masses and estimates of the distance to the source. PyCBC Live distance estimates are available for all events, except the ones with a dagger (†), where GstLAL triggers and `BAYESTAR` distance estimates are used. Probabilities issued as low-latency public alerts, in the third column, are derived from the preferred search trigger in GraceDB. Bold-faced events correspond to PyCBC Live preferred triggers, events in italics correspond to MBTAOnline preferred triggers, typewriter-font corresponds to a SPIIR preferred trigger, and the rest correspond to GstLAL preferred triggers. If two sets of GCN probabilities are shown, the second set is a later update based on posterior support from parameter estimation. To compute PE probabilities, in the fourth column, we use samples re-weighted to a prior with uniform merger rate in the co-moving frame. The source chirp mass computed from PE is also shown.

their chirp mass, their effective distances and their SNR to compute the chirp-mass based probabilities. The candidate GW200105_162426 was detected by PyCBC Live as a LIGO Livingston single-detector trigger, and thereby was not reported in GraceDB. Even so, we use its single-trigger parameters to compute the chirp-mass based probabilities.

The 5 candidates of O3b without a PyCBC Live trigger are GW191204_171526, GW191222_033537, GW200112_155838, GW200302_015811 and GW200316_215756. All of them have a *preferred trigger* from the GstLAL online search, thus we compute the chirp-mass based probabilities using their `BAYESTAR` preliminary luminosity distances, chirp masses and SNRs.

4.6.2 GCN Alert probabilities

As discussed in Sec. 4.1.1, the GCN Notices and Circulars always include a probability of the source to be of terrestrial origin. In order to make an effective comparison with the chirp-mass based method, we rescaled the GCN Circular probabilities to the total probability of astrophysical origin.

The set of probabilities sent on initial GCN Circulars is computed within the LVK rapid alert infrastructure, where the probability estimation method depends on the pipeline that reported the *preferred trigger* of the candidate event.

Some events in Tables 4.1 and 4.2 present two sets of GCN Circulars probabilities. Second sets correspond to a later update based on posterior support from PE. For GW190426_152155, an initial Circular [159] was sent in low latency, giving the candidate event a rescaled 57% BNS probability, but a Source Classification update [160] was sent 10 days later assigning the event a 60% probability of NSBH origin. For GW190728_064510, the low-latency Circular [161] reports a 52% probability of being a MassGap, but a few hours later an update on Source Classification [162] was made public, including a PE-based classification that gives the event a 95% BBH probability. Lastly, for GW190814, the source classification sent in the initial Circular [150] was based on point mass estimates, assigning an estimate of 100% MassGap probability to the candidate event. A few hours later, an update on Source Classification [163] was available, where the PE-based classification gives a $> 99\%$ NSBH probability. Lastly, for GW191216_213338, an initial Circular [164] was sent in low latency, giving the candidate a 100% probability of MassGap origin. A week later, a Source Classification update [165] was made public, including a $> 99\%$ BBH probability.

The probabilities sent in Notices and Circulars are limited in precision to 1% and in some cases are stated as an upper or lower limit. We use numerical values obtained from `p_astro.json` data files available at GraceDB.

4.6.3 Probabilities from GWTC-2 and GWTC-3 PE

We may compare the chirp-mass based probabilities with the PE results computed for the catalogs using samples published in the Data Releases of GWTC-2 [157] and GWTC-3 [158]. Here we use samples re-weighted to have a luminosity distance prior that corresponds to a uniform merger rate in the co-moving frame of the source, which are also used for PE results in GWTC-2 and GWTC-3. The probabilities for the four CBC categories are computed by distributing the samples in the different regions of the component mass plane, counting how

many samples fall in each area and dividing them between the total number of samples: we use `PEPredicates` code[4] accessed via the `PESummary` package [166] to carry out the calculation.

For some events, for instance GW190426_152155, a fraction of samples have component mass under the $1\,M_\odot$ limit usually taken as the minimum NS mass. These samples are not assigned to any astrophysical class, thus the sum of probabilities is not 100% in such cases. In contrast, our method generally assumes zero probability of a source having component mass $< 1\,M_\odot$, thus our probabilities do sum to 100%.

4.6.4 Discussion of results

Finally, in this section we discuss the main features of the method for confirmed GW events identified in low latency during O3, and compare them with the classifications issued via GCN and with those resulting from detailed offline PE.

The events naturally fall into several groups according to the PE chirp mass. In Fig. 4.13 we compare the redshifted chirp masses from the low-latency searches and the PE analysis: there is no apparent bias except for higher $\mathcal{M}$ binaries, where in some cases the searches underestimate the value relative to PE. This deviation is expected at least for the PyCBC Live pipeline, given the results obtained using the simulated signals described in Section 4.5 (see Fig. 4.8).

For a large number of high- or moderately high-mass BBH signals, all methods give probabilities of 100% to the BBH class, a result expected even if the $\mathcal{M}$ and distance values used for the estimate have relatively large errors. There are several signals with somewhat lower chirp mass than the majority of BBH, in the approximate range of $7 - 9\,M_\odot$, for which our method gives significantly large probabilities to the MassGap (MG) class in addition to BBH. These signals are all classified as BBH with high probability by PE, indicating that the data disfavour asymmetric masses in the MG range, as opposed to our method which neglects information on mass ratio. However, our method still assigns high probability to the most likely true class (BBH). The GCN probabilities for these events are either 100% BBH or 100% MG (for instance GW190930_133541), thus in some cases assigning zero probability to the most likely origin.

Two events, GW190814 and GW190924_021846, have chirp mass consistent with BBH, MG and NSBH origin. They were assigned as 100% MG in

[4] `https://pypi.org/project/pepredicates/`

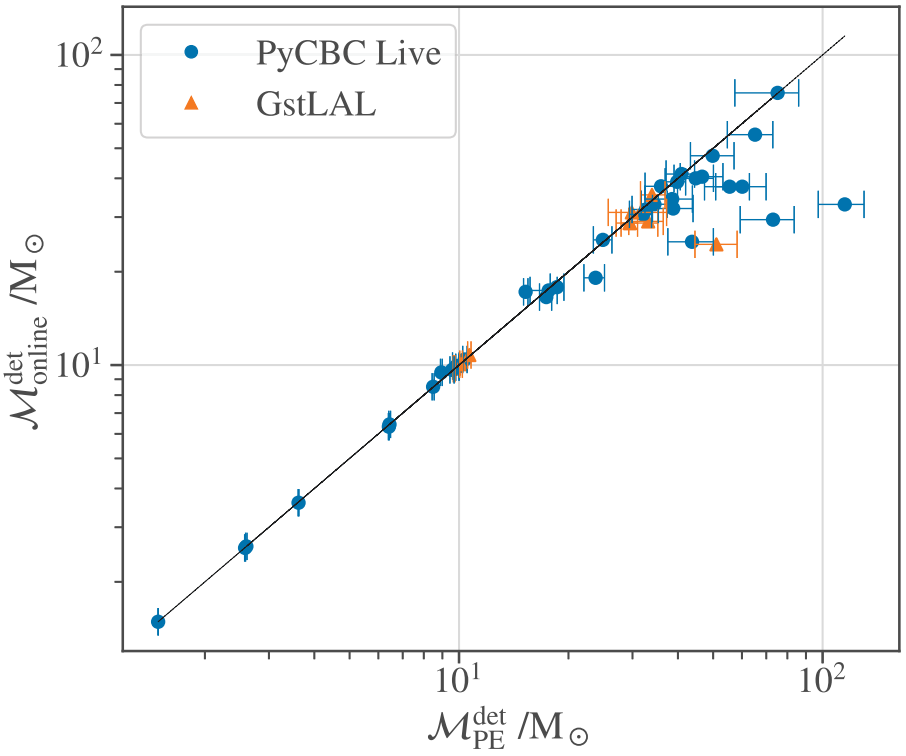

Figure 4.13: Scatter plot of the $\mathcal{M}^{\rm det}$ estimated by the low-latency pipelines, against the $\mathcal{M}^{\rm det}$ (median and 90% credible interval) from PE samples for the 45 O3 events selected. Chirp masses of PyCBC Live triggers are plotted if available; if not available, the trigger chirp mass of the preferred event is plotted (here, all preferred events are from GstLAL).

GCN alerts, however detailed PE indicates their probable true class as either certainly NSBH (for GW190814), and conversely BBH or MG with nearly equal probability (GW190924_021846). Our method assigns NSBH origin the highest probability for these events, with MG the next most likely and small nonzero $p_{\rm BBH}$. Thus in one case we correctly identify the most likely class, and in the other we at least do not assign zero probability to the correct class.

Three further events have chirp masses inconsistent with BBH, but allow MG and NSBH origin: the marginal candidate GW190426_152155 and the first NSBH detections, GW200105_162426 and GW200115_042309 [167]. All three are most likely NSBH according to PE analysis, with nonzero MG probabilities for the first and last. GCN alerts issued in low latency correctly identify the most likely class only for GW200105_162426, whereas our method assigns all three as NSBH with over 50% probability (though also with significant nonzero $p_{\rm MG}$).

Finally, only the event GW190425 [168] has a chirp mass consistent with BNS origin. It was assigned a 100% $p_{\rm BNS}$ by both our method and the low-latency GCN alert, in agreement with the PE result.

Results without MassGap category

Here we present the chirp-mass based probabilities of the 45 selected events to be consistent with a BNS, NSBH or BBH origin. In this case, we only compare these probabilities against the ones obtained using the PE samples. Results are presented in Table 4.3.

For events with $\mathcal{M} > 10\,{\rm M}_\odot$, there is no change with respect to the previous results: all were assigned a 100% $p_{\rm BBH}$ by our method and by PE analysis. Therefore, they are not shown in Table 4.3. For lower chirp mass binaries with a high PE probability of being BBH, with $\mathcal{M}$ between $7-9\,{\rm M}_\odot$, the previous probability of MG origin is transferred into the BBH region, thus the BBH probability now matches the PE results. For two events with a chirp mass consistent with MG, NSBH and BBH origin (GW190814 and GW190924_021846), their $p_{\rm MG}$ is assigned to the BBH probablity. For both events, our method continues to find NSBH as the most likely source class, followed closely by BBH. From the PE analysis GW190814 is still assigned a 100% probability of NSBH origin, and GW190924_021846 now has very high $p_{\rm BBH}$.

Regarding the three events inconsistent with BBH origin, but with some probability of being MG or NSBH, there are differences depending on whether they are consistent with BNS or not. For GW190426_152155, inconsistent with BNS origin, its MG probability is converted to BBH probability. For GW200105_162426 and GW200115_042309, that have some probability of

Event Name	Chirp-Mass Based			GWTC-2,-3 PE			
	BNS	NSBH	BBH	BNS	NSBH	BBH	$\mathcal{M}(M_\odot)$
GW190425	100	0	0	99.5	0	0	1.4
GW190426_152155	6.0	94.0	0	1.1	93.6	0	2.4
GW190707_093326	0	7.2	92.8	0	0	100	8.5
GW190720_000836	0	4.0	96.0	0	0	100	8.9
GW190728_064510 †	0	2.4	97.6	0	0	100	8.6
GW190814	0	51.7	48.3	0	100	0	6.1
GW190924_021846	0	55.7	44.3	0	3.9	96.1	5.8
GW190930_133541	0	13.7	86.3	0	<0.1	>99.9	8.5
GW191105_143521	0	12.2	87.8	0	<0.1	>99.9	7.8
GW191129_134029	0	28.1	71.9	0	0	100	7.3
GW191204_171526 †	0	4.2	95.8	0	0	100	8.6
GW191216_213338	0	0.6	99.4	0	0	100	8.3
GW200105_162426	0	85.0	15.0	0	99.3	0.7	3.4
GW200115_042309	7.0	93.0	0	0.7	98.9	0	2.4
GW200316_215756 †	0	2.6	97.4	0	<0.1	>99.9	8.8

Table 4.3: Source probabilities for O3 events without the MassGap category (in %). Only events with a probability of BBH less than 100% are shown. PyCBC Live distance estimates are available for all events, except the ones with a dagger (†), where GstLAL triggers and `BAYESTAR` distance estimates are used.

BNS origin, their p_{MG} is allocated to the NSBH class. Now, the three events are most likely NSBH according to both our method and the PE analysis.

The single event highly consistent with BNS origin, GW190425, is as before assigned $p_{\mathrm{BNS}} \simeq 100\%$ both by our method and by PE.

In general, the removal of the MassGap category results in our method being more consistent with the results from the PE analysis.

Effect of redshift correction

Lastly, we discuss how the correction to the chirp mass for the bias caused by the redshift affects the distribution of source probabilities. We compare the probabilities obtained using our chirp-mass based method with and without this correction for the selected 45 events of O3. Results are presented in Table 4.4, where only the events with $p_{\mathrm{BBH}} < 100\%$ are shown; the table also compares our redshift estimates to the PE values published in GWTC-2 and GWTC-3. In general, as ignoring the redshift bias overestimates the value of the chirp mass of the event, the probabilities are shifted towards the values that more massive systems would have. Also, the shifts in the assigned proba-

Event	Chirp-Mass Based				Chirp-Mass Based w/o z				z	
	BNS	MG	NSBH	BBH	BNS	MG	NSBH	BBH	Estimated	GWTC-2,-3
GW190425	100	0	0	0	94.5	5.5	0	0	0.03 ± 0.01	$0.03^{+0.01}_{-0.02}$
GW190426_152155	6.0	40.3	53.7	0	0.3	37.1	62.5	0	0.07 ± 0.02	$0.08^{+0.04}_{-0.03}$
GW190707_093326	0	46.2	7.2	46.6	0	32.6	0	67.4	0.17 ± 0.04	$0.16^{+0.07}_{-0.07}$
GW190720_000836	0	46.8	4	49.2	0	23.3	0	76.7	0.21 ± 0.05	$0.16^{+0.12}_{-0.06}$
GW190728_064510 †	0	47.2	2.4	50.4	0	29.0	0	71.0	0.16 ± 0.04	$0.18^{+0.05}_{-0.07}$
GW190814	0	31.4	51.7	16.9	0	33.4	45.9	20.7	0.06 ± 0.01	$0.05^{+0.009}_{-0.010}$
GW190924_021846	0	30.1	55.7	14.2	0	34.0	44.0	22.0	0.12 ± 0.03	$0.12^{+0.04}_{-0.04}$
GW190930_133541	0	44.0	13.7	42.3	0	31.1	0	68.9	0.23 ± 0.06	$0.15^{+0.06}_{-0.06}$
GW191105_143521	0	44.5	12.2	43.3	0	35.5	0	64.5	0.18 ± 0.05	$0.20^{+0.09}_{-0.09}$
GW191129_134029	0	39.3	28.1	32.6	0	46.9	4.9	48.2	0.16 ± 0.04	$0.16^{+0.05}_{-0.06}$
GW191204_171526 †	0	47.2	4.2	48.6	0	34.1	0	65.9	0.14 ± 0.03	$0.13^{+0.04}_{-0.05}$
GW191216_213338	0	47.5	0.6	51.9	0	38.1	0	61.9	0.08 ± 0.02	$0.16^{+0.12}_{-0.06}$
GW200105_162426	0	15.0	85.0	0	0	17.9	82.1	0	0.07 ± 0.02	$0.07^{+0.02}_{-0.03}$
GW200115_042309	7.0	40.8	52.2	0	1.1	37.7	61.2	0	0.07 ± 0.02	$0.06^{+0.03}_{-0.02}$
GW200316_215756 †	0	46.4	2.6	51.0	0	17.6	0	82.4	0.24 ± 0.06	$0.22^{+0.08}_{-0.08}$

Table 4.4: Source probabilities for O3 events, comparing the results with and without the redshift correction (in %). Only events with a probability of BBH less than 100% are shown. PyCBC Live distance estimates are available for all events, except the ones with a dagger (†), where GstLAL triggers are used. We also show our redshift estimates from search pipeline triggers, with a 1σ uncertainty estimate, and compare with the PE values (median and symmetric 90% interval).

bilities are of order $100\% \times z$. This comparison is done using the fit of Eq. (4.3) with $C_D = 0.749$ as obtained from O3a events. With the slightly smaller value $C_D = 0.576$, our estimated probabilities would be shifted slightly towards the values obtained without any redshift correction.

Although the detailed pattern of changes in probability including the MG class is complicated, we see that for instance for GW190425, omitting the redshift correction leads to a small but nonzero $p_{\rm MG}$. At the other extreme, for events with a source chirp mass between $7 - 9\,{\rm M}_\odot$, their $p_{\rm NSBH}$ falls to $\sim 0\%$, whereas their $p_{\rm BBH}$ grows significantly. While this result happens to lead to estimated probabilities close to PE, this outcome is due to an accidental combination of different biases.

We note that our estimated redshifts are almost all within the PE 90% range, thus we may expect to able to obtain an unbiased redshift estimate (albeit with possibly large statistical errors).

Name	PyCBC-broad				PyCBC-BBH		
	p_{BBH}	p_{NSBH}	p_{BNS}	p_{astro}	p_{BBH}	p_{NSBH}	p_{astro}
GW190707_093326	0.93	0.07	0.00	1.00	0.93	0.07	1.0
GW190720_000836	0.95	0.05	0.00	1.00	1.00	0.00	1.00
GW190725_174728	0.79	0.17	0.00	0.96	0.58	0.24	0.82
GW190728_064510	0.97	0.03	0.00	1.00	0.97	0.03	1.00
GW190814	0.54	0.46	0.00	1.00	...	...	...
GW190924_021846	0.44	0.56	0.00	1.00	0.44	0.56	1.00
GW190930_133541	0.93	0.07	0.00	1.00	0.85	0.15	1.00

Table 4.5: Source probabilities for the high significance GW candidates published in GWTC-2.1 for which either p_{BNS} or p_{NSBH} is greater than 1%. The bold-faced name indicate that the event was not previously reported in GWTC-2 [122]. Empty values indicate that the pipeline did not find the event with a FAR smaller than the threshold of 2 per day. This Table reproduces the results for both PyCBC offline analysis published on `TABLE III` of [7].

4.7 Deployment in production for LVK results

Although this method was not deployed in O3, in part due to the earlier than expected end of the run, it is now available for O4, running within the infrastructure of PyCBC Live. During the first half of the fourth observing run (O4a), the LVK collaboration observed a signal from the coalescence of two bodies with component masses consistent with NSBH origin, named GW230529_181500 [169]. The initial alert [170] contained the astrophysical probabilities estimated with our method, with $p_{\mathrm{NSBH}} = 0.62$, followed by $p_{\mathrm{BNS}} = 0.31$ and a probability of being of terrestrial origin $p_{\mathrm{terr}} = 0.07$.

4.7.1 Use on offline data

The method was also employed to estimate the astrophysical source probabilities p_{BNS}, p_{NSBH} and p_{BBH} for the candidate events found offline in O3 by the `PyCBC-broad` and `PyCBC-BBH` analysis. The difference between these analysis was discussed in Sec 3.2. These probabilities were scaled to the probability of the event to be of astrophysical origin, p_{astro}. They are published in the transient catalogues GWTC-2.1 [7] and GWTC-3 [8], for the confident CBC events with $p_{\mathrm{astro}} > 0.5$ and FAR less than certain threshold. The values published in GWTC-2.1 are reproduced in Table 4.5, whereas the probabilities of GWTC-3 are gathered in Table 4.6.

	PyCBC-broad				PyCBC-BBH		
Name	p_{BBH}	p_{NSBH}	p_{BNS}	p_{astro}	p_{BBH}	p_{NSBH}	p_{astro}
GW191118_212859	*<0.01*	*0.04*	*<0.01*	*0.05*	...	...	...
200121_031748	...	...	...	...	*<0.01*	*<0.01*	*<0.01*
GW200201_203549	*<0.01*	*<0.01*	*<0.01*	*<0.01*	...	...	...
GW200311_103121	*<0.01*	*<0.01*	*0.19*	*0.19*	...	...	...
GW191103_012549	0.67	0.10	<0.01	0.77	0.81	0.14	0.94
GW191105_143521	0.81	0.19	<0.01	>0.99	0.81	0.19	>0.99
GW191126_115259	*0.38*	*<0.01*	*<0.01*	*0.39*	0.69	0.01	0.70
GW191127_050227	*0.47*	*<0.01*	*<0.01*	*0.47*	0.74	<0.01	0.74
GW191129_134029	0.72	0.28	<0.01	>0.99	0.72	0.28	>0.99
GW191204_171526	0.98	0.02	<0.01	>0.99	0.98	0.02	>0.99
GW191216_213338	0.91	0.09	<0.01	>0.99	0.91	0.09	>0.99
GW191219_163120	0.20	0.63	<0.01	0.82	...	...	...
GW191222_033537	>0.99	<0.01	<0.01	>0.99	>0.99	<0.01	>0.99
GW200115_042309	<0.01	0.93	0.07	>0.99	...	...	...
GW200202_154313	...	...	...	...	0.67	0.33	>0.99
GW200210_092254	0.31	0.22	<0.01	0.53	0.31	0.23	0.54
GW200316_215756	0.98	<0.01	<0.01	0.98	0.95	0.03	0.98

Table 4.6: Source probabilities published in GWTC-3 for GW candidates with $p_{\mathrm{astro}} > 0.5$ and marginal candidates with FAR$<2.0\,\mathrm{yr}^{-1}$, for which either p_{BNS} or p_{NSBH} is non-zero. Results in italics represent events with $p_{\mathrm{astro}} < 0.5$, and mpty values indicate that the event was not found by the analysis. This Table reproduces the values on `TABLE XIII` of [8] for both PyCBC offline analysis.

4.8 Conclusions

In this chapter we present a new method to directly estimate CBC source distances and source classifications from the output of the PyCBC Live online search pipeline, while adding less than 50 ms of alert latency. These classifications are obtained using the template chirp mass point estimates of the search, correcting for the bias caused by cosmological redshift. We applied the method to confirmed GW events identified by LIGO-Virgo in low latency during O3, as well as to a large population of simulated astrophysical signals. For high and low chirp mass binary systems, classifications tend to be accurate, assigning high or very high probabilities to the correct class. On the other hand, for sources with intermediate chirp masses, the method always gives some probability to the correct category, but also significant nonzero probabilities to other categories. This behaviour is expected, due to systematic errors and statistical measurement uncertainty in the binary mass ratio, which our method does not completely account for. Estimates of source distances have a large statistical uncertainty, but we show that an unbiased estimate may be obtained at least for systems with chirp masses up to $40\,M_\odot$. For more massive systems, chirp masses and distances show a bias in recovery, possibly due to a limitation of the search template bank.

As noted above, extending the method to obtain more accurate classification probabilities will require information on the binary mass ratio. To obtain an unbiased estimate we will also need to account for component spins; thus, future extensions of this method will consider a higher dimensional parameter space, as done in [171]. This will be the starting point for the development of the fast parameter estimation method described in Chapter 5.

5

FOLLOW-UP OF GW CBCs II: FASTPE.
A FISHER APPROXIMATION SOURCE TRIGGER PARAMETER ESTIMATOR

5.1 Introduction

As discussed in the introductory section of the previous chapter, being able to provide an accurate source classification is essential for determining the priority of follow-up observations. However, the binary intrinsic parameters recovered by the search through matched-filtering the signal with a template bank, suffer from a large variety of biases. Therefore, the ability to perform rapid parameter estimation on candidate events is becoming a challenge for low-latency pipelines.

Detailed parameter estimation methods are based on stochastic sampling algorithms, that evaluate the likelihood at millions of points in the parameter space, making them computationally costly and therefore unsuitable for multi-messenger follow-up. This issue is particularly problematic for low-mass systems, as their gravitational waveforms are longer. Recently, there has been efforts to reduce the time of running of parameter estimation, via dimensionality reduction techniques [172], pre-computing certain components of the inference [173] or through massive parallelizations [174]. However, their computational time still exceeds the time frame of the LVK first alerts, which occur within the first 10 minutes after the merger.

In this chapter, we present the developing of `FASTPE`, a new algorithm for performing parameter estimation in very low-latency. This method utilizes the trigger event detected by the search as a starting point and estimates the uncertainties in the parameters across the different directions of the parameter space using a Fisher matrix approximation, keeping the running time around

1 minute.

5.2 Objectives

The objective of `FASTPE` is to determine the expected uncertainties in binary masses and spins from the distribution of the posterior probability samples, and to produce these posterior samples using the information provided by a CBC search immediately after detection. The development of this method has been conducted within the PyCBC Live pipeline, but it can easily be adapted to other online searches since the inputs to the method are common products of low-latency pipelines.

`FASTPE` uses the template point estimates of the trigger detected by the search as an approximation to the maximum likelihood (ML) point in the parameter space and measures the variations of the likelihood around that maximum point, a behaviour well characterized by the Fisher matrix. To do so, we generate a set of samples by placing random points in the parameter space of component masses and aligned spins. To speed up the calculation, we restrict the generated samples to be in a narrow contour of chirp mass centered in the trigger chirp mass value, since we expect the low-latency search to recover it with high accuracy for low-mass binaries. To explore the parameter space, we compute the distances between the samples and the ML point in the space of PN parameters using the Fisher-Matrix approximation [171]. In the higher-dimensional space of the PN expansion coefficients, the Fisher matrix is nearly constant, allowing for a single evaluation during the distances calculation. Then, we compute likelihood differences between the samples and the maximum likelihood point, and construct posterior probabilities for the intrinsic parameters of the binary via rejection sampling. The computational time of `FASTPE` is highly dependent on the number of initial samples. Nevertheless, it has show to achieve results compatible with more expensive parameter estimation methods in approximately 1 minute.

We will start by discussing the framework of parameter uncertainties, the Fisher matrix approximation and the space of PN parameters in the first section of the chapter. Then, we will describe the main features of the method in Sec. 5.4. A check with simulated signals is included in Sec 5.5. Finally, a comparison with parameter estimation samples from more detailed methods is presented in Sec. 5.6.

5.3 Theoretical framework

In this section, we describe the analytical approach we use to compute the likelihood differences that arise from deviating from the maximum likelihood point. These deviations are caused by both statistical errors and systematic biases; however, in this work, we do not try to address the latter, as they tend to be less dominant for relatively low SNR events, that are currently the majority of detections.

5.3.1 Uncertainties in parameter recovery

We start by quantifying the agreement of two waveforms $h(\theta)$ and $h(\hat{\theta})$, described by the same waveform model, but parametrized by two points close in the parameter space, θ and $\hat{\theta} = \theta - \Delta\theta$. We compute the waveform difference as

$$\left\|h(\theta) - h(\hat{\theta})\right\|^2 = \left\langle h(\theta) - h(\hat{\theta}) \middle| h(\theta) - h(\hat{\theta}) \right\rangle , \tag{5.1}$$

where $\langle \cdot | \cdot \rangle$ is the *inner product* of Eq. (2.29) and $\left\|h\right\|$ is the *norm* of a waveform h. We can expand the difference as

$$\begin{aligned} \left\langle h(\theta) - h(\hat{\theta}) \middle| h(\theta) - h(\hat{\theta}) \right\rangle &= \left\|h(\theta)\right\|^2 + \left\|h(\hat{\theta})\right\|^2 - 2\left\langle h((\theta) \middle| h(\hat{\theta}) \right\rangle \\ &= \rho_h^2 \left(1 + \frac{\left\|h(\hat{\theta})\right\|^2}{\rho_h^2} - 2\frac{\left\langle h(\theta) \middle| h(\hat{\theta}) \right\rangle}{\rho_h^2} \right) \\ &\approx 2\rho_h^2 (1 - M(\theta, \hat{\theta})) , \end{aligned} \tag{5.2}$$

where $M(\theta, \hat{\theta})$ is the *match* between the waveforms (see Eq. (2.52)), and we have approximated the waveform SNRs to be nearly equal $||h(\theta)|| \approx ||h(\hat{\theta})|| = \rho_h^2$. Writing this expression in terms of the *mismatch* $\bar{M} = 1 - M$ we obtain the approximate relation [175]

$$\bar{M}(\theta, \hat{\theta}) \approx \min_{\Delta t \Delta \phi} \frac{\left\|h(\theta) - h(\hat{\theta})\right\|^2}{2\rho_h^2} . \tag{5.3}$$

Here we made explicit the maximization of the match (and therefore minimization of the mismatch) over time and phase shifts between the two waveforms. With the mismatch as a tool to quantify the uncertainties (or "closeness") between two waveforms, we will study how the likelihood varies between two points close in the parameter space.

5.3.2 Likelihood uncertainties

We start by assuming that the point estimate found by the search corresponds to the waveform $h(\theta_{\rm ML})$ that maximizes the likelihood, namely, a maximum likelihood (ML) estimator $\theta_{\rm ML}$. The likelihood of a signal s with respect to this model is proportional to

$$\mathcal{L}(s|\theta_{\rm ML}) \propto \exp\left[-\frac{1}{2}\big\langle s - h(\theta_{\rm ML})\big|s - h(\theta_{\rm ML})\big\rangle\right] . \tag{5.4}$$

Now, we want to study how the likelihood varies across the parameter space when the waveform is parametrized with other set of coordinates $\hat{\theta}$ very close to the maximum likelihood point $\hat{\theta} = \theta_{\rm ML} - \Delta\theta$. We assume that the signal is given by $s = h(\hat{\theta})$ in absence of noise. The likelihood of $h(\hat{\theta})$ is then given by

$$\mathcal{L}(\hat{\theta}|\theta_{\rm ML}) = \mathcal{C} \cdot \exp\left[-\frac{1}{2}\big\langle h(\hat{\theta}) - h(\theta_{\rm ML})\big|h(\hat{\theta}) - h(\theta_{\rm ML})\big\rangle\right] , \tag{5.5}$$

where we made explicit the the proportionality constant on the likelihood $\mathcal{C}$, and the inner product is the waveform difference of Eq. (5.1). Introducing the approximation of the mismatch (5.3), we get

$$\mathcal{L}(\hat{\theta}|\theta_{\rm ML}) = \mathcal{C} \cdot \exp\left[-\rho_h^2 \bar{M}(\hat{\theta}, \theta_{\rm ML})\right] , \tag{5.6}$$

where ρ_h is the optimal SNR of $h(\theta_{\rm ML})$. If we evaluate this likelihood at the maximum point, $\hat{\theta} = \theta_{\rm ML}$, the mismatch is zero and

$$\mathcal{L}_{\rm max} = \mathcal{C} . \tag{5.7}$$

Then, the likelihood at a point $\hat{\theta}$ relative to the maximum likelihood $\mathcal{L}_{\rm max}$ is approximately

$$\Delta \ln \mathcal{L}(\hat{\theta}|\theta_{\rm ML}) = \ln \mathcal{L}(\hat{\theta}|\theta_{\rm ML}) - \ln \mathcal{L}_{\rm max} \approx -\rho_h^2 \bar{M}(\hat{\theta}, \theta_{\rm ML}) , \tag{5.8}$$

which is a function of the difference between the waveforms. We will compute these differences under a Fisher matrix linearization in the subsequent section.

5.3.3 Fisher Matrix approximation

In order to find a connection between waveform differences and the Fisher matrix, we start by expanding the waveform around the difference in parameters $\Delta\theta = \hat{\theta} - \theta_{\rm ML}$ as

$$h(\hat{\theta}) = h(\theta_{\rm ML} + \Delta\theta) \approx h(\theta_{\rm ML}) + \frac{\partial h(\theta_{\rm ML})}{\partial \theta_i}\Delta\theta_i + ... \tag{5.9}$$

Under the assumption of the linear signal approximation (LSA) [176], valid for high-SNR values, this expansion can be truncated at first-order in the partial derivatives. Then, the distance can also be linearized as

$$\begin{aligned} \left\| h(\hat{\theta}) - h(\theta_{\rm ML}) \right\|^2 &= \left\langle h(\hat{\theta}) - h(\theta_{\rm ML}) \middle| h(\hat{\theta}) - h(\theta_{\rm ML}) \right\rangle \\ &\approx \left\langle \frac{\partial h(\theta_{\rm ML})}{\partial \theta_i} \middle| \frac{\partial h(\theta_{\rm ML})}{\partial \theta_j} \right\rangle \Delta\theta_i \Delta\theta_j \,, \end{aligned} \tag{5.10}$$

where we can identify the Fisher matrix [176] as the metric of the parameter space

$$\Gamma_{ij} = \left\langle \frac{\partial h(\theta_{\rm ML})}{\partial \theta_i} \middle| \frac{\partial h(\theta_{\rm ML})}{\partial \theta_j} \right\rangle . \tag{5.11}$$

Then, the mismatch can be calculated as

$$\bar{M}(\hat{\theta}, \theta_{\rm ML}) \approx \frac{\Gamma_{ij}\Delta\theta_i\Delta\theta_j}{2\rho_h^2} \,, \tag{5.12}$$

and the likelihood difference of Eq. (5.8) becomes Gaussian

$$\Delta \ln \mathcal{L}(\hat{\theta}|\theta_{\rm ML}) \approx -\frac{1}{2}\,\Gamma_{ij}\Delta\theta_i\Delta\theta_j \,. \tag{5.13}$$

The Fisher matrix is a suitable tool to compute parameter estimation, since its eigenvectors and eigenvalues give, respectively, the principal directions and the accuracy of the measurement in those directions. However, it is not trivial to compute in a parameter space of masses and spins, given the existing correlations between these parameters. To overcome this problem, we will compute the waveform differences in a higher-dimensional parameter space where the Fisher matrix becomes almost flat: the space of PN expansion coefficients. We will follow the methodology given in [177].

5.3.4 Post-Newtonian parameters

For low-mass binaries, their waveforms are dominated by the inspiral stage and, therefore, are well approximated by a PN expansion. Since the data analysis for GW is typically described in the frequency domain, we will use the TaylorF2 PN approximant described in Sec. 2.1.2, with

$$\tilde{h}(f) = \mathcal{A}\left(\frac{f}{f_0}\right)^{-7/6} e^{i\Psi_{\rm PN}(f)}\,, \tag{5.14}$$

where we have introduced a reference frequency f_0 to make the coefficients in the expansion dimensionless (similarly to v/c). The choice of this frequency does not affect the likelihood differences and we have set it to $f_0 = 20\,\text{Hz}$ in this work. Since we are working in the restricted waveform approximation (see Sec. 2.1.2), the amplitude $\mathcal{A}$ is a normalization factor for the waveform to have a certain optimal SNR $\left\|\tilde{h}\right\| = \rho_{\tilde{h}}^2$. The phase $\Psi_{\rm PN}(f)$ can be expanded within the PN formalism as

$$\Psi_{\rm PN}(f) = \sum_{k=0}^{N}\left(\frac{f}{f_0}\right)^{k-5/3}\left[\psi_k + \psi_k^{\log}\log\left(f/f_0\right)\right]\,. \tag{5.15}$$

The *PN coefficients* of the expansion ψ_k and $\psi_k^{\log}$ contain non-spinning contributions up to 3.5PN (Eq. (3.18) of [49]), spin-orbit (SO) effects at 1.5PN, 2.5PN, 3PN (tail-induced term) and 3.5PN orders (Eq. (3.17) of [178]), and spin-squared corrections (spin-spin (SS), self-interaction spin and quadrupolar monopole) at 2PN and 3PN orders (Eq. (6.24) of [179] and Eq. (9) of [180]).

These coefficients are of special interest, because we can re-parametrize the parameter space in terms of these parameters, that are independent from each other in the higher-dimensional space of coordinates

$$\lambda_m = \{\psi_k\}\bigcup\{\psi_k^{\log}\}\,. \tag{5.16}$$

A large number of these parameters are zero in the framework of GR. The 10 remaining parameters are

$$\lambda_m = \{\psi_0, \psi_2, ..., \psi_8, \psi_5^{\log}, \psi_6^{\log}\}\,, \quad \text{with} \quad m = 0, ..., 10\,. \tag{5.17}$$

Among these parameters, two are particularly worth discussing. The coefficient ψ_5 corresponds to the coalescence phase, while ψ_8 represents the coalescence

time. Specifically, they correspond to the terms

$$\begin{aligned}\psi_5 &= -\frac{\pi}{4} - 2\phi_c\,,\\ \psi_8 &= 2\pi f t_c\,,\end{aligned} \tag{5.18}$$

of the TaylorF2 phasing of Eq. (2.11). When computing waveform differences, we will project both parameters out of the Fisher matrix.

The metric in this parameter space is given by an nearly-flat Γ_{ij}, i.e. a Fisher matrix almost independent of the parameters. This makes the assumption of high-SNR for the calculation of the distance much more accurate for larger parameter variations, as well as an approach computationally convenient to compute waveform differences.

In this re-parametrization, the Fisher matrix is given by

$$\Gamma_{ij} = \left\langle \frac{\partial\tilde{h}}{\partial\lambda_i} \middle| \frac{\partial\tilde{h}}{\partial\lambda_j} \right\rangle , \tag{5.19}$$

which is the inner product of Eq. (2.29) of

$$\frac{\partial\tilde{h}}{\partial\lambda_i} = i\mathcal{A}\left(\frac{f}{f_0}\right)^{-7/6} \frac{\partial\Psi_{\rm PN}}{\partial\lambda_i} e^{i\Psi_{\rm PN}}\,, \tag{5.20}$$

resulting in

$$\Gamma_{ij} = 4\,|\mathcal{A}|^2 {\rm Re}\int_{f_{\rm min}}^{f_{\rm max}} \left(\frac{f}{f_0}\right)^{-7/3} \frac{\Psi_i^*\Psi_j}{S_n(f)} df\,, \tag{5.21}$$

with $\Psi_i = \partial\Psi_{\rm PN}/\partial\lambda_i$. The derivatives of the phase with respect to the independent PN coefficients are [181]

$$\begin{aligned}\Psi_k &= \frac{\partial\Psi_{\rm PN}}{\partial\psi_k} = \left(\frac{f}{f_0}\right)^{(k-5)/3}\,,\\ \Psi_k^{\log} &= \frac{\partial\Psi_{\rm PN}}{\partial\psi_k^{\log}} = \left(\frac{f}{f_0}\right)^{(k-5)/3} \log(f/f_0)\,.\end{aligned} \tag{5.22}$$

The result is a 10×10 matrix of the form

$$\Gamma_{ij} = \left(\begin{array}{c|c} \begin{array}{c} \Psi^*_{k(i)}\Psi_{k(j)} \\ (8\times 8) \end{array} & \begin{array}{c} \Psi^*_{k(i)}\Psi^{\log}_{k(j)} \\ (8\times 2) \end{array} \\ \hline \begin{array}{c} \Psi^{\log *}_{k(i)}\Psi_{k(j)} \\ (2\times 8) \end{array} & \begin{array}{c} \Psi^{\log *}_{k(i)}\Psi^{\log}_{k(j)} \\ (2\times 2) \end{array} \end{array} \right) , \tag{5.23}$$

where $k(i), k(j) = 0, 2, ..., 8$ for $i, j = 0, ..., 7$, corresponding to the linear terms Ψ_k, and $k(i), k(j) = 5, 6$ for $i, j = 8, 9$, place of the logarithmic terms $\Psi^{\log}_k$. We can express this matrix in the general form given in [171] as

$$\Gamma_{ij} = 4\,|\mathcal{A}|^2 I^{\delta}_{\kappa}\,, \tag{5.24}$$

with

$$I^{\delta}_{\kappa} = \int_{f_{\min}}^{f_{\max}} \left(\frac{f}{f_0}\right)^{\kappa} \frac{\log^{\delta}(f/f_0)}{S_n(f)} df\,. \tag{5.25}$$

Here, the exponents κ and δ are functions of the indices of the Fisher matrix i and j:

- δ accounts for the number of logarithmic coefficients in $\Psi^*_i\Psi_j$. Therefore, it is restricted to $\delta = \{0, 1, 2\}$.
- κ depends on the PN order of the coefficients. With the correspondence $i \to k(i)$ of (5.23), it is given by $\kappa = [k(i) + k(j) - 17]/3$.

The frequency limits in the integral are given by the lower cutoff frequency of the search, which we take to be $f_{\min} = 20\,\text{Hz}$ [8], and an upper frequency cutoff. We chose the f_{ISCO} of Eq. (1.61) as the upper frequency cutoff, hence maintaining a small dependence on the total mass of the system.

The Fisher matrix of Eq. (5.24) is not normalized, and should be regarded as the Fisher matrix for the SNR ρ_h of the waveform $\tilde{h}$ of Eq. (5.14). To extract the dependence on the SNR we require $\left\|\tilde{h}\right\| = \rho_h^2$, giving an amplitude factor of

$$|\mathcal{A}|^2 = \frac{\rho_h^2}{4\, I^0_{-7/3}}\,. \tag{5.26}$$

Therefore, we can express the Fisher matrix as

$$\Gamma_{ij} = \rho_h^2 \hat{\Gamma}_{ij} \,, \tag{5.27}$$

where $\hat{\Gamma}_{ij}$ is a normalized Fisher matrix for the SNR of 1 given by

$$\hat{\Gamma}_{ij} = \frac{I^{\delta}_{\kappa}}{I^{0}_{-7/3}} \,. \tag{5.28}$$

With this mathematical toolkit, we now describe the main features of `FASTPE`, following the flow of the algorithm from the trigger point of the search until the computation of the posterior samples.

5.4 Methodology

The `FASTPE` algorithm take as inputs the template intrinsic parameters of masses and aligned spins, the SNR and the estimated PSD for each detector present, and a number N of initial samples. We will first describe the application of the method to the data of one detector, and we will give an extension to the multiple detector case later in Section 5.4.4. To illustrate the method, we will apply the different steps to the PyCBC Live SNR-optimized trigger of GW200115 [167], a gravitational wave event consistent with NSBH origin, with component masses $5.7^{+1.8}_{-2.1}\,\mathrm{M}_{\odot}$ and $1.5^{+0.7}_{-0.3}\,\mathrm{M}_{\odot}$.

5.4.1 Generation of points in the parameter space

To explore the parameter space of masses and spins, we generate an initial set of random points $\hat{\theta} = (m_1, m_2, s_{1z}, s_{2z})$ to which we refer as *samples*. We sample masses and spins in two different ways.

Masses

As already discussed, the chirp mass is the combination of parameters measured with best accuracy by low-latency pipelines for low-mass events. Then, as for the source classification method, we restrict the masses to be near the point estimate chirp mass given by the search, in a contour defined by an uncertainty $\Delta\mathcal{M}$. In the Newtonian approximation, the relation between the chirp mass and its uncertainty grows as $\Delta(\ln M) \propto \mathcal{M}^{5/3}$ for a fixed SNR [139]. This motivates the search for an estimation of the relationship $\Delta\mathcal{M} = f(\mathcal{M})$. To relate these quantities, we use the *chirp time* variable [72], that is a function

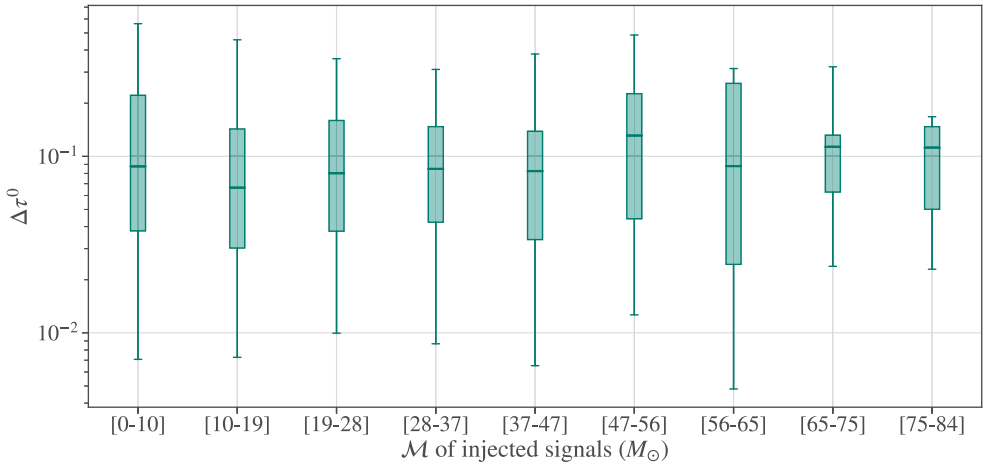

Figure 5.1: Distribution of the uncertainty in chirp time, $\Delta\tau_0$, for different intervals of chirp mass $\mathcal{M}$. We show median values, and 50% (box), 90% (whiskers) credible intervals.

of the chirp mass as

$$\tau_0 = A_0 \mathcal{M}^{-5/3}\,, \tag{5.29}$$

where A_0 is a constant given by

$$A_0 = \frac{5}{256(\pi f_{\rm low})^{8/3}}\,, \tag{5.30}$$

only dependent on the lower cut-off frequency $f_{\rm low}$. As a default value, we follow the setting of $f_{\rm low}$ to 20 Hz from the parameter estimation results of GWTC-3 [8]. Using a set of simulated astrophysical signals (described in Section 4.5), we studied the uncertainty in chirp time $\Delta\tau_0$ for different intervals of chirp mass. The result from this analysis is presented in Fig. 5.1. It can be seen from the figure that the accuracy of the chirp time is fairly constant during all the range of chirp masses studied, and that falls below 1 s. To keep a conservative limit, we choose a constant chirp time window of $\Delta\tau_0$=2 s. With this constant window, we define a $\tau_0^{\rm max} = \tau_0 + \Delta\tau_0$ and a $\tau_0^{\rm min} = \tau_0 - \Delta\tau_0$, that are then translated to their corresponding limits on chirp mass using the relation on (5.29). Note that a minimum in chirp time corresponds to a maximum in chirp mass, so to prevent chirp masses to go infinitely high we set a sanity boundary on 200 $\mathrm{M}_\odot$. Then, chirp mass values are sampled uniformly between the estimated limits. The other mass quantity we sample on is the

mass ratio q. We bound the lower limit in mass ratio as

$$q^{\min} = \frac{m_2^{\min}}{m_1^{\max}}\,, \tag{5.31}$$

where $m_2^{\min}$ and $m_1^{\min}$ are the limits on masses defined by the intersection of the permitted chirp mass region, and the forbidden boundaries of the parameter space $m_i < 1\,\mathrm{M}_\odot$, $m_i > 60\,\mathrm{M}_\odot$. We sample uniformly between $q^{\min}$ and 1. Therefore, our prior will be uniform in ($\mathcal{M}$, q) instead of (m_1, m_2), and we will have to address this difference by a transformation of coordinates when we evaluate the likelihood.

Another possible parametrization would be by means of the symmetric mass ratio, but the Jacobian of the transformation of coordinates $(\mathcal{M}, \eta) \longrightarrow (m_1, m_2)$ diverges at $m_1 = m_2$.

Spins

We generate samples uniform in spin magnitudes $a_i = |\vec{S}_i|/m_i^2$ and isotropic in spin orientations θ_i. Since up to date neutron starts have shown very small values of spin magnitudes, we define some limits in spin values depending on the chirp mass. We set two $\mathcal{M}(m_1, m_2)$ limits, that are $\mathcal{M}_{\mathrm{BNS}} = \mathcal{M}(3, 1) \approx 1.465\,\mathrm{M}_\odot$ and $\mathcal{M}_{\mathrm{NSBH}} = \mathcal{M}(3, 3) \approx 2.612\,\mathrm{M}_\odot$. If the higher limit of the chirp mass contour is smaller than $\mathcal{M}_{\mathrm{BNS}}$, both spin magnitudes are bounded to $a_1, a_2 < 0.4$. If it is between both limits, only the spin for the secondary mass is constricted to $a_2 < 0.4$. In all the other cases, the maximum magnitude for the spins is $a_i < 0.998$. An option to change the configuration to aligned spins is also included in the code.

5.4.2 Estimation of mismatches

We estimate the mismatches between the generated samples and the maximum likelihood point given by the search with the approximate relation of Eq. (5.12). To do so, we compute the normalized Fisher matrix of Eq. 5.28 by evaluating the integral of Eq. (5.25) for each element of the matrix and dividing it by $I^0_{-7/3}$. Then, as mentioned in Sec. 5.3.4, we project the PN parameters corresponding to the coalescence phase (ψ_5) and coalescence time (ψ_8) out of the Fisher matrix following [171]

$$\tilde{\Gamma}_{ij} = \hat{\Gamma}_{ij} - \sum_{a,b} \hat{\Gamma}_{ia} \gamma^{ab} \hat{\Gamma}_{bj}\,, \tag{5.32}$$

where $a, b = 4, 7$ are the indices of ψ_5 and ψ_8 in the Fisher matrix, and γ is the inverse of the two-dimensional submatrix given by

$$\gamma = \begin{pmatrix} \hat{\Gamma}_{44} & \hat{\Gamma}_{47} \\ \hat{\Gamma}_{74} & \hat{\Gamma}_{77} \end{pmatrix}^{-1} . \tag{5.33}$$

Since the Fisher matrix is independent of the parameters of the generated samples, it needs to be computed only once during the mismatches calculation. After this, we divide the Fisher matrix by a *fudge-factor* F squared, that we will discuss in Sec. 5.5.1, resulting in an effective Fisher matrix

$$\bar{\Gamma}_{ij} = \frac{\tilde{\Gamma}_{ij}}{F^2} . \tag{5.34}$$

We then convert the physical coordinates of the trigger point and the samples to vectors of PN coefficients $\{\theta_i\} \to \{\lambda_i\}$. To do so, we use a function in the `LALSimInspiralTaylor` module of `LALSimulation` [182]. After this, we can finally compute the differences between the samples and the ML point in the space of PN coefficients, and multiply them with the effective Fisher matrix of Eq. (5.34) as

$$\bar{M}(\hat{\theta}, \theta_{\rm ML}) = \bar{M}(\hat{\lambda}, \lambda_{\rm ML}) = \frac{1}{2} \bar{\Gamma}_{ij} \Delta\lambda_i \Delta\lambda_j . \tag{5.35}$$

For GW200115, we obtained the mismatches presented in Fig. 5.2. In these figures, the correlations between intrinsic parameters can be appreciated.

5.4.3 Likelihood and posterior

To obtain a collection of posterior samples, we calculate approximate likelihood ratios with the mismatches of Eq. (5.35) as

$$\Delta \ln \mathcal{L} \approx -\rho^2 \bar{M}(\hat{\theta}, \theta_{\rm ML}) , \tag{5.36}$$

where ρ^2 is the matched-filter SNR of the signal at the detector.

Change of priors via re-weighting

Since the sampling of points in the parameter space was performed assuming a uniform prior over chirp mass and mass ratio $\pi(\mathcal{M}, q)$, the estimated likelihood and hence the estimated posterior are uniform over these variables. However, we want the posterior to be uniform in component masses, as those are the physical parameters of interest. Because both sets of coordinates are

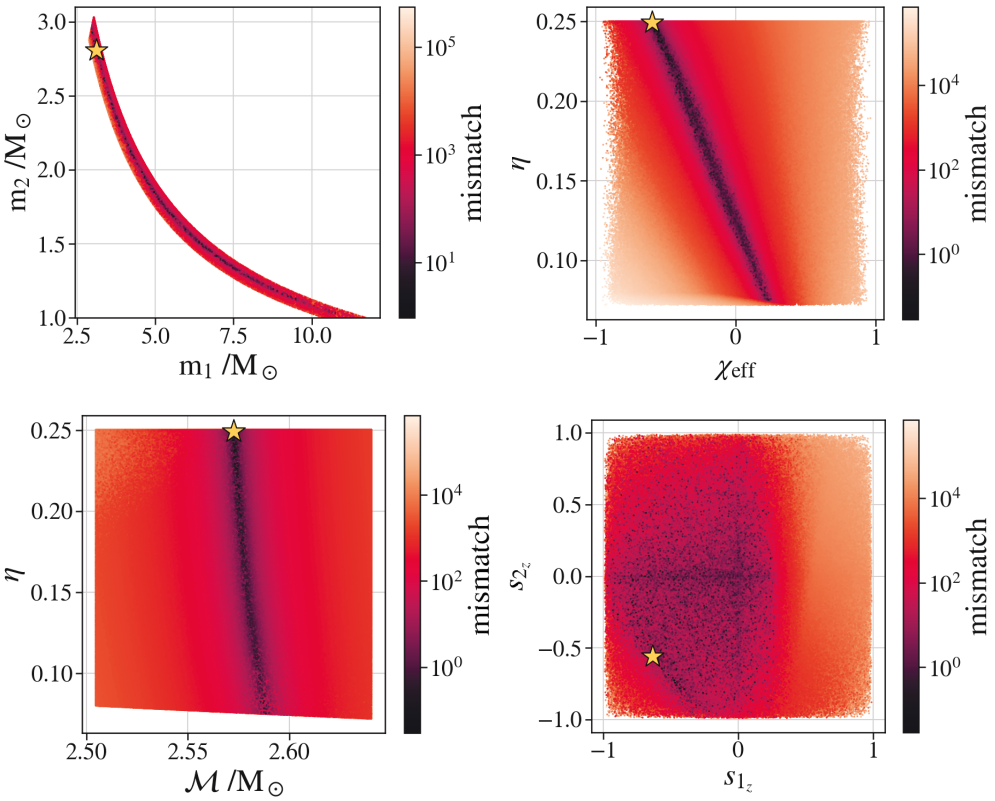

Figure 5.2: Representation of the mismatches calculated for GW200115. The mismatch represents the closeness of the points in parameter space, with a smaller mismatch representing more agreement. The yellow star points at the template point estimate, which falls in the regions of smallest mismatch.

parametrizations of the same space, the estimated posterior $p_{\mathcal{M},q}(\theta|d)$ can be used to calculate the desired posterior $p_{m_1,m_2}(\theta|d)$ as

$$p_{m_1,m_2}(\theta|d) = \frac{\pi(m_1,m_2)}{\pi(\mathcal{M},q)} p_{\mathcal{M},q}(\theta|d)\,. \tag{5.37}$$

The priors are related through the Jacobian of the transformation of coordinates $\mathcal{J}$ [183] as

$$\pi(\mathcal{M},q) = \mathcal{J}\cdot p(m_1,m_2)\,, \tag{5.38}$$

where the Jacobian is given by

$$\mathcal{J} = \det \begin{vmatrix} \frac{\partial m1}{\partial \mathcal{M}} & \frac{\partial m_1}{\partial q} \\ \frac{\partial m_2}{\partial \mathcal{M}} & \frac{\partial m_2}{\partial q} \end{vmatrix} = \frac{m_1^2}{\mathcal{M}}\,. \tag{5.39}$$

For each sample in parameter space S, the relative posterior probability density against the maximum likelihood (ML) point is then calculated as

$$\frac{p(\hat{\theta}_{\rm S}|d)}{p(\theta_{\rm ML}|d)} = \frac{\mathcal{L}(d|\hat{\theta}_{\rm S})\left(\frac{m_1^2}{\mathcal{M}}\right)_{\rm S}}{\mathcal{L}_{\rm max}\left(\frac{m_1^2}{\mathcal{M}}\right)_{\rm ML}} = \frac{\mathcal{L}(d|\hat{\theta}_{\rm S})\cdot\mathcal{J}_{\rm S}}{\mathcal{L}_{\rm max}\cdot\mathcal{J}_{\rm ML}}\,. \tag{5.40}$$

Rejection sampling

As it can be seen in Fig. 5.2, after calculating the mismatches each point in parameter space is assigned a probability with respect to the trigger point, related with the relative likelihood as in (5.36). We now apply a rejection sampling that preferentially keeps samples with a posterior PDF value close to the maximum. Our rejection sampling statistic is an array of random numbers distributed uniformly between 0 and 1. To be able to apply it to our data, we need to divide our relative posterior by its maximum value, in order to have a uniform distribution between 0 and 1 to evaluate. We then keep the samples where the posterior divided by its maximum is greater than the rejection sampling random value.

5.4.4 Multiple detector case

Up to this point, we have only discussed the methodology for the data of a single detector. However, `FASTPE` can be applied in the multiple detector case as follows. Since the data in each detector is independent from the others, it

is possible to compute a joint likelihood for a network of N detectors as

$$\mathcal{L}^{\rm net} = \prod_{n}^{N} \mathcal{L}_n \,, \tag{5.41}$$

which transforms to a sum for the logarithmic likelihood of Eq. (5.36). Therefore, we can compute the relative likelihood of the samples as

$$\Delta \ln \mathcal{L}^{\rm net} = -\frac{1}{2} \bar{\Gamma}^{\rm net}_{ij} \Delta\lambda_i \Delta\lambda_j \,, \tag{5.42}$$

by constructing a *joint* Fisher matrix $\bar{\Gamma}^{\rm net}_{ij}$ summing the individual Fisher matrices weighted by the square of the SNR of the signal at the corresponding detector

$$\bar{\Gamma}^{\rm net}_{ij} = \sum_{n}^{N} \rho_n^2 \bar{\Gamma}^{n}_{ij} \,. \tag{5.43}$$

5.5 Check against simulated signals

In order to check the accuracy of `FASTPE` , we ran it with the set of simulated injections described in Sec. 4.5. Before running the method, we apply thresholds in the chirp mass, the SNR and the FAR, to omit events outside of the limits of validity of the method. We restrict the masses to have a maximum chirp mass of an unequal NSBH with $m_1 = 30\,\mathrm{M}_\odot$ and $m_2 = 3\,\mathrm{M}_\odot$, giving a threshold of $\mathcal{M} < 7.4\,\mathrm{M}_\odot$. We require a minimum network SNR of 10, and a minimum FAR corresponding to the alert threshold: FAR < 2/day.

5.5.1 Fudge-factor

Before discussing the application of the method on the set of injections, we now address the decision to add a fudge-factor F in the calculation of the Fisher matrix of Eq. (5.34). While evaluating a preliminary study on the set of simulated signals, we noticed a bias in the method: it was underestimating the errors. This can be explained by the fact that for calculating our approximate likelihood we are not considering the presence of noise. We introduced the said fudge-factor as a way to reduce the SNR and allow the parameters to have more coverage. A F=2 has shown to mitigate this bias, while allowing more percentage of the initial samples to be kept on the posterior. This value is used for all subsequent results. A histogram of the remaining samples for two different values of F, where this effect is visible, is presented in Fig. 5.3.

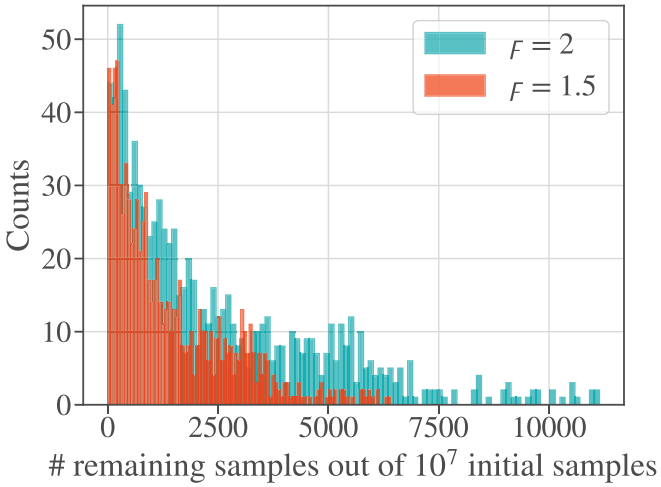

Figure 5.3: Number of remaining samples that pass the rejection sampling out of $N = 10^7$ initial samples.

5.5.2 Evaluation of computing time

Using the entire set of simulated signals (after applying the threshold), we recorded the computing time that took for each injection to pass through the `FASTPE` algorithm. This is presented as a histogram in the Figure 5.4. It shows a quasi-gaussian distribution centered around 1 minute for 10^7 initial samples. While the computing time of the algorithm is highly dependent on the number of initial samples generated, this represents a good agreement between being able to construct posteriors with a decent amount of final samples, and the latency added to the pipeline.

5.5.3 Self-consistency of the method

To test the self-consistency of `FASTPE` and look for the presence of biases in the method, we performed a percentile-percentile-plot (pp-plot) test. It is constructed for each parameter by counting the number of final samples that lay below the value of the true (injected) parameter, and converting them to a percentile of probability. In case of absent bias, the histogram is expected to follow the diagonal line. This means, that for a consistent analysis a p% of the injections should have a p% of samples below their true values. Now we address how to apply it to our distribution of injected signals.

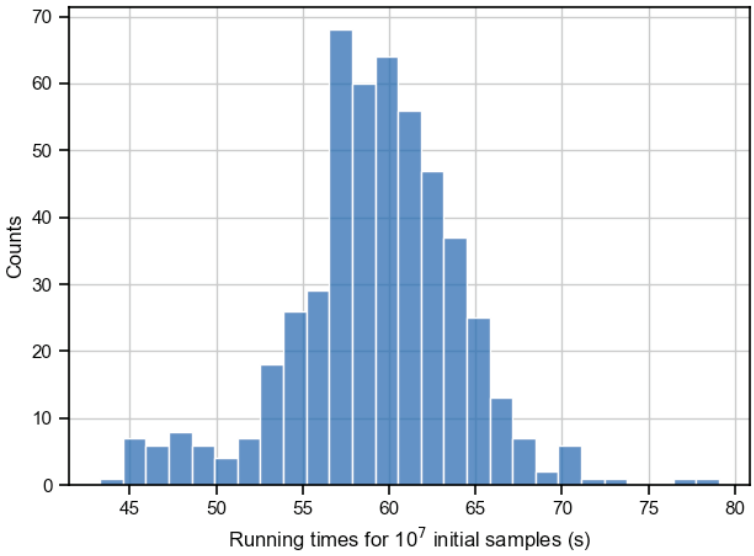

Figure 5.4: Histogram distribution of computing time for 10^7 initial samples.

With the thresholds previously described applied, the distribution of the signals in the plane of component masses presents density changes between the injections corresponding to the different astrophysical categories, as can be seen in Fig. 5.5. By splitting the set of signals into the different categories, the only category presenting a uniform distribution of signals is BNS. Since we want to find the possible biases present in the method, and `FASTPE` assumes a uniform prior in the component masses, the non-uniform distribution of simulated signals for NSBH and BBH are not suitable for this analysis, since we cannot distinguish between a bias in the method or in the prior. The BNS population presented an additional source of bias: the templates were generated with different approximants for injections with total mass smaller than $4\,\mathrm{M}_\odot$ and greater than $4\,\mathrm{M}_\odot$. Therefore, at the moment, we restrict the analysis to the BNS population of simulated signals, with $\mathrm{M} < 4\,\mathrm{M}_\odot$. The spins of these injections are aligned or anti-aligned, with magnitudes $a_i \leq 0.05$. After choosing this population of signals, we ran `FASTPE` and present the resulting pp-plots in Fig. 5.6. We notice that all mass and spin parameters show a good match with the diagonal line, except for the chirp mass, that appears symmetrically biased with respect to the 0.5 percentile. This deviation might be explained giving that the allowed range of chirp mass is very narrow, and the pp-plots only show relative errors. Hence, a small deviation in the chirp

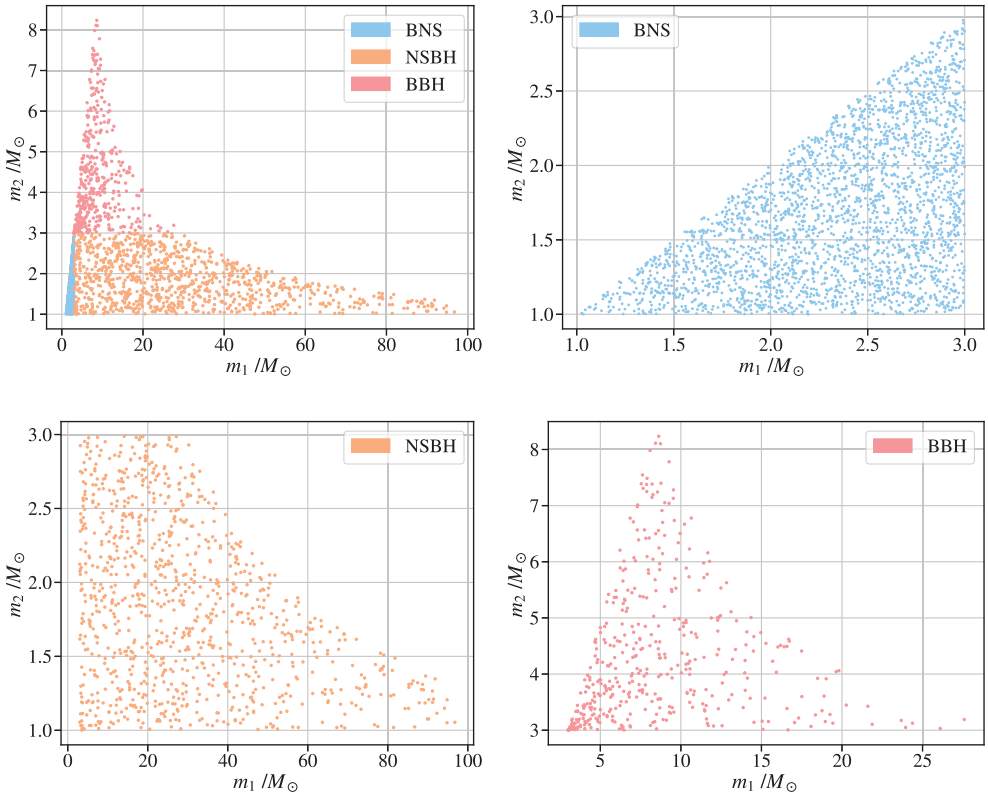

Figure 5.5: Distribution of the set of simulated signals employed for checking the biases present in `FASTPE`. The top-left figure represents the distribution of the set with the condition $\mathcal{M} < 7.4\,\mathrm{M}_\odot$. The other three figures depict the density distribution of signals in each of the three astrophysical categories.

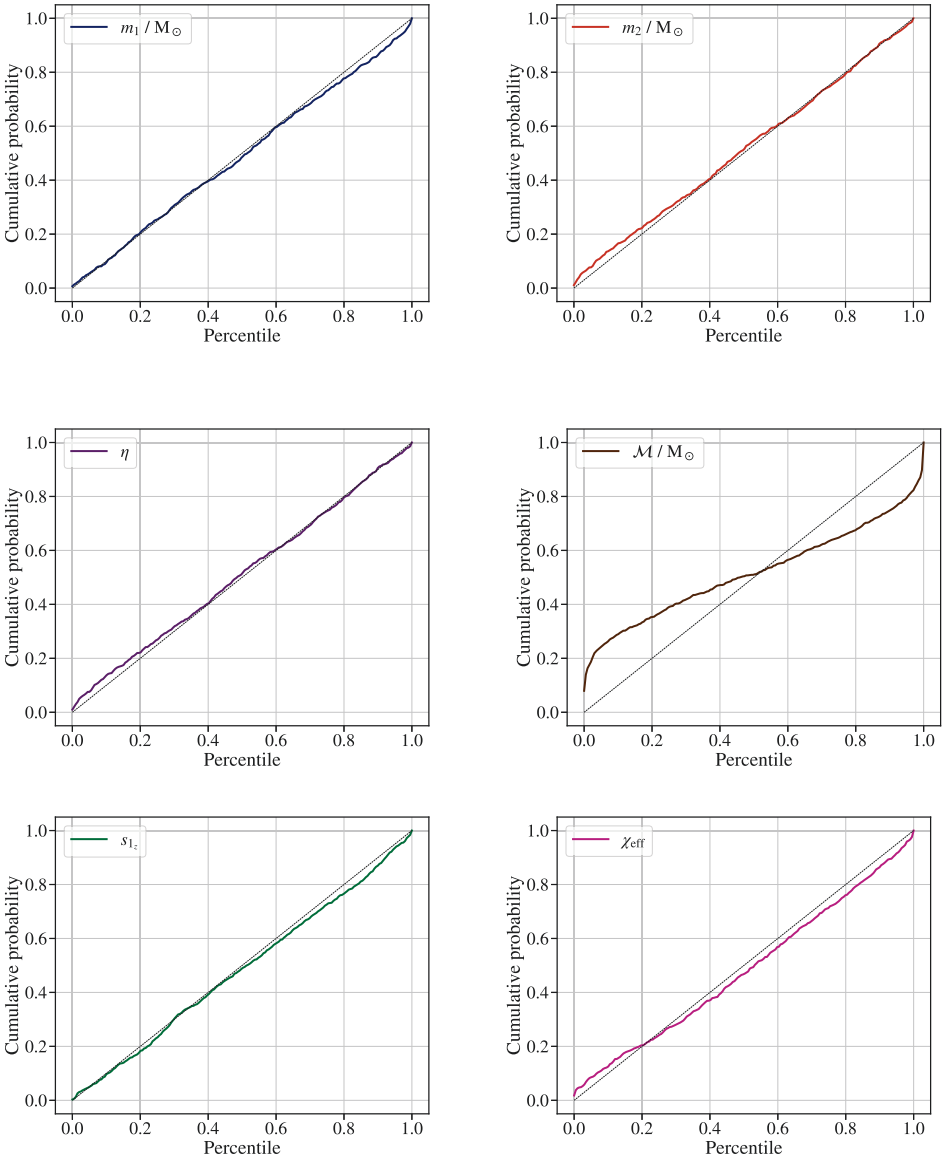

Figure 5.6: pp-plots distributions for different mass and spin parameters.

mass value could cause a large deviation in the relative difference with respect to the real value of the chirp mass.

While this result shows a good result of the accuracy of the method, it has to be further tested against NSBH and BBH signals.

5.6 Comparison with GW catalog events

In this section, we present a comparison between the results yielded by `FASTPE` against the PE posterior samples published in the different data releases of the catalogs GWTC-1 [184], GWTC-2 [157], GWTC-2.1 [185] and GWTC-3 [186]. The events selected are low-mass events, with a source-frame chirp mass $\mathcal{M} < 7.4\,\mathrm{M}_{\odot}$.

For the `FASTPE` results we used the trigger point estimates, the matched-filter SNRs and the estimated PSDs of the online triggers of the events, available in `GraceDB`. The ranking for picking a particular trigger was: 1) PyCBC Live with SNR-optimization; 2) Preferred event, independently of the pipeline. This shows the adaptability of the algorithm to other online pipelines. Since at the moment `FASTPE` does not take into account the effect of cosmological redshift on the masses, all the results in this section are given in the reference frame of the detector. Events are ordered by their detector-frame chirp masses.

We compare the posterior distributions of component masses $(m_1 - m_2)$ and aligned spins $(s_{1_z} - s_{2_z})$, symmetric mass ratio, chirp mass and effective spin $(\mathcal{M} - \eta,\ \chi_{\mathrm{eff}} - \eta)$. We present a figure for each pair of parameters, with a central panel showing the two-dimensional joint posteriors and two side panels showing the one-dimensional posterior distributions of the individual parameters. Central two-dimensional contours represent 90% credible regions, whereas side dashed lines indicate 90% credible intervals.

The PE samples released along the catalogs usually contain more than one dataset, depending on the waveform approximant and the prior on the spins employed. Since `FASTPE` shows a dependency with the chosen prior, we match the spin limits to the ones of the dataset they are being compared with. A detailed description is given for each event.

GW170817

This event was published in GWTC-1, with $\mathcal{M} = 1.198\,\mathrm{M}_\odot$. Online data was highly corrupted due to the presence of a huge glitch in Livingston. Hence, we preferred to use the PyCBC trigger uploaded after a preliminary analysis to remove it, with $\mathcal{M} = 1.198\,\mathrm{M}_\odot$ and $\rho_{\mathrm{net}} = 28.9$. PE samples were made with two different configurations of spins: HighSpin $a_i < 0.89$ and LowSpin $a_i < 0.05$. `FASTPE` priors are set to these values for both configurations.

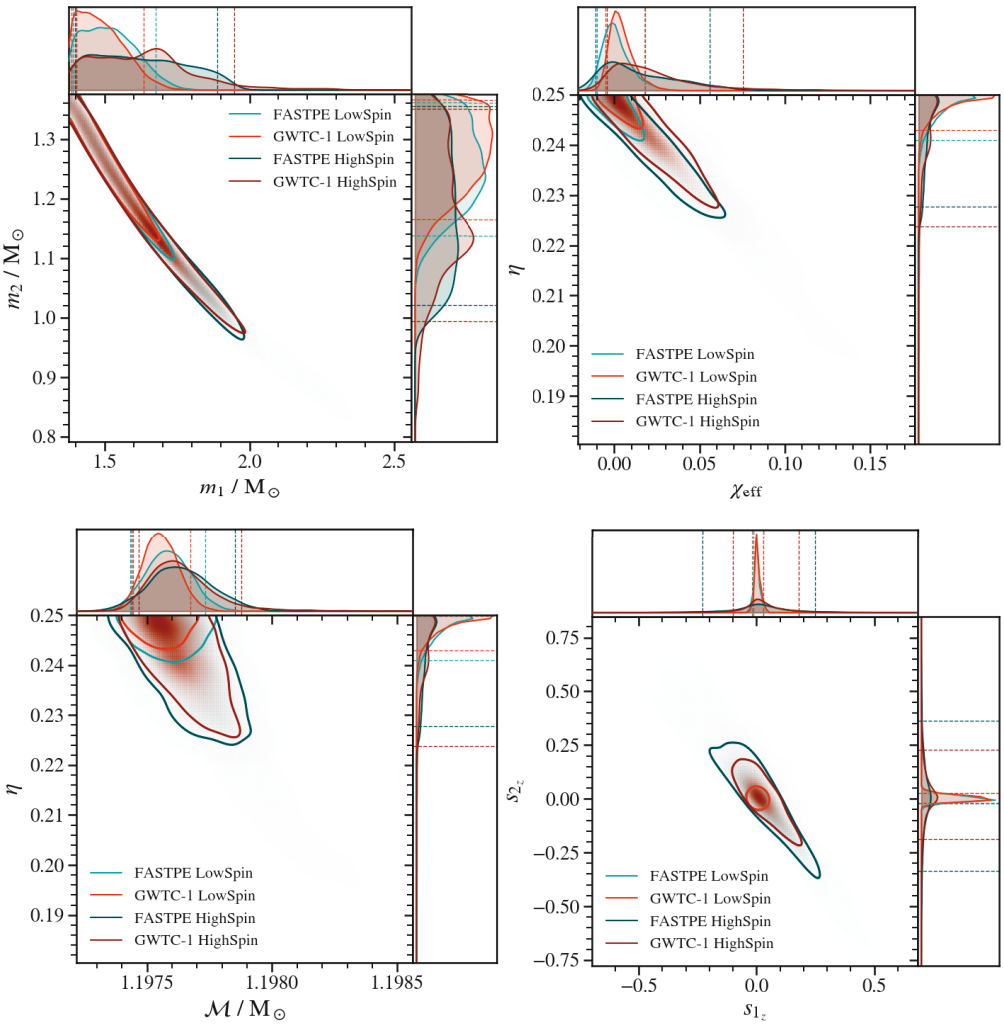

Figure 5.7: Comparison between `FASTPE` and catalog PE samples for the event GW170817.

GW190425

GW190425 is published in GWTC-2.1, with $\mathcal{M} = 1.48\,\mathrm{M}_\odot$. For `FASTPE` we used GstLAL preferred event, with $\mathcal{M} = 1.49\,\mathrm{M}_\odot$ and $\rho_{\mathrm{net}} = 13.1$. Available PE samples present two different configurations of spins: HighSpin $a_i < 0.89$ and LowSpin $a_i < 0.05$.

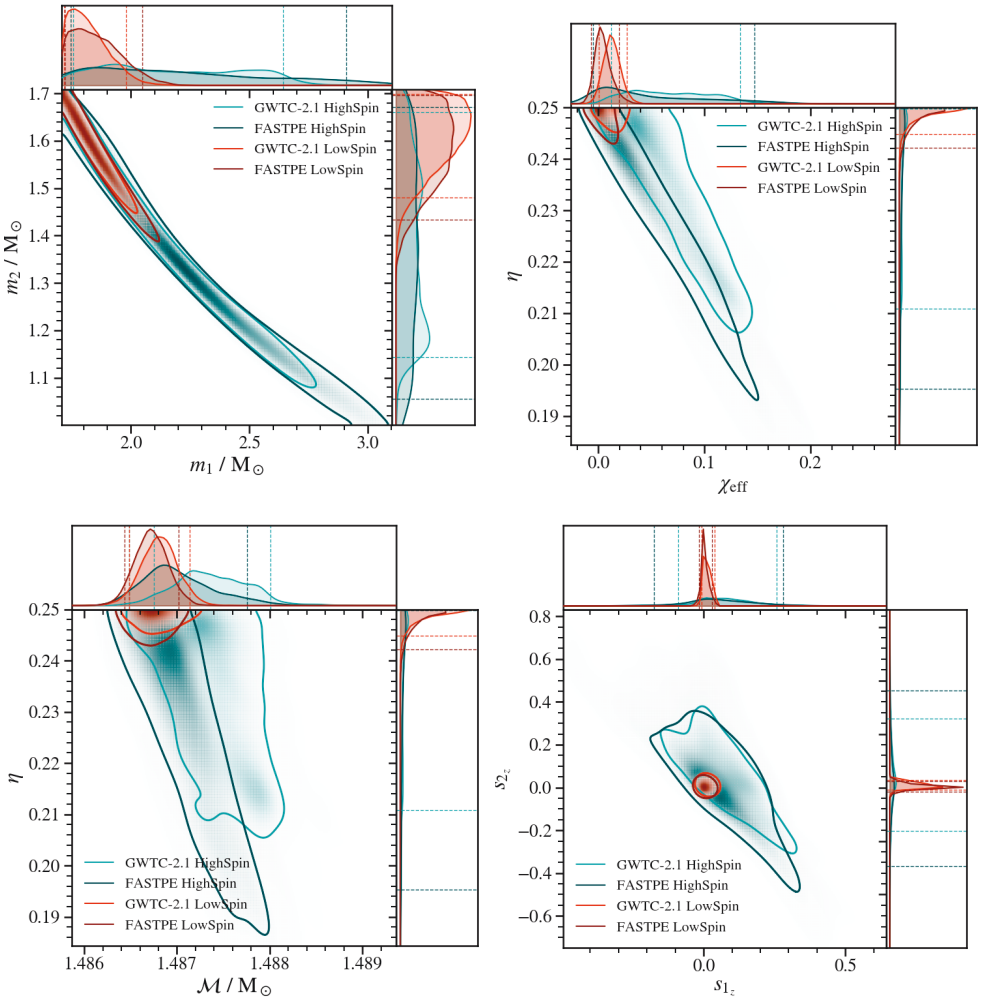

Figure 5.8: Comparison between `FASTPE` and catalog PE samples for the event GW190425.

GW200115_042309

This event is published in GWTC-3, with $\mathcal{M} = 2.58\,\mathrm{M}_\odot$. It was recovered by SNR-optimized PyCBC Live with $\mathcal{M} = 2.57\,\mathrm{M}_\odot$ and $\rho_{\mathrm{net}} = 11.3$. Available PE samples present two different configurations of spins: HighSpin $a_i < 0.89$ and LowSpin $a_i < 0.05$.

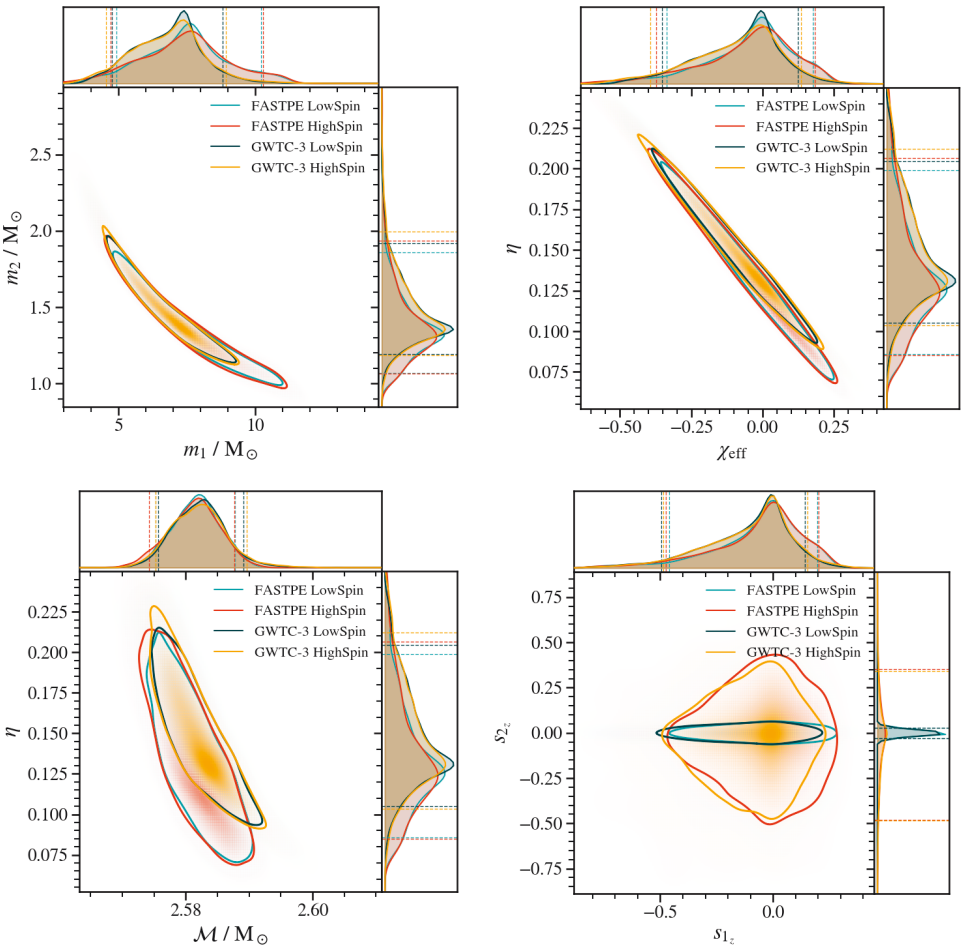

Figure 5.9: Comparison between `FASTPE` and catalog PE samples for the event GW200115_042309.

GW190426_152155

Published in GWTC-2, with $\mathcal{M} = 2.60\,\mathrm{M}_\odot$, it was reconsidered in GWTC-2.1 as a marginal event, without PE samples in the data release. We used a GstLAL trigger, with $\mathcal{M} = 2.59\,\mathrm{M}_\odot$ and $\rho_{\mathrm{net}} = 10.1$. PE samples present a typical NSBH spin prior with $a_1 < 0.9$ and $a_2 < 0.05$. We matched the prior in the LowSpin results, and the results with the default spin prior of `FASTPE` are presented as a comparison.

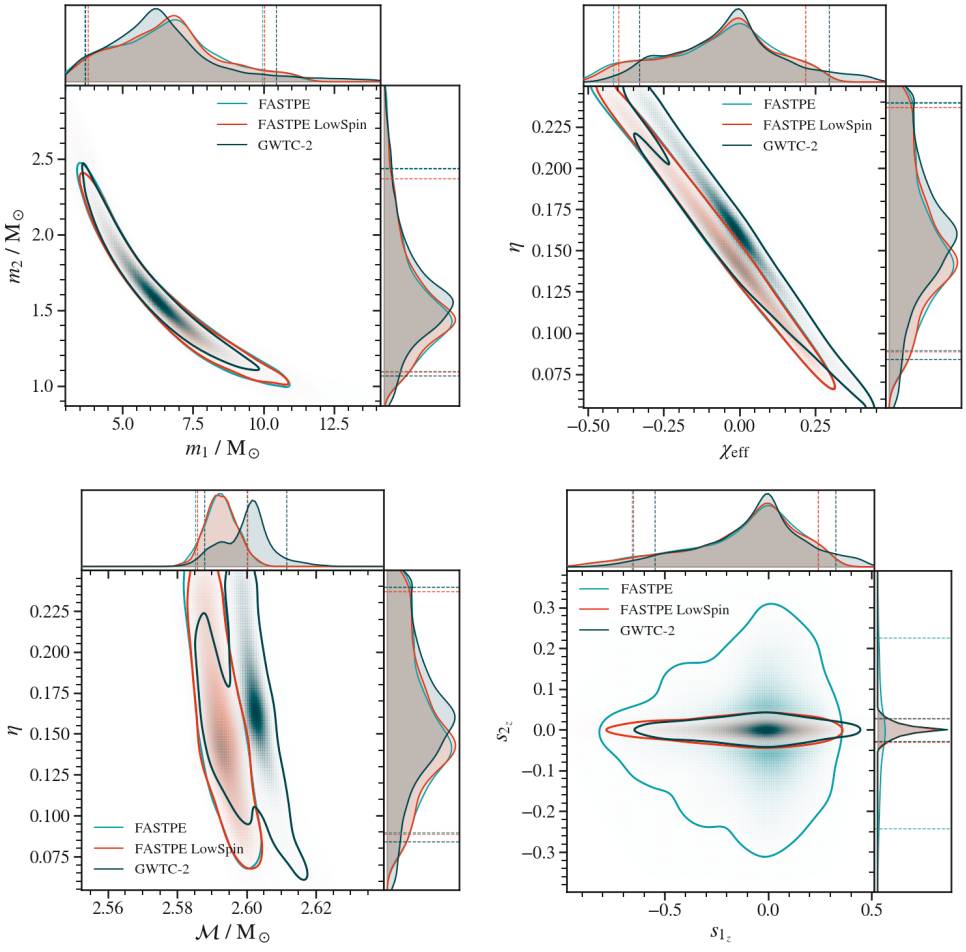

Figure 5.10: Comparison between `FASTPE` and catalog PE samples for the event GW190426_152155.

GW200105_162426

This event is published in GWTC-3 as a marginal event, with $\mathcal{M} = 3.63\,\mathrm{M}_\odot$. For `FASTPE` we used GstLAL preferred event, with $\mathcal{M} = 3.61\,\mathrm{M}_\odot$ and $\rho_{\mathrm{net}} = 13.9$. Available PE samples present a spin prior consistent with BBH origin $a_i < 0.99$.

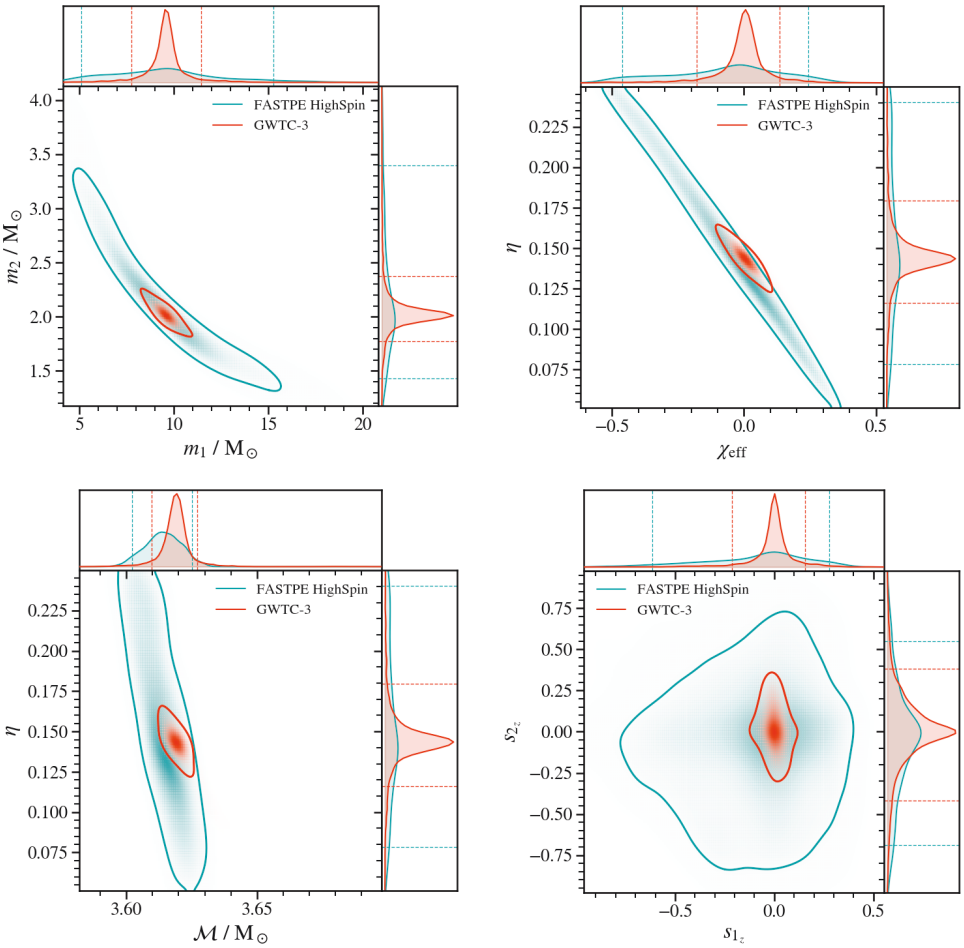

Figure 5.11: Comparison between `FASTPE` and catalog PE samples for the event GW200105_162426.

GW190917_114630

This event is published in GWTC-2.1, with $\mathcal{M} = 4.26\,\mathrm{M}_\odot$. For `FASTPE` we used GstLAL preferred event, with $\mathcal{M} = 4.2\,\mathrm{M}_\odot$ and $\rho_{\mathrm{net}} = 9.4$. Available PE samples present a spin prior consistent with BBH origin $a_i < 0.99$.

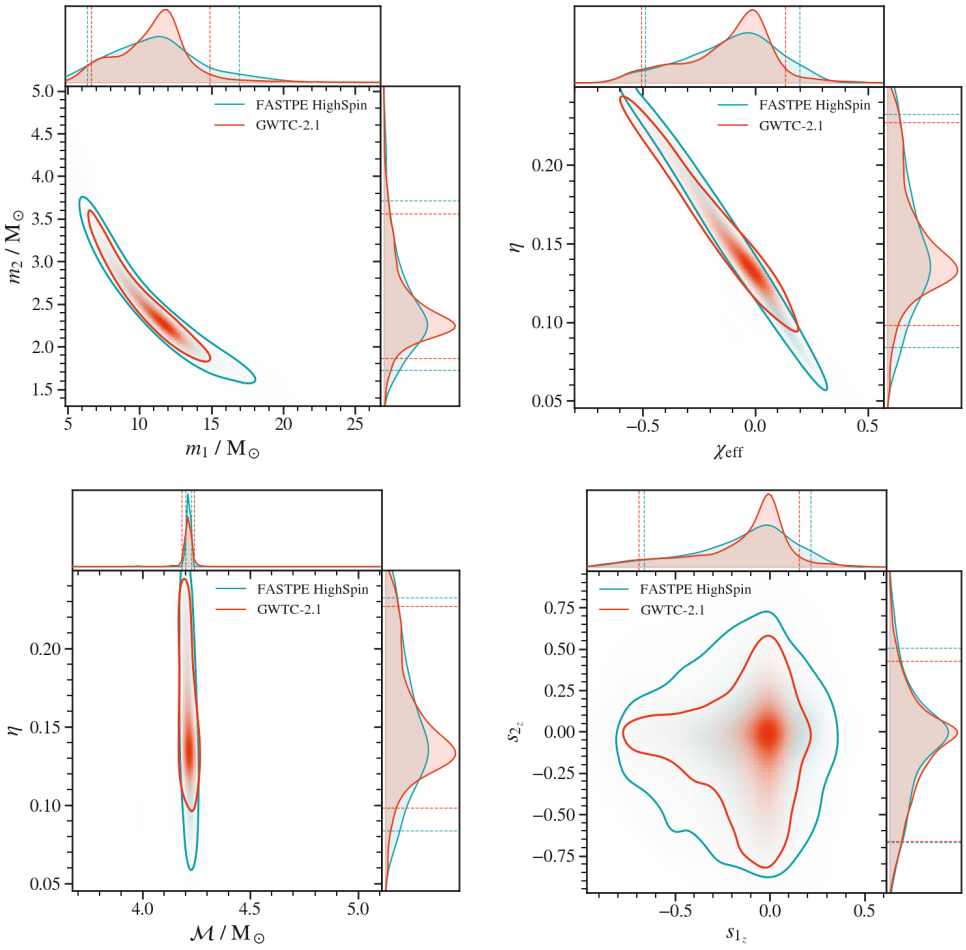

Figure 5.12: Comparison between `FASTPE` and catalog PE samples for the event GW190917_114630.

GW191219_163120

This event is published in GWTC-3, with $\mathcal{M} = 4.78\,\mathrm{M}_\odot$. For `FASTPE` we used a PyCBC offline trigger, with $\mathcal{M} = 4.69\,\mathrm{M}_\odot$ and $\rho_{\mathrm{net}} = 8.5$. Available PE samples present a spin prior consistent with BBH origin $a_i < 0.99$.

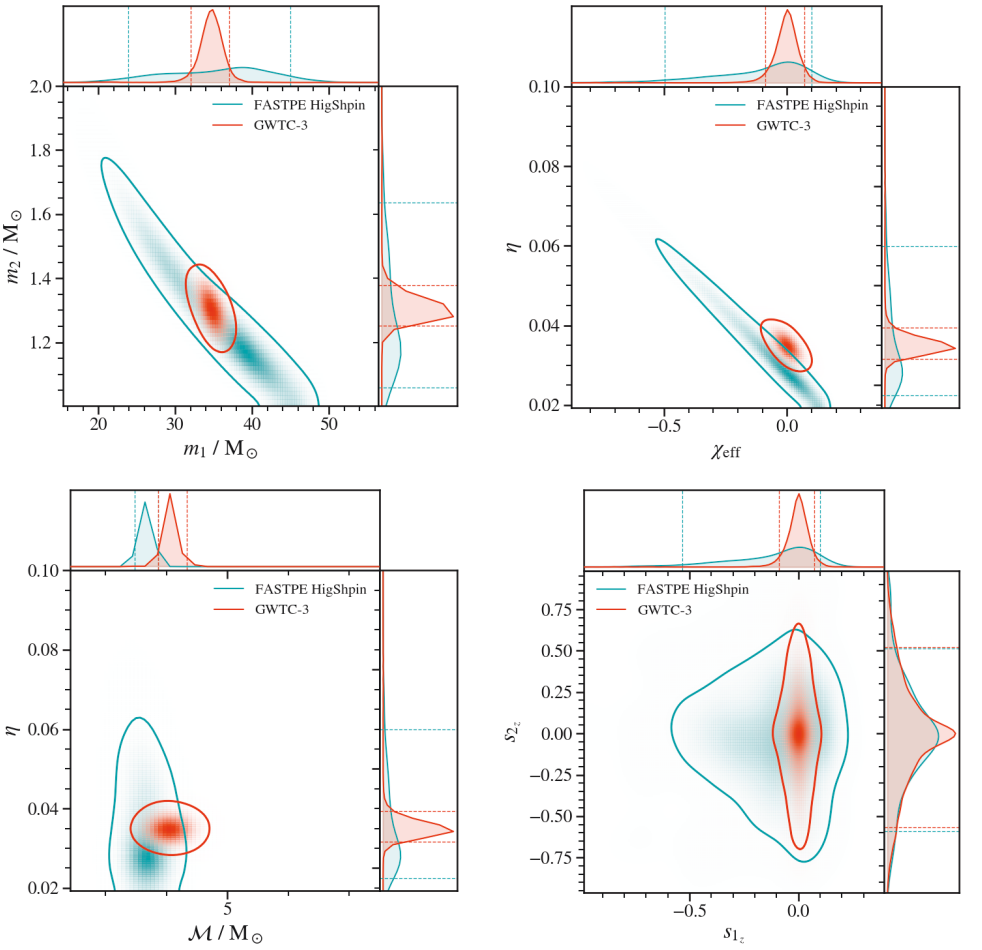

Figure 5.13: Comparison between `FASTPE` and catalog PE samples for the event GW191219_163120.

GW190814

This event is published in GWTC-2.1, with $\mathcal{M} = 6.42\,\mathrm{M}_\odot$. For `FASTPE` we used GstLAL preferred event, with $\mathcal{M} = 6.34\,\mathrm{M}_\odot$ and $\rho_{\mathrm{net}} = 24.5$. Available PE samples present a spin prior consistent with BBH $a_i < 0.99$.

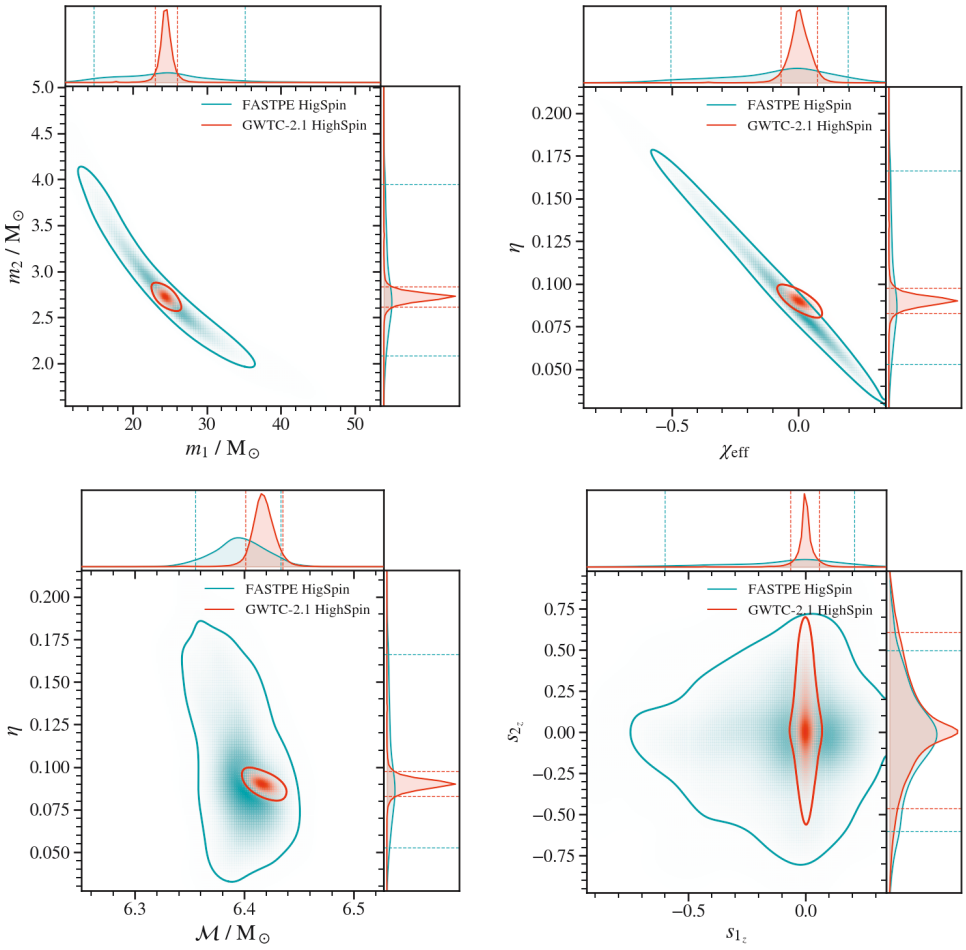

Figure 5.14: Comparison between `FASTPE` and catalog PE samples for the event GW190814.

GW190924_021846

This event is published in GWTC-2.1, with $\mathcal{M} = 6.44\,\mathrm{M}_\odot$. For `FASTPE` we used GstLAL preferred event, with $\mathcal{M} = 6.46\,\mathrm{M}_\odot$ and $\rho_{\mathrm{net}} = 13.2$. Available PE samples present a spin prior consistent with BBH origin $a_i < 0.99$.

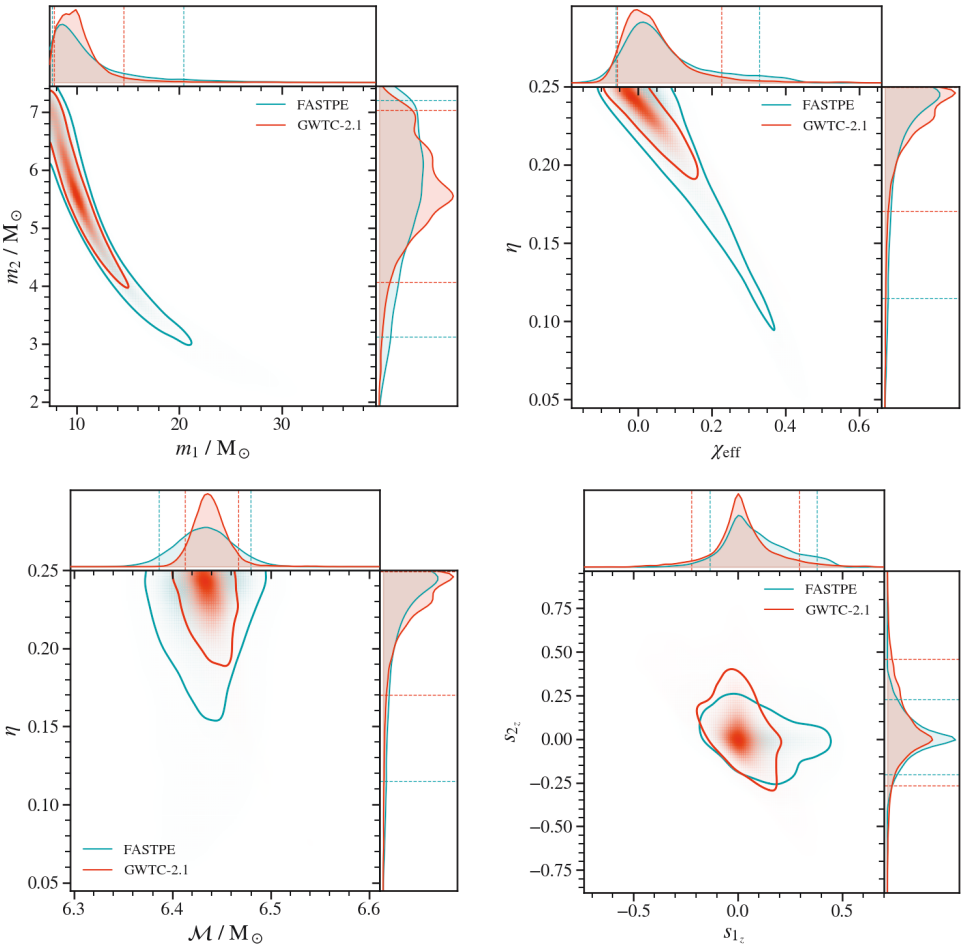

Figure 5.15: Comparison between `FASTPE` and catalog PE samples for the event GW190924_021846.

GW200210_092254

This event is published in GWTC-3, with $\mathcal{M} = 7.81\,\mathrm{M}_\odot$. For `FASTPE` we used a PyCBC offline event, with $\mathcal{M} = 5.08\,\mathrm{M}_\odot$ and $\rho_{\mathrm{net}} = 8.9$. Available PE samples present a spin prior consistent with BBH $a_i < 0.99$.

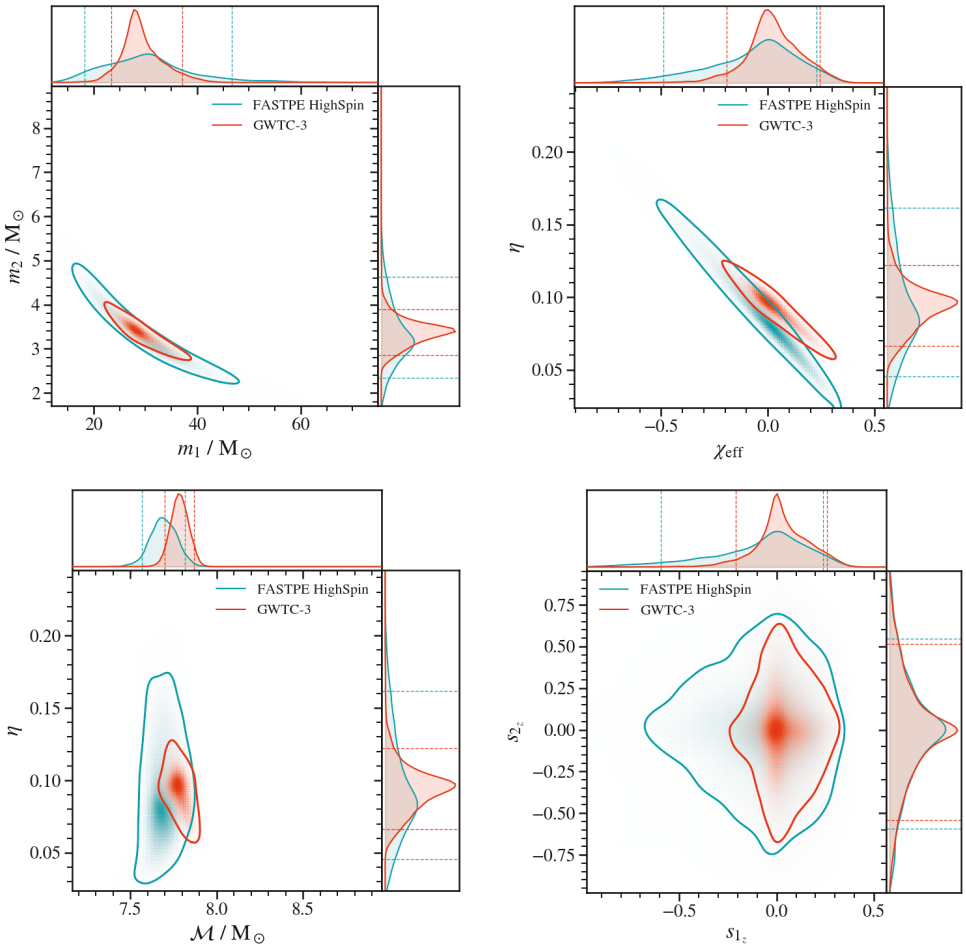

Figure 5.16: Comparison between `FASTPE` and catalog PE samples for the event GW200210_092254.

GW191129_134029

This event is published in GWTC-3, with $\mathcal{M} = 8.48\,\mathrm{M}_\odot$. For `FASTPE` we used GstLAL preferred event, with $\mathcal{M} = 8.5\,\mathrm{M}_\odot$ and $\rho_{\mathrm{net}} = 13.1$. Available PE samples present a spin prior consistent with BBH $a_i < 0.99$.

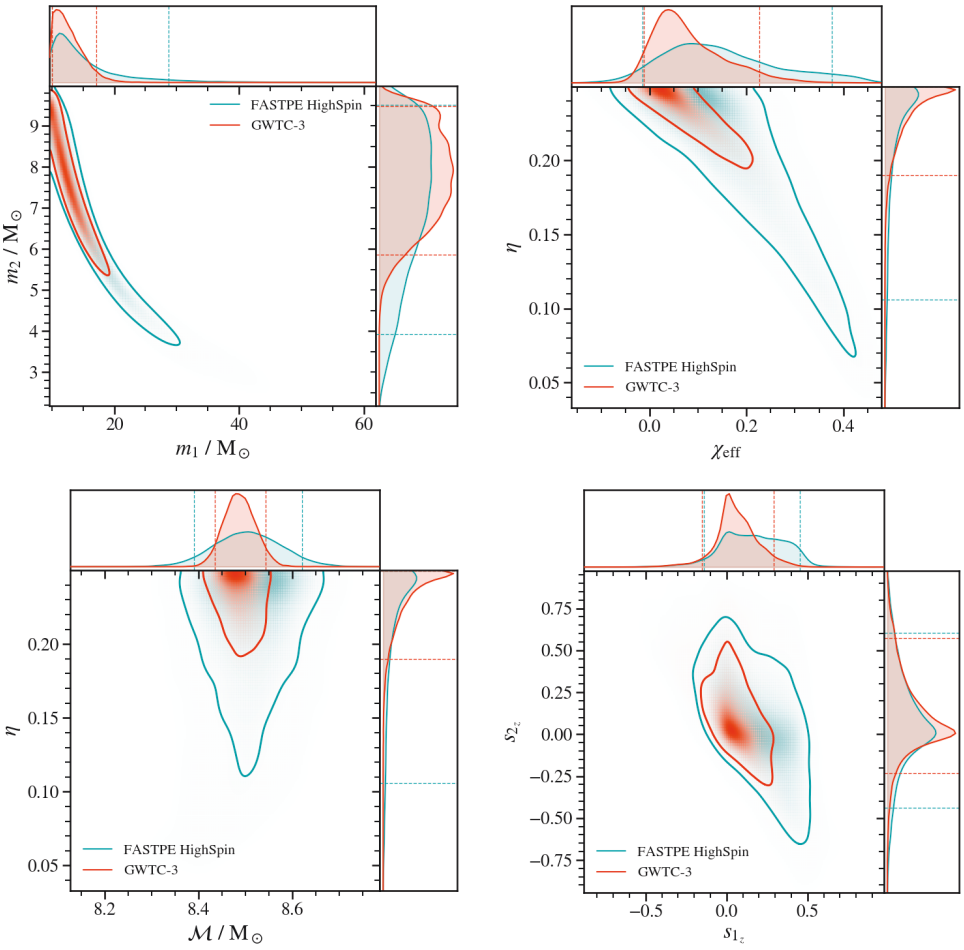

Figure 5.17: Comparison between `FASTPE` and catalog PE samples for the event GW191129_134029.

5.6.1 Discussion of results

To discuss the results presented in the previous contour plots, we divide the different binary events with respect to their astrophysical category.

For the events consistent with BNS origin, GW170817 and GW190425, the posteriors estimated with `FASTPE` are quite similar to the PE ones for both of the spin configurations. For GW190425 in the HighSpin configuration, there is a small disagreement in $\chi_{\rm eff}$ and $\mathcal{M}$. Nevertheless, these are of the order of ~ 0.025 and $\sim 0.001\,\mathrm{M}_\odot$ respectively. In the case of events consistent with NSBH origin, the discussion is slightly more complicated. For three of these events, GW200115_042309, GW190426_152155 and GW190917_114630, the extension of the `FASTPE` posterior distributions is comparable to the PE results. GW200115_042309 shows a deviation in the $\mathcal{M}-\eta$ distribution, but the individual posterior peaks show a good agreement. In the case of GW190426_152155, the chirp mass PE posterior show a bump close to the peak. `FASTPE` results are centered in that secondary peak, affecting mainly the chirp mass posterior, that shows a deviation from PE of the order of $\sim 0.01\,\mathrm{M}_\odot$. The four remaining NSBH events, GW200105_162426, GW191219_163120, GW190814 and GW200210_092254 show `FASTPE` posterior distributions much larger than PE ones. While the event GW200105_162426 corresponds to a moderately-asymmetric system, the other three show a large asymmetry in their component masses. These large asymmetries may be sign of complicated physical effects that are not included in `FASTPE` waveforms, as the presence of higher order modes in the signal of GW190814. For the events consistent with low-mass BBH systems, GW190924_021846 and GW191129_134029, the posterior distributions estimated with `FASTPE` are slightly larger than the PE ones, but their peaks and credible intervals are in good agreement.

The observed differences in the extension of posterior distributions between `FASTPE` and more detailed PE methods are expected for various reasons. First, we do not use the standard PE likelihood, but an approximate likelihood that is quadratic in the parameter differences and we do the calculation neglecting the noise. Additionally, `FASTPE` uses a specific waveform model that does not include effects of precession, higher-order modes or tidal effects. In contrast, PE typically employs different waveform models and accounts for these effects, which can carry additional information about the system.

5.7 Conclusions and future work

We have developed a method to estimate uncertainties in component masses and spins, able to produce posterior samples in approximately 1 minute. We employed three main assumptions to maintain the computing time in a scale suitable for the first follow-up alerts, between the first 10 minutes after detection. We start by assuming that the trigger found by the search corresponds to the template that maximizes the likelihood, and that the uncertainties would be Gaussian, centered at the maximum point. We are neglecting the presence of noise and the possibility of existence of various maxima points, in which case this approximation would loose its validity. In order to keep a reasonable number of initial samples, we restrict them to a narrow contour around the estimated value of the chirp mass. This is usually accurate for BNS signals; however, we must study the range of validity of this approximation by further tests including more massive systems. The third assumption is the employment of the Fisher matrix approximation evaluated in the space of PN expansion parameters, where it only has to be evaluated once for all the set of samples. Even though the Fisher matrix approximation is only valid for high-SNR events, which is not the case for current GW detections, with SNRs $\sim$10, the use of the PN expansion parameters as the coordinates of the space where the Fisher matrix is nearly constant, improves the accuracy of the approximation in the case of low-SNR and large differences in parameters.

As for applications in follow-up for multi-messenger campaign observations, `FASTPE` is a natural upgrade to the current source classification method described in Chapter 4, since the added information on the distribution of component masses and spins restricts the chirp mass contour to an ellipsoid in the plane of component masses. Another potential application in multi-messenger astronomy is the ability to predict certain properties of kilonova emission with a better estimation of the intrinsic parameters [146]. An advantage of the posterior samples generated by `FASTPE` is that they are not correlated with one another, unlike in the case of a MCMC sampling distribution. These samples could be used by more detailed PE methods as a set of pre-calculated samples to re-calculate the posterior with a real likelihood computation.

This method has been tested over a uniform set of BNS samples, showing barely any bias for the masses and spins parameters, except for the chirp mass. This bias is caused by the method being highly dependent of the initial value of chirp mass, yielding narrow posterior distributions around that point, even though the actual difference between the injected and the recovered value is typically on the order of $\sim$0.1 for the cases we consider. However, even though the results look promising when we compare the posterior distributions

obtained by `FASTPE` with the posterior samples published in the data releases of the GWTC catalogs, computed with much more detailed PE algorithms, we still do not have a quantitative estimation of the accuracy. Another pending test is the comparison with other rapid parameter estimation methods, such as `BILBY OnlinePE` [187].

As future work, the accuracy of the method could be improved by accounting for additional effects in the waveform, such as the spin-induced precession of the binary's orbit or the contribution of higher-order modes, as is done in the `simple-pe` algorithm [188]. Additionally, we plan to incorporate an estimation of the redshift in the near future. Currently, we are not taking into account the redshift of the masses with respect to their source-frame value, and all the results presented here compare masses in the detector-frame. This can be addressed by using the marginalized distance posterior computed in low-latency by `BAYESTAR` [153] and uploaded to GraceDB after detection.

Conclusions

In this thesis, we aimed to improve the existing analyses of gravitational-wave data from the ground-based detector network of the LIGO-Virgo-KAGRA Collaboration. Specifically, our work focused on the detection and follow-up of gravitational wave (GW) signals emitted by compact binary coalescence (CBC) systems using CBC modeled searches.

The content of this thesis is divided in 5 chapters. The first three serve as an introduction for the original scientific results that are presented in the last section of the third chapter, as well as in the two last chapters. In Chapter 1, we presented an overview of the fundamental basis of GW theory, focused on GW signals produced by CBCs, and a basic approach to gravitational-wave detectors. In Chapter 2, we outlined the existing methods to analyze the data in GW detectors, from the detection of the signal to the estimation of the parameters of the source. An introduction to waveform modeling within the post-Newtonian theory was also given in this chapter. Chapter 3 is divided between an introductory part, where we presented an overview of GW search algorithms, and an original scientific work in the last section. The introductory sections are focused on describing the general characteristics of the PyCBC search for CBCs. This search operate in two different latencies, *online* (near real-time) and *offline*. The rest of the thesis is constituted by original scientific work, which is summarized below.

In Chapter 3, Section 3.4, we presented our contribution to the development and application of a new *offline* PyCBC-based search designed to find GW signals emitted by intermediate-mass black hole (IMBH) binaries, named `PyCBC-IMBH`. In particular, in Section 3.4.2, we described the implementation of an additional search veto that removes the excess of loud triggers arising in the proximity of auto-gated loud non-Gaussian transients. This additional veto enhanced the sensitivity of `PyCBC-IMBH`, with a mean increase in the sensitive volume-time by a factor of 1.3 for the entire total mass range of the search at an inverse false alarm rate (IFAR) of 100 years.

In Chapters 4 and 5, we presented the main contributions of this thesis: the development and implementation in the *online* `PyCBC Live` search of two algorithms designed to aid in follow-up decisions to enable multi-messenger searches for counterpart events by electromagnetic and neutrino observatories. Specifically, these new methods aim to estimate the intrinsic properties of the source in very low latency, improving the information sent in the first rapid alerts within the first 10 minutes after detection.

The first algorithm, described in Chapter 4, estimates the probabilities of a GW event to belong to one of the different CBC astrophysical categories: BNS, NSBH and BBH. This classification method uses the template chirp mass estimates from `PyCBC-Live` and corrects them for the bias caused by cosmological redshift. This method improved the previous classification algorithm and has been running within the pipeline since the beginning of the fourth period of observation (O4) with an added latency of approximately 50 ms.

The second method, named `FASTPE`, is presented in Chapter 5. This new algorithm aims to rapidly forecast the uncertainties in binary masses and spins relative to the candidate identified by `PyCBC Live`, applying a Fisher-matrix approximation for the likelihood to a physical prior distribution. This method is able to produce credible regions of masses and spins that could inform follow-up searches and/or more detailed parameter estimation analysis while keeping a computational time of approximately 1 minute.

Summing up, the work done in thesis contributes to the existing efforts to improve both *offline* and *online* GW analysis methods, enhancing our ability to detect and characterize gravitational wave events and advancing our understanding of the physics of compact binary coalescences and their multi-messenger counterparts.

Bibliography

[1] Albert Einstein. "The foundation of the general theory of relativity." In: *Annalen Phys.* 49.7 (1916). Ed. by Jong-Ping Hsu and D. Fine, pp. 769–822. DOI: 10.1002/andp.19163540702.

[2] B. P. Abbott et al. "Observation of Gravitational Waves from a Binary Black Hole Merger". In: *Phys. Rev. Lett.* 116.6 (2016), p. 061102. DOI: 10.1103/PhysRevLett.116.061102. arXiv: 1602.03837 [gr-qc].

[3] B. Schutz. *A First Course in General Relativity*. 2nd. Cambridge University Press, 2009. ISBN: 9780521887052.

[4] M. Maggiore. *Gravitational Waves. Vol. 1: Theory and Experiments*. Oxford University Press, 2007. ISBN: 978-0-19-171766-6, 978-0-19-852074-0. DOI: 10.1093/acprof:oso/9780198570745.001.0001.

[5] S. M. Carroll. *Spacetime and Geometry: An Introduction to General Relativity*. Addison Wesley, 2004. ISBN: 978-0-8053-8732-2.

[6] B. P. Abbott et al. "GWTC-1: A Gravitational-Wave Transient Catalog of Compact Binary Mergers Observed by LIGO and Virgo during the First and Second Observing Runs". In: *Phys. Rev. X* 9.3 (2019), p. 031040. DOI: 10.1103/PhysRevX.9.031040. arXiv: 1811.12907 [astro-ph.HE].

[7] R. Abbott et al. "GWTC-2.1: Deep extended catalog of compact binary coalescences observed by LIGO and Virgo during the first half of the third observing run". In: *Phys. Rev. D* 109.2 (2024), p. 022001. DOI: 10.1103/PhysRevD.109.022001. arXiv: 2108.01045 [gr-qc].

[8] R. Abbott et al. "GWTC-3: Compact Binary Coalescences Observed by LIGO and Virgo during the Second Part of the Third Observing Run". In: *Phys. Rev. X* 13.4 (2023), p. 041039. DOI: 10.1103/PhysRevX.13.041039. arXiv: 2111.03606 [gr-qc].

[9] J. M. Weisberg, J. H. Taylor, and L. A. Fowler. "Gravitational waves from an orbiting pulsar". In: *Scientific American* 245 (Oct. 1981), pp. 74–82. DOI: 10.1038/scientificamerican1081-74.

[10] J. H. Taylor and J. M. Weisberg. "A new test of general relativity - Gravitational radiation and the binary pulsar PSR 1913+16". In: *ApJ* 253 (Feb. 1982), pp. 908–920. DOI: 10.1086/159690.

[11] J. Weber. "Detection and Generation of Gravitational Waves". In: *Phys. Rev.* 117 (1 1960), pp. 306–313. DOI: 10.1103/PhysRev.117.306. URL: https://link.aps.org/doi/10.1103/PhysRev.117.306.

[12] C. Cahillane and G. Mansell. "Review of the Advanced LIGO Gravitational Wave Observatories Leading to Observing Run Four". In: *Galaxies* 10.1 (2022), p. 36. DOI: 10.3390/galaxies10010036. arXiv: 2202.00847 [gr-qc].

[13] P. Fritschel, D. Shoemaker, and R. Weiss. "Demonstration of light recycling in a Michelson interferometer with Fabry–Perot cavities". In: *Appl. Opt.* 31.10 (1992), pp. 1412–1418. DOI: 10.1364/AO.31.001412. URL: https://opg.optica.org/ao/abstract.cfm?URI=ao-31-10-1412.

[14] A. Buonanno and Y. Chen. "Quantum noise in second generation, signal-recycled laser interferometric gravitational-wave detectors". In: *Phys. Rev. D* 64 (4 2001), p. 042006. DOI: 10.1103/PhysRevD.64.042006. URL: https://link.aps.org/doi/10.1103/PhysRevD.64.042006.

[15] M. Tse et al. "Quantum-Enhanced Advanced LIGO Detectors in the Era of Gravitational-Wave Astronomy". In: *Phys. Rev. Lett.* 123.23, 231107 (Dec. 2019), p. 231107. DOI: 10.1103/PhysRevLett.123.231107.

[16] T. A. Apostolatos et al. "Spin-induced orbital precession and its modulation of the gravitational waveforms from merging binaries". In: *Phys. Rev. D* 49 (12 1994), pp. 6274–6297. DOI: 10.1103/PhysRevD.49.6274. URL: https://link.aps.org/doi/10.1103/PhysRevD.49.6274.

[17] Bernard F. Schutz. "Networks of gravitational wave detectors and three figures of merit". In: *Class. Quant. Grav.* 28 (2011), p. 125023. DOI: 10.1088/0264-9381/28/12/125023. arXiv: 1102.5421 [astro-ph.IM].

[18] Stephen Fairhurst. "Triangulation of gravitational wave sources with a network of detectors". In: *New J. Phys.* 11 (2009). [Erratum: New J.Phys. 13, 069602 (2011)], p. 123006. DOI: 10.1088/1367-2630/11/12/123006. arXiv: 0908.2356 [gr-qc].

[19] B. P. Abbott et al. "LIGO: The Laser interferometer gravitational-wave observatory". In: *Rept. Prog. Phys.* 72 (2009), p. 076901. DOI: 10.1088/0034-4885/72/7/076901. arXiv: 0711.3041 [gr-qc].

[20] J. Aasi et al. "Advanced LIGO". In: *Class. Quant. Grav.* 32 (2015), p. 074001. DOI: 10.1088/0264-9381/32/7/074001. arXiv: 1411.4547 [gr-qc].

[21] Teviet Creighton. "Tumbleweeds and airborne gravitational noise sources for LIGO". In: *Class. Quant. Grav.* 25 (2008), p. 125011. DOI: 10.1088/0264-9381/25/12/125011. arXiv: gr-qc/0007050.

[22] C. M. Caves. "Quantum Mechanical Noise in an Interferometer". In: *Phys. Rev. D* 23 (1981), pp. 1693–1708. DOI: 10.1103/PhysRevD.23.1693.

[23] A. Buikema et al. "Sensitivity and performance of the Advanced LIGO detectors in the third observing run". In: *Phys. Rev. D* 102 (6 2020), p. 062003. DOI: 10.1103/PhysRevD.102.062003. URL: https://link.aps.org/doi/10.1103/PhysRevD.102.062003.

[24] F. Acernese et al. "Advanced Virgo: a second-generation interferometric gravitational wave detector". In: *Class. Quant. Grav.* 32.2 (2015), p. 024001. DOI: 10.1088/0264-9381/32/2/024001. arXiv: 1408.3978 [gr-qc].

[25] Y. Aso et al. "Interferometer design of the KAGRA gravitational wave detector". In: *Phys. Rev. D* 88 (4 2013), p. 043007. DOI: 10.1103/PhysRevD.88.043007. URL: https://link.aps.org/doi/10.1103/PhysRevD.88.043007.

[26] B. Willke et al. "The GEO 600 gravitational wave detector". In: *Class. Quant. Grav.* 19 (2002). Ed. by D. G. Blair, pp. 1377–1387. DOI: 10.1088/0264-9381/19/7/321.

[27] M. Saleem et al. "The science case for LIGO-India". In: *Class. Quant. Grav.* 39.2 (2022), p. 025004. DOI: 10.1088/1361-6382/ac3b99. arXiv: 2105.01716 [gr-qc].

[28] M. Maggiore et al. "Science Case for the Einstein Telescope". In: *JCAP* 03 (2020), p. 050. DOI: 10.1088/1475-7516/2020/03/050. arXiv: 1912.02622 [astro-ph.CO].

[29] P. Amaro-Seoane et al. "Laser Interferometer Space Antenna". In: (Feb. 2017). arXiv: 1702.00786 [astro-ph.IM].

[30] M. Armano et al. "Beyond the Required LISA Free-Fall Performance: New LISA Pathfinder Results down to 20 μHz". In: *Phys. Rev. Lett.* 120.6 (2018), p. 061101. DOI: 10.1103/PhysRevLett.120.061101.

[31] C. J. Moore, R. H. Cole, and C. P. L. Berry. "Gravitational-wave sensitivity curves". In: *Class. Quant. Grav.* 32.1 (2015), p. 015014. DOI: 10.1088/0264-9381/32/1/015014. arXiv: 1408.0740 [gr-qc].

[32] P. C. Peters. "Gravitational Radiation and the Motion of Two Point Masses". In: *Phys. Rev.* 136 (4B 1964), B1224–B1232. DOI: 10.1103/PhysRev.136.B1224. URL: https://link.aps.org/doi/10.1103/PhysRev.136.B1224.

[33] A. Bohé et al. "Improved effective-one-body model of spinning, nonprecessing binary black holes for the era of gravitational-wave astrophysics with advanced detectors". In: *Phys. Rev. D* 95.4 (2017), p. 044028. DOI: 10.1103/PhysRevD.95.044028. arXiv: 1611.03703 [gr-qc].

[34] Maarten Baes, Peter Camps, and Dries Van De Putte. "Analytical expressions and numerical evaluation of the luminosity distance in a flat cosmology". In: *Mon. Not. Roy. Astron. Soc.* 468.1 (2017), pp. 927–930. DOI: 10.1093/mnras/stx537. arXiv: 1702.08860 [astro-ph.CO].

[35] P. A. R. Ade et al. "Planck 2015 results. XIII. Cosmological parameters". In: *Astron. Astrophys.* 594 (2016), A13. DOI: 10.1051/0004-6361/201525830. arXiv: 1502.01589 [astro-ph.CO].

[36] Alessandra Buonanno and B. S. Sathyaprakash. "Sources of Gravitational Waves: Theory and Observations". In: *General Relativity and Gravitation: A Centennial Perspective*. Ed. by Abhay Ashtekar et al. Cambridge University Press, 2015, 287–346. arXiv: 1410.7832 [gr-qc].

[37] Verónica Villa-Ortega et al. "Self-consistent treatment of thermal effects in neutron-star post-mergers: observational implications for third-generation gravitational-wave detectors". In: (Oct. 2023). arXiv: 2310.20378 [gr-qc].

[38] Miquel Miravet-Tenés et al. "Identifying thermal effects in neutron star merger remnants with model-agnostic waveform reconstructions and third-generation detectors". In: (Jan. 2024). arXiv: 2401.02493 [gr-qc].

[39] Luca Baiotti and Luciano Rezzolla. "Binary neutron star mergers: a review of Einstein's richest laboratory". In: *Rept. Prog. Phys.* 80.9 (2017), p. 096901. DOI: 10.1088/1361-6633/aa67bb. arXiv: 1607.03540 [gr-qc].

[40] A. Buonanno and T. Damour. "Effective one-body approach to general relativistic two-body dynamics". In: *Phys. Rev. D* 59 (1999), p. 084006. DOI: 10.1103/PhysRevD.59.084006. arXiv: gr-qc/9811091.

[41] Serguei Ossokine et al. "Multipolar Effective-One-Body Waveforms for Precessing Binary Black Holes: Construction and Validation". In: *Phys. Rev. D* 102.4 (2020), p. 044055. DOI: 10.1103/PhysRevD.102.044055. arXiv: 2004.09442 [gr-qc].

[42] Geraint Pratten et al. "Computationally efficient models for the dominant and subdominant harmonic modes of precessing binary black holes". In: *Phys. Rev. D* 103.10 (2021), p. 104056. DOI: 10.1103/PhysRevD.103.104056. arXiv: 2004.06503 [gr-qc].

[43] Vijay Varma et al. "Surrogate models for precessing binary black hole simulations with unequal masses". In: *Phys. Rev. Research.* 1 (2019), p. 033015. DOI: 10.1103/PhysRevResearch.1.033015. arXiv: 1905.09300 [gr-qc].

[44] Luc Blanchet. *Post-Newtonian Theory for Gravitational Waves.* 2024. DOI: 10.48550/arXiv.1310.1528. arXiv: 1310.1528 [gr-qc].

[45] Soichiro Isoyama, Riccardo Sturani, and Hiroyuki Nakano. "Post-Newtonian templates for gravitational waves from compact binary inspirals". In: (Dec. 2020). DOI: 10.1007/978-981-15-4702-7_31-1. arXiv: 2012.01350 [gr-qc].

[46] Luc Blanchet et al. "Gravitational wave forms from inspiralling compact binaries to second postNewtonian order". In: *Class. Quant. Grav.* 13 (1996), pp. 575–584. DOI: 10.1088/0264-9381/13/4/002. arXiv: gr-qc/9602024.

[47] Luc Blanchet et al. "Gravitational-Wave Phasing of Quasicircular Compact Binary Systems to the Fourth-and-a-Half Post-Newtonian Order". In: *Phys. Rev. Lett.* 131 (12 2023), p. 121402. DOI: 10.1103/PhysRevLett.131.121402. URL: https://link.aps.org/doi/10.1103/PhysRevLett.131.121402.

[48] Michael Boyle et al. "High-accuracy numerical simulation of black-hole binaries: Computation of the gravitational-wave energy flux and comparisons with post-Newtonian approximants". In: *Phys. Rev. D* 78 (2008), p. 104020. DOI: 10.1103/PhysRevD.78.104020. arXiv: 0804.4184 [gr-qc].

[49] Alessandra Buonanno et al. "Comparison of post-Newtonian templates for compact binary inspiral signals in gravitational-wave detectors". In: *Phys. Rev. D* 80 (2009), p. 084043. DOI: 10.1103/PhysRevD.80.084043. arXiv: 0907.0700 [gr-qc].

[50] Thibault Damour, Bala R. Iyer, and B. S. Sathyaprakash. "A Comparison of search templates for gravitational waves from binary inspiral". In: *Phys. Rev. D* 63 (2001). [Erratum: Phys.Rev.D 72, 029902 (2005)], p. 044023. DOI: 10.1103/PhysRevD.63.044023. arXiv: gr-qc/0010009.

[51] P. Ajith et al. "Data formats for numerical relativity waves". In: *arXiv e-prints*, arXiv:0709.0093 (Sept. 2007), arXiv:0709.0093. DOI: 10.48550/arXiv.0709.0093. arXiv: 0709.0093 [gr-qc].

[52] E. T. Newman and R. Penrose. "Note on the Bondi-Metzner-Sachs Group". In: *Journal of Mathematical Physics* 7.5 (May 1966), pp. 863–870. ISSN: 0022-2488. DOI: 10.1063/1.1931221. URL: https://doi.org/10.1063/1.1931221.

[53] Kip S. Thorne. "Multipole expansions of gravitational radiation". In: *Rev. Mod. Phys.* 52 (2 1980), pp. 299–339. DOI: 10.1103/RevModPhys.52.299. URL: https://link.aps.org/doi/10.1103/RevModPhys.52.299.

[54] R. Abbott et al. "GW190814: Gravitational Waves from the Coalescence of a 23 Solar Mass Black Hole with a 2.6 Solar Mass Compact Object". In: *Astrophys. J. Lett.* 896.2 (2020), p. L44. DOI: 10.3847/2041-8213/ab960f. arXiv: 2006.12611 [astro-ph.HE].

[55] R. Abbott et al. "GW190412: Observation of a Binary-Black-Hole Coalescence with Asymmetric Masses". In: *Phys. Rev. D* 102.4 (2020), p. 043015. DOI: 10.1103/PhysRevD.102.043015. arXiv: 2004.08342 [astro-ph.HE].

[56] Cameron Mills and Stephen Fairhurst. "Measuring gravitational-wave higher-order multipoles". In: *Phys. Rev. D* 103.2 (2021), p. 024042. DOI: 10.1103/PhysRevD.103.024042. arXiv: 2007.04313 [gr-qc].

[57] Lawrence E. Kidder. "Using full information when computing modes of post-Newtonian waveforms from inspiralling compact binaries in circular orbit". In: *Phys. Rev. D* 77 (2008), p. 044016. DOI: 10.1103/PhysRevD.77.044016. arXiv: 0710.0614 [gr-qc].

[58] Eric Thrane and Colm Talbot. "An introduction to Bayesian inference in gravitational-wave astronomy: parameter estimation, model selection, and hierarchical models". In: *Publ. Astron. Soc. Austral.* 36 (2019), e010. DOI: 10.1017/pasa.2019.2. arXiv: 1809.02293 [astro-ph.IM].

[59] Robert E. Kass and Adrian E. Raftery. "Bayes Factors". In: *J. Am. Statist. Assoc.* 90.430 (1995), pp. 773–795. DOI: 10.1080/01621459.1995.10476572.

[60] Benjamin P Abbott et al. "A guide to LIGO–Virgo detector noise and extraction of transient gravitational-wave signals". In: *Class. Quant. Grav.* 37.5 (2020), p. 055002. DOI: 10.1088/1361-6382/ab685e. arXiv: 1908.11170 [gr-qc].

[61] Lee S. Finn. "Detection, measurement and gravitational radiation". In: *Phys. Rev. D* 46 (1992), pp. 5236–5249. DOI: 10.1103/PhysRevD.46.5236. arXiv: gr-qc/9209010.

[62] T. Dent and J. Veitch. "Optimizing gravitational-wave searches for a population of coalescing binaries: Intrinsic parameters". In: *Phys. Rev. D* 89.6 (2014), p. 062002. DOI: 10.1103/PhysRevD.89.062002. arXiv: 1311.7174 [gr-qc].

[63] Warren G. Anderson et al. "An Excess power statistic for detection of burst sources of gravitational radiation". In: *Phys. Rev. D* 63 (2001), p. 042003. DOI: 10.1103/PhysRevD.63.042003. arXiv: gr-qc/0008066.

[64] Leonard Wainstein, V. D. Zubakov, and Albert A. Mullin. "Extraction of signals from noise". In: 1970. URL: https://api.semanticscholar.org/CorpusID:118545667.

[65] Piotr Jaranowski and Andrzej Krolak. "Gravitational-Wave Data Analysis. Formalism and Sample Applications: The Gaussian Case". In: *Living Rev. Rel.* 8 (2005), p. 3. DOI: 10.12942/lrr-2012-4. arXiv: 0711.1115 [gr-qc].

[66] C.W. Helstrom et al. *Statistical Theory of Signal Detection*. International series of monographs on electronics and instrumentation. Elsevier Science, 1968. ISBN: 9781483156859.

[67] B. Allen et al. "FINDCHIRP: An Algorithm for detection of gravitational waves from inspiraling compact binaries". In: *Phys. Rev. D* 85 (2012), p. 122006. DOI: 10.1103/PhysRevD.85.122006. arXiv: gr-qc/0509116.

[68] Benjamin J. Owen. "Search templates for gravitational waves from inspiraling binaries: Choice of template spacing". In: *Phys. Rev. D* 53 (1996), pp. 6749–6761. DOI: 10.1103/PhysRevD.53.6749. arXiv: gr-qc/9511032.

[69] Theocharis A. Apostolatos. "Search templates for gravitational waves from precessing, inspiraling binaries". In: *Phys. Rev. D* 52 (2 1995), pp. 605–620. DOI: 10.1103/PhysRevD.52.605. URL: https://link.aps.org/doi/10.1103/PhysRevD.52.605.

[70] C. Messenger, R. Prix, and M. A. Papa. "Random template banks and relaxed lattice coverings". In: *Phys. Rev. D* 79 (2009), p. 104017. DOI: 10.1103/PhysRevD.79.104017. arXiv: 0809.5223 [gr-qc].

[71] Benjamin J. Owen and B. S. Sathyaprakash. "Matched filtering of gravitational waves from inspiraling compact binaries: Computational cost and template placement". In: *Phys. Rev. D* 60 (1999), p. 022002. DOI: 10.1103/PhysRevD.60.022002. arXiv: gr-qc/9808076.

[72] Thomas Cokelaer. "Gravitational waves from inspiralling compact binaries: Hexagonal template placement and its efficiency in detecting physical signals". In: *Phys. Rev. D* 76 (2007), p. 102004. DOI: 10.1103/PhysRevD.76.102004. arXiv: 0706.4437 [gr-qc].

[73] Stanislav Babak. "Building a stochastic template bank for detecting massive black hole binaries". In: *Class. Quant. Grav.* 25 (2008), p. 195011. DOI: 10.1088/0264-9381/25/19/195011. arXiv: 0801.4070 [gr-qc].

[74] Ian W. Harry, Bruce Allen, and B. S. Sathyaprakash. "A Stochastic template placement algorithm for gravitational wave data analysis". In: *Phys. Rev. D* 80 (2009), p. 104014. DOI: 10.1103/PhysRevD.80.104014. arXiv: 0908.2090 [gr-qc].

[75] Soumen Roy, Anand S. Sengupta, and Nilay Thakor. "Hybrid geometric-random template-placement algorithm for gravitational wave searches from compact binary coalescences". In: *Phys. Rev. D* 95.10 (2017), p. 104045. DOI: 10.1103/PhysRevD.95.104045. arXiv: 1702.06771 [gr-qc].

[76] J. Veitch et al. "Parameter estimation for compact binaries with ground-based gravitational-wave observations using the LALInference software library". In: *Phys. Rev. D* 91.4 (2015), p. 042003. DOI: 10.1103/PhysRevD.91.042003. arXiv: 1409.7215 [gr-qc].

[77] Christian Rover, Renate Meyer, and Nelson Christensen. "Bayesian inference on compact binary inspiral gravitational radiation signals in interferometric data". In: *Class. Quant. Grav.* 23 (2006), pp. 4895–4906. DOI: 10.1088/0264-9381/23/15/009. arXiv: gr-qc/0602067.

[78] Marc van der Sluys et al. "Parameter estimation of spinning binary inspirals using Markov-chain Monte Carlo". In: *Class. Quant. Grav.* 25 (2008), p. 184011. DOI: 10.1088/0264-9381/25/18/184011. arXiv: 0805.1689 [gr-qc].

[79] John Skilling. "Nested sampling for general Bayesian computation". In: *Bayesian Analysis* 1.4 (2006), pp. 833 –859. DOI: 10.1214/06-BA127. URL: https://doi.org/10.1214/06-BA127.

[80] J. Veitch and A. Vecchio. "Bayesian coherent analysis of in-spiral gravitational wave signals with a detector network". In: *Phys. Rev. D* 81 (2010), p. 062003. DOI: 10.1103/PhysRevD.81.062003. arXiv: 0911.3820 [astro-ph.CO].

[81] Greg Ashton et al. "Nested sampling for physical scientists". In: *Nature* 2 (2022). DOI: 10.1038/s43586-022-00121-x. arXiv: 2205.15570 [stat.CO].

[82] Samantha A. Usman et al. "The PyCBC search for gravitational waves from compact binary coalescence". In: *Class. Quant. Grav.* 33.21 (2016), p. 215004. DOI: 10.1088/0264-9381/33/21/215004. arXiv: 1508.02357 [gr-qc].

[83] Alexander H. Nitz et al. "Detecting binary compact-object mergers with gravitational waves: Understanding and Improving the sensitivity of the PyCBC search". In: *Astrophys. J.* 849.2 (2017), p. 118. DOI: 10.3847/1538-4357/aa8f50. arXiv: 1705.01513 [gr-qc].

[84] Alexander Harvey Nitz. "Distinguishing short duration noise transients in LIGO data to improve the PyCBC search for gravitational waves from high mass binary black hole mergers". In: *Class. Quant. Grav.* 35.3 (2018), p. 035016. DOI: 10.1088/1361-6382/aaa13d. arXiv: 1709.08974 [gr-qc].

[85] Gareth S. Cabourn Davies and Ian W. Harry. "Establishing significance of gravitational-wave signals from a single observatory in the PyCBC offline search". In: *Class. Quant. Grav.* 39.21 (2022), p. 215012. DOI: 10.1088/1361-6382/ac8862. arXiv: 2203.08545 [gr-qc].

[86] C. Messick et al. "Analysis framework for the prompt discovery of compact binary mergers in gravitational-wave data". In: *Physical Review D* 95.4 (Feb. 2017). ISSN: 2470-0029. DOI: 10.1103/physrevd.95.042001. URL: http://dx.doi.org/10.1103/PhysRevD.95.042001.

[87] Surabhi Sachdev et al. "The GstLAL Search Analysis Methods for Compact Binary Mergers in Advanced LIGO's Second and Advanced Virgo's First Observing Runs". In: (Jan. 2019). arXiv: 1901.08580 [gr-qc].

[88] Kipp C. et al. "GstLAL: A software framework for gravitational wave discovery". In: (2020). arXiv: 2010.05082 [astro-ph.IM].

[89] F. Aubin et al. "The MBTA pipeline for detecting compact binary coalescences in the third LIGO–Virgo observing run". In: *Class. Quant. Grav.* 38.9 (2021), p. 095004. DOI: 10.1088/1361-6382/abe913. arXiv: 2012.11512 [gr-qc].

[90] S. Klimenko et al. “A wavelet method for detection of gravitational wave bursts”. In: *Class. Quant. Grav.* 21 (2004), S1819–S1830. DOI: 10.1088/0264-9381/21/20/025.

[91] S. Klimenko et al. “Method for detection and reconstruction of gravitational wave transients with networks of advanced detectors”. In: *Phys. Rev. D* 93.4 (2016), p. 042004. DOI: 10.1103/PhysRevD.93.042004. arXiv: 1511.05999 [gr-qc].

[92] Alexander H. Nitz et al. “Rapid detection of gravitational waves from compact binary mergers with PyCBC Live”. In: *Phys. Rev. D* 98.2 (2018), p. 024050. DOI: 10.1103/PhysRevD.98.024050. arXiv: 1805.11174 [gr-qc].

[93] Tito Dal Canton et al. “Real-time Search for Compact Binary Mergers in Advanced LIGO and Virgo’s Third Observing Run Using PyCBC Live”. In: *Astrophys. J.* 923.2 (2021), p. 254. DOI: 10.3847/1538-4357/ac2f9a. arXiv: 2008.07494 [astro-ph.HE].

[94] Chad Hanna et al. “Fast evaluation of multidetector consistency for real-time gravitational wave searches”. In: *Phys. Rev. D* 101.2 (2020), p. 022003. DOI: 10.1103/PhysRevD.101.022003. arXiv: 1901.02227 [gr-qc].

[95] T. Adams et al. “Low-latency analysis pipeline for compact binary coalescences in the advanced gravitational wave detector era”. In: *Class. Quant. Grav.* 33.17 (2016), p. 175012. DOI: 10.1088/0264-9381/33/17/175012. arXiv: 1512.02864 [gr-qc].

[96] Jing Luan et al. “Towards low-latency real-time detection of gravitational waves from compact binary coalescences in the era of advanced detectors”. In: *Phys. Rev. D* 85 (2012), p. 102002. DOI: 10.1103/PhysRevD.85.102002. arXiv: 1108.3174 [gr-qc].

[97] Qi Chu. “Low-latency detection and localization of gravitational waves from compact binary coalescences”. English. PhD thesis. The University of Western Australia, 2017. DOI: 10.4225/23/5987feb0a789c.

[98] Ian W. Harry et al. “Investigating the effect of precession on searches for neutron-star-black-hole binaries with Advanced LIGO”. In: *Phys. Rev. D* 89.2 (2014), p. 024010. DOI: 10.1103/PhysRevD.89.024010. arXiv: 1307.3562 [gr-qc].

[99] Ian Harry et al. “Searching for Gravitational Waves from Compact Binaries with Precessing Spins”. In: *Phys. Rev. D* 94.2 (2016), p. 024012. DOI: 10.1103/PhysRevD.94.024012. arXiv: 1603.02444 [gr-qc].

[100] J. Calderón Bustillo et al. “Impact of gravitational radiation higher order modes on single aligned-spin gravitational wave searches for binary black holes”. In: *Phys. Rev. D* 93.8 (2016), p. 084019. DOI: 10.1103/PhysRevD.93.084019. arXiv: 1511.02060 [gr-qc].

[101] Tito Dal Canton and Ian W. Harry. “Designing a template bank to observe compact binary coalescences in Advanced LIGO’s second observing run”. In: (May 2017). arXiv: 1705.01845 [gr-qc].

[102] Alejandro Bohé et al. “Improved effective-one-body model of spinning, nonprecessing binary black holes for the era of gravitational-wave astrophysics with advanced detectors”. In: *Phys. Rev. D* 95.4 (2017), p. 044028. DOI: 10.1103/PhysRevD.95.044028. arXiv: 1611.03703 [gr-qc].

[103] Soumen Roy, Anand S. Sengupta, and Parameswaran Ajith. “Effectual template banks for upcoming compact binary searches in Advanced-LIGO and Virgo data”. In: *Phys. Rev. D* 99.2 (2019), p. 024048. DOI: 10.1103/PhysRevD.99.024048. arXiv: 1711.08743 [gr-qc].

[104] B. P. Abbott et al. “Characterization of transient noise in Advanced LIGO relevant to gravitational wave signal GW150914”. In: *Class. Quant. Grav.* 33.13 (2016), p. 134001. DOI: 10.1088/0264-9381/33/13/134001. arXiv: 1602.03844 [gr-qc].

[105] Derek Davis et al. “LIGO detector characterization in the second and third observing runs”. In: *Class. Quant. Grav.* 38.13 (2021), p. 135014. DOI: 10.1088/1361-6382/abfd85. arXiv: 2101.11673 [astro-ph.IM].

[106] B P Abbott et al. “Effects of data quality vetoes on a search for compact binary coalescences in Advanced LIGO’s first observing run”. In: *Class. Quant. Grav.* 35.6 (2018), p. 065010. DOI: 10.1088/1361-6382/aaaafa. arXiv: 1710.02185 [gr-qc].

[107] T. Dal Canton et al. “Effect of sine-Gaussian glitches on searches for binary coalescence”. In: *Class. Quant. Grav.* 31 (2014), p. 015016. DOI: 10.1088/0264-9381/31/1/015016. arXiv: 1304.0008 [gr-qc].

[108] B. P. Abbott et al. “Observation of Gravitational Waves from a Binary Black Hole Merger”. In: *Phys. Rev. Lett.* 116.6 (2016), p. 061102. DOI: 10.1103/PhysRevLett.116.061102. arXiv: 1602.03837 [gr-qc].

[109] F.J. Harris. “On the use of windows for harmonic analysis with the discrete Fourier transform”. In: *Proceedings of the IEEE* 66.1 (1978), pp. 51–83. DOI: 10.1109/PROC.1978.10837.

[110] Bruce Allen. "χ^2 time-frequency discriminator for gravitational wave detection". In: *Phys. Rev. D* 71 (2005), p. 062001. DOI: 10.1103/PhysRevD.71.062001. arXiv: gr-qc/0405045.

[111] Gareth S. Davies et al. "Extending the PyCBC search for gravitational waves from compact binary mergers to a global network". In: *Phys. Rev. D* 102.2 (2020), p. 022004. DOI: 10.1103/PhysRevD.102.022004. arXiv: 2002.08291 [astro-ph.HE].

[112] Jolien D. E. Creighton. "Data analysis strategies for the detection of gravitational waves in nonGaussian noise". In: *Phys. Rev. D* 60 (1999), p. 021101. DOI: 10.1103/PhysRevD.60.021101. arXiv: gr-qc/9901075.

[113] Benjamin P. Abbott et al. "Sensitivity of the Advanced LIGO detectors at the beginning of gravitational wave astronomy". In: *Phys. Rev. D* 93.11 (2016). [Addendum: Phys.Rev.D 97, 059901 (2018)], p. 112004. DOI: 10.1103/PhysRevD.93.112004. arXiv: 1604.00439 [astro-ph.IM].

[114] B. P. Abbott et al. "Multi-messenger Observations of a Binary Neutron Star Merger". In: *Astrophys. J. Lett.* 848.2 (2017), p. L12. DOI: 10.3847/2041-8213/aa91c9. arXiv: 1710.05833 [astro-ph.HE].

[115] B. P. Abbott et al. "Low-latency Gravitational-wave Alerts for Multi-messenger Astronomy during the Second Advanced LIGO and Virgo Observing Run". In: *Astrophys. J.* 875.2 (2019), p. 161. DOI: 10.3847/1538-4357/ab0e8f. arXiv: 1901.03310 [astro-ph.HE].

[116] Sushant Sharma Chaudhary et al. "Low-latency gravitational wave alert products and their performance in anticipation of the fourth LIGO-Virgo-KAGRA observing run". In: *Proc. Nat. Acad. Sci.* 121.18 (2024), e2316474121. DOI: 10.1073/pnas.2316474121. arXiv: 2308.04545 [astro-ph.HE].

[117] Rainer Storn and Kenneth Price. "Differential Evolution – A Simple and Efficient Heuristic for global Optimization over Continuous Spaces". In: *J. Global Optim.* 11.4 (1997), pp. 341–359. DOI: 10.1023/A:1008202821328.

[118] Koustav Chandra et al. "An optimized PyCBC search for gravitational waves from intermediate-mass black hole mergers". In: *Phys. Rev. D* 104 (2021), p. 042004. DOI: 10.1103/PhysRevD.104.042004. arXiv: 2106.00193 [gr-qc].

[119] Laura Ferrarese and Holland Ford. "Supermassive black holes in galactic nuclei: Past, present and future research". In: *Space Sci. Rev.* 116 (2005), pp. 523–624. DOI: 10.1007/s11214-005-3947-6. arXiv: astro-ph/0411247.

[120] M. Coleman Miller and E. J. M Colbert. "Intermediate - mass black holes". In: *Int. J. Mod. Phys. D* 13 (2004), pp. 1–64. DOI: 10.1142/S0218271804004426. arXiv: astro-ph/0308402.

[121] R. Abbott et al. "Tests of general relativity with binary black holes from the second LIGO-Virgo gravitational-wave transient catalog". In: *Phys. Rev. D* 103.12 (2021), p. 122002. DOI: 10.1103/PhysRevD.103.122002. arXiv: 2010.14529 [gr-qc].

[122] R. Abbott et al. "GWTC-2: Compact Binary Coalescences Observed by LIGO and Virgo During the First Half of the Third Observing Run". In: *Phys. Rev. X* 11 (2021), p. 021053. DOI: 10.1103/PhysRevX.11.021053. arXiv: 2010.14527 [gr-qc].

[123] R. Abbott et al. "Population Properties of Compact Objects from the Second LIGO-Virgo Gravitational-Wave Transient Catalog". In: *Astrophys. J. Lett.* 913.1 (2021), p. L7. DOI: 10.3847/2041-8213/abe949. arXiv: 2010.14533 [astro-ph.HE].

[124] R. Abbott et al. "GW190521: A Binary Black Hole Merger with a Total Mass of $150M_{\odot}$". In: *Phys. Rev. Lett.* 125.10 (2020), p. 101102. DOI: 10.1103/PhysRevLett.125.101102. arXiv: 2009.01075 [gr-qc].

[125] R. Abbott et al. "Properties and Astrophysical Implications of the 150 $M_{\odot}$ Binary Black Hole Merger GW190521". In: *Astrophys. J. Lett.* 900.1 (2020), p. L13. DOI: 10.3847/2041-8213/aba493. arXiv: 2009.01190 [astro-ph.HE].

[126] Miriam Cabero et al. "Blip glitches in Advanced LIGO data". In: *Class. Quant. Grav.* 36.15 (2019), p. 15. DOI: 10.1088/1361-6382/ab2e14. arXiv: 1901.05093 [physics.ins-det].

[127] B. P. Abbott et al. "GW170817: Observation of Gravitational Waves from a Binary Neutron Star Inspiral". In: *Phys. Rev. Lett.* 119.16 (2017), p. 161101. DOI: 10.1103/PhysRevLett.119.161101. arXiv: 1710.05832 [gr-qc].

[128] A. Goldstein et al. "An Ordinary Short Gamma-Ray Burst with Extraordinary Implications: Fermi-GBM Detection of GRB 170817A". In: *Astrophys. J. Lett.* 848.2 (2017), p. L14. DOI: 10.3847/2041-8213/aa8f41. arXiv: 1710.05446 [astro-ph.HE].

[129] D. A. Coulter et al. “Swope Supernova Survey 2017a (SSS17a), the optical counterpart to a gravitational wave source”. In: *Science* 358.6370 (2017), pp. 1556–1558. DOI: 10.1126/science.aap9811. eprint: https://www.science.org/doi/pdf/10.1126/science.aap9811. URL: https://www.science.org/doi/abs/10.1126/science.aap9811.

[130] S. J. Smartt et al. “A kilonova as the electromagnetic counterpart to a gravitational-wave source”. In: *Nature* 551.7678 (2017), pp. 75–79. DOI: 10.1038/nature24303. arXiv: 1710.05841 [astro-ph.HE].

[131] LIGO Scientific Collaboration and Virgo Collaboration. In: *GCN* 24045 (2019). URL: https://gcn.gsfc.nasa.gov/gcn3/24045.gcn3.

[132] B. P. Abbott et al. “Prospects for observing and localizing gravitational-wave transients with Advanced LIGO, Advanced Virgo and KAGRA”. In: *Living Rev. Rel.* 21.1 (2018), p. 3. DOI: 10.1007/s41114-020-00026-9. arXiv: 1304.0670 [gr-qc].

[133] Polina Petrov et al. “Data-driven Expectations for Electromagnetic Counterpart Searches Based on LIGO/Virgo Public Alerts”. In: *Astrophys. J.* 924.2 (2022), p. 54. DOI: 10.3847/1538-4357/ac366d. arXiv: 2108.07277 [astro-ph.HE].

[134] LIGO Scientific and Virgo Collaborations. *LIGO/Virgo Public Alerts User Guide*. https://emfollow.docs.ligo.org/userguide/. 2020. URL: https://emfollow.docs.ligo.org/userguide/.

[135] Leo P. Singer and Larry R. Price. “Rapid Bayesian position reconstruction for gravitational-wave transients”. In: *Phys. Rev. D* 93.2 (2016), p. 024013. DOI: 10.1103/PhysRevD.93.024013. arXiv: 1508.03634 [gr-qc].

[136] Gregory Ashton et al. “BILBY: A user-friendly Bayesian inference library for gravitational-wave astronomy”. In: *Astrophys. J. Suppl.* 241.2 (2019), p. 27. DOI: 10.3847/1538-4365/ab06fc. arXiv: 1811.02042 [astro-ph.IM].

[137] Shasvath J. Kapadia et al. “A self-consistent method to estimate the rate of compact binary coalescences with a Poisson mixture model”. In: *Class. Quant. Grav.* 37.4 (2020), p. 045007. DOI: 10.1088/1361-6382/ab5f2d. arXiv: 1903.06881 [astro-ph.HE].

[138] Deep Chatterjee et al. “A Machine Learning Based Source Property Inference for Compact Binary Mergers”. In: *Astrophys. J.* 896.1 (2020), p. 54. DOI: 10.3847/1538-4357/ab8dbe. arXiv: 1911.00116 [astro-ph.IM].

[139] Curt Cutler and Eanna E. Flanagan. "Gravitational waves from merging compact binaries: How accurately can one extract the binary's parameters from the inspiral wave form?" In: *Phys. Rev. D* 49 (1994), pp. 2658–2697. DOI: 10.1103/PhysRevD.49.2658. arXiv: gr-qc/9402014.

[140] Sylvia Biscoveanu, Salvatore Vitale, and Carl-Johan Haster. "The reliability of the low-latency estimation of binary neutron star chirp mass". In: *Astrophys. J. Lett.* 884.2 (2019), p. L32. DOI: 10.3847/2041-8213/ab479e. arXiv: 1908.03592 [astro-ph.HE].

[141] B. F. Schutz. "Determining the Hubble constant from gravitational wave observations". In: *Nature* 323.6086 (Sept. 1986), pp. 310–311. DOI: 10.1038/323310a0.

[142] C. Messenger et al. "Source Redshifts from Gravitational-Wave Observations of Binary Neutron Star Mergers". In: *Phys. Rev. X* 4.4 (2014), p. 041004. DOI: 10.1103/PhysRevX.4.041004. arXiv: 1312.1862 [gr-qc].

[143] Emily Baird et al. "Degeneracy between mass and spin in black-hole-binary waveforms". In: *Phys. Rev. D* 87.2 (2013), p. 024035. DOI: 10.1103/PhysRevD.87.024035. arXiv: 1211.0546 [gr-qc].

[144] Mark Hannam et al. "When can gravitational-wave observations distinguish between black holes and neutron stars?" In: *Astrophys. J. Lett.* 766 (2013), p. L14. DOI: 10.1088/2041-8205/766/1/L14. arXiv: 1301.5616 [gr-qc].

[145] Ben Margalit and Brian D. Metzger. "The Multi-Messenger Matrix: the Future of Neutron Star Merger Constraints on the Nuclear Equation of State". In: *Astrophys. J. Lett.* 880.1 (2019), p. L15. DOI: 10.3847/2041-8213/ab2ae2. arXiv: 1904.11995 [astro-ph.HE].

[146] Cosmin Stachie et al. "Predicting electromagnetic counterparts using low-latency gravitational-wave data products". In: *Mon. Not. Roy. Astron. Soc.* 505.3 (2021), pp. 4235–4248. DOI: 10.1093/mnras/stab1492. arXiv: 2103.01733 [astro-ph.HE].

[147] Cody Messick et al. "Analysis Framework for the Prompt Discovery of Compact Binary Mergers in Gravitational-wave Data". In: *Phys. Rev. D* 95.4 (2017), p. 042001. DOI: 10.1103/PhysRevD.95.042001. arXiv: 1604.04324 [astro-ph.IM].

[148] Qi Chu et al. “SPIIR online coherent pipeline to search for gravitational waves from compact binary coalescences”. In: *Phys. Rev. D* 105.2 (2022), p. 024023. DOI: 10.1103/PhysRevD.105.024023. arXiv: 2011.06787 [gr-qc].

[149] Will M. Farr et al. “Counting And Confusion: Bayesian Rate Estimation With Multiple Populations”. In: *Phys. Rev. D* 91.2 (2015), p. 023005. DOI: 10.1103/PhysRevD.91.023005. arXiv: 1302.5341 [astro-ph.IM].

[150] LIGO Scientific Collaboration and Virgo Collaboration. In: *GCN* 25324 (2019). URL: https://gcn.gsfc.nasa.gov/gcn3/25324.gcn3.

[151] A. Krolak and Bernard F. Schutz. “Coalescing binaries — Probe of the universe”. In: *Gen. Rel. Grav.* 19 (1987), pp. 1163–1171. DOI: 10.1007/BF00759095.

[152] B. P. Abbott et al. “Binary Black Hole Population Properties Inferred from the First and Second Observing Runs of Advanced LIGO and Advanced Virgo”. In: *Astrophys. J. Lett.* 882.2 (2019), p. L24. DOI: 10.3847/2041-8213/ab3800. arXiv: 1811.12940 [astro-ph.HE].

[153] Leo P. Singer and Larry R. Price. “Rapid Bayesian position reconstruction for gravitational-wave transients”. In: *Phys. Rev. D* 93 (2 2016), p. 024013. DOI: 10.1103/PhysRevD.93.024013. URL: https://link.aps.org/doi/10.1103/PhysRevD.93.024013.

[154] Bruce Allen et al. “FINDCHIRP: An Algorithm for detection of gravitational waves from inspiraling compact binaries”. In: *Phys. Rev. D* 85 (2012), p. 122006. DOI: 10.1103/PhysRevD.85.122006. arXiv: gr-qc/0509116.

[155] R. Abbott et al. “GWTC-3: Compact Binary Coalescences Observed by LIGO and Virgo During the Second Part of the Third Observing Run”. In: (Nov. 2021). arXiv: 2111.03606 [gr-qc].

[156] LIGO Scientific Collaboration and Virgo Collaboration. In: *GCN* 24069, 24098, 24141, 24168, 24237, 24377, 24411, 24503, 24522, 24570, 24598, 24621, 24632, 24717, 24922, 24950, 24998, 25012, 25115, 25164, 25187, 25208, 25324, 25333, 25497, 25503, 25753, 25829, 25871, 26182, 26202, 26303, 26334, 26441, 26454, 26543, 26570, 26640, 26715, 26759, 26906, 26926, 27014, 27130, 27184, 27193, 27278, 27358, 27388 (2019-2020). URL: https://gcn.gsfc.nasa.gov/lvc.html.

[157] LIGO Scientific Collaboration and Virgo Collaboration. *GWTC-2 Data Release*. 2020. DOI: 10.7935/99gf-ax93. URL: https://doi.org/10.7935/99gf-ax93.

[158] LIGO Scientific Collaboration and Virgo Collaboration. *GWTC-3 Data Release*. 2021. DOI: 10.7935/b024-1886. URL: https://doi.org/10.7935/b024-1886.

[159] LIGO Scientific Collaboration and Virgo Collaboration. In: *GCN* 24237 (2019). URL: https://gcn.gsfc.nasa.gov/gcn3/24237.gcn3.

[160] LIGO Scientific Collaboration and Virgo Collaboration. In: *GCN* 24411 (2019). URL: https://gcn.gsfc.nasa.gov/gcn3/24411.gcn3.

[161] LIGO Scientific Collaboration and Virgo Collaboration. In: *GCN* 25187 (2019). URL: https://gcn.gsfc.nasa.gov/gcn3/25187.gcn3.

[162] LIGO Scientific Collaboration and Virgo Collaboration. In: *GCN* 25208 (2019). URL: https://gcn.gsfc.nasa.gov/gcn3/25208.gcn3.

[163] LIGO Scientific Collaboration and Virgo Collaboration. In: *GCN* 25333 (2019). URL: https://gcn.gsfc.nasa.gov/gcn3/25333.gcn3.

[164] LIGO Scientific Collaboration and Virgo Collaboration. In: *GCN* 26454 (2019). URL: https://gcn.gsfc.nasa.gov/gcn3/26454.gcn3.

[165] LIGO Scientific Collaboration and Virgo Collaboration. In: *GCN* 26570 (2019). URL: https://gcn.gsfc.nasa.gov/gcn3/26570.gcn3.

[166] Charlie Hoy and Vivien Raymond. "PESummary: the code agnostic Parameter Estimation Summary page builder". In: *SoftwareX* 15 (2021), p. 100765. DOI: 10.1016/j.softx.2021.100765. arXiv: 2006.06639 [astro-ph.IM].

[167] R. Abbott et al. "Observation of Gravitational Waves from Two Neutron Star–Black Hole Coalescences". In: *Astrophys. J. Lett.* 915.1 (2021), p. L5. DOI: 10.3847/2041-8213/ac082e. arXiv: 2106.15163 [astro-ph.HE].

[168] B. P. Abbott et al. "GW190425: Observation of a Compact Binary Coalescence with Total Mass $\sim 3.4 M_{\odot}$". In: *Astrophys. J. Lett.* 892.1 (2020), p. L3. DOI: 10.3847/2041-8213/ab75f5. arXiv: 2001.01761 [astro-ph.HE].

[169] "Observation of Gravitational Waves from the Coalescence of a 2.5 – 4.5 $M_{\odot}$ Compact Object and a Neutron Star". In: (Apr. 2024). arXiv: 2404.04248 [astro-ph.HE].

[170] LIGO Scientific Collaboration and Virgo Collaboration and KAGRA Collaboration. In: *GCN* 33889 (2023). URL: https://gcn.nasa.gov/circulars/33889.txt.

[171] Frank Ohme et al. "Statistical and systematic errors for gravitational-wave inspiral signals: A principal component analysis". In: *Phys. Rev. D* 88.4 (2013), p. 042002. DOI: 10.1103/PhysRevD.88.042002. arXiv: 1304.7017 [gr-qc].

[172] Rory Smith et al. "Fast and accurate inference on gravitational waves from precessing compact binaries". In: *Phys. Rev. D* 94.4 (2016), p. 044031. DOI: 10.1103/PhysRevD.94.044031. arXiv: 1604.08253 [gr-qc].

[173] C. Pankow et al. "Novel scheme for rapid parallel parameter estimation of gravitational waves from compact binary coalescences". In: *Phys. Rev. D* 92.2 (2015), p. 023002. DOI: 10.1103/PhysRevD.92.023002. arXiv: 1502.04370 [gr-qc].

[174] Rory J. E. Smith et al. "Massively parallel Bayesian inference for transient gravitational-wave astronomy". In: *Mon. Not. Roy. Astron. Soc.* 498.3 (2020), pp. 4492–4502. DOI: 10.1093/mnras/staa2483. arXiv: 1909.11873 [gr-qc].

[175] Sean T. McWilliams, Bernard J. Kelly, and John G. Baker. "Observing mergers of non-spinning black-hole binaries". In: *Phys. Rev. D* 82 (2010), p. 024014. DOI: 10.1103/PhysRevD.82.024014. arXiv: 1004.0961 [gr-qc].

[176] Michele Vallisneri. "Use and abuse of the Fisher information matrix in the assessment of gravitational-wave parameter-estimation prospects". In: *Phys. Rev. D* 77 (2008), p. 042001. DOI: 10.1103/PhysRevD.77.042001. arXiv: gr-qc/0703086.

[177] Frank Ohme. "Bridging the Gap between Post-Newtonian Theory and Numerical Relativity in Gravitational-Wave Data Analysis". PhD thesis. Potsdam U., 2012.

[178] Alejandro Bohé, Sylvain Marsat, and Luc Blanchet. "Next-to-next-to-leading order spin–orbit effects in the gravitational wave flux and orbital phasing of compact binaries". In: *Class. Quant. Grav.* 30 (2013), p. 135009. DOI: 10.1088/0264-9381/30/13/135009. arXiv: 1303.7412 [gr-qc].

[179] K. G. Arun et al. "Higher-order spin effects in the amplitude and phase of gravitational waveforms emitted by inspiraling compact binaries: Ready-to-use gravitational waveforms". In: *Phys. Rev. D* 79 (2009). [Erratum: Phys.Rev.D 84, 049901 (2011)], p. 104023. DOI: 10.1103/PhysRevD.79.104023. arXiv: 0810.5336 [gr-qc].

[180] Balazs Mikoczi, Matyas Vasuth, and Laszlo A. Gergely. "Self-interaction spin effects in inspiralling compact binaries". In: *Phys. Rev. D* 71 (2005), p. 124043. DOI: 10.1103/PhysRevD.71.124043. arXiv: astro-ph/0504538.

[181] Duncan A. Brown et al. "Detecting binary neutron star systems with spin in advanced gravitational-wave detectors". In: *Phys. Rev. D* 86 (2012), p. 084017. DOI: 10.1103/PhysRevD.86.084017. arXiv: 1207.6406 [gr-qc].

[182] LIGO Scientific Collaboration, Virgo Collaboration, and KAGRA Collaboration. *LVK Algorithm Library - LALSuite*. Free software (GPL). 2018. DOI: 10.7935/GT1W-FZ16.

[183] T. Callister. "A Thesaurus for Common Priors in Gravitational-Wave Astronomy". In: (Apr. 2021). arXiv: 2104.09508 [gr-qc].

[184] LIGO Scientific Collaboration. *Parameter estimation sample release for GWTC-1*. URL: {https://doi.org/10.7935/KSX7-QQ51}.

[185] LIGO Scientific Collaboration and Virgo Collaboration. *GWTC-2.1: Deep Extended Catalog of Compact Binary Coalescences Observed by LIGO and Virgo During the First Half of the Third Observing Run - Parameter Estimation Data Release*. Version v2. May 2022. DOI: 10.5281/zenodo.6513631. URL: https://doi.org/10.5281/zenodo.6513631.

[186] LIGO Scientific Collaboration, Virgo Collaboration, and KAGRA Collaboration. *GWTC-3: Compact Binary Coalescences Observed by LIGO and Virgo During the Second Part of the Third Observing Run — Parameter estimation data release*. Oct. 2023. DOI: 10.5281/zenodo.8177023. URL: https://doi.org/10.5281/zenodo.8177023.

[187] Soichiro Morisaki et al. "Rapid localization and inference on compact binary coalescences with the Advanced LIGO-Virgo-KAGRA gravitational-wave detector network". In: *Phys. Rev. D* 108.12 (2023), p. 123040. DOI: 10.1103/PhysRevD.108.123040. arXiv: 2307.13380 [gr-qc].

[188] Stephen Fairhurst et al. "Simple parameter estimation using observable features of gravitational-wave signals". In: *Phys. Rev. D* 108.8 (2023), p. 082006. DOI: 10.1103/PhysRevD.108.082006. arXiv: 2304.03731 [gr-qc].

Appendices

A

PUBLISHED CONTENT AND CONTRIBUTIONS [1]

[1] Optimized PyCBC search for gravitational waves from intermediate-mass black hole mergers (2021)

Koustav Chandra[1], **Verónica Villa-Ortega**[2], Thomas Dent[2], Connor McIsaac[3], Archana Pai[1], Ian W. Harry[3], Gareth S. Cabourn Davies[3] and Kanchan Soni[4]

[1] *Department of Physics, Indian Institute of Technology Bombay, Powai, Mumbai 400 076, India*
[2] *IGFAE, Campus Sur, Universidade de Santiago de Compostela, 15782 Santiago de Compostela, Spain*
[3] *University of Portsmouth, Portsmouth PO1 3FX, United Kingdom*
[4] *Inter-University Centre for Astronomy and Astrophysics, Pune 411007, India*

Published in: *Physical Review D* **104**, 042004 – August 2021.
DOI: 10.1103/PhysRevD.104.042004
Impact factor: 5.0 (2022)
Published by: American Physical Society.

Chapter: Certain contents of this publication are reproduced in Chapter 3.
Contribution: The search was divided in 9 blocks of data. I ran the search algorithm for 2 blocks with 2 different configurations and analyzed and summarized the results. I developed the new gating veto that was applied in this search to increase its sensitivity, and I wrote the section of the manuscript devoted to it.

[1] By publication date

[2] Real-time Search for Compact Binary Mergers in Advanced LIGO and Virgo's Third Observing Run Using PyCBC Live (2021)

Tito Dal Canton[1,2,3], Alexander H. Nitz[4,5], Bhooshan Gadre[2], Gareth S. Cabourn Davies[6,7], **Verónica Villa-Ortega**[6], Thomas Dent[6], Ian Harry[2,7] and Liting Xiao[8]

[1] *NASA Goddard Space Flight Center, 8800 Greenbelt Road, Greenbelt, MD 20771, USA*
[2] *Max Planck Institute for Gravitational Physics (Albert Einstein Institute), Am Mühlenberg 1, D-14476 Potsdam-Golm, Germany*
[3] *Université Paris-Saclay, CNRS/IN2P3, IJCLab, F-91405 Orsay, France*
[4] *Max Planck Institute for Gravitational Physics (Albert Einstein Institute), D-30167 Hannover, Germany*
[5] *Leibniz Universität Hannover, D-30167 Hannover, Germany*
[6] *Instituto Galego de Física de Altas Enerxías, Universidade de Santiago de Compostela, E-15782 Santiago de Compostela, Galicia, Spain*
[7] *Institute for Cosmology and Gravitation, University of Portsmouth, 1-8 Burnaby Road, Portsmouth, P01 3FZ, UK*
[8] *LIGO Laboratory, California Institute of Technology, MS 100-36, Pasadena, CA 91125, USA*

Published in: *The Astrophysical Journal* **923**, 254 – December 2021.
DOI: 10.3847/1538-4357/ac2f9a
Impact factor: 4.9 (2022)
Published by: American Astronomical Society.

Chapter: Certain contents of this publication are reproduced in Chapter 4.
Contribution: Among the new improvements to the search, I developed the method to produce the estimation of source probabilities, tested it with the set of simulated signals that is described in the publication, and wrote the section of the manuscript devoted to it.

[3] Rapid source classification and distance estimation for compact binary mergers with PyCBC live (2022)

Verónica Villa-Ortega[1], Thomas Dent[1] and Andrés Curiel Barroso[1]

[1] *Instituto Galego de Física de Altas Enerxías, Universidade de Santiago de Compostela, Rúa de Xoaquín Díaz de Rábago s/n, E-15782, Spain*

Published in: *Monthly Notices of the Royal Astronomical Society*, Vol. 515, Iss 4, pp. 5718–5729 – October 2022.
DOI: 10.1093/mnras/stac2120
Impact factor: 4.8 (2022)
Published by: Oxford University Press on behalf of Royal Astronomical Society.

Chapter: The content of this publication is reproduced in Chapter 4.
Contribution: I developed the method to estimate the probabilities of gravitational events from compact binary sources to belong to the different astrophysical categories that is fully described in the chapter. I tested the method against a population of simulated signals and compared the results against the values published in the publications from the LIGO-Virgo-KAGRA (LVK) collaboration. I wrote the main part of the manuscript.

[4] Salient features of the optimised PyCBC IMBH search (2023)

Koustav Chandra[1], Archana Pai[1], **Verónica Villa-Ortega**[2], Thomas Dent[2], Connor McIsaac[3], Ian W. Harry[3], Gareth S. Cabourn Davies[3] and Kanchan Soni[4]

[1] *Department of Physics, Indian Institute of Technology Bombay, Powai, Mumbai 400 076, India*
[2] *IGFAE, Campus Sur, Universidade de Santiago de Compostela, 15782, Spain*
[3] *University of Portsmouth, Portsmouth PO1 3FX, United Kingdom*
[4] *Inter-University Centre for Astronomy and Astrophysics, Pune 411007, India*

Published in: *The Sixteenth Marcel Grossmann Meeting: On Recent Developments in Theoretical and Experimental General Relativity, Astrophysics, and Relativistic Field Theories.* eISBN: 978-981-12-6977-6, pp. 3277-3285 – March 2023.
DOI: 10.1142/9789811269776_0269
Published by: World Scientific.
 Chapter: Certain contents of this publication are reproduced in Chapter 3.
Contribution: I ran 2/9 blocks of the search with 2 different configurations and analyzed and summarized the results. I developed the new gating veto that was applied in this search to increase its sensitivity.

[5] GWTC-3: Compact Binary Coalescences Observed by LIGO and Virgo during the Second Part of the Third Observing Run (2023)

LIGO Scientific Collaboration, Virgo Collaboration, and KAGRA Collaboration (incl. **Verónica Villa-Ortega**[1])

[1] *Instituto Galego de Física de Altas Enerxías, Universidade de Santiago de Com-*

postela, Rúa de Xoaquín Díaz de Rábago s/n, E-15782, Spain

Published in: *Physical Review X* **13**, 041039 – December 2023.
DOI: 10.1103/PhysRevX.13.041039
Published by: American Physical Society.

Chapter: Certain content of this publication is reproduced in Chapter 4.
Contribution: I analyzed 1/18 blocks of data corresponding to the second half of the third observing run (O3b). I also computed the values on `TABLE XIII` for the columns p_{BBH}, p_{NSBH} and p_{BNS} in `PyCBC-broad` and `PyCBC-BBH` using the method described in Chapter 4.

[6] GWTC-2.1: Deep extended catalog of compact binary coalescences observed by LIGO and Virgo during the first half of the third observing run (2024)

The LIGO Scientific Collaboration and the Virgo Collaboration (incl. **Verónica Villa-Ortega**[1])

[1] *Instituto Galego de Física de Altas Enerxías, Universidade de Santiago de Compostela, Rúa de Xoaquín Díaz de Rábago s/n, E-15782, Spain*

Published in: *Physical Review D* **109**, 022001 – January 2024.
DOI: 10.1103/PhysRevD.109.022001
Published by: American Physical Society.

Chapter: Certain content of this publication is reproduced in Chapter 4.
Contribution: I analyzed 2/22 blocks of data corresponding to the first half of the third observing run (O3a). I also computed the values on `TABLE III` for the PyCBC columns p_{BBH}, p_{NSBH} and p_{BNS} using the method described in Chapter 4.

B

RESUMO DA TESE

Esta tese baséase na detección e seguimento das fusións de sistemas binarios de obxectos compactos (CBCs, polas súas siglas en inglés). No primeiro capítulo preséntanse os conceptos teóricos básicos das ondas gravitacionais, así como unha descrición xeral dos tipos de fontes que as xeran, facendo fincapé nos sistemas binarios de obxectos compactos, e os instrumentos desenvolvidos para a súa detección. No segundo capítulo resúmense os métodos actuais para analizar os datos recollidos polos detectores de ondas gravitacionais, dende a propia detección dos eventos ata a estimación dos parámetros que caracterizan a fonte das ondas. No capítulo 3 introdúcense os algoritmos de busca encargados de atopar os sinais de ondas gravitacionais nos datos do detector e avaliar a significancia dos eventos contra o ruído de fondo. En concreto, descríbense as principais características do algoritmo PyCBC, utilizado durante esta tese. Os capítulos 4 e 5 presentan os dous novos métodos desenvolvidos durante a tese para mellorar a información incluída nas alertas de seguimento de eventos de ondas gravitacionais. No primeiro destes capítulos inclúese unha motivación ao seguimento de eventos de ondas gravitacionais que proveñen de sistemas de baixa masa, así como unha descrición do sistema de alertas entre os detectores de ondas gravitacionais, e os observatorios do espectro electromagnético e de neutrinos. Neste capítulo tamén se describe o primeiro dos métodos desenvolvidos, que estima as probabilidades dun evento (suposto de orixe astrofísica) de pertencer ás distintas categorías de sistemas binarios de obxectos compactos, co obxectivo de informar aos distintos observatorios da probabilidade de que polo menos un dos corpos do sistema sexa unha estrela de neutróns. No seguinte capítulo preséntase o traballo en desenvolvemento do segundo método, deseñado para levar a cabo unha estimación rápida dos parámetros intrínsecos (masas e espíns) dos sistemas binarios de obxectos com-

pactos a través da información obtida polos algoritmos de busca case en tempo real. Neste resumo preséntase unha pequena descrición global dos fundamentos das ondas gravitacionais así como unha explicación da metodoloxía dos algoritmos desenvolvidos e os seus resultados.

B.1 Fundamentos das ondas gravitacionais

As ondas gravitacionais son pequenas flutuacións na curvatura do espazo-tempo causadas polo movemento acelerado de corpos masivos. Estas ondas propáganse polo Universo á velocidade da luz, levando consigo información sobre as propiedades da súa fonte. Aínda que foron predicidas por Albert Einstein en 1916 como solucións á súa teoría da Relatividade Xeral, a súa observación directa non se logrou ata o 14 de setembro de 2015, cando se detectou o primeiro sinal da fusión dun sistema binario de buracos negros (BBH). Hoxe, case 10 anos despois desta primeira detección, a colaboración LIGO-Virgo-KAGRA conta con case 100 detección confirmadas de eventos de ondas gravitacionais procedentes de fusións de sistemas binarios de obxectos compactos, como son as estrelas de neutróns e os buracos negros. Estas observacións proporciónannos novos coñecementos sobre as complexidades do Universo e permiten poñer a proba os límites da Relatividade Xeral.

En principio, todo corpo masivo cunha aceleración non esférica perturba o espazo-tempo, e causa a emisión de ondas gravitacionais. Non obstante, a amplitude destas deformacións é extremadamente pequena, facéndoas non detectables para a maioría das fontes. Deste xeito, as fontes capaces de xerar radiación detectable restrínxense a sistemas movéndose con velocidades ultrarelativistas, ou baixo o efecto de campos gravitacionais fortes. Estes sistemas son tipicamente de orixe astrofísica e altamente dinámicos, como as fusións de sistemas binarios de obxectos compactos, as explosións causadas no colapso dunha supernova ou estrelas de neutróns rotando de forma non simétrica respecto ao eixo de rotación.

B.1.1 Sinal de onda de CBCs

Os sinais emitidos nestes escenarios entran dentro da categoría de sinais modelados, porque as súas formas de onda pódense predicir dentro do marco teórico da Relatividade Xeral. Unha fusión de sistemas binarios de obxectos compactos divídese normalmente en tres etapas: un movemento de espiral cara dentro coñecida como *inspiral*, a fusión ou *merger*, e unha etapa de relaxación do sistema chamada *ringdown*.

Inspiral Nesta etapa os corpos orbitan un con respecto ao outro, emitindo enerxía en forma de ondas gravitacionais no proceso. A órbita redúcese gradualmente debido a esta perda de enerxía. Durante esta fase, que pode durar centos de millóns de anos, a amplitude e a frecuencia das ondas aumenta progresivamente, creando unha forma de sinal característica: o *chirp*.

Merger A fusión ten lugar cando os dous corpos se achegan moi preto e eventualmente chocan nun evento altamente enerxético no que as ondas gravitacionais se emiten nunha explosión de radiación. Esta etapa ten unha duración típica de fraccións de segundo, e caracterízase na forma de onda como un pico na amplitude.

Ringdown Se os corpos son buracos negros, o obxecto resultante despois da fusión é un buraco negro de Kerr perturbado, que oscila ata estabilizarse nun estado relaxado, emitindo ondas gravitacionais cunha amplitude e frecuencia rapidamente decrecente. No caso de que un dos corpos sexa unha estrela de neutróns, o estado final pode ser unha estrela de neutróns masiva, cuxo comportamento é moito máis complexo.

A forma de onda procedente destas fusións está caracterizada por 15 parámetros independentes, divididos en intrínsecos e extrínsecos. Os parámetros intrínsecos básicos son as dúas masas dos obxectos que conforman o sistema, así como as seis compoñentes cartesianas dos seus espíns. Os 7 parámetros extrínsecos restantes localizan a fonde da onda con respecto a cada un dos detectores na Terra, e son a distancia, os dous ángulos polares da orientación no ceo, a inclinación, a polarización da onda e o tempo e a fase da onda na fusión.

B.1.2 Detectores de ondas gravitacionais

Os detectores de ondas gravitacionais actuais son interferómetros de Michelson-Morley avanzados, con dous brazos de varios quilómetros de longo e ortogonais entre sí, deseñados para medir o cambio na lonxitude dos brazos cando son atravesados por unha onda gravitacional. A nivel fundamental, o seu funcionamento é o seguinte. Un feixe láser pre-estabilizado e coherente entra no interferómetro, onde é dividido en dous feixes de igual potencia no espello divisor de feixe. Cada feixe resultante viaxa por cada un dous brazos, atopando ao fondo un espello onde é reflectido de volta ao divisor de feixe, interferindo co feixe do outro brazo. Se a distancia que viaxaron ambos feixes difire, atópanse no divisor de feixe amosando unha diferencia de fase, e un sinal óptico

proporcional a esta diferencia transmítese ao fotodetector de saída. Se ambos feixes viaxaron a mesma distancia, interfiren de xeito destrutivo, e non aparece o sinal óptico no fotodetector.

Estes interferómetros son capaces de medir diferencias na lonxitude dos seus brazos da orde de 10^{-18} m, un tamaño 1000 veces máis pequeno que un protón. Dada esta precisión, aparecen constantemente flutuacións de potencia no fotodetector. Cando estas flutuacións non son causadas polo paso dunha onda gravitacional chámanse ruído. Algunhas fontes de ruído coñecidas son as vibracións da terra causadas por fenómenos naturais ou actividade humana, procesos físicos inherentes ao deseño do detector ou imperfeccións técnicas no mesmo.

B.1.3 Algoritmos de busca de ondas gravitacionais

Despois da toma de datos nos detectores de ondas gravitacionais, os algoritmos de busca analizan estes datos co obxectivo de detectar sinais de onda gravitacional enterrados no ruído presente no detector. Estas buscas pódense clasificar en dous tipos: análises de baixa latencia ou *online*, que permiten obter unha caracterización rápida dos datos e emitir alertas no caso de atopar un posíbel candidato a sinal, e análises *offline*, consistentes nun tratamento máis exhaustivo e preciso dos datos, que permiten confirmar ou descartar os posibles candidatos atopados *online*, así como detectar novos candidatos a sinal. Esta tese realizouse traballando cun algoritmo de busca de fusións de sistemas binarios de obxectos compactos baseado na estadística bayesiana e escrito maioritariamente en Python chamado `PyCBC`, que conta cunha versión de baixa latencia chamada `PyCBC Live`.

O principal método para distinguir sinais de ondas gravitacionais de sistemas binarios de obxectos compactos do ruído do detector chámase filtro adaptado ou *matched filter*. Como a forma das ondas gravitacionais provenientes destes sistemas se pode predicir, é posíbel xerar padróns destas formas de onda, que se almacenan en bancos de padróns. O obxectivo do *matched filter* é ver se os datos conteñen sinais similares a estes padróns de onda. Como os parámetros do sinal non se coñecen a priori, os datos do detector compáranse con tódolos padróns do banco xerado previamente. No caso de que os datos conteñan un sinal semellante a un destes padróns, observase un pico na relación sinal-ruído (SNR), e falamos dunha coincidencia ou *match*. Un sinal real de ondas gravitacionais debe causar unha coincidencia en tódolos detectores da rede no tempo que tardaría a luz en viaxar entre eles. Se isto ocorre, falamos dun candidato a sinal ao que se lle asignan os parámetros característicos do padrón correspondente. A signficancia deste candidato é avaliada polo algo-

ritmo de busca e cuantificada pola relación de falsas alarmas ou FAR. Isto é o número de candidatos a sinal causados por ruído no detector (ou falsas alarmas) que se espera que sexa detectado pola busca cunha signficancia tan alta como o candidato atopado. Canto máis baixo sexa o FAR, máis alta é a probabilidade de que o candidato a sinal sexa de orixe astrofísica e non ruído. Se o FAR supera certo límite, podemos falar de evento ou detección de ondas gravitacionais.

B.2 Seguimento de sinais de ondas gravitacionais

Un dos eventos máis relevantes para a astronomía de ondas gravitacionais foi a primeira observación dun sinal de onda gravitacional procedente dun sistema binario de estrelas de neutróns (BNS). Este evento, chamado GW170817, foi observado polos detectores das colaboracións LIGO e Virgo o 17 de Agosto de 2017. Apenas dous minutos despois da detección do sinal, o telescopio espacial de raios gamma Fermi rexistrou de xeito independente unha explosión de raios gamma procedente da mesma rexión do Universo. Cando as dúas observacións foron correlacionadas, comezou unha extensa campaña de observación en todo o rango do espectro electromagnético. Menos de 11 horas despois da fusión das estrelas de neutróns, detectouse no mesmo punto do ceo o brillo dunha kilonova, e durante os dez seguintes días tamén se observaron sinais de raios X e ondas de radio. Esta foi a primeira (e de momento única) vez que o mesmo evento astrofísico se observou ao mesmo tempo mediante ondas gravitacionais e mediante a súa contrapartida de radiación electromagnética, abrindo a ventá ao campo da astronomía multi-mensaxeiro. Debido á relevancia científica das observacións multi-mensaxeiro, que permiten obter información ata agora descoñecida sobre a natureza das estrelas de neutróns, como a súa ecuación de estado, os esforzos da comunidade astronómica para levar a cabo misións coordinadas de seguimento de sinais de ondas gravitacionais multiplicáronse. Estas contrapartidas electromagnéticas espéranse observar nas fusións de dúas estrelas de neutróns, e nalgúns casos de fusión de unha estrela de neutróns cun buraco negro (NSBH), cando a estrela é disruptada pola forza de marea do buraco. Pola súa natureza, non se espera observar unha contrapartida electromagnética despois dunha fusión de dous buracos negros. Polo tanto, os principais esforzos céntranse no seguimento de eventos de baixa masa, que son máis propensos a implicar polo menos a presenza dunha estrela de neutróns. Con este propósito, cando se observa un evento de ondas gravitacionais, os algoritmos de busca que operan case en tempo real emiten alertas públicas aos observatorios do espectro electromagnético e de neutrinos a través dunha rede

coordinada chamada GCN nos 10 primeiros minutos tras a detección. Estas alertas conteñen, entre outra información, as probabilidades que ten o evento observado de pertencer a cada unha das tres categorías de sistemas binarios de obxectos compactos: BNS, NSBH e BBH.

Dende o final do terceiro período de observación, a principios de 2020, ata que deu comezo o cuarto, a mediados de 2023, leváronse a cabo múltiples melloras na infraestrutura dos detectores de ondas gravitacionais. Estas melloras supoñen un aumento na sensibilidade dos detectores e polo tanto espérase que o número de deteccións aumente de xeito considerable. Non obstante, as capacidades dos observatorios terrestres e espaciais para o seguimento das frecuentes alertas de ondas gravitacionais, están limitadas tanto na súa velocidade de apuntado como no campo de visión e o tempo de observación. Polo tanto, co esperado aumento na frecuencia das deteccións, é fundamental ser capaz de priorizar o seguimento dos eventos que poidan ter un interese astronómico especial. Co obxectivo de facilitar as decisións dos observatorios de seguimento, durante esta tese desenvolvéronse dous métodos para mellorar a información incluída nas alertas.

B.2.1 Estimación da probabilidade de pertenza ás distintas categorías de CBCs

Como se indicou anteriormente, é interesante para o seguimento de sinais de ondas gravitacionais poder estimar rapidamente a probabilidade que ten un posíbel candidato a sinal de pertencer ás distintas categorías de sistemas binarios de obxectos compactos. Asumindo que a orixe do evento é astrofísica, estas categorías son: sistemas binarios de buracos negros (BBH), sistemas binarios de estrelas de neutróns (BNS) e sistemas binarios cunha compoñente buraco negro e outra estrela de neutróns (NSBH). Durante o terceiro período de observación (O3), incluíuse unha cuarta categoría: sistemas binarios con polo menos unha compoñente pertencente ao "oco de masas" ou *Mass Gap*, cunha masa entre 3 e 5 masas solares. Esta categoría foi retirada no cuarto período de observación (O4). O método desenvolvido durante a tese, implementado no algoritmo de baixa latencia `PyCBC Live`, baséase nos datos recuperados polo algoritmo para un posíbel candidato a sinal. Un dos datos que usa o método é a "masa de chío" ou *chirp mass*, unha combinación das masas individuais dos compoñentes do sistema dada por

$$\mathcal{M} = \frac{(m_1 m_2)^{3/5}}{(m_1 + m_2)^{1/5}} \,. \tag{B.1}$$

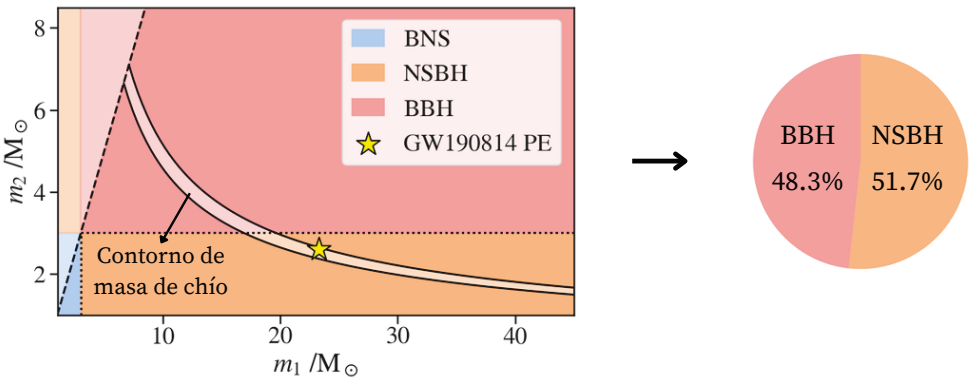

Figura B.1: Exemplo do método de estimación das probabilidades aplicado ao evento GW190814, cunha masa de chío de $\mathcal{M} = 5.99 \pm 0.09 \mathrm{M}_\odot$. As distintas cores representan as áreas das distintas categorías no plano das masas individuais m_1 e m_2, onde o límite entre estrela de neutróns e buraco negro sitúase nas $3\,\mathrm{M}_\odot$. A estrela amarela representa o punto das masas atopadas polos algoritmos de estimación de parámetros, que cae dentro do contorno de masa de chío. Na figura da dereita represéntanse as probabilidades estimadas de que o sinal sexa un evento de dous buracos negros e de que un dos obxectos sexa unha estrela de neutróns.

Para sistemas de baixa masa o algoritmo é capaz de recuperar esta cantidade cunha precisión moi alta, polo que as masas individuais están restrinxidas nun contorno no plano de masas dado por unha liña de masa de chío constante e a súa incerteza $\mathcal{M} \pm \Delta\mathcal{M}$. A idea principal do método é que as probabilidades das distintas categorías asúmense proporcionais ás áreas das distintas rexións do plano de masas dentro deste contorno de masa de chío. Un exemplo aplicado ao evento GW190814, cunha masa de chío de $\mathcal{M} = 5.99 \pm 0.09 \mathrm{M}_\odot$, preséntase na Figura B.1.

O método tamén emprega as distancias efectivas á fonte do sinal, unha cantidade que, entre outros factores, inclúe información da distancia luminosa á fonte. A masa de chío medida no sistema de referencia do detector inclúe unha corrección á masa polo desprazamento ao vermello ou *redshift*, z, provocado pola distancia luminosa entre a fonte e o detector $\mathcal{M}^{\mathrm{det}} = (1+z)\mathcal{M}$. Como as probabilidades se calculan mediante a masa de chío no sistema de referencia da fonte, é necesario estimar o valor desta corrección. Deste xeito, levouse a cabo un axuste entre as distancias efectivas recuperadas por `PyCBC Live` e as correspondentes distancias luminosas calculadas a posteriori mediante outro algoritmo chamado `BAYESTAR` para obter unha relación entre ámbalas dúas. Esta estimación da distancia luminosa permite a estimación do *redshift* do

sinal, que á súa vez permite estimar a masa de chío no sistema de referencia da fonte.

Co obxectivo de comprobar a eficacia do método, este aplicouse a un conxunto de sinais de ondas gravitacionais xerados artificialmente mediante datos do período de observación O2, inxectados nos datos do detector e recuperados por `PyCBC Live`. Este estudo permitiu demostrar que a efectividade é moi alta para sistemas BBH e NSBH e bastante aceptable para sistemas BNS, mellorando en calquera dos casos os resultados do método empregado ata aquel entón. Este novo método empregouse no cálculo dos valores publicados no terceiro catálogo de ondas gravitacionais da colaboración LIGO-Virgo-KAGRA (GWTC-3) e atópase neste momento funcionando en O4 dentro de `PyCBC Live`, onde xa contribuíu na detección do evento GW230529_181500.

B.2.2 FASTPE: Unha estimación rápida dos parámetros intrínsecos de CBCs

Unha forma de mellorar a clasificación de sinais de ondas gravitacionais descrita na sección anterior é empregar, ademais da masa de chío, información sobre as masas e espíns dos obxectos responsables do sinal. Cando un algoritmo de busca de baixa latencia atopa un candidato a sinal xera un *trigger* cos parámetros do padrón que presentou a máxima relación sinal-ruído co candidato a sinal. Debido a varios factores como a presenza de ruído no detector, ou o feito de que os padróns do banco non cobren todo o espazo de parámetros, as masas e os espíns dos *triggers* atopados online poden presentar grandes valores de incerteza. Os métodos de estimación de parámetros existentes empregan técnicas para evitar estas fontes de incerteza, a cambio dun tempo de computación máis longo, non axeitado para as alertas rápidas de seguimento. Polo tanto, as estimacións case en tempo real dos parámetros intrínsecos dos candidatos a sinal consisten agora un reto para os algoritmos de busca online. Nesta tese desenvolveuse un novo método rápido de estimación destes parámetros intrínsecos, chamado `FASTPE`, capaz de estimar as incertezas nas masas e espíns nun tempo de computación aproximado de 1 minuto.

Este método emprega o *trigger* detectado pola busca como punto de partida no espazo de parámetros de masas e espíns. A continuación, xera unha gran cantidade de puntos de mostra neste espazo de parámetros, chamados *samples*, e estima a distancia entre eles e o *trigger* inicial. Como a distancia mídese nun espazo de parámetros correspóndese coa diferencia entre as formas de onda dun sinal descrito polos parámetros do *trigger* e dos descritos polos parámetros dos *samples* xerados. Para simplificar este cálculo, transfórmase o espazo de parámetros das masas e espíns a un espazo xerado polos coeficientes

da expansión post-newtoniana da forma de onda. Estes coeficientes son independentes entre sí, algo que non pasa coas masas e os espíns. Deste xeito, a métrica deste espazo de coeficientes é case chá, e o cálculo das distancias resulta moito máis eficiente. As distancias calculadas convértense en distribucións de probabilidade bayesiana no espazo de parámetros orixinal para atopar os intervalos de confianza onde existe unha probabilidade alta de atopar as masas e os espíns dos obxectos do candidato a sinal.

Para detectar posibles nesgos no método, este aplicouse aos mesmos sinais xerados artificialmente descritos na sección anterior. Dado que as masas e espíns destes sinais se coñecen, podemos avaliar a magnitude das desviacións dos resultados estimados co método e os parámetros físicos correctos. Neste momento, só se estudaron para sinais correspondentes a sistemas BNS, onde non se observan nesgos nos resultados provocados polo método. Por último, `FASTPE` se aplicou a algúns eventos de baixa masa do terceiro período de observación. En gran parte dos casos, o algoritmo é capaz de recrear con bastante precisión nun minuto os intervalos de confianza calculados cos métodos detallados de estimación de parámetros *offline* publicados no catálogo GWTC-3 meses despois da observación do sinal. No futuro, espérase que este método sexa implementado en `PyCBC Live`.

.

C

FIGURES AND TABLES

List of Figures

List of Tables

Copyright licenses of Figures and Tables

Order Date	08-May-2024	**Type of Use**	Republish in a thesis/dissertation
Order License ID	1482098-2		
ISSN	0034-4885	**Publisher**	IOP Publishing
		Portion	Image/photo/illustration

LICENSED CONTENT

Publication Title	Reports on Progress in Physics	**Country**	United Kingdom of Great Britain and Northern Ireland
Author/Editor	Institute of Physics (Great Britain), Physical Society (Great Britain), Institute of Physics and the Physical Society., Institute of Physics Publishing.	**Rightsholder**	IOP Publishing, Ltd
		Publication Type	Journal
Date	01/01/1934		
Language	English		

REQUEST DETAILS

Portion Type	Image/photo/illustration	**Distribution**	Worldwide
Number of Images / Photos / Illustrations	1	**Translation**	Original language of publication
Format (select all that apply)	Print, Electronic	**Copies for the Disabled?**	No
		Minor Editing Privileges?	No
Who Will Republish the Content?	Academic institution	**Incidental Promotional Use?**	No
Duration of Use	Life of current and all future editions	**Currency**	EUR
Lifetime Unit Quantity	Up to 499		
Rights Requested	Main product		

NEW WORK DETAILS

Title	Analysis and follow-up of gravitational wave signals from mergers of compact binaries	**Institution Name**	Universidade de Santiago de Compostela
		Expected Presentation Date	2024-09-30
Instructor Name	Thomas Dent		

ADDITIONAL DETAILS

Order Reference Number	N/A	**The Requesting Person / Organization to Appear on the License**	Verónica Villa Ortega

REQUESTED CONTENT DETAILS

Title, Description or Numeric Reference of the Portion(s)	Figure 5	**Title of the Article / Chapter the Portion Is From**	LIGO: the Laser Interferometer Gravitational-Wave Observatory
Editor of Portion(s)	IOP PUBLISHING	**Author of Portion(s)**	Institute of Physics (Great Britain); Physical Society (Great Britain); Institute of Physics and the Physical Society.; Institute of Physics Publishing.
Volume / Edition	N/A	**Issue, if Republishing an Article From a Serial**	N/A
Page or Page Range of Portion	11	**Publication Date of Portion**	2009-06-30

RIGHTSHOLDER TERMS AND CONDITIONS

These special terms and conditions are in addition to the standard terms and conditions for CCC's Republication Service and, together with those standard terms and conditions, govern the use of the Works. As the User you will make all reasonable efforts to contact the author(s) of the article which the Work is to be reused from, to seek consent for your intended use. Contacting one author who is acting expressly as authorised agent for their co-author(s) is acceptable. User will reproduce the following wording prominently alongside the Work: the source of the Work, including author, article title, title of journal, volume number, issue number (if relevant), page range (or first page if this is the only information available) and date of first publication; and a link back to the article (via DOI); and if practicable, and IN ALL CASES for new works published under any of the Creative Commons licences, the words "© IOP Publishing. Reproduced with permission. All rights reserved" Without the express permission of the author(s) and the Rightsholder of the article from which the Work is to be reused, User shall not use it in any way which, in the opinion of the Rightsholder, could: (i) distort or alter the author(s)' original intention(s) and meaning; (ii) be prejudicial to the honour or reputation of the author(s); and/or (iii) imply endorsement by the author(s) and/or the Rightsholder. This licence does not apply to any article which is credited to another source and which does not have the copyright line '© IOP Publishing Ltd'. User must check the copyright line of the article from which the Work is to be reused to check that IOP Publishing Ltd has all the necessary rights to be able to grant permission. User is solely responsible for identifying and obtaining separate licences and permissions from the copyright owner for reuse of any such third party material figures which the Rightsholder is not the copyright owner of. The Rightsholder shall not reimburse any fees which User pays for a republication license for such third party content. This licence does not apply to any material figure which is credited to another source in the Rightsholder's publication or has been obtained from a third party. User must check the Version of Record of the article from which the Work is to be reused, to check whether any of the material in the Work is third party material. Third party citations and/or copyright notices and/or permissions statements may not be included in any other version of the article from which the Work is to be reused and so cannot be relied upon by the User. User is solely responsible for identifying and obtaining separate licences and permissions from the copyright owner for reuse of any such third party material figures where the Rightsholder is not the copyright owner. The Rightsholder shall not reimburse any fees which User pays for a republication license for such third party content. User and CCC acknowledge that the Rightsholder may, from time to time, make changes or additions to these special terms and conditions without express notification, provided that these shall not apply to permissions already secured and paid for by User prior to such change or addition. User acknowledges that the Rightsholder (which includes companies within its group and third parties for whom it publishes its titles) may make use of personal data collected through the service in the course of their business. If User is the author of the Work, User may automatically have the right to reuse it under the rights granted back when User transferred the copyright in the article to the Rightsholder. User should check the copyright form and the relevant author rights policy to check whether permission is required. If User is the author of the Work and does require permission for proposed reuse of the Work, User should select 'Author of requested content' as the Requestor Type. The Rightsholder shall not reimburse any fees which User pays for a republication license. If User is the author of the article which User wishes to reuse in User's thesis or dissertation, the republication licence covers the right to include the Version of Record of the article, provided it is not then shared or deposited online. User must include citation details. Where User wishes to share their thesis or dissertation online, they should remove the Version of Record before uploading it. User may include a Preprint or the Accepted Manuscript (after the embargo period) in the online version of the thesis or dissertation, provided they do so in accordance with the Rightsholder's policies on sharing Preprints or Accepted Manuscripts. User may need to obtain separate permission for any third party content included within the article. User must check this with the copyright owner of such third party content. Any online or commercial use of User's thesis or dissertation containing the article, including publication via ProQuest, would need to be expressly notified in writing to the Rightsholder at the time of request and would require separate written permission from the Rightsholder. As well as CCC, the Rightsholder shall have the right to bring any legal action that it deems necessary to enforce its rights should it consider that the Work infringes those rights in any way. For content reuse requests that qualify for permission under the STM Permissions Guidelines, which may be updated from time to time, the STM Permissions Guidelines supplement the terms and conditions contained in this license.

If you are producing a new book or article to be published by another STM Signatory publisher, please choose "Reuse in a book under STM Guidelines" or "Reuse in a journal under STM Guidelines." You can consult the STM Guidelines website to see whether your new publisher is a signatory to the STM Permissions Guidelines.

Marketplace Permissions General Terms and Conditions

The following terms and conditions ("General Terms"), together with any applicable Publisher Terms and Conditions, govern User's use of Works pursuant to the Licenses granted by Copyright Clearance Center, Inc. ("CCC") on behalf of the applicable Rightsholders of such Works through CCC's applicable Marketplace transactional licensing services (each, a "Service").

1) **Definitions.** For purposes of these General Terms, the following definitions apply:

"License" is the licensed use the User obtains via the Marketplace platform in a particular licensing transaction, as set forth in the Order Confirmation.

"Order Confirmation" is the confirmation CCC provides to the User at the conclusion of each Marketplace transaction. "Order Confirmation Terms" are additional terms set forth on specific Order Confirmations not set forth in the General Terms that can include terms applicable to a particular CCC transactional licensing service and/or any Rightsholder-specific terms.

"Rightsholder(s)" are the holders of copyright rights in the Works for which a User obtains licenses via the Marketplace platform, which are displayed on specific Order Confirmations.

"Terms" means the terms and conditions set forth in these General Terms and any additional Order Confirmation Terms collectively.

"User" or "you" is the person or entity making the use granted under the relevant License. Where the person accepting the Terms on behalf of a User is a freelancer or other third party who the User authorized to accept the General Terms on the User's behalf, such person shall be deemed jointly a User for purposes of such Terms.

"Work(s)" are the copyright protected works described in relevant Order Confirmations.

2) **Description of Service.** CCC's Marketplace enables Users to obtain Licenses to use one or more Works in accordance with all relevant Terms. CCC grants Licenses as an agent on behalf of the copyright rightsholder identified in the relevant Order Confirmation.

3) **Applicability of Terms.** The Terms govern User's use of Works in connection with the relevant License. In the event of any conflict between General Terms and Order Confirmation Terms, the latter shall govern. User acknowledges that Rightsholders have complete discretion whether to grant any permission, and whether to place any limitations on any grant, and that CCC has no right to supersede or to modify any such discretionary act by a Rightsholder.

4) **Representations; Acceptance.** By using the Service, User represents and warrants that User has been duly authorized by the User to accept, and hereby does accept, all Terms.

5) **Scope of License; Limitations and Obligations.** All Works and all rights therein, including copyright rights, remain the sole and exclusive property of the Rightsholder. The License provides only those rights expressly set forth in the terms and conveys no other rights in any Works

6) **General Payment Terms.** User may pay at time of checkout by credit card or choose to be invoiced. If the User chooses to be invoiced, the User shall: (i) remit payments in the manner identified on specific invoices, (ii) unless otherwise specifically stated in an Order Confirmation or separate written agreement, Users shall remit payments upon receipt of the relevant invoice from CCC, either by delivery or notification of availability of the invoice via the Marketplace platform, and (iii) if the User does not pay the invoice within 30 days of receipt, the User may incur a service charge of 1.5% per month or the maximum rate allowed by applicable law, whichever is less. While User may exercise the rights in the License immediately upon receiving the Order Confirmation, the License is automatically revoked and is null and void as if it had never been issued, if CCC does not receive complete payment on a timely basis.

7) **General Limits on Use.** Unless otherwise provided in the Order Confirmation, any grant of rights to User (i) involves only the rights set forth in the Terms and does not include subsequent or additional uses, (ii) is non-exclusive and non-transferable, and (iii) is subject to any and all limitations and restrictions (such as, but not limited to, limitations on duration of use or circulation) included in the Terms. Upon completion of the licensed use as set forth in the Order Confirmation, User shall either secure a new permission for further use of the Work(s) or immediately cease any new use of the Work(s) and shall render inaccessible (such as by deleting or by removing or severing links or other locators) any further copies of the Work. User may only make alterations to the Work if and as expressly set forth in the Order Confirmation. No Work may be used in any way that is unlawful, including without limitation if such use would violate applicable sanctions laws or regulations, would be defamatory, violate the rights of third parties (including such third

parties' rights of copyright, privacy, publicity, or other tangible or intangible property), or is otherwise illegal, sexually explicit, or obscene. In addition, User may not conjoin a Work with any other material that may result in damage to the reputation of the Rightsholder. Any unlawful use will render any licenses hereunder null and void. User agrees to inform CCC if it becomes aware of any infringement of any rights in a Work and to cooperate with any reasonable request of CCC or the Rightsholder in connection therewith.

8) **Third Party Materials.** In the event that the material for which a License is sought includes third party materials (such as photographs, illustrations, graphs, inserts and similar materials) that are identified in such material as having been used by permission (or a similar indicator), User is responsible for identifying, and seeking separate licenses (under this Service, if available, or otherwise) for any of such third party materials; without a separate license, User may not use such third party materials via the License.

9) **Copyright Notice.** Use of proper copyright notice for a Work is required as a condition of any License granted under the Service. Unless otherwise provided in the Order Confirmation, a proper copyright notice will read substantially as follows: "Used with permission of [Rightsholder's name], from [Work's title, author, volume, edition number and year of copyright]; permission conveyed through Copyright Clearance Center, Inc." Such notice must be provided in a reasonably legible font size and must be placed either on a cover page or in another location that any person, upon gaining access to the material which is the subject of a permission, shall see, or in the case of republication Licenses, immediately adjacent to the Work as used (for example, as part of a by-line or footnote) or in the place where substantially all other credits or notices for the new work containing the republished Work are located. Failure to include the required notice results in loss to the Rightsholder and CCC, and the User shall be liable to pay liquidated damages for each such failure equal to twice the use fee specified in the Order Confirmation, in addition to the use fee itself and any other fees and charges specified.

10) **Indemnity.** User hereby indemnifies and agrees to defend the Rightsholder and CCC, and their respective employees and directors, against all claims, liability, damages, costs, and expenses, including legal fees and expenses, arising out of any use of a Work beyond the scope of the rights granted herein and in the Order Confirmation, or any use of a Work which has been altered in any unauthorized way by User, including claims of defamation or infringement of rights of copyright, publicity, privacy, or other tangible or intangible property.

11) **Limitation of Liability.** UNDER NO CIRCUMSTANCES WILL CCC OR THE RIGHTSHOLDER BE LIABLE FOR ANY DIRECT, INDIRECT, CONSEQUENTIAL, OR INCIDENTAL DAMAGES (INCLUDING WITHOUT LIMITATION DAMAGES FOR LOSS OF BUSINESS PROFITS OR INFORMATION, OR FOR BUSINESS INTERRUPTION) ARISING OUT OF THE USE OR INABILITY TO USE A WORK, EVEN IF ONE OR BOTH OF THEM HAS BEEN ADVISED OF THE POSSIBILITY OF SUCH DAMAGES. In any event, the total liability of the Rightsholder and CCC (including their respective employees and directors) shall not exceed the total amount actually paid by User for the relevant License. User assumes full liability for the actions and omissions of its principals, employees, agents, affiliates, successors, and assigns.

12) **Limited Warranties.** THE WORK(S) AND RIGHT(S) ARE PROVIDED "AS IS." CCC HAS THE RIGHT TO GRANT TO USER THE RIGHTS GRANTED IN THE ORDER CONFIRMATION DOCUMENT. CCC AND THE RIGHTSHOLDER DISCLAIM ALL OTHER WARRANTIES RELATING TO THE WORK(S) AND RIGHT(S), EITHER EXPRESS OR IMPLIED, INCLUDING WITHOUT LIMITATION IMPLIED WARRANTIES OF MERCHANTABILITY OR FITNESS FOR A PARTICULAR PURPOSE. ADDITIONAL RIGHTS MAY BE REQUIRED TO USE ILLUSTRATIONS, GRAPHS, PHOTOGRAPHS, ABSTRACTS, INSERTS, OR OTHER PORTIONS OF THE WORK (AS OPPOSED TO THE ENTIRE WORK) IN A MANNER CONTEMPLATED BY USER; USER UNDERSTANDS AND AGREES THAT NEITHER CCC NOR THE RIGHTSHOLDER MAY HAVE SUCH ADDITIONAL RIGHTS TO GRANT.

13) **Effect of Breach.** Any failure by User to pay any amount when due, or any use by User of a Work beyond the scope of the License set forth in the Order Confirmation and/or the Terms, shall be a material breach of such License. Any breach not cured within 10 days of written notice thereof shall result in immediate termination of such License without further notice. Any unauthorized (but licensable) use of a Work that is terminated immediately upon notice thereof may be liquidated by payment of the Rightsholder's ordinary license price therefor; any unauthorized (and unlicensable) use that is not terminated immediately for any reason (including, for example, because materials containing the Work cannot reasonably be recalled) will be subject to all remedies available at law or in equity, but in no event to a payment of less than three times the Rightsholder's ordinary license price for the most closely analogous licensable use plus Rightsholder's and/or CCC's costs and expenses incurred in collecting such payment.

14) **Additional Terms for Specific Products and Services.** If a User is making one of the uses described in this Section 14, the additional terms and conditions apply:

a) ***Print Uses of Academic Course Content and Materials (photocopies for academic coursepacks or classroom handouts).*** For photocopies for academic coursepacks or classroom handouts the following additional terms apply:

i) The copies and anthologies created under this License may be made and assembled by faculty members individually or at their request by on-campus bookstores or copy centers, or by off-campus copy shops and other similar entities.

ii) No License granted shall in any way: (i) include any right by User to create a substantively non-identical copy of the Work or to edit or in any other way modify the Work (except by means of deleting material immediately preceding or following the entire portion of the Work copied) (ii) permit "publishing ventures" where any particular anthology would be systematically marketed at multiple institutions.

iii) Subject to any Publisher Terms (and notwithstanding any apparent contradiction in the Order Confirmation arising from data provided by User), any use authorized under the academic pay-per-use service is limited as follows:

A) any License granted shall apply to only one class (bearing a unique identifier as assigned by the institution, and thereby including all sections or other subparts of the class) at one institution;

B) use is limited to not more than 25% of the text of a book or of the items in a published collection of essays, poems or articles;

C) use is limited to no more than the greater of (a) 25% of the text of an issue of a journal or other periodical or (b) two articles from such an issue;

D) no User may sell or distribute any particular anthology, whether photocopied or electronic, at more than one institution of learning;

E) in the case of a photocopy permission, no materials may be entered into electronic memory by User except in order to produce an identical copy of a Work before or during the academic term (or analogous period) as to which any particular permission is granted. In the event that User shall choose to retain materials that are the subject of a photocopy permission in electronic memory for purposes of producing identical copies more than one day after such retention (but still within the scope of any permission granted), User must notify CCC of such fact in the applicable permission request and such retention shall constitute one copy actually sold for purposes of calculating permission fees due; and

F) any permission granted shall expire at the end of the class. No permission granted shall in any way include any right by User to create a substantively non-identical copy of the Work or to edit or in any other way modify the Work (except by means of deleting material immediately preceding or following the entire portion of the Work copied).

iv) Books and Records; Right to Audit. As to each permission granted under the academic pay-per-use Service, User shall maintain for at least four full calendar years books and records sufficient for CCC to determine the numbers of copies made by User under such permission. CCC and any representatives it may designate shall have the right to audit such books and records at any time during User's ordinary business hours, upon two days' prior notice. If any such audit shall determine that User shall have underpaid for, or underreported, any photocopies sold or by three percent (3%) or more, then User shall bear all the costs of any such audit; otherwise, CCC shall bear the costs of any such audit. Any amount determined by such audit to have been underpaid by User shall immediately be paid to CCC by User, together with interest thereon at the rate of 10% per annum from the date such amount was originally due. The provisions of this paragraph shall survive the termination of this License for any reason.

b) ***Digital Pay-Per-Uses of Academic Course Content and Materials (e-coursepacks, electronic reserves, learning management systems, academic institution intranets)*** For uses in e-coursepacks, posts in electronic reserves, posts in learning management systems, or posts on academic institution intranets, the following additional terms apply:

i) The pay-per-uses subject to this Section 14(b) include:

A) **Posting e-reserves, course management systems, e-coursepacks for text-based content,** which grants authorizations to import requested material in electronic format, and allows electronic access to this material to members of a designated college or university class, under the direction of an instructor designated by the college or university, accessible only under appropriate electronic controls (e.g., password);

B) **Posting e-reserves, course management systems, e-coursepacks for material consisting of photographs or other still images not embedded in text,** which grants not only the authorizations described in Section 14(b)(i)(A) above, but also the following authorization: to include the requested material in course materials for use consistent with Section 14(b)(i)(A) above, including any necessary resizing, reformatting or modification of the resolution of such requested material (provided that such modification does not alter the underlying editorial content or meaning of the requested material, and provided that the resulting modified content is used solely within the scope of, and in a manner consistent with, the particular authorization described in the Order Confirmation and the Terms), but not including any other form of manipulation, alteration or editing of the requested material;

C) **Posting e-reserves, course management systems, e-coursepacks or other academic distribution for audiovisual content,** which grants not only the authorizations described in Section 14(b)(i)(A) above, but also

the following authorizations: (i) to include the requested material in course materials for use consistent with Section 14(b)(i)(A) above; (ii) to display and perform the requested material to such members of such class in the physical classroom or remotely by means of streaming media or other video formats; and (iii) to "clip" or reformat the requested material for purposes of time or content management or ease of delivery, provided that such "clipping" or reformatting does not alter the underlying editorial content or meaning of the requested material and that the resulting material is used solely within the scope of, and in a manner consistent with, the particular authorization described in the Order Confirmation and the Terms. Unless expressly set forth in the relevant Order Conformation, the License does not authorize any other form of manipulation, alteration or editing of the requested material.

ii) Unless expressly set forth in the relevant Order Confirmation, no License granted shall in any way: (i) include any right by User to create a substantively non-identical copy of the Work or to edit or in any other way modify the Work (except by means of deleting material immediately preceding or following the entire portion of the Work copied or, in the case of Works subject to Sections 14(b)(1)(B) or (C) above, as described in such Sections) (ii) permit "publishing ventures" where any particular course materials would be systematically marketed at multiple institutions.

iii) Subject to any further limitations determined in the Rightsholder Terms (and notwithstanding any apparent contradiction in the Order Confirmation arising from data provided by User), any use authorized under the electronic course content pay-per-use service is limited as follows:

A) any License granted shall apply to only one class (bearing a unique identifier as assigned by the institution, and thereby including all sections or other subparts of the class) at one institution;

B) use is limited to not more than 25% of the text of a book or of the items in a published collection of essays, poems or articles;

C) use is limited to not more than the greater of (a) 25% of the text of an issue of a journal or other periodical or (b) two articles from such an issue;

D) no User may sell or distribute any particular materials, whether photocopied or electronic, at more than one institution of learning;

E) electronic access to material which is the subject of an electronic-use permission must be limited by means of electronic password, student identification or other control permitting access solely to students and instructors in the class;

F) User must ensure (through use of an electronic cover page or other appropriate means) that any person, upon gaining electronic access to the material, which is the subject of a permission, shall see:

- a proper copyright notice, identifying the Rightsholder in whose name CCC has granted permission,
- a statement to the effect that such copy was made pursuant to permission,
- a statement identifying the class to which the material applies and notifying the reader that the material has been made available electronically solely for use in the class, and
- a statement to the effect that the material may not be further distributed to any person outside the class, whether by copying or by transmission and whether electronically or in paper form, and User must also ensure that such cover page or other means will print out in the event that the person accessing the material chooses to print out the material or any part thereof.

G) any permission granted shall expire at the end of the class and, absent some other form of authorization, User is thereupon required to delete the applicable material from any electronic storage or to block electronic access to the applicable material.

iv) Uses of separate portions of a Work, even if they are to be included in the same course material or the same university or college class, require separate permissions under the electronic course content pay-per-use Service. Unless otherwise provided in the Order Confirmation, any grant of rights to User is limited to use completed no later than the end of the academic term (or analogous period) as to which any particular permission is granted.

v) Books and Records; Right to Audit. As to each permission granted under the electronic course content Service, User shall maintain for at least four full calendar years books and records sufficient for CCC to determine the numbers of copies made by User under such permission. CCC and any representatives it may designate shall have the right to audit such books and records at any time during User's ordinary business hours, upon two days' prior notice. If any such audit shall determine that User shall have underpaid for, or underreported, any electronic copies used by three percent (3%) or more, then User shall bear all the costs of any such audit; otherwise, CCC

shall bear the costs of any such audit. Any amount determined by such audit to have been underpaid by User shall immediately be paid to CCC by User, together with interest thereon at the rate of 10% per annum from the date such amount was originally due. The provisions of this paragraph shall survive the termination of this license for any reason.

c) ***Pay-Per-Use Permissions for Certain Reproductions (Academic photocopies for library reserves and interlibrary loan reporting) (Non-academic internal/external business uses and commercial document delivery)*** The License expressly excludes the uses listed in Section (c)(i)-(v) below (which must be subject to separate license from the applicable Rightsholder) for: academic photocopies for library reserves and interlibrary loan reporting; and non-academic internal/external business uses and commercial document delivery.

i) electronic storage of any reproduction (whether in plain-text, PDF, or any other format) other than on a transitory basis;

ii) the input of Works or reproductions thereof into any computerized database;

iii) reproduction of an entire Work (cover-to-cover copying) except where the Work is a single article;

iv) reproduction for resale to anyone other than a specific customer of User;

v) republication in any different form. Please obtain authorizations for these uses through other CCC services or directly from the rightsholder.

Any license granted is further limited as set forth in any restrictions included in the Order Confirmation and/or in these Terms.

d) ***Electronic Reproductions in Online Environments (Non-Academic-email, intranet, internet and extranet)*** For "electronic reproductions", which generally includes e-mail use (including instant messaging or other electronic transmission to a defined group of recipients) or posting on an intranet, extranet or Intranet site (including any display or performance incidental thereto), the following additional terms apply:

i) Unless otherwise set forth in the Order Confirmation, the License is limited to use completed within 30 days for any use on the Internet, 60 days for any use on an intranet or extranet and one year for any other use, all as measured from the "republication date" as identified in the Order Confirmation, if any, and otherwise from the date of the Order Confirmation.

ii) User may not make or permit any alterations to the Work, unless expressly set forth in the Order Confirmation (after request by User and approval by Rightsholder); provided, however, that a Work consisting of photographs or other still images not embedded in text may, if necessary, be resized, reformatted or have its resolution modified without additional express permission, and a Work consisting of audiovisual content may, if necessary, be "clipped" or reformatted for purposes of time or content management or ease of delivery (provided that any such resizing, reformatting, resolution modification or "clipping" does not alter the underlying editorial content or meaning of the Work used, and that the resulting material is used solely within the scope of, and in a manner consistent with, the particular License described in the Order Confirmation and the Terms.

15) **Miscellaneous.**

a) User acknowledges that CCC may, from time to time, make changes or additions to the Service or to the Terms, and that Rightsholder may make changes or additions to the Rightsholder Terms. Such updated Terms will replace the prior terms and conditions in the order workflow and shall be effective as to any subsequent Licenses but shall not apply to Licenses already granted and paid for under a prior set of terms.

b) Use of User-related information collected through the Service is governed by CCC's privacy policy, available online at www.copyright.com/about/privacy-policy/.

c) The License is personal to User. Therefore, User may not assign or transfer to any other person (whether a natural person or an organization of any kind) the License or any rights granted thereunder; provided, however, that, where applicable, User may assign such License in its entirety on written notice to CCC in the event of a transfer of all or substantially all of User's rights in any new material which includes the Work(s) licensed under this Service.

d) No amendment or waiver of any Terms is binding unless set forth in writing and signed by the appropriate parties, including, where applicable, the Rightsholder. The Rightsholder and CCC hereby object to any terms contained in any writing prepared by or on behalf of the User or its principals, employees, agents or affiliates and purporting to govern or otherwise relate to the License described in the Order Confirmation, which terms are in any way inconsistent with any Terms set forth in the Order Confirmation, and/or in CCC's standard operating procedures, whether such writing is prepared prior to, simultaneously with or subsequent to the Order Confirmation, and whether such writing appears on a copy of the Order Confirmation or in a separate instrument.

e) The License described in the Order Confirmation shall be governed by and construed under the law of the State of New York, USA, without regard to the principles thereof of conflicts of law. Any case, controversy, suit, action, or proceeding arising out of, in connection with, or related to such License shall be brought, at CCC's sole discretion, in any federal or state court located in the County of New York, State of New York, USA, or in any federal or state court whose geographical jurisdiction covers the location of the Rightsholder set forth in the Order Confirmation. The parties expressly submit to the personal jurisdiction and venue of each such federal or state court.

Last updated October 2022

American Physical Society
Reuse and Permissions License

18-May-2024

This license agreement between the American Physical Society ("APS") and Verónica Villa Ortega ("You") consists of your license details and the terms and conditions provided by the American Physical Society and SciPris.

Licensed Content Information

License Number:	**RNP/24/MAY/079166**
License date:	18-May-2024
DOI:	10.1103/PhysRevD.102.022004
Title:	Extending the PyCBC search for gravitational waves from compact binary mergers to a global network
Author:	Gareth S. Davies et al.
Publication:	Physical Review D
Publisher:	American Physical Society
Cost:	USD $ 0.00

Request Details

Does your reuse require significant modifications: No

Specify intended distribution locations:	Worldwide
Reuse Category:	Reuse in a thesis/dissertation
Requestor Type:	Student
Items for Reuse:	Figures/Tables
Number of Figure/Tables:	1
Figure/Tables Details:	Figure 3 Diagram showing how background coincidences are formed by time shifts for comparison with three-detector coincidences.
Format for Reuse:	Print and Electronic
Total number of print copies:	Up to 1000

Information about New Publication:

University/Publisher:	Universidade de Santiago de Compostela
Title of dissertation/thesis:	Analysis and follow-up of gravitational wave signals from mergers of compact binaries
Author(s):	Verónica Villa Ortega
Expected completion date:	Sep. 2024

License Requestor Information

Name:	Verónica Villa Ortega
Affiliation:	Individual
Email Id:	v.villaortega@gmail.com
Country:	Spain

American Physical Society
Reuse and Permissions License

17-May-2024

This license agreement between the American Physical Society ("APS") and Verónica Villa Ortega ("You") consists of your license details and the terms and conditions provided by the American Physical Society and SciPris.

Licensed Content Information

License Number:	**RNP/24/MAY/079138**
License date:	17-May-2024
DOI:	10.1103/PhysRevD.109.022001
Title:	GWTC-2.1: Deep extended catalog of compact binary coalescences observed by LIGO and Virgo during the first half of the third observing run
Author:	R. Abbott et al. (The LIGO Scientific Collaboration and the Virgo Collaboration)
Publication:	Physical Review D
Publisher:	American Physical Society
Cost:	USD $ 0.00

Request Details

Does your reuse require significant modifications: No

Specify intended distribution locations:	Worldwide
Reuse Category:	Reuse in a thesis/dissertation
Requestor Type:	Author of requested content
Items for Reuse:	Figures/Tables
Number of Figure/Tables:	1
Figure/Tables Details:	TABLE III. Source probabilities for high significance GW events.
Format for Reuse:	Print and Electronic
Total number of print copies:	Up to 1000

Information about New Publication:

University/Publisher:	Universidade de Santiago de Compostela
Title of dissertation/thesis:	Analysis and follow-up of gravitational wave signals from mergers of compact binaries
Author(s):	Verónica Villa Ortega
Expected completion date:	Sep. 2024

License Requestor Information

Name:	Verónica Villa Ortega
Affiliation:	Individual
Email Id:	v.villaortega@gmail.com
Country:	Spain

PARTIES:

1. **Cambridge University Press** (Licensor); and
2. **Verónica Villa Ortega** (Licensee).

Thank you for your recent permission request. Some permission requests for use of material published by the Licensor, such as this one, are now being facilitated by PLSclear.

Set out in this licence cover sheet (the **Licence Cover Sheet**) are the principal terms under which Licensor has agreed to license certain Licensed Material (as defined below) to Licensee. The terms in this Licence Cover Sheet are subject to the attached General Terms and Conditions, which together with this Licence Cover Sheet constitute the licence agreement (the **Licence**) between Licensor and Licensee as regards the Licensed Material. The terms set out in this Licence Cover Sheet take precedence over any conflicting provision in the General Terms and Conditions.

Free Of Charge Licence Terms

Licence Date:	08/05/2024
PLSclear Ref No:	93687

The Licensor

Company name:	Cambridge University Press
Address:	University Printing House Shaftesbury Road Cambridge CB2 8BS GB

The Licensee

Licensee Contact Name:	Verónica Villa Ortega
Licensee Address:	Rúa Voces Ceibes 2, 1A Santiago de Compostela 15706 Spain

Licensed Material

title:	General Relativity and Gravitation A Centennial Perspective
ISBN:	9781107037311
publisher:	Cambridge University Press

Are you requesting permission to reuse the cover of the publication?	No
Figure number & title	Figure 6.1 Current range of validity of the main analytical and numerical methods to solve the two- body problem.
Page numbers	291
Are you the author of the content that you are requesting to reuse?	No
Will you be changing or editing the image?	No

For Use In Licensee's Publication(s)

usage type	Book, Journal, Magazine or Academic Paper-Thesis or Dissertation
Will your dissertation be placed in an online repository?	Yes
Author	Verónica Villa Ortega
Estimated publication date	2024-09-31
Language	English
Title of dissertation/thesis	Analysis and follow-up of gravitational wave signals from mergers of compact binaries
University or institution	Universidade de Santiago de Compostela
Unlimited circulation?	Yes

Rights Granted

Exclusivity:	Non-Exclusive
Format:	Thesis or Dissertation
Language:	English
Territory:	World
Duration:	Lifetime of Licensee's Edition
Maximum Circulation:	Unlimited

GENERAL TERMS AND CONDITIONS

1. Definitions and Interpretation

1.1 Capitalised words and expressions in these General Terms and Conditions have the meanings given to them in the Licence Cover Sheet.

1.2 In this Licence any references (express or implied) to statutes or provisions are references to those statutes or provisions as amended or re-enacted from time to time. The term including will be construed as illustrative, without limiting the sense or scope of the words preceding it. A reference to in writing or written includes faxes and email. The singular includes the plural and vice versa.

2. Grant of Rights

2.1 The Licensor grants to Licensee the non-exclusive right to use the Licensed Material as specified in the Licence Cover Sheet.

2.2 The rights licensed to Licensee under this Licence do not include the right to use any third party copyright material incorporated in the Licensed Material. Licensee should check the Licensed Material carefully and seek permission for the use of any such third party copyright material from the relevant copyright owner(s).

2.3 Unless otherwise stated in the Licence Cover Sheet, the Licensed Material may be:

2.3.1 subjected to minor editing, including for the purposes of creating alternative formats to provide access for a beneficiary person (provided that any such editing does not amount to derogatory treatment); and/or

2.3.2 used for incidental promotional use (such as online retail providers' search facilities).

2.4 Save as expressly permitted in this Licence or as otherwise permitted by law, no use or modification of the Licensed Material may be made by Licensee without Licensor's prior written permission.

3. Copyright Notice and Acknowledgement

3.1 Licensee must ensure that the following notices and acknowledgements are reproduced prominently alongside each reproduction by Licensee of the Licensed Material:

3.1.1 the title and author of the Licensed Material;

3.1.2 the copyright notice included in the Licensed Material; and

3.1.3 the statement "Reproduced with permission of The Licensor through PLSclear."

4. Reversion of Rights

4.1 The rights licensed to Licensee under this Licence will terminate immediately and automatically upon the earliest of the following events to occur:

4.1.1 the Licensed Material not being used by Licensee within 18 months of the Licence Date;

4.1.2 expiry of the Licence Duration; or

4.1.3 the Maximum Circulation being reached.

5. Miscellaneous

5.1 By using the Licensed Material, Licensee will be deemed to have accepted all the terms and conditions contained in this Licence.

5.2 This Licence contains the entire understanding and agreement of the parties relating to its subject matter and supersedes in all respects any previous or other existing arrangements, agreements or understandings between the parties whether oral or written in relation to its subject matter.

5.3 Licensee may not assign this Licence or any of its rights or obligations hereunder to any third party without Licensor's prior written consent.

5.4 This Licence is governed by and shall be construed in accordance with the laws of England and Wales and the parties hereby irrevocably submit to the non-exclusive jurisdiction of the Courts of England and Wales as regards any claim, dispute or matter arising under or in relation to this Licence.

Order Date	18-May-2024	**Type of Use**	Republish in a thesis/dissertation
Order License ID	1485600-1		
ISSN	0264-9381	**Publisher**	IOP Publishing
		Portion	Chart/graph/table/figure

LICENSED CONTENT

Publication Title	Classical and Quantum Gravity	**Country**	United Kingdom of Great Britain and Northern Ireland
Author/Editor	Institute of Physics (Great Britain)	**Rightsholder**	IOP Publishing, Ltd
Date	01/01/1984	**Publication Type**	Journal
Language	English		

REQUEST DETAILS

Portion Type	Chart/graph/table/figure	**Distribution**	Worldwide
Number of Charts / Graphs / Tables / Figures Requested	1	**Translation**	Original language of publication
		Copies for the Disabled?	No
Format (select all that apply)	Print, Electronic	**Minor Editing Privileges?**	No
Who Will Republish the Content?	Academic institution	**Incidental Promotional Use?**	No
Duration of Use	Life of current and all future editions	**Currency**	EUR
Lifetime Unit Quantity	Up to 499		
Rights Requested	Main product		

NEW WORK DETAILS

Title	Analysis and follow-up of gravitational wave signals from mergers of compact binaries	**Institution Name**	Universidade de Santiago de Compostela
		Expected Presentation Date	2024-09-30
Instructor Name	Thomas Dent		

ADDITIONAL DETAILS

Order Reference Number	N/A	**The Requesting Person / Organization to Appear on the License**	Verónica Villa Ortega

REQUESTED CONTENT DETAILS

Title, Description or Numeric Reference of the Portion(s)	Figure 2	**Title of the Article / Chapter the Portion Is From**	The PyCBC search for gravitational waves from compact binary coalescence
Editor of Portion(s)	IOP Science	**Author of Portion(s)**	Institute of Physics (Great Britain)
Volume / Edition	N/A	**Issue, if Republishing an Article From a Serial**	N/A
Page or Page Range of Portion	9	**Publication Date of Portion**	2016-10-07

RIGHTSHOLDER TERMS AND CONDITIONS

These special terms and conditions are in addition to the standard terms and conditions for CCC's Republication Service and, together with those standard terms and conditions, govern the use of the Works. As the User you will make all reasonable efforts to contact the author(s) of the article which the Work is to be reused from, to seek consent for your intended use. Contacting one author who is acting expressly as authorised agent for their co-author(s) is acceptable. User will reproduce the following wording prominently alongside the Work: the source of the Work, including author, article title, title of journal, volume number, issue number (if relevant), page range (or first page if this is the only information available) and date of first publication; and a link back to the article (via DOI); and if practicable, and IN ALL CASES for new works published under any of the Creative Commons licences, the words "© IOP Publishing. Reproduced with permission. All rights reserved" Without the express permission of the author(s) and the Rightsholder of the article from which the Work is to be reused, User shall not use it in any way which, in the opinion of the Rightsholder, could: (i) distort or alter the author(s)' original intention(s) and meaning; (ii) be prejudicial to the honour or reputation of the author(s); and/or (iii) imply endorsement by the author(s) and/or the Rightsholder. This licence does not apply to any article which is credited to another source and which does not have the copyright line '© IOP Publishing Ltd'. User must check the copyright line of the article from which the Work is to be reused to check that IOP Publishing Ltd has all the necessary rights to be able to grant permission. User is solely responsible for identifying and obtaining separate licences and permissions from the copyright owner for reuse of any such third party material/figures which the Rightsholder is not the copyright owner of. The Rightsholder shall not reimburse any fees which User pays for a republication license for such third party content. This licence does not apply to any material/figure which is credited to another source in the Rightsholder's publication or has been obtained from a third party. User must check the Version of Record of the article from which the Work is to be reused, to check whether any of the material in the Work is third party material. Third party citations and/or copyright notices and/or permissions statements may not be included in any other version of the article from which the Work is to be reused and so cannot be relied upon by the User. User is solely responsible for identifying and obtaining separate licences and permissions from the copyright owner for reuse of any such third party material/figures where the Rightsholder is not the copyright owner. The Rightsholder shall not reimburse any fees which User pays for a republication license for such third party content. User and CCC acknowledge that the Rightsholder may, from time to time, make changes or additions to these special terms and conditions without express notification, provided that these shall not apply to permissions already secured and paid for by User prior to such change or addition. User acknowledges that the Rightsholder (which includes companies within its group and third parties for whom it publishes its titles) may make use of personal data collected through the service in the course of their business. If User is the author of the Work, User may automatically have the right to reuse it under the rights granted back when User transferred the copyright in the article to the Rightsholder. User should check the copyright form and the relevant author rights policy to check whether permission is required. If User is the author of the Work and does require permission for proposed reuse of the Work, User should select 'Author of requested content' as the Requestor Type. The Rightsholder shall not reimburse any fees which User pays for a republication license. If User is the author of the article which User wishes to reuse in User's thesis or dissertation, the republication licence covers the right to include the Version of Record of the article, provided it is not then shared or deposited online. User must include citation details. Where User wishes to share their thesis or dissertation online, they should remove the Version of Record before uploading it. User may include a Preprint or the Accepted Manuscript (after the embargo period) in the online version of the thesis or dissertation, provided they do so in accordance with the Rightsholder's policies on sharing Preprints or Accepted Manuscripts. User may need to obtain separate permission for any third party content included within the article. User must check this with the copyright owner of such third party content. Any online or commercial use of User's thesis or dissertation containing the article, including publication via ProQuest, would need to be expressly notified in writing to the Rightsholder at the time of request and would require separate written permission from the Rightsholder. As well as CCC, the Rightsholder shall have the right to bring any legal action that it deems necessary to enforce its rights should it consider that the Work infringes those rights in any way. For content reuse requests that qualify for permission under the STM Permissions Guidelines, which may be updated from time to time, the STM Permissions Guidelines supplement the terms and conditions contained in this license.

If you are producing a new book or article to be published by another STM Signatory publisher, please choose "Reuse in a book under STM Guidelines" or "Reuse in a journal under STM Guidelines." You can consult the STM Guidelines website to see whether your new publisher is a signatory to the STM Permissions Guidelines.

Marketplace Permissions General Terms and Conditions

The following terms and conditions ("General Terms"), together with any applicable Publisher Terms and Conditions, govern User's use of Works pursuant to the Licenses granted by Copyright Clearance Center, Inc. ("CCC") on behalf of the applicable Rightsholders of such Works through CCC's applicable Marketplace transactional licensing services (each, a "Service").

1) **Definitions.** For purposes of these General Terms, the following definitions apply:

"License" is the licensed use the User obtains via the Marketplace platform in a particular licensing transaction, as set forth in the Order Confirmation.

"Order Confirmation" is the confirmation CCC provides to the User at the conclusion of each Marketplace transaction. "Order Confirmation Terms" are additional terms set forth on specific Order Confirmations not set forth in the General Terms that can include terms applicable to a particular CCC transactional licensing service and/or any Rightsholder-specific terms.

"Rightsholder(s)" are the holders of copyright rights in the Works for which a User obtains licenses via the Marketplace platform, which are displayed on specific Order Confirmations.

"Terms" means the terms and conditions set forth in these General Terms and any additional Order Confirmation Terms collectively.

"User" or "you" is the person or entity making the use granted under the relevant License. Where the person accepting the Terms on behalf of a User is a freelancer or other third party who the User authorized to accept the General Terms on the User's behalf, such person shall be deemed jointly a User for purposes of such Terms.

"Work(s)" are the copyright protected works described in relevant Order Confirmations.

2) **Description of Service.** CCC's Marketplace enables Users to obtain Licenses to use one or more Works in accordance with all relevant Terms. CCC grants Licenses as an agent on behalf of the copyright rightsholder identified in the relevant Order Confirmation.

3) **Applicability of Terms.** The Terms govern User's use of Works in connection with the relevant License. In the event of any conflict between General Terms and Order Confirmation Terms, the latter shall govern. User acknowledges that Rightsholders have complete discretion whether to grant any permission, and whether to place any limitations on any grant, and that CCC has no right to supersede or to modify any such discretionary act by a Rightsholder.

4) **Representations; Acceptance.** By using the Service, User represents and warrants that User has been duly authorized by the User to accept, and hereby does accept, all Terms.

5) **Scope of License; Limitations and Obligations.** All Works and all rights therein, including copyright rights, remain the sole and exclusive property of the Rightsholder. The License provides only those rights expressly set forth in the terms and conveys no other rights in any Works

6) **General Payment Terms.** User may pay at time of checkout by credit card or choose to be invoiced. If the User chooses to be invoiced, the User shall: (i) remit payments in the manner identified on specific invoices, (ii) unless otherwise specifically stated in an Order Confirmation or separate written agreement, Users shall remit payments upon receipt of the relevant invoice from CCC, either by delivery or notification of availability of the invoice via the Marketplace platform, and (iii) if the User does not pay the invoice within 30 days of receipt, the User may incur a service charge of 1.5% per month or the maximum rate allowed by applicable law, whichever is less. While User may exercise the rights in the License immediately upon receiving the Order Confirmation, the License is automatically revoked and is null and void as if it had never been issued, if CCC does not receive complete payment on a timely basis.

7) **General Limits on Use.** Unless otherwise provided in the Order Confirmation, any grant of rights to User (i) involves only the rights set forth in the Terms and does not include subsequent or additional uses, (ii) is non-exclusive and non-transferable, and (iii) is subject to any and all limitations and restrictions (such as, but not limited to, limitations on duration of use or circulation) included in the Terms. Upon completion of the licensed use as set forth in the Order Confirmation, User shall either secure a new permission for further use of the Work(s) or immediately cease any new use of the Work(s) and shall render inaccessible (such as by deleting or by removing or severing links or other locators) any further copies of the Work. User may only make alterations to the Work if and as expressly set forth in the Order Confirmation. No Work may be used in any way that is unlawful, including without limitation if such use would violate applicable sanctions laws or regulations, would be defamatory, violate the rights of third parties (including such third parties' rights of copyright, privacy, publicity, or other tangible or intangible property), or is otherwise illegal, sexually explicit, or obscene. In addition, User may not conjoin a Work with any other material that may result in damage to the reputation of the Rightsholder. Any unlawful use will render any licenses hereunder null and void. User agrees to inform

CCC if it becomes aware of any infringement of any rights in a Work and to cooperate with any reasonable request of CCC or the Rightsholder in connection therewith.

8) **Third Party Materials.** In the event that the material for which a License is sought includes third party materials (such as photographs, illustrations, graphs, inserts and similar materials) that are identified in such material as having been used by permission (or a similar indicator), User is responsible for identifying, and seeking separate licenses (under this Service, if available, or otherwise) for any of such third party materials; without a separate license, User may not use such third party materials via the License.

9) **Copyright Notice.** Use of proper copyright notice for a Work is required as a condition of any License granted under the Service. Unless otherwise provided in the Order Confirmation, a proper copyright notice will read substantially as follows: "Used with permission of [Rightsholder's name], from [Work's title, author, volume, edition number and year of copyright]; permission conveyed through Copyright Clearance Center, Inc." Such notice must be provided in a reasonably legible font size and must be placed either on a cover page or in another location that any person, upon gaining access to the material which is the subject of a permission, shall see, or in the case of republication Licenses, immediately adjacent to the Work as used (for example, as part of a by-line or footnote) or in the place where substantially all other credits or notices for the new work containing the republished Work are located. Failure to include the required notice results in loss to the Rightsholder and CCC, and the User shall be liable to pay liquidated damages for each such failure equal to twice the use fee specified in the Order Confirmation, in addition to the use fee itself and any other fees and charges specified.

10) **Indemnity.** User hereby indemnifies and agrees to defend the Rightsholder and CCC, and their respective employees and directors, against all claims, liability, damages, costs, and expenses, including legal fees and expenses, arising out of any use of a Work beyond the scope of the rights granted herein and in the Order Confirmation, or any use of a Work which has been altered in any unauthorized way by User, including claims of defamation or infringement of rights of copyright, publicity, privacy, or other tangible or intangible property.

11) **Limitation of Liability.** UNDER NO CIRCUMSTANCES WILL CCC OR THE RIGHTSHOLDER BE LIABLE FOR ANY DIRECT, INDIRECT, CONSEQUENTIAL, OR INCIDENTAL DAMAGES (INCLUDING WITHOUT LIMITATION DAMAGES FOR LOSS OF BUSINESS PROFITS OR INFORMATION, OR FOR BUSINESS INTERRUPTION) ARISING OUT OF THE USE OR INABILITY TO USE A WORK, EVEN IF ONE OR BOTH OF THEM HAS BEEN ADVISED OF THE POSSIBILITY OF SUCH DAMAGES. In any event, the total liability of the Rightsholder and CCC (including their respective employees and directors) shall not exceed the total amount actually paid by User for the relevant License. User assumes full liability for the actions and omissions of its principals, employees, agents, affiliates, successors, and assigns.

12) **Limited Warranties.** THE WORK(S) AND RIGHT(S) ARE PROVIDED "AS IS." CCC HAS THE RIGHT TO GRANT TO USER THE RIGHTS GRANTED IN THE ORDER CONFIRMATION DOCUMENT. CCC AND THE RIGHTSHOLDER DISCLAIM ALL OTHER WARRANTIES RELATING TO THE WORK(S) AND RIGHT(S), EITHER EXPRESS OR IMPLIED, INCLUDING WITHOUT LIMITATION IMPLIED WARRANTIES OF MERCHANTABILITY OR FITNESS FOR A PARTICULAR PURPOSE. ADDITIONAL RIGHTS MAY BE REQUIRED TO USE ILLUSTRATIONS, GRAPHS, PHOTOGRAPHS, ABSTRACTS, INSERTS, OR OTHER PORTIONS OF THE WORK (AS OPPOSED TO THE ENTIRE WORK) IN A MANNER CONTEMPLATED BY USER; USER UNDERSTANDS AND AGREES THAT NEITHER CCC NOR THE RIGHTSHOLDER MAY HAVE SUCH ADDITIONAL RIGHTS TO GRANT.

13) **Effect of Breach.** Any failure by User to pay any amount when due, or any use by User of a Work beyond the scope of the License set forth in the Order Confirmation and/or the Terms, shall be a material breach of such License. Any breach not cured within 10 days of written notice thereof shall result in immediate termination of such License without further notice. Any unauthorized (but licensable) use of a Work that is terminated immediately upon notice thereof may be liquidated by payment of the Rightsholder's ordinary license price therefor; any unauthorized (and unlicensable) use that is not terminated immediately for any reason (including, for example, because materials containing the Work cannot reasonably be recalled) will be subject to all remedies available at law or in equity, but in no event to a payment of less than three times the Rightsholder's ordinary license price for the most closely analogous licensable use plus Rightsholder's and/or CCC's costs and expenses incurred in collecting such payment.

14) **Additional Terms for Specific Products and Services.** If a User is making one of the uses described in this Section 14, the additional terms and conditions apply:

a) ***Print Uses of Academic Course Content and Materials (photocopies for academic coursepacks or classroom handouts).*** For photocopies for academic coursepacks or classroom handouts the following additional terms apply:

i) The copies and anthologies created under this License may be made and assembled by faculty members individually or at their request by on-campus bookstores or copy centers, or by off-campus copy shops and other similar entities.

ii) No License granted shall in any way: (i) include any right by User to create a substantively non-identical copy of the Work or to edit or in any other way modify the Work (except by means of deleting material immediately preceding or following the entire portion of the Work copied) (ii) permit "publishing ventures" where any particular anthology would be systematically marketed at multiple institutions.

iii) Subject to any Publisher Terms (and notwithstanding any apparent contradiction in the Order Confirmation arising from data provided by User), any use authorized under the academic pay-per-use service is limited as follows:

A) any License granted shall apply to only one class (bearing a unique identifier as assigned by the institution, and thereby including all sections or other subparts of the class) at one institution;

B) use is limited to not more than 25% of the text of a book or of the items in a published collection of essays, poems or articles;

C) use is limited to no more than the greater of (a) 25% of the text of an issue of a journal or other periodical or (b) two articles from such an issue;

D) no User may sell or distribute any particular anthology, whether photocopied or electronic, at more than one institution of learning;

E) in the case of a photocopy permission, no materials may be entered into electronic memory by User except in order to produce an identical copy of a Work before or during the academic term (or analogous period) as to which any particular permission is granted. In the event that User shall choose to retain materials that are the subject of a photocopy permission in electronic memory for purposes of producing identical copies more than one day after such retention (but still within the scope of any permission granted), User must notify CCC of such fact in the applicable permission request and such retention shall constitute one copy actually sold for purposes of calculating permission fees due; and

F) any permission granted shall expire at the end of the class. No permission granted shall in any way include any right by User to create a substantively non-identical copy of the Work or to edit or in any other way modify the Work (except by means of deleting material immediately preceding or following the entire portion of the Work copied).

iv) Books and Records; Right to Audit. As to each permission granted under the academic pay-per-use Service, User shall maintain for at least four full calendar years books and records sufficient for CCC to determine the numbers of copies made by User under such permission. CCC and any representatives it may designate shall have the right to audit such books and records at any time during User's ordinary business hours, upon two days' prior notice. If any such audit shall determine that User shall have underpaid for, or underreported, any photocopies sold or by three percent (3%) or more, then User shall bear all the costs of any such audit; otherwise, CCC shall bear the costs of any such audit. Any amount determined by such audit to have been underpaid by User shall immediately be paid to CCC by User, together with interest thereon at the rate of 10% per annum from the date such amount was originally due. The provisions of this paragraph shall survive the termination of this License for any reason.

b) ***Digital Pay-Per-Uses of Academic Course Content and Materials (e-coursepacks, electronic reserves, learning management systems, academic institution intranets)*** For uses in e-coursepacks, posts in electronic reserves, posts in learning management systems, or posts on academic institution intranets, the following additional terms apply:

i) The pay-per-uses subject to this Section 14(b) include:

A) **Posting e-reserves, course management systems, e-coursepacks for text-based content,** which grants authorizations to import requested material in electronic format, and allows electronic access to this material to members of a designated college or university class, under the direction of an instructor designated by the college or university, accessible only under appropriate electronic controls (e.g., password);

B) **Posting e-reserves, course management systems, e-coursepacks for material consisting of photographs or other still images not embedded in text,** which grants not only the authorizations described in Section 14(b)(i)(A) above, but also the following authorization: to include the requested material in course materials for use consistent with Section 14(b)(i)(A) above, including any necessary resizing, reformatting or modification of the resolution of such requested material (provided that such modification does not alter the underlying editorial content or meaning of the requested material, and provided that the resulting modified content is used solely within the scope of, and in a manner consistent with, the particular authorization described in the Order Confirmation and the Terms), but not including any other form of manipulation, alteration or editing of the requested material;

C) **Posting e-reserves, course management systems, e-coursepacks or other academic distribution for audiovisual content,** which grants not only the authorizations described in Section 14(b)(i)(A) above, but also the following authorizations: (i) to include the requested material in course materials for use consistent with Section 14(b)(i)(A) above; (ii) to display and perform the requested material to such members of such class in the physical classroom or remotely by means of streaming media or other video formats; and (iii) to "clip" or reformat the requested material for purposes of time or content management or ease of delivery, provided

that such "clipping" or reformatting does not alter the underlying editorial content or meaning of the requested material and that the resulting material is used solely within the scope of, and in a manner consistent with, the particular authorization described in the Order Confirmation and the Terms. Unless expressly set forth in the relevant Order Conformation, the License does not authorize any other form of manipulation, alteration or editing of the requested material.

ii) Unless expressly set forth in the relevant Order Confirmation, no License granted shall in any way: (i) include any right by User to create a substantively non-identical copy of the Work or to edit or in any other way modify the Work (except by means of deleting material immediately preceding or following the entire portion of the Work copied or, in the case of Works subject to Sections 14(b)(1)(B) or (C) above, as described in such Sections) (ii) permit "publishing ventures" where any particular course materials would be systematically marketed at multiple institutions.

iii) Subject to any further limitations determined in the Rightsholder Terms (and notwithstanding any apparent contradiction in the Order Confirmation arising from data provided by User), any use authorized under the electronic course content pay-per-use service is limited as follows:

A) any License granted shall apply to only one class (bearing a unique identifier as assigned by the institution, and thereby including all sections or other subparts of the class) at one institution;

B) use is limited to not more than 25% of the text of a book or of the items in a published collection of essays, poems or articles;

C) use is limited to not more than the greater of (a) 25% of the text of an issue of a journal or other periodical or (b) two articles from such an issue;

D) no User may sell or distribute any particular materials, whether photocopied or electronic, at more than one institution of learning;

E) electronic access to material which is the subject of an electronic-use permission must be limited by means of electronic password, student identification or other control permitting access solely to students and instructors in the class;

F) User must ensure (through use of an electronic cover page or other appropriate means) that any person, upon gaining electronic access to the material, which is the subject of a permission, shall see:

- a proper copyright notice, identifying the Rightsholder in whose name CCC has granted permission,
- a statement to the effect that such copy was made pursuant to permission,
- a statement identifying the class to which the material applies and notifying the reader that the material has been made available electronically solely for use in the class, and
- a statement to the effect that the material may not be further distributed to any person outside the class, whether by copying or by transmission and whether electronically or in paper form, and User must also ensure that such cover page or other means will print out in the event that the person accessing the material chooses to print out the material or any part thereof.

G) any permission granted shall expire at the end of the class and, absent some other form of authorization, User is thereupon required to delete the applicable material from any electronic storage or to block electronic access to the applicable material.

iv) Uses of separate portions of a Work, even if they are to be included in the same course material or the same university or college class, require separate permissions under the electronic course content pay-per-use Service. Unless otherwise provided in the Order Confirmation, any grant of rights to User is limited to use completed no later than the end of the academic term (or analogous period) as to which any particular permission is granted.

v) Books and Records; Right to Audit. As to each permission granted under the electronic course content Service, User shall maintain for at least four full calendar years books and records sufficient for CCC to determine the numbers of copies made by User under such permission. CCC and any representatives it may designate shall have the right to audit such books and records at any time during User's ordinary business hours, upon two days' prior notice. If any such audit shall determine that User shall have underpaid for, or underreported, any electronic copies used by three percent (3%) or more, then User shall bear all the costs of any such audit; otherwise, CCC shall bear the costs of any such audit. Any amount determined by such audit to have been underpaid by User shall immediately be paid to CCC by User, together with interest thereon at the rate of 10% per annum from the date such amount was originally due. The provisions of this paragraph shall survive the termination of this license for any reason.

c) ***Pay-Per-Use Permissions for Certain Reproductions (Academic photocopies for library reserves and interlibrary loan reporting) (Non-academic internal/external business uses and commercial document delivery)*** The License expressly excludes the uses listed in Section (c)(i)-(v) below (which must be subject to separate license from the applicable Rightsholder) for: academic photocopies for library reserves and interlibrary loan reporting; and non-academic internal/external business uses and commercial document delivery.

i) electronic storage of any reproduction (whether in plain-text, PDF, or any other format) other than on a transitory basis;

ii) the input of Works or reproductions thereof into any computerized database;

iii) reproduction of an entire Work (cover-to-cover copying) except where the Work is a single article;

iv) reproduction for resale to anyone other than a specific customer of User;

v) republication in any different form. Please obtain authorizations for these uses through other CCC services or directly from the rightsholder.

Any license granted is further limited as set forth in any restrictions included in the Order Confirmation and/or in these Terms.

d) ***Electronic Reproductions in Online Environments (Non-Academic-email, intranet, internet and extranet)*** For "electronic reproductions", which generally includes e-mail use (including instant messaging or other electronic transmission to a defined group of recipients) or posting on an intranet, extranet or Intranet site (including any display or performance incidental thereto), the following additional terms apply:

i) Unless otherwise set forth in the Order Confirmation, the License is limited to use completed within 30 days for any use on the Internet, 60 days for any use on an intranet or extranet and one year for any other use, all as measured from the "republication date" as identified in the Order Confirmation, if any, and otherwise from the date of the Order Confirmation.

ii) User may not make or permit any alterations to the Work, unless expressly set forth in the Order Confirmation (after request by User and approval by Rightsholder); provided, however, that a Work consisting of photographs or other still images not embedded in text may, if necessary, be resized, reformatted or have its resolution modified without additional express permission, and a Work consisting of audiovisual content may, if necessary, be "clipped" or reformatted for purposes of time or content management or ease of delivery (provided that any such resizing, reformatting, resolution modification or "clipping" does not alter the underlying editorial content or meaning of the Work used, and that the resulting material is used solely within the scope of, and in a manner consistent with, the particular License described in the Order Confirmation and the Terms.

15) **Miscellaneous.**

a) User acknowledges that CCC may, from time to time, make changes or additions to the Service or to the Terms, and that Rightsholder may make changes or additions to the Rightsholder Terms. Such updated Terms will replace the prior terms and conditions in the order workflow and shall be effective as to any subsequent Licenses but shall not apply to Licenses already granted and paid for under a prior set of terms.

b) Use of User-related information collected through the Service is governed by CCC's privacy policy, available online at www.copyright.com/about/privacy-policy/.

c) The License is personal to User. Therefore, User may not assign or transfer to any other person (whether a natural person or an organization of any kind) the License or any rights granted thereunder; provided, however, that, where applicable, User may assign such License in its entirety on written notice to CCC in the event of a transfer of all or substantially all of User's rights in any new material which includes the Work(s) licensed under this Service.

d) No amendment or waiver of any Terms is binding unless set forth in writing and signed by the appropriate parties, including, where applicable, the Rightsholder. The Rightsholder and CCC hereby object to any terms contained in any writing prepared by or on behalf of the User or its principals, employees, agents or affiliates and purporting to govern or otherwise relate to the License described in the Order Confirmation, which terms are in any way inconsistent with any Terms set forth in the Order Confirmation, and/or in CCC's standard operating procedures, whether such writing is prepared prior to, simultaneously with or subsequent to the Order Confirmation, and whether such writing appears on a copy of the Order Confirmation or in a separate instrument.

e) The License described in the Order Confirmation shall be governed by and construed under the law of the State of New York, USA, without regard to the principles thereof of conflicts of law. Any case, controversy, suit, action, or proceeding arising out of, in connection with, or related to such License shall be brought, at CCC's sole discretion, in any federal or state court located in the County of New York, State of New York, USA, or in any federal or state court

whose geographical jurisdiction covers the location of the Rightsholder set forth in the Order Confirmation. The parties expressly submit to the personal jurisdiction and venue of each such federal or state court.

Last updated October 2022

D

COPYRIGHT LICENSES OF PUBLICATIONS

American Physical Society
Reuse and Permissions License

07-May-2024

This license agreement between the American Physical Society ("APS") and Verónica Villa Ortega ("You") consists of your license details and the terms and conditions provided by the American Physical Society and SciPris.

Licensed Content Information

License Number:	**RNP/24/MAY/078815**
License date:	07-May-2024
DOI:	10.1103/PhysRevD.104.042004
Title:	Optimized PyCBC search for gravitational waves from intermediate-mass black hole mergers
Author:	Koustav Chandra et al.
Publication:	Physical Review D
Publisher:	American Physical Society
Cost:	USD $ 0.00

Request Details

Does your reuse require significant modifications: No

Specify intended distribution locations:	Worldwide
Reuse Category:	Reuse in a thesis/dissertation
Requestor Type:	Author of requested content
Items for Reuse:	Whole Article
Format for Reuse:	Print and Electronic
Total number of print copies:	Up to 1000

Information about New Publication:

University/Publisher:	Universidade de Santiago de Compostela
Title of dissertation/thesis:	Analysis and follow-up of gravitational wave signals from mergers of compact binaries
Author(s):	Verónica Villa Ortega
Expected completion date:	Sep. 2024

License Requestor Information

Name:	Verónica Villa Ortega
Affiliation:	Individual
Email Id:	v.villaortega@gmail.com
Country:	Spain

American Physical Society
Reuse and Permissions License

TERMS AND CONDITIONS

The American Physical Society (APS) is pleased to grant the Requestor of this license a non-exclusive, non-transferable permission, limited to Print and Electronic format, provided all criteria outlined below are followed.

1. You must also obtain permission from at least one of the lead authors for each separate work, if you haven't done so already. The author's name and affiliation can be found on the first page of the published Article.
2. For electronic format permissions, Requestor agrees to provide a hyperlink from the reprinted APS material using the source material's DOI on the web page where the work appears. The hyperlink should use the standard DOI resolution URL, http://dx.doi.org/{DOI}. The hyperlink may be embedded in the copyright credit line.
3. For print format permissions, Requestor agrees to print the required copyright credit line on the first page where the material appears: "Reprinted (abstract/excerpt/figure) with permission from [(FULL REFERENCE CITATION) as follows: Author's Names, APS Journal Title, Volume Number, Page Number and Year of Publication.] Copyright (YEAR) by the American Physical Society."
4. Permission granted in this license is for a one-time use and does not include permission for any future editions, updates, databases, formats or other matters. Permission must be sought for any additional use.
5. Use of the material does not and must not imply any endorsement by APS.
6. APS does not imply, purport or intend to grant permission to reuse materials to which it does not hold copyright. It is the requestor's sole responsibility to ensure the licensed material is original to APS and does not contain the copyright of another entity, and that the copyright notice of the figure, photograph, cover or table does not indicate it was reprinted by APS with permission from another source.
7. The permission granted herein is personal to the Requestor for the use specified and is not transferable or assignable without express written permission of APS. This license may not be amended except in writing by APS.
8. You may not alter, edit or modify the material in any manner.
9. You may translate the materials only when translation rights have been granted.
10. APS is not responsible for any errors or omissions due to translation.
11. You may not use the material for promotional, sales, advertising or marketing purposes.
12. The foregoing license shall not take effect unless and until APS or its agent, Aptara, receives payment in full in accordance with Aptara Billing and Payment Terms and Conditions, which are incorporated herein by reference.
13. Should the terms of this license be violated at any time, APS or Aptara may revoke the license with no refund to you and seek relief to the fullest extent of the laws of the USA. Official written notice will be made using the contact information provided with the permission request. Failure to receive such notice will not nullify revocation of the permission.
14. APS reserves all rights not specifically granted herein.
15. This document, including the Aptara Billing and Payment Terms and Conditions, shall be the entire agreement between the parties relating to the subject matter hereof.

The first detection of a binary neutron star coalescence with an electromagnetic counterpart in August 2017 marked the beginning of gravitational-wave multi-messenger astronomy. This thesis explores the follow-up of gravitational wave events from compact binary coalescences, focusing on obtaining rapid and accurate estimations of source parameters essential for enabling multi-messenger observation campaigns. The work details the development and implementation of two algorithms capable of estimating the properties of the source, including the probabilities of containing neutron star or black hole components, as well as accurate estimates of intrinsic masses and spins for low-mass binary systems.